2006

Analysis of conjugate heat transfer in tube-in-block heat exchangers for some engineering applications

Abdullatif Abdulhadi Gari
University of South Florida

Analysis of Conjugate Heat Transfer in Tube-in-Block Heat Exchangers for Some Engineering Applications

by

Abdullatif Abdulhadi Gari

A dissertation submitted in partial fulfillment
of the requirements for the degree of
Doctor of Philosophy
Department of Mechanical Engineering
College of Engineering
University of South Florida

Major Professor: Muhammad M. Rahman, Ph.D.
Roger Crane, Ph.D.
Yehia Hammad, Ph.D.
Autar Kaw, Ph.D.
Stanley Kranc, Ph.D.

Date of Approval:
June 22, 2006

Keywords: microchannels, magnetic refrigerators, electronic cooling, nanofluids, snow melting

Dedication

To Dad for his guidance (1944-2003) and To Mom for her patience.

Acknowledgements

I would like to thank Dr. Rahman for his guidance, support, and patience. I also would like to thank the committee members and faculty members of the Mechanical Engineering Department at the University of South Florida for their teaching and support. I also would like to thank my colleagues who worked with me under Dr. Rahman's supervision for their cooperation and help.

Table of Contents

List of Figures

List of Nomenclature

d	channel diameter, m
D	dimensionless channel diameter, d/H
g_o	heat generation rate, W/m^3
G	magnetic field strength, T
h	heat transfer coefficient, W/m^2-K
h*	dimensionless heat transfer coefficient, $h*L/k_s$
H	height of the substrate, m
k	thermal conductivity, W/m-K
L	channel length, m
nr	number of intervals in r-direction within the tube
nx	number of intervals in x-direction
ny	number of intervals in y-direction
nz	number of intervals in z-direction
p	pressure, Pa
r	distance in radial direction, m
Re	Reynolds number, $\rho Vd/\mu$
S	volume of the solid substrate, m^3
T	temperature, ^oC
V	velocity of fluid, m/s
W	half of the tube spacing, m
x	distance along x-direction, m
y	distance along y-direction, m
z	distance along z-direction, m
Z	dimensionless distance along axial direction, x/L

Greek Symbols

α	thermal diffusivity, m^2/s
ρ	density, kg/m^3
ν	kinematic viscosity, m^2/s
ϕ	angular coordinate, radian
θ	dimensionless temperature, $(T-Tin)/[(g_o.S)/(k_s.d)]$

Subscripts

f	fluid
in	inlet
max	maximum
r	radial
s	solid
z	axial
ϕ	angular

Analysis of Conjugate Heat Transfer in Tube-in-Block Heat Exchangers for Some Engineering Applications

Abdullatif Abdulhadi Gari

ABSTRACT

This project studied the effect of different parameters on the conjugate heat transfer in tube-in-block heat exchangers for various engineering applications. These included magnetic coolers (or heaters) associated with a magnetic refrigeration system, high heat flux coolers for electronic equipment, and hydronic snow melting system embedded in concrete slabs. The results of this research will help in designing the cooling/heating systems and select their appropriate geometrical dimensions and material for specific applications. Types of problems studied in this project are: steady state circular microchannels with heat source in the gadolinium substrate, transient heat transfer in circular microchannels with time varying heat source in a gadolinium substrate, transient heat transfer in composite trapezoidal microchannels of silicon and gadolinium with constant and time varying heat source, steady state heat transfer in microchannels using fluids suspended with nanoparticles, and analysis of steady state and transient heat transfer in a hydronic snow melting system. For each of these problems a numerical simulation model was developed. The mass, momentum, and energy conservation equations were solved in the fluid region and energy conservation in the

solid region of the heat exchanger to arrive at the velocity and temperature distributions. Detailed parametric study was carried out for each problem. Parameters were Reynolds number, heat source value, channel diameter or channel height, solid materials and working fluids. Results are presented in terms of solid-fluid interface temperature, heat flow rate, heat transfer coefficient, and Nusselt number along the length of the channel and with the progression of time. The results showed that an increase in Reynolds number decreases the interface temperature but increases the heat flow rate and Nusselt number. When the heat source varied with time, by applying and removing the magnetic field, the interface temperature, heat flow rate, and Nusselt number attained a periodic variation with time. The decrease in the diameter at constant Reynolds number decreases the interface temperature and increases the heat flow rate at the fluid-solid interface.

Chapter 1 – Introduction and Literature Review

1.1 Introduction

Tube-in-block is the most popular heat exchangers in the industry. Some of the applications that use this type of heat exchangers are: Magnetic refrigeration, electronic cooling, and hydronic snow melting system. Magnetic refrigeration and electronic cooling use tube-in-block heat exchangers at a microscopic scale.

Magnetic refrigeration profits from the fact that the temperature of certain materials increases when placed in a magnetic field, and likewise decreases when the magnetic field is removed. This phenomenon is known as the "magnetocaloric effect". Figure 1.1 shows a schematic drawing of the bed and heat exchanger assembly. This study is concerned with the magnetocaloric beds only. The magnocaloric beds are microchannels fabricated in a magnocaloric material substrate. The material used in this project is gadolinium. When a microchannel consists of Gadolinium substrate is exposed to a magnetic field, it generates heat in the Gadolinium substrate. This heat generation in the system is dissipated with fluid flowing through the microchannels.

Electronic cooling is a technique that removes heat from a silicon wafer. It consists of microchannels embedded in a chip substrate on one side and electronic circuits located on the other side of the wafer. A cover plate made of pyrex glass is bonded on the microchannels to form the closed channel construction. The wafer with the

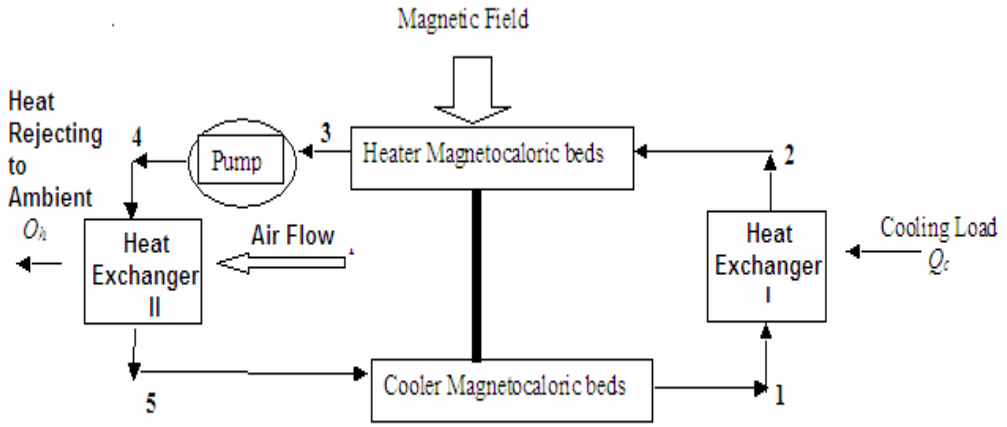

Figure 1.1: Schematic drawing of the bed heat exchanger assembly for magnetic refrigerating [1]

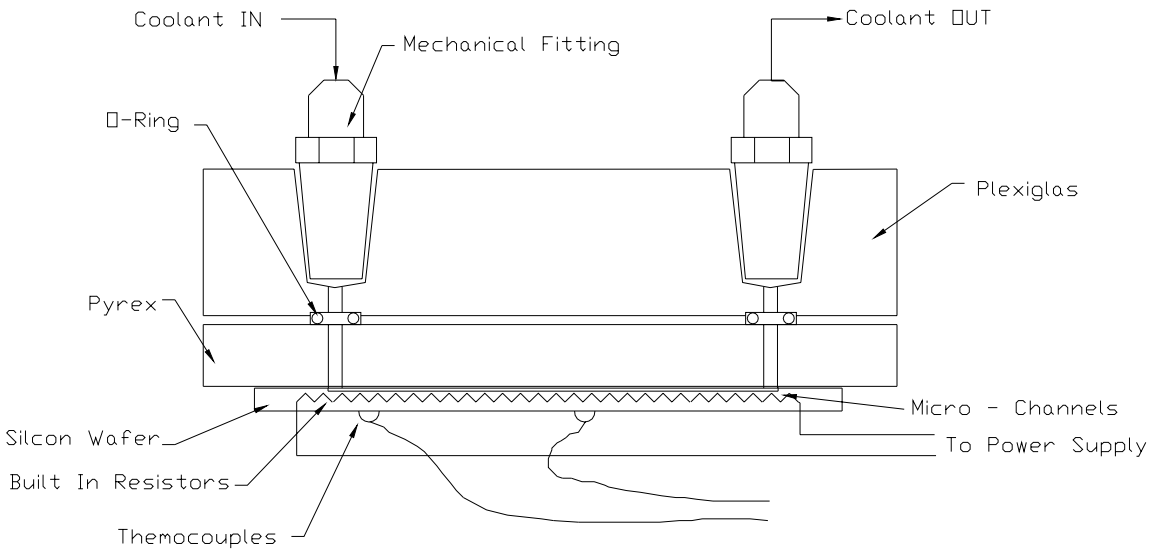

Figure 1.2: Schematic drawing for a microchannel test fixture used for electronic cooling [2]

pyrex cover plate was mounted on a Plexiglas plate containing inlet and outlet connections for fluid flow (figure 1.2). The increase in power dissipation of electronic circuits led researchers to study varieties of different designs to improve and come up with better microchannel performances. Some researchers introduced a way to achieve high heat dissipation by increasing the thermal conductivity of the fluid with the suspension of nanoparticles of a solid that has much higher thermal conductivity than the fluid. Different microchannel geometries as well as substrate materials and working fluid coolants have great effect on the heat dissipation performance.

Hydronic snow melting system is widely used in the industry for a range of applications such as side walks, driveways, bridges and airplane runways. The purpose of this system is to melt snow and clear the road pedestrians and vehicles. It consists of piping system embedded in concrete slab where hot fluid pumped in to warm up the slab. The pipes are placed in spiral pattern to distribute heat equally within the slab. Hot fluid runs through the pipes to heat up the slab and melt the accumulated snow on the surface. Figure 1.3 shows a schematic drawing for the hydronic snow melting system.

This work presents a parametric study for fluid flow and heat transfer in the applications of magnetic refrigeration, electronic cooling, and hydronic snow melting application. Some of these parameters include Reynolds number, magnetic field and tube diameter. The results are presented as the peripheral average interface temperature, heat flow rate, heat transfer coefficient, and Nusselt number. Steady state as well as transient cases were considered in this study to arrive to an understanding about the performance of tube-in-block heat exchangers.

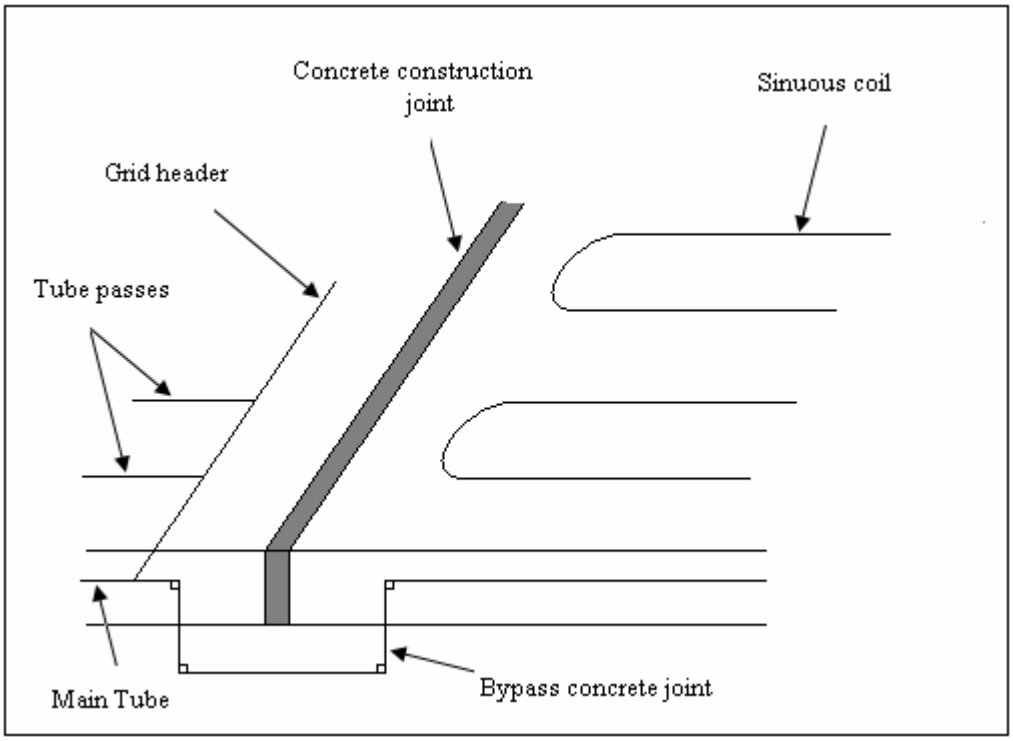

Figure 1.3: Schematic drawing for hydronic snow melting system [3]

1.2 Literature Review

1.2.1 Steady State Heat Transfer in Rectangular and Trapezoidal Microchannels

Peng and Peterson [4] experimentally investigated single-phase forced convective heat transfer of water in small rectangular microchannels for different diameters. The results stated that the geometry had a significant effect on the single-phase convective heat transfer. It was also found that the laminar heat transfer is dependent upon the aspect ratio. The turbulent was found to be a function of a non-dimensional variable Z, such that Z=0.5 is the optimum configuration regardless the channel's aspect ratio. Empirical correlations were suggested for calculating both the heat transfer and the pressure drop. Papautsky et al. [5] described the effect of a rectangular microchannel aspect ratio on

laminar friction constant. The experimental data obtained for the water showed an approximate 20% increase in the friction constant for a specified driving potential when compared to micro-scale predictions from the classical Navier-Stokes theory. Lower aspect ratio also showed a substantial increase of 20% in friction constant. The experiment data also showed a similar increase when low Reynolds numbers are used (less than 100). Qu et. al. [6] investigated heat transfer characteristics of water flowing through trapezoidal silicon microchannels. A numerical analysis was also carried out by solving a conjugate heat transfer problem to determine the temperature field in both solid and fluid regions. When comparing the experimental results to those numerical predictions it was found that Nusselt number found experimentally is much lower. This may be due to the effects of surface roughness of the microchannel walls. A modified relation that was established based on roughness-viscosity model was suggested to account for the roughness-viscosity effects in future experimental work.

Rahman [2] presented new experimental measurements for pressure drop and heat transfer coefficient in microchannel heat sinks. Two different channel patterns were used: the parallel pattern and the series pattern. Channels of different depths or aspect ratio were studied while water was used as the working fluid. Flow rate, pressure and temperature were measured at several locations in the wafer to calculate the local and average Nusselt number and coefficient of friction in the device for different flow rate, channel size, and channel configuration. Yang et al. [7] studied the entry flow induced by an applied electrical potential through microchannels between two parallel plates. A nonlinear, two dimensional Poisson equation, zeta potential and Nernst-Planck equation were numerically solved using a finite difference method. A body force was included in

the full Navier-Stokes equations. The effect of the entrance region on the fluid velocity distribution, charge density boundary layer, entrance length, and shear stress are discussed. It was found that the thickness of electrical double layer (EDL) in the entry region is thinner than that in the fully developed region. The change in the velocity profile was apparent in the entry region and the axial velocity profile is no longer flat across the channel height when the Reynolds number is large. Quadir et. al. [8] applied a finite element method to evaluate the performance of microchannel heat exchangers used in electronic packaging. The finite element method was proved satisfactory to predict the surface temperature and fluid temperature when compared with other results obtained from different concepts. This method allows us to calculate the total thermal resistance of the microchannel heat sink from the surface and fluid temperature fields. This methodology added an advantage of modeling a non-uniform surface heat flux distribution and could be used as an alternative to massive CFD calculations.

Rahman and Shevade [9] studied square and rectangular microchannel with heat generation in the substrate. Water was the working fluid in a gadolinium substrate. The governing equations in both solid and fluid regions were solved numerically for the velocity and temperature profiles. Varying the aspect ratio, Reynolds number, and heat generation, it was found that Nusselt number is larger near the entrance and decreases downstream due to the development of the thermal boundary layer. It was also noticed that for larger Reynolds number the outlet temperature decreased and the average heat transfer coefficient increased. Rahman et. al. [10] has studied the analysis of heat transfer processes during the heat up and cool down phases of a magnetic material substrate when subjected to a magnetic field. A computer simulation of fluid flow and heat transfer are

carried out. Rectangular and square microchannels were considered where water was the working fluid and Gadolinium was the substrate material. The parametric study included heat generation, aspect ratio and Reynolds number. They found a sinusoidal behavior for the heat transfer coefficient along time. Tunc and Bayazitoglu [11] studied the convection heat transfer in rectangular microchannel and assumed a fully developed both thermally and hydrodynamically fluid flow. Because of the rectangular cross-section shape momentum equations were solved first and then substituted in the energy equation. The integral transform technique is applied twice, once for velocity and once for temperature. This gives a uniform temperature and uniform heat flux boundary conditions. The results showed similar behavior to previous studies on circular microtubes. The values of Nusselt number were presented by varying the aspect ratio. Pfund et al. [12] determined friction factor for high aspect ratio microchannels. Reynolds number was between 60 and 3450. Pressure drop were measured within the channel. Transition to turbulence was observed with flow visualization. Kohl et al. [13] experimentally examined the pressure drop in microchannels. Straight channel test section with rectangular microchannels was used. Koo and Kleinstreuer [14] investigated the effects of viscous dissipation on the temperature field and ultimately on the friction factor using dimensional analysis and computer simulation. It turned out that for microconduits, viscous dissipation is a strong function of the channel aspect ratio, Reynolds number, Eckert number, Prandtl number, and conduit hydraulic diameter.

1.2.2 Steady State Heat Transfer in Circular Microchannels

Lelea et al. [15] conducted an experimental and numerical research on heat transfer and fluid flow in microtubes. The diameters selected were 0.1, 0.3 and 0.5 mm and Reynolds number range used was up to 800. Distilled water was used as the working fluid and stainless steel as the substrate material. The experimental results confirmed the conventional or classical theories are applicable for water flow through microchannel of above size. Yu et. al. [16] investigated fluid flow and heat transfer characteristics of dry nitrogen gas and water in microtubes with diameters of 19, 52, and 102 micrometers were investigated with Reynolds number ranging from 250 20,000 and Prandtl number ranging from 0.7 to 5. Lower values for the product f*Re were observed for smaller diameters. The reduction in f*Re was more for laminar flow. The heat transfer and Nusselt number were much higher in the turbulent regime for smaller diameters. Adams et. al. [17] investigated turbulent, single phase forced convention of water in circular microchannels with diameters of 0.76 and 1.09 mm. It was found that Nusselt number resulted are higher than those predicted by traditional large channel correlations. Based on data presented and earlier data for smaller diameter channels, a generalized correlation was developed for the Nusselt number for turbulent, single-phase, forced convection in circular microchannels.

Owhaib and Palm [18] experimentally investigated the heat transfer characteristics of single-phase forced convention of R-134a through microtubes. The diameters were 1.7, 1.2, and 0.8 mm and both laminar and turbulent flows were employed with Reynolds number from less than 1,000 to 17,000. The results were compared to both correlations suggested for macroscale and microscale channels. The experimental results in the

turbulent regime showed agreement with correlations of the classical macroscale correlations but not with any of the suggested correlations for microchannels. The experimental results for the heat transfer coefficient in the laminar region were almost identical for all three diameters. Celata et. al. [19] studied the experimental researches carried out in single phase heat transfer and flow in capillary tubes. The laminar and transition regimes were analyzed in detail to clarify the discrepancies among the results obtained by different researchers. The examined experiments showed that the friction factor is in good agreement with the Hagen-Poiseuille theory for Reynolds numbers below 600-800. The transition from laminar to turbulent regime occurred at Reynolds number between 1900 and 2500. Diabatic experiments showed that heat transfer correlations in laminar and turbulent regimes, developed for conventional tubes, were not properly adequate for heat transfer coefficients predictions in microtubes. Rao and Rahman [20] investigated a steady state laminar flow for a circular microtube in a rectangular substrate. Silicon, Silicon Carbide, and stainless steel were used for substrate materials while water and FC-72 were used as the coolants. In addition, Reynolds number and geometrical dimensions were varied for a thorough investigation. The results showed that Nusselt number was highest for the Silicon substrate and FC-72 coolant case and lowest for the stainless substrate and water coolant case. It also showed that increasing the hydraulic diameter and Reynolds number results in higher average Nusselt number.

Nield and Kuznetsov [21] analytically examined steady laminar flow of an incompressible fluid through a tube of almost circular cross-section, first for the case of a tube whose wall is wavy in the azimuthal direction, and then for one wavy in the axial direction. Giulio and D'Agaro [22] investigated the roughness effects on heat transfer and

pressure losses in microscale tubes and channels using a finite element CFD code. Surface roughness was explicitly modeled through a set of randomly generated peaks along the ideal smooth surface. Grohmann [23] presented an experimental technique and experimental results of heat transfer measurements in microtubes of 250 and 500 μm diameter. The data obtained with single phase argon showed no physical difference of heat transfer mechanism between micro- and macrotubes. Broderick et al. [24] analyzed the thermally developing electro-osmotically generated flow within circular microtubes with finite Debye-layer thickness. The effect of variations in the relative microtube radius and strength of the Joule and viscous heating on the thermal transport were explored over the possible ranges of the governing parameters. Chakraborty [25] developed closed form expressions for Nusselt number variation in a thermally fully developed microtube flow, under a combined influence of electroosmotic forces and imposed pressure gradient. Significant insights were also developed regarding the influence of adverse pressure gradients on the thermal transport in the presence of aiding electroosmotic effects. Hwang and Kim [26] investigated the pressure drop characteristics in microtubes using R-134a as the test fluid. A new correlation to predict the two-phase flow pressure drop in microtubes was developed.

1.2.3 Transient Heat Transfer in Microchannels

Yang et. al. [27] studied transient aspects of electroosmotic flow in a slit microchannel. Exact solution for the electrical potential profile and the transient electroosmotic flow field are obtained. This was done by solving the complete Poisson-Boltzmann equation and the Navier-Stokes equation under an analytical approximation

for the hyperbolic sine function. The characteristics of the transient electroosmotic flow were discussed under influences of the electric double layer and geometric size of the microchannel.

1.2.4 Heat Transfer Using Nanofluids

There are researchers who worked on nanofluids such as Eastman et. al. [28] who studied nanofluids for ethylene glycol suspended with copper and oxide nanoparticles. Based on his calculations, there was a significant increase in the fluid thermal conductivity by 40% for 0.3% volume fraction of copper in ethylene glycol for diameters less than 10 nm. The effects are anomalous based on previous theoretical calculations that had predicted a strong effect of particle shape on effective nanofluid thermal conductivity, but no effect on either particle size or particle thermal conductivity. Keblinski et.al. [29] explained the increase in the composite thermal conductivity due to grain size reduction by exploring four possible explanations: Brownian motion of the particles, molecular-level layering of the liquid at the liquid/particle interface, the nature of the heat transport in the nanoparticles, and the effects of nanoparticles clustering. He concluded that the key factor to understand the thermal properties of nanofluids are the ballistic, rather than diffusive, nature of heat transport in the nanoparticles, combined with direct or fluid-mediated clustering effects that provide paths for rapid heat transport. Cheng and Law [30] have introduced an exponential model to calculate the effective viscosity for a fluid suspended with nanoparticles. Theoretical consideration is restricted to the dilute condition without effects of dynamic particle interactions and fluid turbulence. This led to power series expressed in terms of particle concentration. The

derivation then extended using an exponential model for the condition of high particle concentration. His model was found to be comparable to various empirical formulas available in the literature.

Putra et. al. [31] has investigated natural convection for nanofluids inside horizontal cylinder heated from one end and cooled from the other. His experiment resulted in paradoxical behavior of heat transfer deterioration. He investigated this deterioration in the heat transfer and its dependence on parameters such as the particle concentration, material of the particles and the geometry of the containing cavity. He suggested more investigation done before practical applications of cooling system using nanofluids to understand the physical phenomenon. Bang and Chang [32] have studied the boiling heat transfer characteristics of water suspended with nanoparticles of alumina with different volume concentration. Pool boiling heat transfer coefficients and phenomena were compared with those of pure water. The experimental results show that these nanofluids have poor heat transfer performance compared to pure water in natural convection and nucleate boiling. On the other hand, CHF has been enhanced in not only horizontal but also vertical pool boiling. Comparisons to the Rhosenow correlation showed that the correlation can potentially predict the performance with an appropriate modified liquid-surface combination factor and changed physical properties of the base liquid. Vadasz et. al. [33] has investigated theoretically the impressive increase in thermal conductivity of nanofluids achieved experimentally in the literature. His work was done on a macroscale level aiming to explain the possible mechanism behind the impressive increase in the composite thermal conductivity. He explained that the thermal wave effects via hyperbolic heat conduction could have been the reason behind the excessive

improved effective thermal conductivity. He suggested that alternative possibilities should be investigated before reaching an ultimate conclusion.

Wen and Ding [34] examined the effect of particle migration on heat transfer under a fully developed laminar flow regime. The flow model takes into account the effects of shear-induced and viscosity-gradient-induced particle migration as well as self diffusion due to Brownian motion, which is coupled with an energy equation. The results suggest a significant non-uniformity in particle concentration. This leads to a higher Nusselt number compared to constant thermal conductivity assumption. Further improvement of the model is needed to take into account other factors such as entrance effects, dynamics of particles and particle-wall interactions. Maiga et. al.[35] has studied the forced convection flow of water-Al_2O_3 and ethylene glycol-Al_2O_3 nanofluids inside a uniformly heated tube that is submitted to a constant and uniform heat flux at the wall. It was found that nanoparticles enhanced the heat transfer at the tube wall for both laminar and turbulent flows. The improvement of heat transfer increases even more with the increase in nanoparticles concentration. The presence of nanoparticles also produces adverse effect on the wall friction that increases with the particle volume concentration. Results also showed that the ethylene glycol- Al_2O_3 mixture gives a far better heat transfer enhancement than water-Al_2O_3 mixture. Wang and Xu [36] measured the effective thermal conductivities for fluids suspended with nanoparticles by a steady state parallel method. They tested water, vacuum pump fluid, engine oil and ethylene glycol suspended with Al_2O_3 and CuO. Their experimental results showed that nanofluids have higher thermal conductivities than those of base fluids. Compared to theoretical models, the predicted thermal conductivities of mixtures are much lower than the measured data.

They suggested that more comprehensive theory is needed to fully explain the nanofluid behavior.

1.2.5 Hydronic Snow Melting System

Before 1952, researchers only considered the energy required to melt the snow. In 1952, Chapman published two articles considering the requirements of heat and mass transfer. The first [37] one described five energy requirements for the snow melting process. These five energy requirements are the heat of fusion, sensible heat gain from snowfall, heat of vaporization, heat transfer by radiation and convection, and back loss to the ground. The sum of the first four terms equals the required heat output at the upper surface. The second [38] article suggested considering a frequency distribution of the loads. The article confirms that the actual load should be determined on an hourly basis. Then make a frequency distribution analysis to set the design capacity. The author introduced the concept of free area ratio in this article. Chapman [39] also showed that four factors contribute to the total load. None of the four factors can be singled out. Only the frequency analysis of combined four loads is sufficient to determine the required thermal output of the system. He also addressed the issue of relating the inches of water equivalent to inches of snowfall topic. Updated design guidelines and recommendations were presented by Ramsey et al [40]. He reviewed and identified recommended revisions to the current ASHRAE snow melting load calculation procedures. It also provided sample results based on the revised procedure. The load at the melting surface included sensible and snow melting loads along with the heat losses due to convection, radiation, and evaporation. The correlations used are accepted for turbulent convection heat transfer

coefficient. The convection and evaporation losses are calculated as functions of wind speed and the characteristic dimensions of the slab. Calculations are performed for a baseline case using the wind speed as reported from the meteorological data.

Kilkis [41] studied the complex hydronic space conditioning and snow melting circuits. These systems operate at moderate supply temperature at the expense of large temperature drop and wide diversity of generally oversized equipment. He presented a simple analytical algorithm that can accurately calculate equipment temperature drop and heating capacity, energy loss and fluid flow rate in a complex circuit. Kilkis has also published two papers in 1994. In the first article [42], he discussed the need to develop a universal and simple technique that does not require extensive manipulation of meteorological data in the first publication. He recommended that the design algorithm should require only the air temperature, wind speed and maximum recorded daily snowfall in order to calculate the heat requirement. In the second publication [43] he developed a simple analytical technique to predict the transfer of heat in the snow melting slab while retaining sufficient accuracy. Bounded by ASHRAE guidelines, his method was applied for a limited design range using metal pipes. Results of sample designs were compared to solutions used finite element method. The comparison indicated sufficient accuracy for engineering calculations. Rees et al [44] addressed the issue that the transient response of snow melting systems for pavement are operated intermittently and that it has a significant effect on the overall system performance. He developed a two-dimensional numerical transient analysis method that includes a boundary condition model able to deal with different snow melting conditions. Parametric study was carried out examining the transient effects using real storm data for a real storm event and the

results were presented. He found that effects of storm structure were of most significance. He also presented calculations of the back and edge losses under transient conditions.

1.3 Objectives

From the microchannel literature review, it appears that none of the previous studies have addressed the heat generation within the substrate material for circular micro tubes. The main emphasis of this study is to develop a simulation model for fluid flow and heat transfer in circular microchannels by taking into account the heat generation in the solid due to applied magnetic field, conduction in the solid and convection of heat to the fluid. Gadolinium was chosen to be the solid substrate material and water as the working fluid. Detailed parametric study is carried out to study the effect of Reynolds number, heat generation rate and diameter of the tube. Steady state and transient cases were studied to better understand the effect of different parameters on the performance of the system.

Nanofluids were investigated in the literature review. Researchers presented experimental and theoretical work on nanofluids. One researcher presented a molecular dynamic simulation based on mathematical model to explore four possible explanations for the significant increase in the nanofluids thermal conductivity. The simulation did not show a parametric study to understand the effect of different parameters on the system. This project suggests that nanofluid is applied into an existing microtube model developed by Rao and Rahman [20] and study the nanofluids under different conditions. This could result in new understanding to the behavior of nanofluids under conditions existing in the literature. Different solid substrate material and working nanofluids were

chosen. Parametric study was carried out to study the effect of Reynolds number, and diameter of the tube.

Literature has provided a number of hydronic snow melting researches to calculate the heat load required for snow melting at different steady and transient conditions. Results were tabulated for different conditions and parameters. These results of previous work are based on a two dimensional calculations ignoring the fact that the fluid looses heat and drops in temperature while transferring through the slab in the third direction. As the fluid temperature drops along the slab in the axial direction, it decreases the heat flow rate to the system and thus the snow melting process. Design parameters were studied in previous work for calculation of the heat load required for snow melting at different conditions. Their direct effect on the heat flow rate and snow melting performance was not emphasized. In this project, a three dimensional model was presented to study the heat flow rate process within the slab and at the snow melting surface. A numerical simulation was developed to solve the nonlinear system of discretisized equations of conservation laws in the model. Parametric study was carried out studying the effect of several parameters on the performance of steady state system. The transient effect was analyzed under two different storm conditions.

The main objectives of the current work are:

- To develop a numerical model for fluid flow and heat transfer in tube-in-block heat exchangers exposed to different kinds of boundary conditions.
- To conduct a parametric study to understand how different parameters affect the performance of tube-in-block heat exchangers.

- To explore both steady state and transient models to understand how the time factor affects the performance of tube-in-block heat exchangers.
- To study different designs of tube-in-block heat exchangers expands our choices to use the appropriate design for a certain application.

Chapter 2 – Steady State Heat Transfer in Circular Microchannels During Magnetic Heating or Cooling

2.1 Mathematical Model

The problem in hand is a microchannel assembly with circular channels in a rectangular solid (Gadolinium) substrate. The channel/substrate extends to a length L. The thickness of the substrate (or the distance between tubes in the vertical direction) is H and distance between tubes in the horizontal direction is 2W. Figure 2.1 shows a schematic drawing of the model. Fluid (water) flows through circular channels with diameter D and length L as single pass from inlet to outlet manifold. Due to symmetry, the analysis can be done by considering half of a tube and associated solid material as shown in figure 2.2. Magnetic field (G) is applied and the heat (g_o) is generated throughout the substrate. Heat is conducted through the substrate solid material then convected to the working fluid in the microchannels.

The governing equations for the conservation of mass, momentum, and energy in the liquid region are [45]:

$$\frac{\partial V_r}{\partial r}+\frac{1}{r}V_r+\frac{1}{r}\frac{\partial V_\phi}{\partial \phi}+\frac{\partial V_z}{\partial z}=0 \tag{1}$$

$$\left(V_r\frac{\partial V_r}{\partial r}+\frac{V_\phi}{r}\frac{\partial V_r}{\partial \phi}+V_z\frac{\partial V_r}{\partial z}-\frac{1}{r}V_\phi^2\right)= -\frac{1}{\rho_f}\frac{\partial p}{\partial r}+\nu\left[\frac{\partial^2 V_r}{\partial r^2}+\frac{1}{r}\frac{\partial V_r}{\partial r}+\frac{1}{r^2}\frac{\partial^2 V_r}{\partial \phi^2}+\frac{\partial^2 V_r}{\partial z^2}-\frac{V_r}{r^2}-\frac{2}{r^2}\frac{\partial V_\phi}{\partial \phi}\right] \tag{2}$$

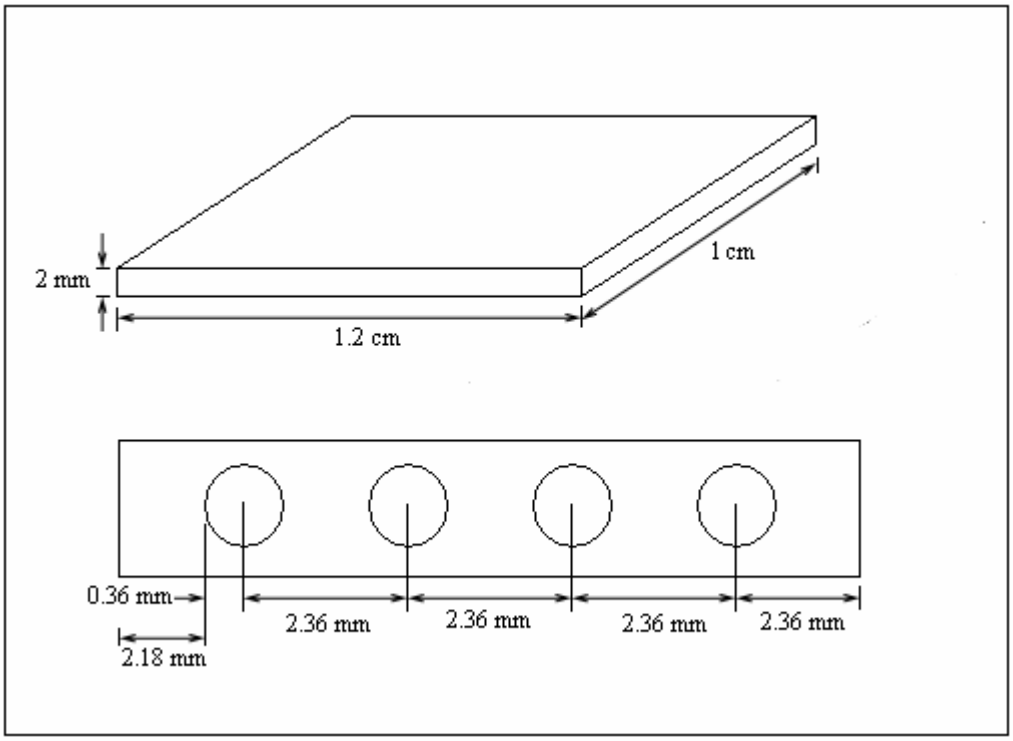

Figure 2.1: Schematic drawing for the circular microchannel model

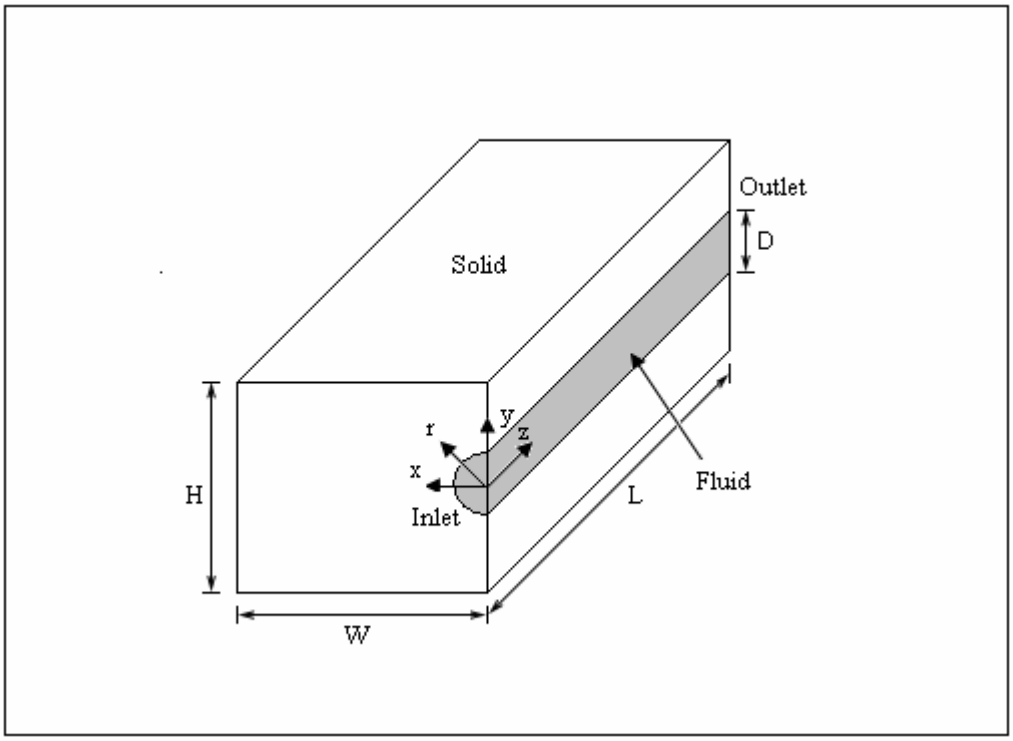

Figure 2.2: Schematic drawing for the circular microchannel simulated model

$$\left(V_r\frac{\partial V_\phi}{\partial r}+\frac{V_\phi}{r}\frac{\partial V_\phi}{\partial \phi}+V_z\frac{\partial V_\phi}{\partial z}-\frac{V_r V_\phi}{r}\right)= \\ -\frac{1}{\rho_f r}\frac{\partial p}{\partial \phi}+\nu\left[\frac{\partial^2 V_\phi}{\partial r^2}+\frac{1}{r}\frac{\partial V_\phi}{\partial r}+\frac{1}{r^2}\frac{\partial^2 V_\phi}{\partial \phi^2}+\frac{\partial^2 V_\phi}{\partial z^2}-\frac{V_\phi}{r^2}+\frac{2}{r^2}\frac{\partial V_r}{\partial \phi}\right] \tag{3}$$

$$\left(V_r\frac{\partial V_z}{\partial r}+\frac{V_\phi}{r}\frac{\partial V_z}{\partial \phi}+V_z\frac{\partial V_z}{\partial z}\right)=-\frac{1}{\rho_f}\frac{\partial p}{\partial z}+\nu\left[\frac{\partial^2 V_z}{\partial r^2}+\frac{1}{r}\frac{\partial V_z}{\partial r}+\frac{1}{r^2}\frac{\partial^2 V_z}{\partial \phi^2}+\frac{\partial^2 V_r}{\partial z^2}\right] \tag{4}$$

$$\left(V_r\frac{\partial T_f}{\partial r}+\frac{V_\phi}{r}\frac{\partial T_f}{\partial \phi}+V_z\frac{\partial T_f}{\partial z}\right)=\alpha_f\left[\frac{\partial^2 T_f}{\partial r^2}+\frac{1}{r}\frac{\partial T_f}{\partial r}+\frac{1}{r^2}\frac{\partial^2 T_f}{\partial \phi^2}+\frac{\partial^2 T_f}{\partial z^2}\right] \tag{5}$$

Considering constant thermal conductivity, the energy conservation equation in the solid region with heat generation is [46]:

$$\left[\frac{\partial^2 T_s}{\partial x^2}+\frac{\partial^2 T_s}{\partial y^2}+\frac{\partial^2 T_s}{\partial z^2}\right]+\frac{g_o}{k}=0 \tag{6}$$

Note that a cylindrical coordinate system was used to model convection within the circular tube while a cartesian coordinate system was used to model conduction within the solid substrate material.

Equations (1) to (6) are subject to the following boundary conditions:

At z = 0, 0 ≤ r < d/2: $V_r=0, V_\phi=0, V_z=V_{z,in}, T_f=T_{f,in}$ (7)

At z = 0, r ≥ d/2, 0 < x < W, 0 < y < H: $\frac{\partial T_s}{\partial z}=0$ (8)

At z = L, r < d/2: $p=0$ (9)

At z = L, r ≥ d/2, 0 < x < W, 0 < y < H: $\frac{\partial T_s}{\partial z}=0$ (10)

At x = 0, -d/2 ≤ y ≤ +d/2, 0 ≤ z ≤ L: $V_\phi=0, \frac{\partial V_r}{\partial x}=0, \frac{\partial V_z}{\partial x}=0, \frac{\partial T_f}{\partial x}=0$ (11)

At x = 0, -H/2 ≤ y ≤ -d/2, 0 ≤ z ≤ L: $$\frac{\partial T_s}{\partial x} = 0 \quad (12)$$

At x = 0, +d/2 ≤ y ≤ +H/2, 0 ≤ z ≤ L: $$\frac{\partial T_s}{\partial x} = 0 \quad (13)$$

At x = W, -H/2 ≤ y ≤ +H/2, 0 ≤ z ≤ L: $$\frac{\partial T_s}{\partial x} = 0 \quad (14)$$

At y = -H/2, 0 ≤ x ≤ W, 0 ≤ z ≤ L: $$\frac{\partial T_s}{\partial y} = 0 \quad (15)$$

At y = +H/2, 0 ≤ x ≤ W, 0 ≤ z ≤ L: $$\frac{\partial T_s}{\partial y} = 0 \quad (16)$$

At 0 ≤ z ≤ L, r = d/2: $$T_f = T_s, k_f \frac{\partial T_f}{dr} = k_s \frac{\partial T_s}{dr} \quad (17)$$

2.2 Numerical Simulation and Parametric Study

The governing equations along with the boundary conditions were solved using the Galerkin finite element method. Four-node quadrilateral elements were used. In each element, the velocity, pressure, and temperature fields were approximated which led to a set of equations that defined the continuum. The Newton-Raphson algorithm was used to solve the nonlinear system of discretized equations. An iterative procedure was used to arrive at the solution for the velocity and temperature fields. The solution was considered converged when the field values did not change from one iteration to the next, and the residuals for each variable became negligible.

For the numerical computations, the height (H) and the half width (W) of the model were set to 0.2 cm and 0.236 cm respectively. The original (repeating) case used a diameter of 0.036 cm. Diameter was changed from 0.012 cm to 0.048 cm having a (d/H)

ratio of 0.06 to 0.24. Reynolds number was varied between 1000 and 2200. Magnetic field (G) value of 5 and 10 T were used to study the effects of changing the magnetic field. Magnetic field value was translated into heat generation per unit volume in the substrate material (g_o) by using experimental data of Pechasky and Gschneider [47]. Gadolinium was used as the solid substrate material. Gadolinium is one of the materials that generate significant heating and cooling when exposed to a magnetic field under room temperature. Water was used as the primary working fluid. Two more fluids, namely Ammonia and R134a, were used to compare their results to those of water. The local solid-fluid interface temperature, heat transfer coefficient and Nusselt number were calculated from the computed velocity and temperature distributions.

2.3 Results and Discussion

The distribution of cells in the computational domain was determined from a series of tests with different number of elements in the x, y, r (within the tube), and z directions. The results obtained by using (nx = 6, ny = 12, nr = 6, nz = 20) that had an average error of 1.29% and a maximum error less than 2% compared to (nx = 10, ny = 20, nr = 10, nz = 40). Figure 2.3 shows the dimensionless peripheral average interface temperature for different grid systems. Quantitative error analysis is one way to validate the accuracy of the results from a grid independent study. This was performed and presented in Appendix H.

Figure 2.4 shows the local Nusselt number variation around the tube periphery for different axial locations. The effect of the substrate's rectangular shape is obvious along the angular direction of the tube. It may be noticed that local Nusselt number is

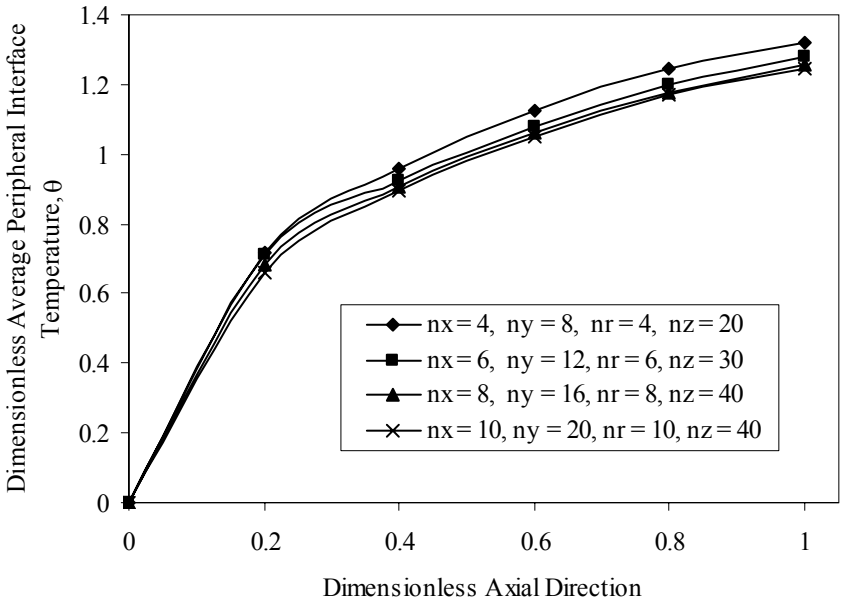

Figure 2.3: Local dimensionless peripheral average interface temperature for different grid sizes (Re = 1600, G = 5 T, d = 0.036 cm, Water)

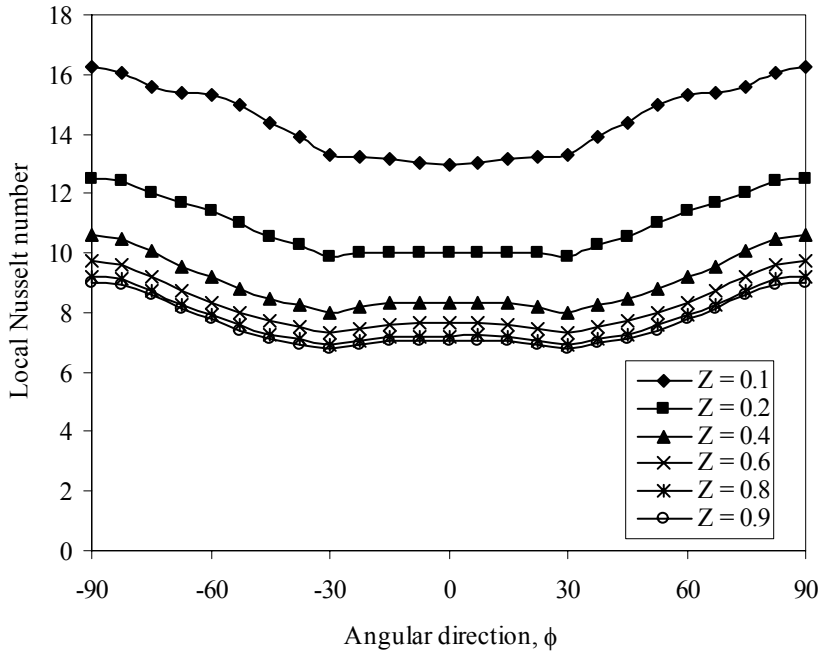

Figure 2.4: Local Nusselt number variation for different axial locations along the angular direction (Re = 1600, G = 5 T, d = 0.036 cm, Water)

minimum at angular locations corresponding to the corners of the substrate where thermal resistance within the solid is maximum. It changes slightly in the middle part of the tube, whereas becomes larger at both top and bottom ends. The variation indicates that shape of the substrate influences the local heat transfer rate as expected in a conjugate problem.

Figure 2.5 shows the effects of both the change in Reynolds number and magnetic field strength on the dimensionless peripheral average interface temperature. Heat is generated in the substrate causing the temperature to rise. The low inlet temperature cools down the substrate. As the fluid travels through the channel, its temperature increases providing less cooling to the substrate. This causes the interface temperature to increase along the axial direction. Higher Reynolds number decreases the interface temperature by providing more cooling to the interface. Higher magnetic field generates more heat in the substrate causing an increase in the interface temperature. On the other hand, the dimensionless peripheral average interface temperature does not change with the magnetic field. Figure 2.6 shows the effects of both the change in Reynolds number and magnetic field value on the Nusselt number. Interface temperature increases along the axial direction causing the temperature gradient in the solid to decrease. As a result, the heat flow rate decreases along the axial direction. The Nusselt number directly depends on the heat flow rate and thus it decreases along the axial direction. At lower Reynolds number, a lower fluid velocity causes both the fluid and interface temperatures to increase. The increase in the interface temperature is larger than the increase in the fluid bulk temperature causing an increase in the bulk-interface temperature difference. This increase in the bulk-interface temperature difference decreases the Nusselt number with the lowering of Reynolds number. The change in the

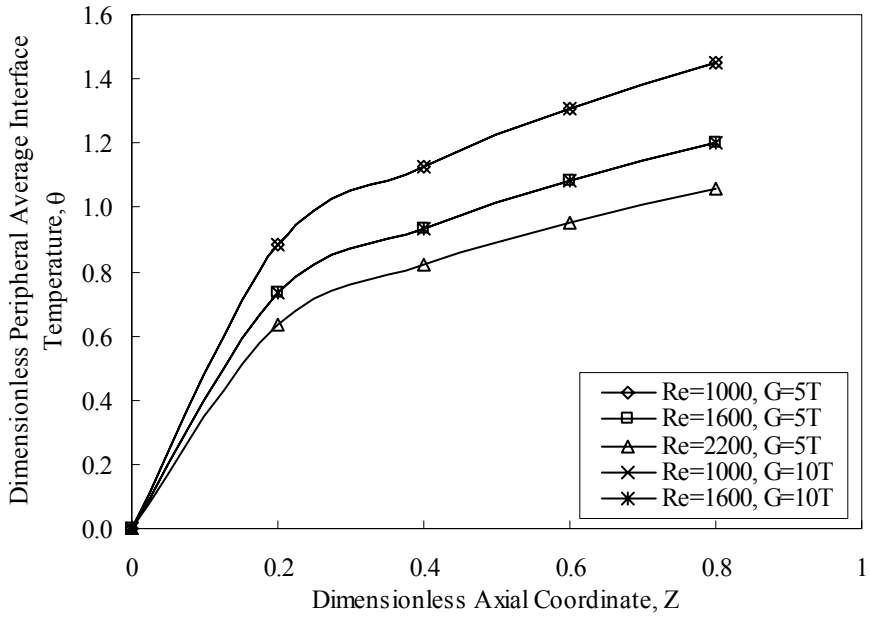

Figure 2.5: Local dimensionless peripheral average interface temperature along axial coordinate at various Reynolds numbers (d = 0.036 cm, Water)

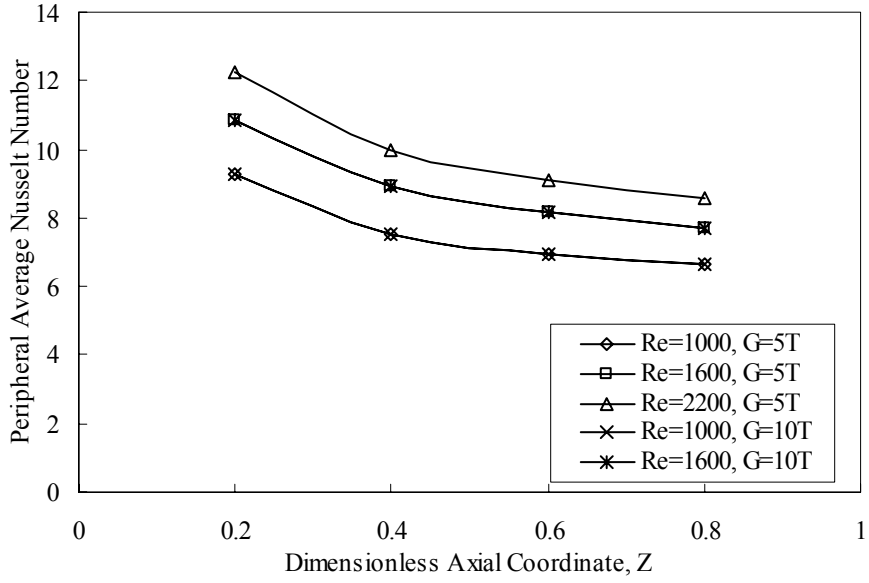

Figure 2.6: Local peripheral average Nusselt number along axial coordinate at various Reynolds numbers (d = 0.036 cm, Water)

magnetic field value had no significant effect on the heat transfer coefficient. This is because with the increase of magnetic field strength, both heat flux at the interface and difference between interface and bulk fluid temperature increases by the same amount. Therefore, there was no significant change in Nusselt number with the change in the magnetic field.

The change in diameter of the channel is examined next. When changing the diameter, the velocity will change for a constant Reynolds number or the Reynolds number will change for a constant velocity. Figure 2.7 shows the local dimensionless peripheral average interface temperature along the axial direction for different diameters at constant Reynolds number. Smaller diameter at the same Reynolds number gives higher fluid velocity. This should decrease the interface temperature. On the contrary, smaller diameter also results in larger solid volume causing more heat generated from the solid body. This increases the heat flow to the fluid. This study shows that the interface temperature is decreasing with diameter, which means that the interface temperature is affected more by the change of the volume of the solid substrate. Figure 2.8 shows the variation of the dimensionless peripheral average heat transfer coefficient for different diameters of the channel. As the tube diameter decreases, the interface temperature increases causing the interface-bulk temperature difference to increase. Temperature in the solid substrate increases due to more heat generation caused by the increase in the solid volume. This causes an increase in heat flow rate. The heat transfer coefficient is the ratio of the heat flow rate to the interface-bulk temperature difference. This study showed that the increase in the heat flow rate is much more than the increase in the interface-bulk temperature difference. The net result is an increase in the heat transfer

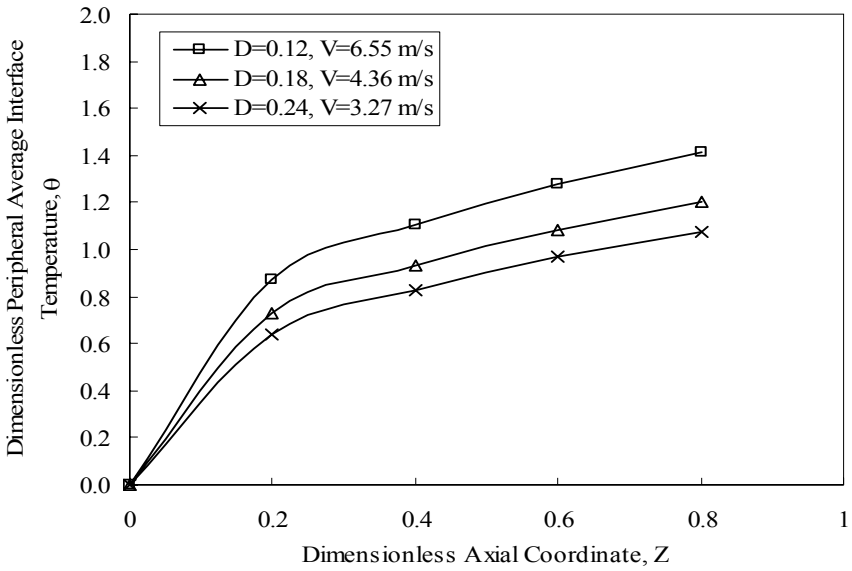

Figure 2.7: Local dimensionless peripheral average interface temperature along axial coordinate at various diameters and constant Reynolds numbers (Re = 1600, G = 5 T, Water)

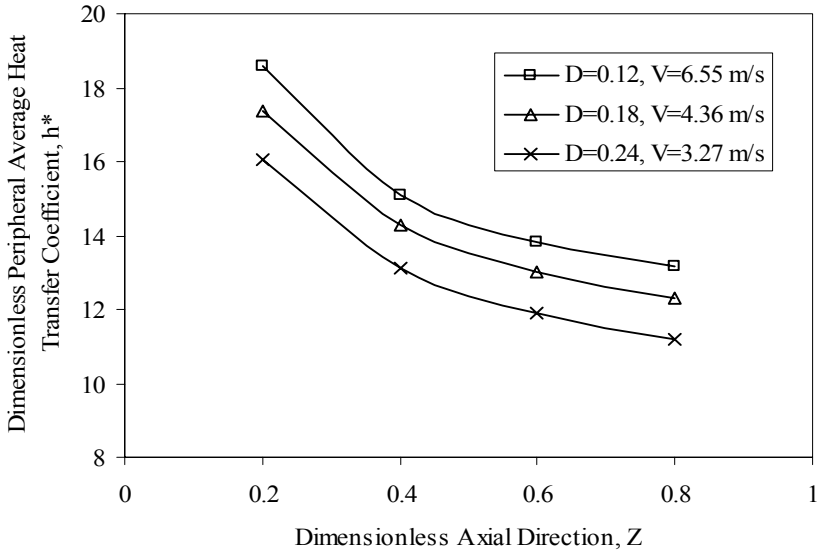

Figure 2.8: Local dimensionless peripheral average heat transfer coefficient along axial coordinate at various diameters and constant Reynolds numbers (Re = 1600, G = 5 T, Water)

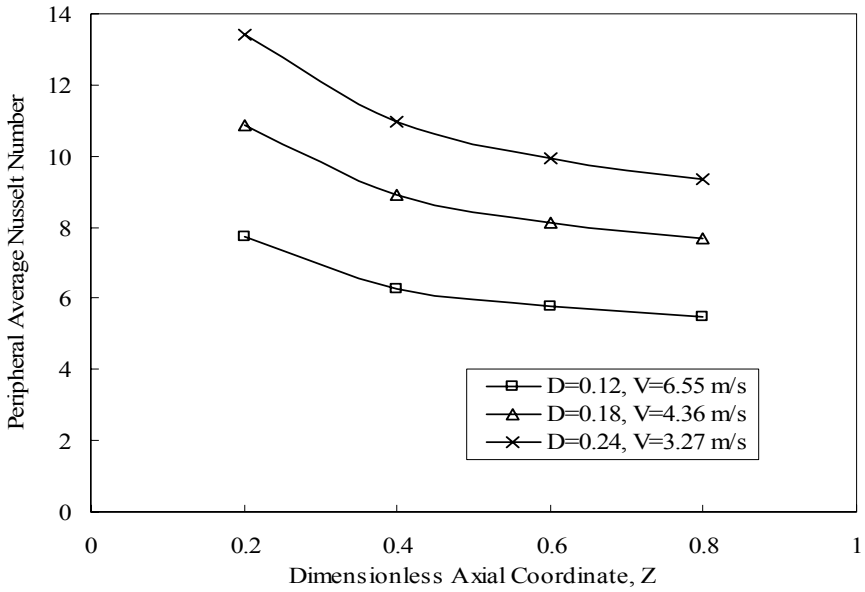

Figure 2.9: Local peripheral average Nusselt number along axial coordinate at various diameters and constant Reynolds numbers (Re = 1600, G = 5 T, Water)

coefficient as the diameter becomes smaller. Figure 2.9 shows the variation of the Peripheral average Nusselt number for different channel diameters. Nusselt number directly depends on the heat transfer coefficient and the channel diameter. The decrease in the channel diameter overcomes the increase in the heat transfer coefficient. The net result is a decrease in Nusselt number due to the decrease in channel diameter.

Figure 2.10 shows the effect of changing the diameter on the dimensionless peripheral average interface temperature while keeping the fluid velocity at the entrance constant. Smaller diameter results in larger solid substrate providing more heat generation. This increases the heat flow rate to the fluid, and hence, increases the interface temperature. Figure 2.11 shows the effect of changing the diameter on the peripheral average Nusselt number while keeping the fluid velocity at the entrance

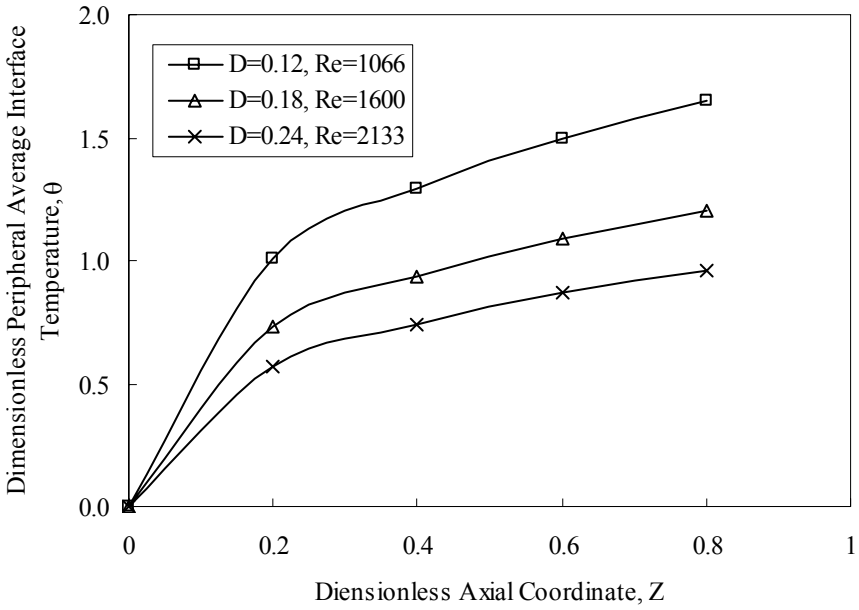

Figure 2.10: Local dimensionless peripheral average interface temperature along axial coordinate at various diameters and constant inlet velocity (V_{in} = 4.367 m/s, G = 5 T, Water)

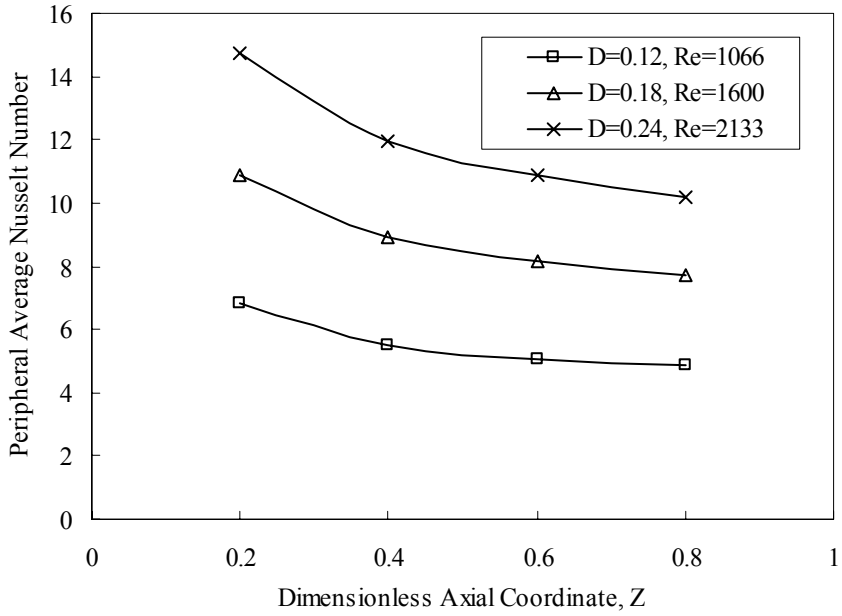

Figure 2.11: Local Peripheral average Nusselt number along axial coordinate at various diameters and constant inlet velocity (V_{in} = 4.367 m/s, G = 5 T, Water)

constant. As the tube diameter decreases, the interface temperature increases causing the interface-bulk temperature difference to increase. Temperature in the solid substrate increases due to more heat generation caused by the increase in the solid volume. This causes an increase in heat flow rate. The heat transfer coefficient is the ratio of the heat flow rate to the interface-bulk temperature difference. The increase in the interface-bulk temperature difference overcomes the increase in the heat flow rate resulting in a decrease in the heat transfer coefficient. Nusselt number has similar trend as those of the heat transfer coefficient because of its direct dependence on the heat transfer coefficient. Note that both the diameter and the heat transfer coefficient are decreasing together as the tube diameter decreases.

Figure 2.12 shows the local peripheral average Nusselt number variation for different working fluids at two different axial locations. As explained above, Nusselt number is smaller around larger solid area because of the smaller temperature gradient in the larger solid region. Nusselt number for water is the highest. Figure 2.13 shows the dimensionless peripheral average interface temperature changes along the axial coordinate for different working fluids at the same Reynolds number. To run the fluids as liquid at the appropriate temperature range the inlet temperature was chosen as –30 ^{o}C for both ammonia and R-134a refrigerants. Inlet velocities for these fluids were selected in such a way that Reynolds number remains constant. The lowest velocity was obtained for R-134a and the highest for water. This contributed to different performance of these three working fluids. A higher fluid velocity results in lower rate of increase of interface temperature along the axial direction. A much higher rate of increase of interface temperature is given by R-134a which has the lowest inlet velocity for the same Reynolds

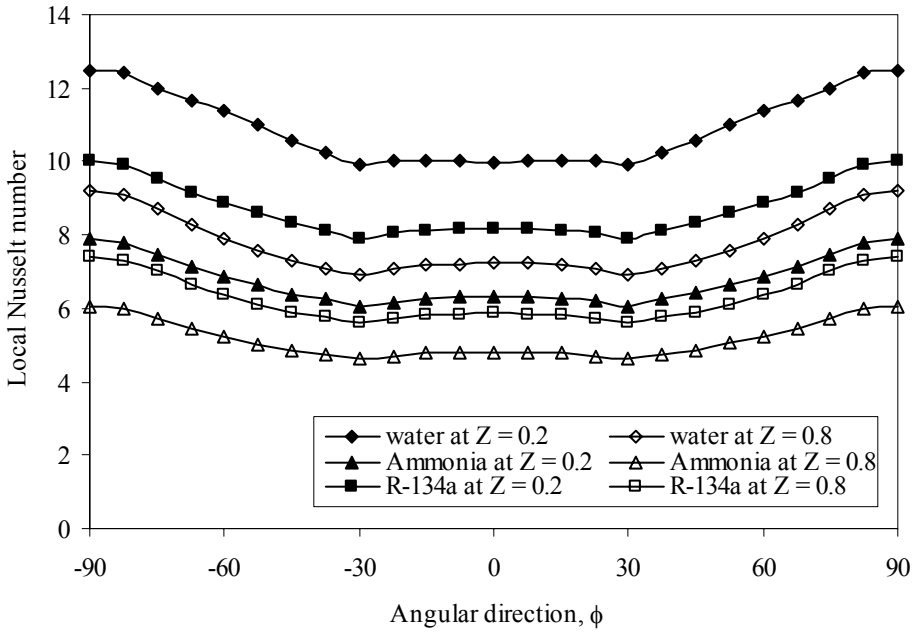

Figure 2.12: Local Nusselt number variation for different working fluids along the angular direction (Re = 1600, G = 5 T, d = 0.036 cm)

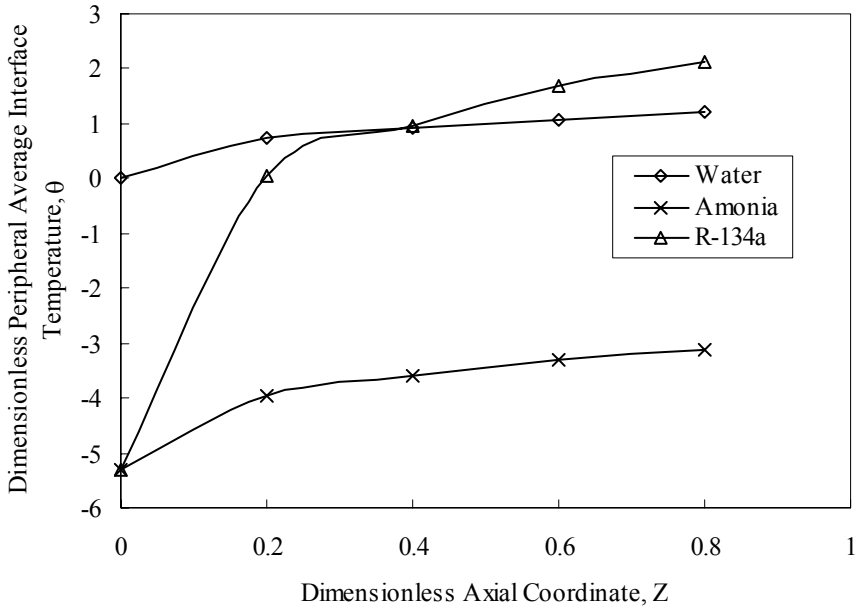

Figure 2.13: Local dimensionless peripheral average interface temperature along axial coordinate for different fluids (Re = 1600, G = 5 T, d = 0.036 cm)

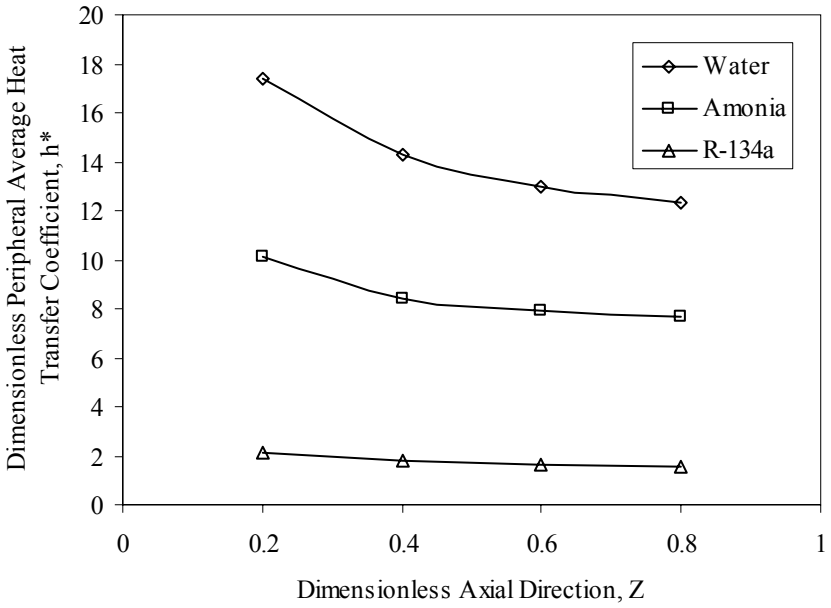

Figure 2.14: Local dimensionless peripheral average heat transfer coefficient along axial coordinate for different fluids (Re = 1600, G = 5 T, d = 0.036 cm, Water)

number. Figure 2.14 shows the dimensionless peripheral average heat transfer coefficient changes along the axial coordinate for different working fluids at the same Reynolds number. The interface temperature increases along the axial direction. This decreases the temperature gradient at the interface, and hence, the heat flow rate to the fluid. It also increases the interface-bulk temperature difference. Both of these cause the heat transfer coefficient to decrease along the axial direction. An increase in inlet velocity decreases the interface temperature. This increases the temperature gradient at the interface, and hence, the heat flow rate to the fluid. It also decreases the interface-bulk temperature difference. Both of these cause the heat transfer coefficient to increase. Therefore, water has the highest heat transfer coefficient while R-134a has the lowest. It may be noted that the decrease in the interface-bulk temperature difference was much larger than the

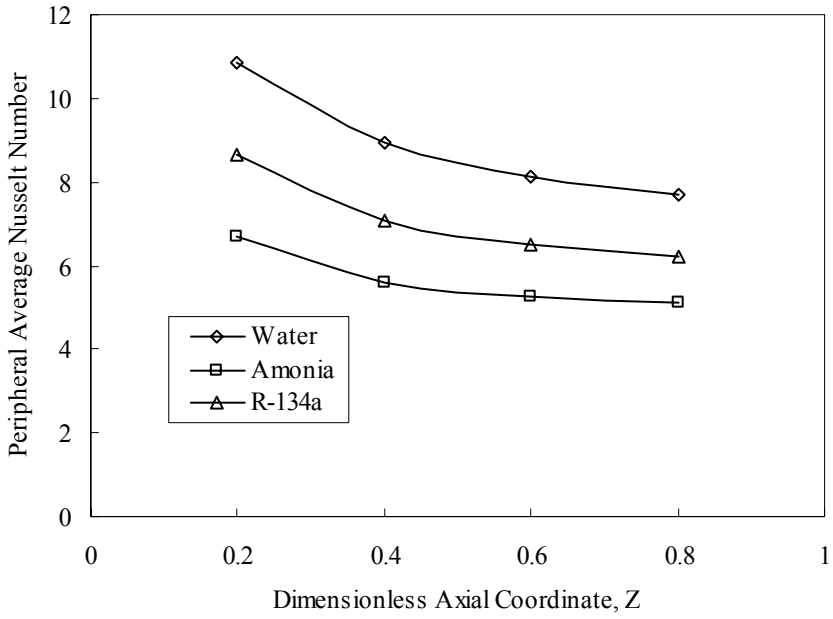

Figure 2.15: Local peripheral average Nusselt number along axial coordinate for different fluids (Re = 1600, G = 5 T, d = 0.036 cm, Water)

increase in the heat flow rate. Figure 2.15 shows the peripheral average Nusselt number changes along the axial coordinate for different working fluids at the same Reynolds number. Nusselt number depends directly on the heat transfer coefficient and the fluid thermal conductivity. R-134a has lower thermal conductivity compared to water and ammonia. This causes its Nusselt number to be higher than it is for ammonia.

The maximum dimensionless temperature in the substrate occurs in the farthest corner from the channel entrance. A higher Reynolds number enhances the heat flow rate to the fluid and, thus, decreases the maximum temperature in the system. A smaller diameter at constant Reynolds number results in higher fluid velocity but lower mass flow rate. A smaller mass flow rate means higher temperature in the system and hence higher maximum temperature. This is shown in figure 2.16. Figure 2.17 shows the

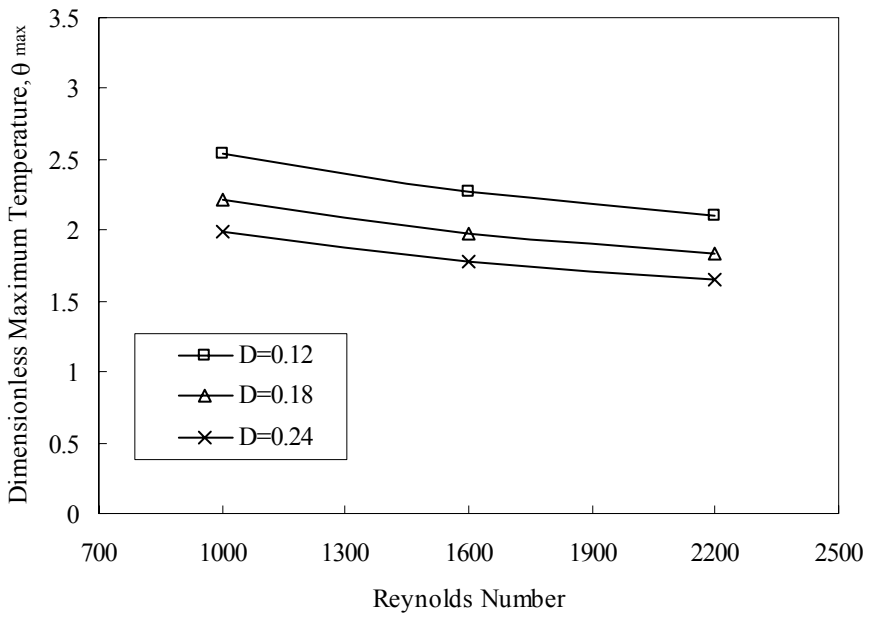

Figure 2.16: Dimensionless maximum temperature in the system at various diameters (with constant Reynolds number) and Reynolds number (G = 5 T, Water)

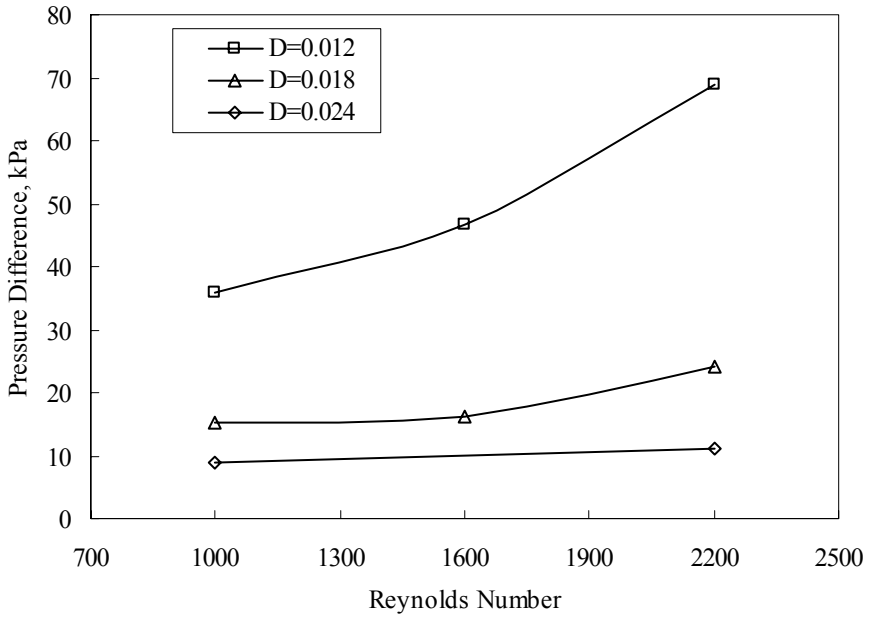

Figure 2.17: Pressure drop in the model at various diameters (with constant Reynolds number) and Reynolds number (G = 5 T, Water)

pressure drop from inlet to exit of the channel that resulted for various diameters and Reynolds numbers. The pressure drop is higher for smaller diameter. This is expected because the flow encounters larger frictional resistance from the walls. The pressure drop also increases with Reynolds number. This is because higher velocities cause higher frictional resistance.

Figures 2.18 and 2.19 show the dimensionless peripheral average heat transfer coefficient and peripheral average Nusselt number at Z = 0.4 and Z = 0.8 along the axial direction from the inlet for various Reynolds number and diameters. For the same diameter, the increase in Reynolds number, or the inlet velocity, decreases the interface temperature. This increases the temperature gradient at the interface, and hence, the heat flow rate to the fluid. It also decreases the interface-bulk temperature difference. The increase in the heat flow rate and the decrease in the interface-bulk temperature difference both causes the heat transfer coefficient to increase, and hence, the Nusselt number. For the same Reynolds number, smaller diameter gives higher velocity which results in lower interface temperature. Lower interface temperature, as previously discussed, results in an increase the heat flow rate and a decrease in the interface-bulk temperature difference. This increases the heat transfer coefficient for smaller diameter. Nusselt number is the product of the heat transfer coefficient and the diameter. The decrease in the diameter overcomes the increase in the heat transfer coefficient. As a result, Nusselt number decreases as the diameter becomes smaller. It can be observed that an overall decrease of the Nusselt number occurs along the tube axial direction.

Figures 2.20 and 2.21 show a comparison with previous experimental results for flow in a microtube with constant wall heat flux to validate the numerical results for this

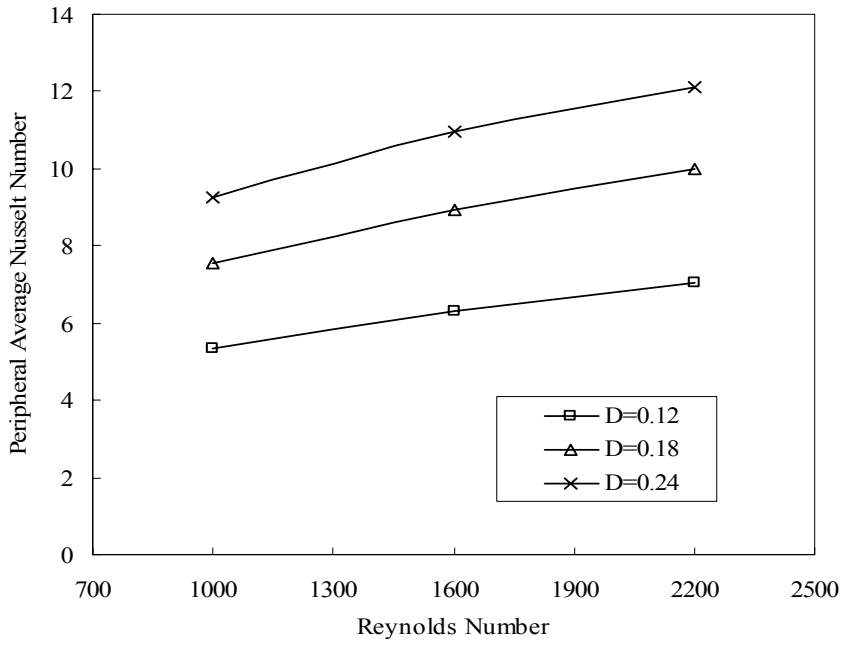

Figure 2.18: Local average Nusselt number at z = 0.4 cm for various diameter (with constant Reynolds number) and Reynolds number (G = 5 T, Water)

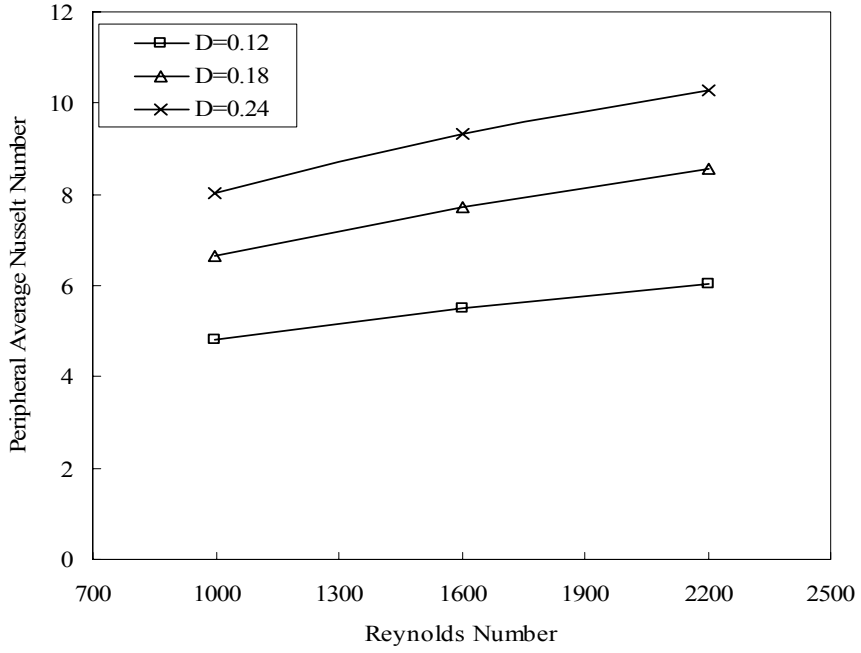

Figure 2.19: Local average Nusselt number at z = 0.8 cm for various diameters (with constant Reynolds number) and Reynolds number (G = 5 T, Water)

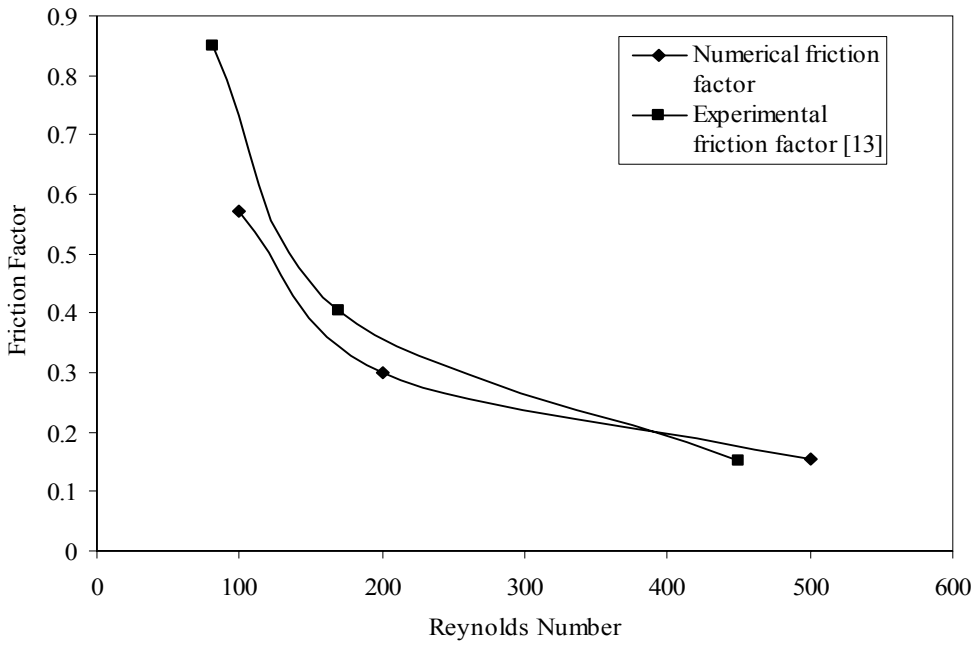

Figure 2.20: Comparison for friction factor results to existing experimental results in the literature

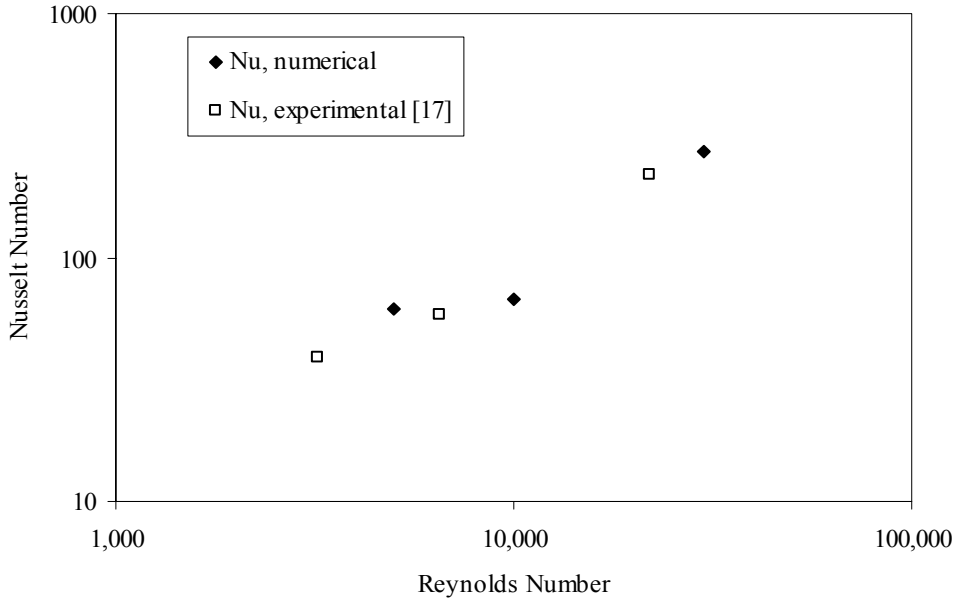

Figure 2.21: Comparison for Nusselt number results to existing experimental results in the literature

project. In the absence of any test data for magnetic heaters (or coolers), these are most appropriate comparisons that could be done. Figure 2.20 shows a good agreement between the numerical and experimental results for the friction coefficient at different Reynolds numbers in Kohl et al. [13]. Small difference appeared between the two results and could be referred to the approximations used to conduct the numerical simulation as well as errors involved in experimental measurements. Circular microtube with diameter equals to the hydraulic diameter of the channel used in the experiment was simulated. Only one channel was considered in this comparison out of the 5 channels in the experimental work. Adams et al. [17] examined turbulent, single-phase forced convection of water in circular microchannels. A generalized correlation for the Nusselt number for turbulent, single phase forced convection in circular microchannels was developed. Figure 2.21 shows a comparison of their Nusselt number data at different Reynolds number with predictions by numerical simulation.

Interpolation was made to obtain the error range for the experimental data presented in Kohl et al. [13] and Adams et al. [17] compared to our work. It was found that the error range for Kohl et al. [13] was 5.58 % and 16.27 % at Reynolds number of 170 and 450 respectively. Also the error range for Adams et al. [17] was 7.71 % and 16.34 % at Reynolds number of 6,500 and 22,000 respectively. Adams et al. [17] presented the difference between his experimental and predicted Nusselt number values were less than 18.6%. Design of experiment is one way to study the effect of different parameters and parameter combinations. A detailed was done in Appendix H. The percentage difference for the entrance effect was found to be ranging from 42.0 % to 43.4 % along the microchannel axial direction. When compared to the large tube correlation it

was found that the percentage difference ranges from 25.7 % to 22.4 % along the microchannel axial direction.

2.4 Conclusions

A study of parameters that affect convective heat transfer in circular microchannels during heat generation in the substrate due to an applied magnetic field was done. Generally the interface temperature increases along the axial direction of the fluid flow due to heat generation in the substrate. Lower Reynolds number results in higher interface temperature but lower Nusselt number. A higher magnetic field strength also results in higher interface temperature but has no effect on Nusselt number. Smaller diameter for a constant Reynolds number gives higher interface temperature and heat transfer coefficient but it decreases Nusselt number. Decreasing the diameter at constant inlet velocity increases the interface temperature but decreases the Nusselt number. The maximum temperature occurs at the farthest corner of the substrate from the channel entrance. A higher Reynolds number decreases the maximum temperature in the system. A smaller diameter at constant Reynolds number results in higher maximum temperature. Among the working fluid examined, water has the highest Nusselt number while ammonia has the lowest. Pressure drop was found to be higher for smaller diameter at constant Reynolds number. The peripheral average heat transfer coefficient was found to decrease with diameter at constant Reynolds number and increase with increasing Reynolds number. This study provided a foundation for the prediction of heat transfer coefficient during magnetic heating or cooling of the substrate material. It will be used for the design of experiments for practical demonstration of a magnetic microcooler.

Chapter 3 – Transient Heat Transfer in Circular Microchannels Under Time Varying Heat Source

3.1 Mathematical Model

The problem in hand consists of circular microchannels inside a rectangular magnetic material substrate. Fluid is entering the microchannels at constant inlet temperature. The magnetic material substrate is subjected to a magnetic field resulting in heat source and heat sink periodically. The boundary conditions at all sides are considered adiabatic. Because of the symmetry along the width of the wafer, only half of the pipe is simulated. The pipe at the left edge was considered to take into consideration the side end effect. The material of the substrate was Gadolinium while the working fluid was water. Figure 3.1 shows a 3-D model studied in this project. Boundary conditions at the bottom, left and top are adiabatic while it is symmetrical at the right side.

The governing equations for the conservation of mass, momentum, and energy for the fluid in Cartesian coordinate are [45]:

$$\frac{\partial V_r}{\partial r}+\frac{1}{r}V_r+\frac{1}{r}\frac{\partial V_\phi}{\partial \phi}+\frac{\partial V_z}{\partial z}=0 \tag{1}$$

$$\begin{aligned}&\frac{\partial V_r}{\partial t}+\left(V_r\frac{\partial V_r}{\partial r}+\frac{V_\phi}{r}\frac{\partial V_r}{\partial \phi}+V_z\frac{\partial V_r}{\partial z}-\frac{1}{r}V_\phi^2\right)=\\&-\frac{1}{\rho_f}\frac{\partial p}{\partial r}+\nu\left[\frac{\partial^2 V_r}{\partial r^2}+\frac{1}{r}\frac{\partial V_r}{\partial r}+\frac{1}{r^2}\frac{\partial^2 V_r}{\partial \phi^2}+\frac{\partial^2 V_r}{\partial z^2}-\frac{V_r}{r^2}-\frac{2}{r^2}\frac{\partial V_\phi}{\partial \phi}\right]\end{aligned} \tag{2}$$

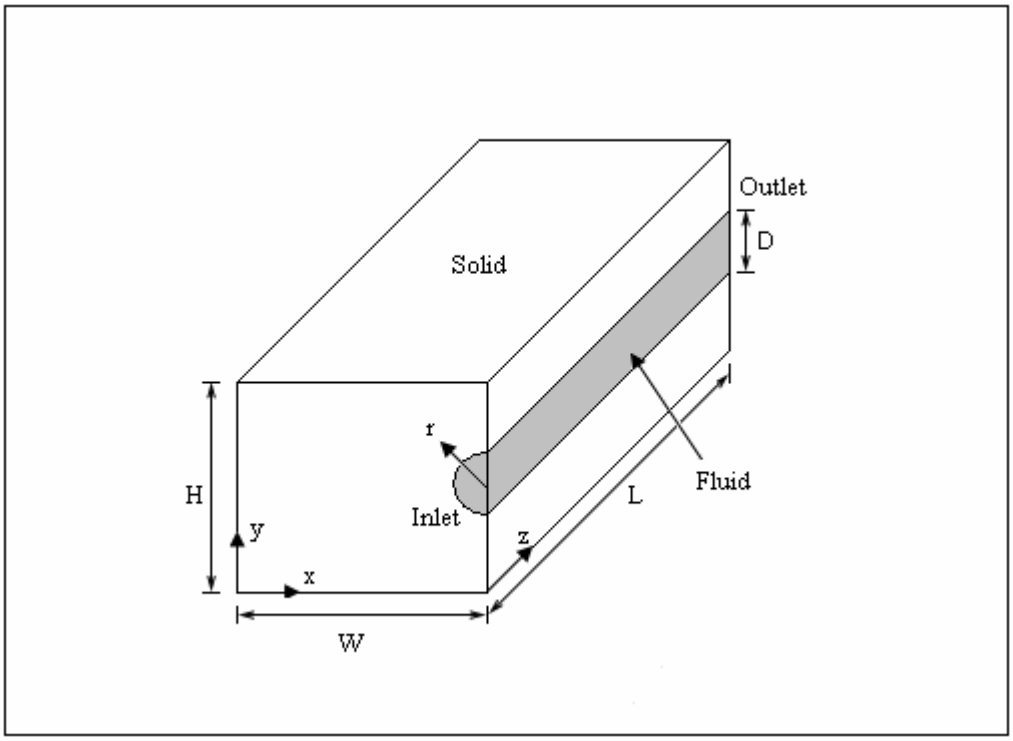

Figure 3.1: Schematic for microchannel heat exchanger model

$$\frac{\partial V_\phi}{\partial t}+\left(V_r\frac{\partial V_\phi}{\partial r}+\frac{V_\phi}{r}\frac{\partial V_\phi}{\partial \phi}+V_z\frac{\partial V_\phi}{\partial z}-\frac{V_r V_\phi}{r}\right)= -\frac{1}{\rho_f r}\frac{\partial p}{\partial \phi}+\nu\left[\frac{\partial^2 V_\phi}{\partial r^2}+\frac{1}{r}\frac{\partial V_\phi}{\partial r}+\frac{1}{r^2}\frac{\partial^2 V_\phi}{\partial \phi^2}+\frac{\partial^2 V_\phi}{\partial z^2}-\frac{V_\phi}{r^2}+\frac{2}{r^2}\frac{\partial V_r}{\partial \phi}\right] \tag{3}$$

$$\frac{\partial V_z}{\partial t}+\left(V_r\frac{\partial V_z}{\partial r}+\frac{V_\phi}{r}\frac{\partial V_z}{\partial \phi}+V_z\frac{\partial V_z}{\partial z}\right)= -\frac{1}{\rho_f}\frac{\partial p}{\partial z}+\nu\left[\frac{\partial^2 V_z}{\partial r^2}+\frac{1}{r}\frac{\partial V_z}{\partial r}+\frac{1}{r^2}\frac{\partial^2 V_z}{\partial \phi^2}+\frac{\partial^2 V_z}{\partial z^2}\right] \tag{4}$$

$$\frac{\partial T_f}{\partial t}+\left(V_r\frac{\partial T_f}{\partial r}+\frac{V_\phi}{r}\frac{\partial T_f}{\partial \phi}+V_z\frac{\partial T_f}{\partial z}\right)=\alpha_f\left[\frac{\partial^2 T_f}{\partial r^2}+\frac{1}{r}\frac{\partial T_f}{\partial r}+\frac{1}{r^2}\frac{\partial^2 T_f}{\partial \phi^2}+\frac{\partial^2 T_f}{\partial z^2}\right] \tag{5}$$

For transient heat transfer with uniform heat generation and constant thermal conductivity, the energy conservation equation in the solid region is [46]:

$$\left[\frac{\partial^2 T_s}{\partial x^2}+\frac{\partial^2 T_s}{\partial y^2}+\frac{\partial^2 T_s}{\partial z^2}\right]+\frac{g_o}{k}=\frac{1}{\alpha}\frac{\partial T_s}{\partial t} \tag{6}$$

Equations (1) to (6) are subject to the following Initial and boundary conditions:

At t = 0: $T_s = T_f = T_{in}$ (7)

At z = 0 and r ≤ d/2: $V_r = 0, V_\phi = 0, V_z = V_{z,in}, T_f = T_{f,in}$ (8)

At z = 0 and r > d/2: $\frac{\partial T_s}{\partial z} = 0$ (9)

At z = L and r ≤ d/2: $p = 0$ (10)

At z = L and r > d/2: $\frac{\partial T_s}{\partial z} = 0$ (11)

At x = 0, 0 ≤ z ≤ L, 0 ≤ y ≤ H: $\frac{\partial T_s}{\partial x} = 0$ (12)

At x = W, 0 ≤ z ≤ L, (H-d)/2 ≤ y ≤ (H+d)/2: $V_\phi = 0, \frac{\partial V_r}{\partial x} = 0, \frac{\partial V_z}{\partial x} = 0, \frac{\partial T_f}{\partial x} = 0$ (13)

At x = W, 0 ≤ z ≤ L, 0 ≤ y ≤ (H-d)/2: $\frac{\partial T_s}{\partial x} = 0$ (14)

At x = W, 0 ≤ z ≤ L, 0 ≤ y ≤ (H+d)/2: $\frac{\partial T_s}{\partial x} = 0$ (15)

At y = 0, 0 ≤ x ≤ W, 0 ≤ z ≤ L: $\frac{\partial T_s}{\partial y} = 0$ (16)

At y = H, 0 ≤ x ≤ W, 0 ≤ z ≤ L: $\frac{\partial T_s}{\partial y} = 0$ (17)

At r = d/2 and 0 ≤ z ≤ L: $V_r = 0, V_\phi = 0, V_z = 0, T_f = T_s, k_f \frac{\partial T_f}{\partial r} = k_s \frac{\partial T_s}{\partial r}$ (18)

3.2 Numerical Simulation and Parametric Study

The governing equations along with the boundary conditions were solved using the Galerkin finite element method. The Newton-Raphson algorithm was used to solve the nonlinear system of discretized equations. An iterative procedure was used to arrive at the solution for the velocity and temperature fields. The solution was considered converged when the field values did not change from one iteration to the next, and the residuals for each variable became negligible.

For the numerical computations, the height (H) and the half width (W) of the model were set to a constant value, 0.2 cm and 0.236 cm respectively. The length of the channel (L) was also a constant value of 2.5 cm. To represent the heat generation and cooling process numerically, the magnetic field value (G) was fluctuated between the values of +2 and -2 T. Time period of 2 seconds was used. The first period was chosen to be one half of the selected time length since it started from the initial condition. Diameter of 0.036 cm and Reynolds number of 1600 were used for this case. One parameter was changed while all other parameters kept constant to study the effect of each parameter separately. Parameters included the magnetic field that was changed to the values of +4 and -4 T. Time length was one parameter and changed to 10 seconds. To study the effect of diameter, it was reduced to 0.012 cm. Reynolds number effect was studied and was changed to 1000.

3.3 Results and Discussion

The local interface temperature, heat flow rate, heat transfer coefficient and Nusselt number were calculated from the resulted velocity and temperature distribution.

Figure 3.2 shows the maximum temperature in the model. The heat generation occurred in the 1st, 3rdand 5th periods while the cooling process occurred in the 2nd and 4th periods. The maximum temperature in the model occurred in the solid region at the outlet edge corner of the substrate. It can be observed that the maximum temperature in the system increases when heat is generated in the system while it decreases when the system is cooled. Because the inlet temperature to the system is 20 ^{o}C, the maximum temperature does not drop below this value. Figure 3.3 shows the interface temperature at different axial locations of the microchannel. Sinusoidal behavior is observed for the interface temperature as the heat generation and cooling process alternates. As heat is generated the interface temperature increases while it decreases when cooling process takes over. The interface temperature increase along the axial direction is slow at the beginning of the transient process because of the initial condition effect. The temperature range gets larger along the axial direction due to larger fluid bulk temperature which slows down the heating or cooling process. Figure 3.4 shows that the heat flow rate is supplied to and rejected from the fluid as the heat generation and cooling process alternates in the system. Similarly to the interface temperature, a sinusoidal behavior is observed in the heat flow rate as heat generation and cooling process alternates. The heat flow rate increase in value for each of the heat generation and cooling process and the initial condition effect diminishes over time. As the fluid travels through the channel its bulk temperature increases providing heat transfer resistance. This decreases the interface-solid temperature difference and thus the heat flow rate. Figure 3.5 shows the Nusselt number behavior over a period of 9 seconds. The Nusselt number behavior is affected by the heat flow rate and the interface-bulk temperature difference. The increase in the heat flow rate

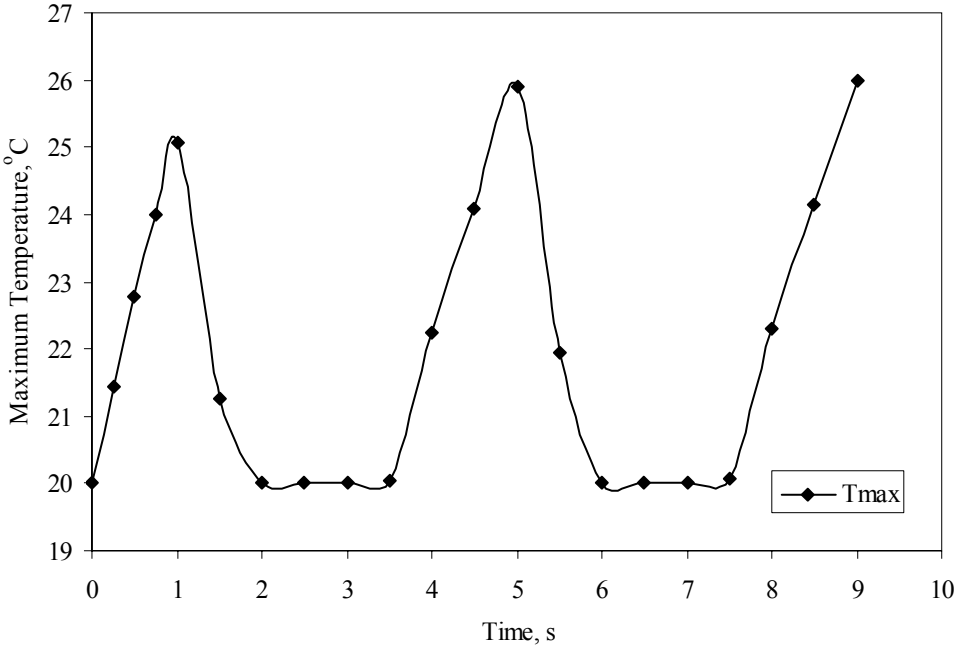

Figure 3.2: Maximum temperature over 9 seconds (Re = 1600, G = ±2 T, d = 0.036 cm)

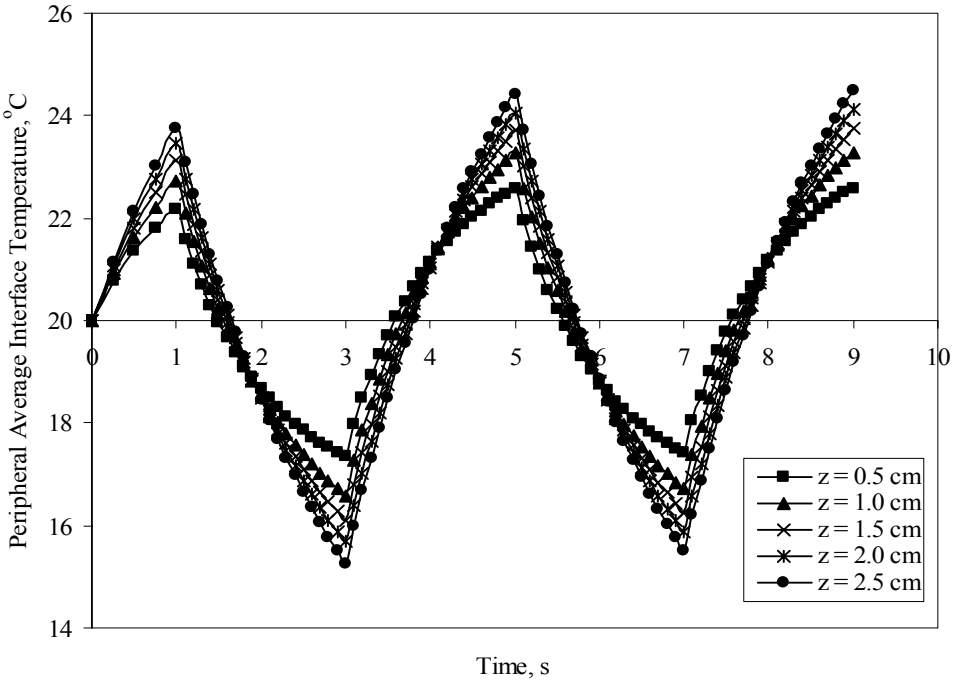

Figure 3.3: Peripheral average interface temperature at different axial locations over 9 seconds (Re = 1600, G = ±2 T, d = 0.036 cm)

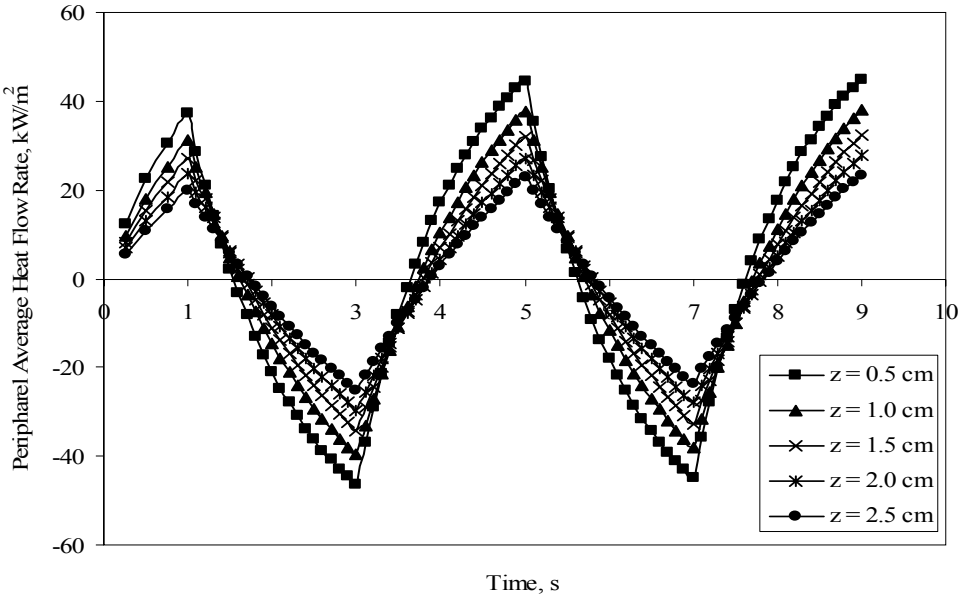

Figure 3.4: Peripheral average heat flow rate at different axial locations over 9 seconds (Re = 1600, G = ±2 T, d = 0.036 cm)

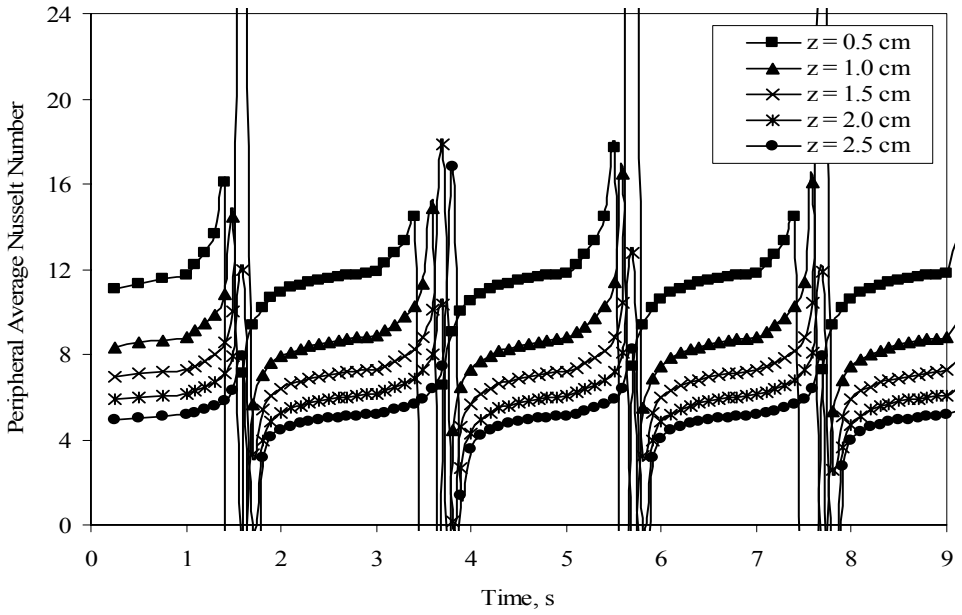

Figure 3.5: Peripheral average Nusselt number at different axial locations over 9 seconds (Re = 1600, G = ±2 T, d = 0.036 cm)

increases the Nusselt number. As heat generation and cooling process alternates the interface-bulk temperature difference alternates positive and negative values. This temperature difference becomes zero at certain time in each time period. This causes Nusselt number to be infinite at that time. After the heating and cooling processes alternates the system Nusselt number increases from negative infinite value to the actual value. The increase in the heat flow rate increases Nusselt number thereafter. Since the Nusselt number behavior is understood, only fewer points along time will be plotted to the results of the other cases.

Figure 3.6 shows the maximum temperature in the model when magnetic field of 4 T is used. Comparing to figure 3.2 the maximum temperature is higher because of the higher value of heat generation used. Figure 3.7 shows the heat flow rate at the interface using magnetic field of 4 T. Higher heat generation results in higher interface and solid temperatures in the model. Interface-solid temperature difference also increases with the increase in heat generation. The value of the heat generation diminished the effect of the initial condition and increased the heat flow rate along time. The interface-solid temperature difference is higher closer to the tube inlet because the inlet fluid temperature increases the interface-solid temperature difference. Similarly to the previous case, the heat flow rate decreases along the axial direction. Figure 3.8 shows the Nusselt number over 9 seconds time period using magnetic field of 4 T. The Nusselt number shows similar behavior to the previous case. Compared to figure 3.5, Nusselt number is not affected by the change in the magnetic field value.

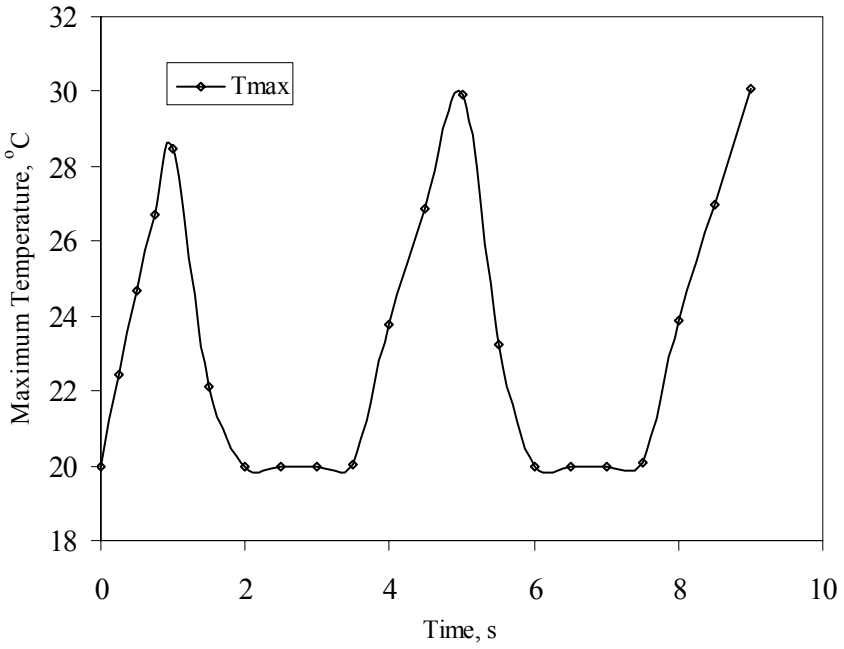

Figure 3.6: Maximum temperature over 9 seconds with G = ±4 T (Re = 1600, d = 0.036 cm)

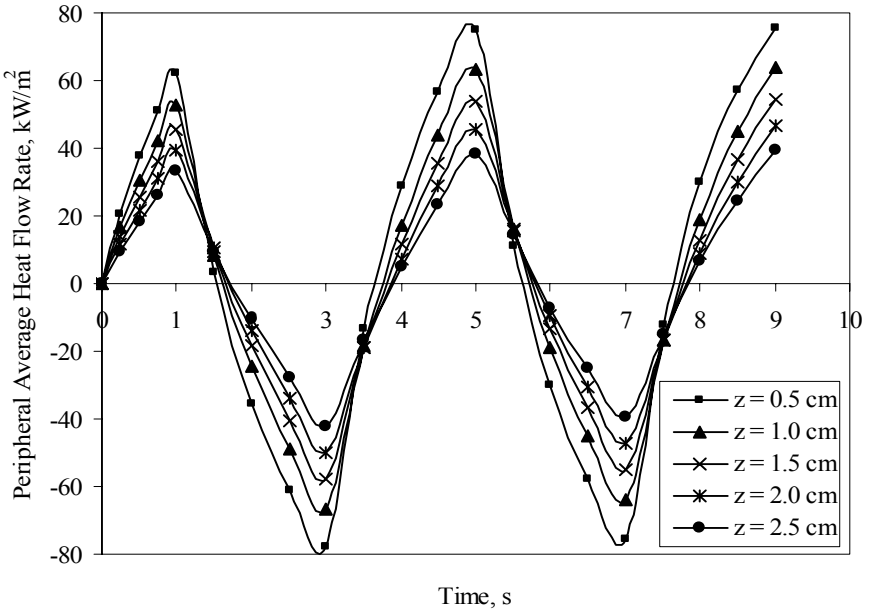

Figure 3.7: Peripheral average heat flow rate at different axial locations over 9 seconds with G = ±4 T (Re = 1600, d = 0.036 cm)

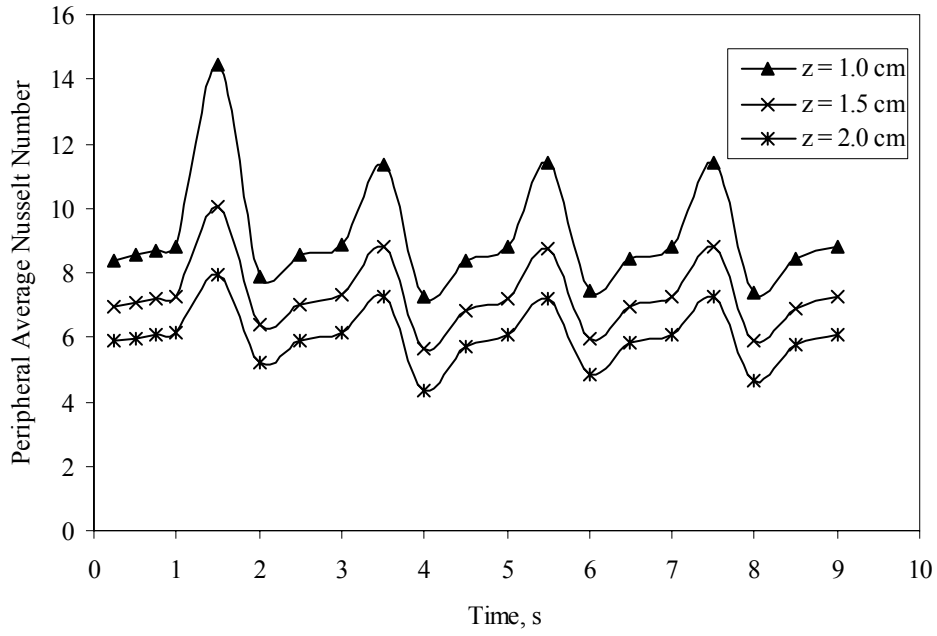

Figure 3.8: Peripheral average Nusselt number at different axial locations with G = ±4 T (Re = 1600, d = 0.036 cm)

Figure 3.9 shows the heat flow rate in the model when the diameter of 0.012 cm is used. Compared to figure 3.4, the values of heat flow rate is higher. As the diameter decreases, the solid volume increases causing more heat generation. This will increase the value of the heat flow rate at the interface. This is similar to the effect of increasing the magnetic field in the previous case. Comparing to figure 3.7, doubling the magnetic field has higher effect on the heat flow rate increase. Figure 3.10 shows Nusselt number behavior when diameter of 0.012 cm is used. The increase in Nusselt number is a direct result for the heat flow rate increase. The Nusselt number has similar behavior as the case of higher magnetic field value. The higher Nusselt number value at the beginning of each time period has similar explanation of those discussed in the previous case.

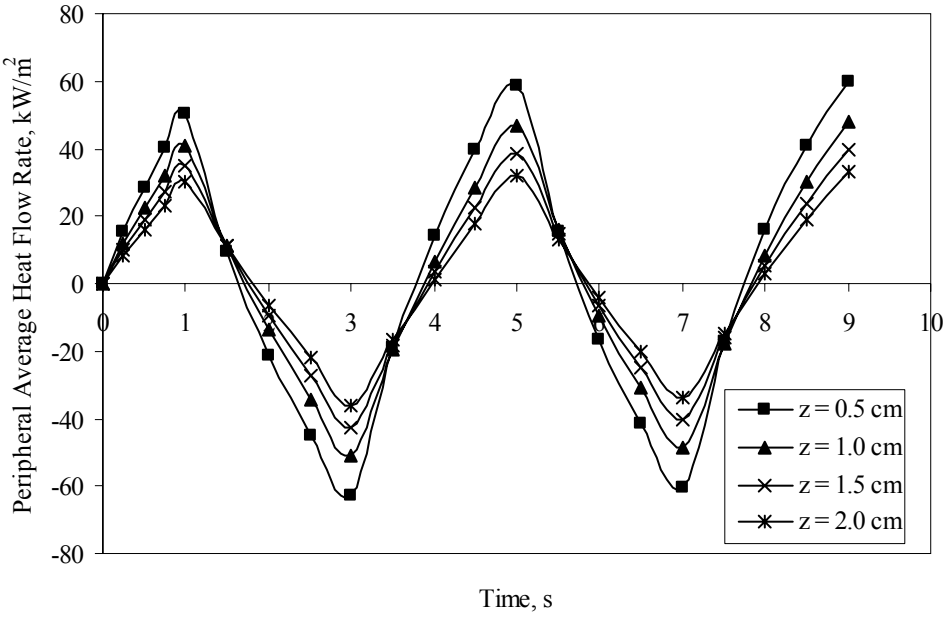

Figure 3.9: Peripheral average heat flow rate at different axial locations with d = 0.012 cm (Re = 1600, G = ±2 T)

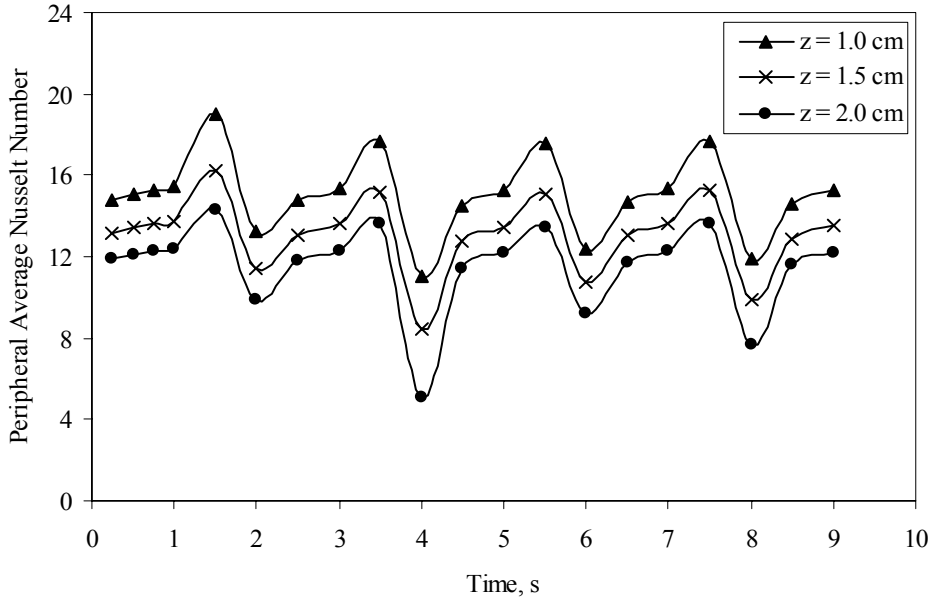

Figure 3.10: Peripheral average Nusselt number at different axial locations with d = 0.012 cm (Re = 1600, G = ±2 T)

Figure 3.11 shows the heat flow rate of the model at the fluid-solid interface surface for Reynolds number of 1000. The absolute values of the heat flow rate are lower compared to figure 3.4. Lower velocity means higher bulk temperature and thus less interface-bulk heat transfer. This results in less heat flow rate to the fluid. Figure 3.12 shows the Nusselt number behavior in the model for Reynolds number of 1000. Nusselt number directly decreases with the heat flow rate. Therefore, Nusselt number is also less for lower Reynolds numbers. This is clearly shown when the figure is compared to figure 3.5.

3.4 Conclusions

Study of the parameters of the circular microchannel model with transient heat generation was done. Mathematical model was developed and computations were done to solve the system. The effect of different parameters was studied. The results showed the behavior of the maximum temperature, interface temperature. The maximum temperature in the model does not drop below 20 ^{o}C because of the inlet temperature condition. The interface temperature, heat flow rate, and Nusselt number showed sinusoidal behavior as heat generation and cooling process alternates. The heat flow rate increase in value within each time period. The absolute value of heat flow rate is used when calculating the Nusselt number. This causes Nusselt number to increase during each time period. Notice that Nusselt number reaches high values at the beginning of each time period. This is because the interface-bulk temperatures difference becomes very small in value at which both temperatures alternate in value. Higher magnetic field increases the heat flow rate to the fluid as well as Nusselt number. Larger diameter decreases fluid velocity causing

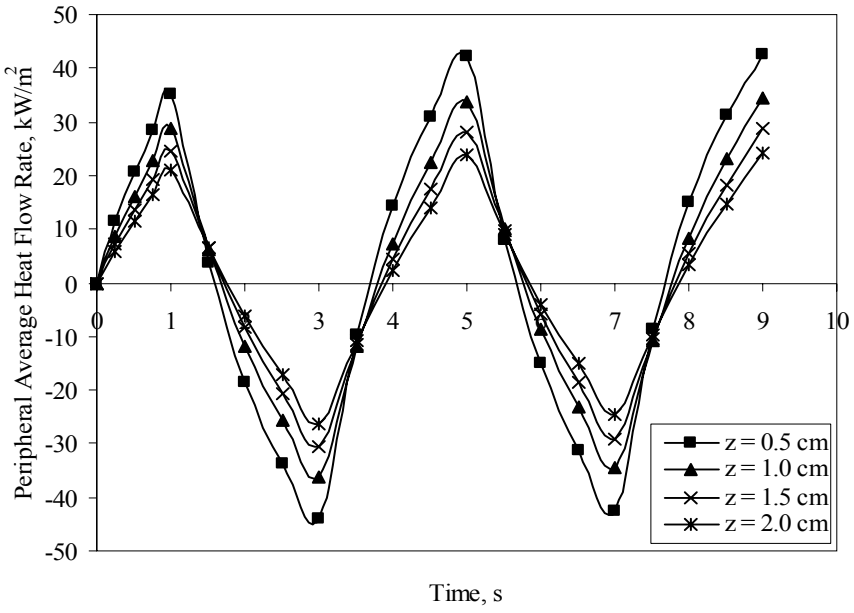

Figure 3.11: Peripheral average heat flow rate at different axial locations with Re = 1000 (G = ±2 T, d = 0.036 cm)

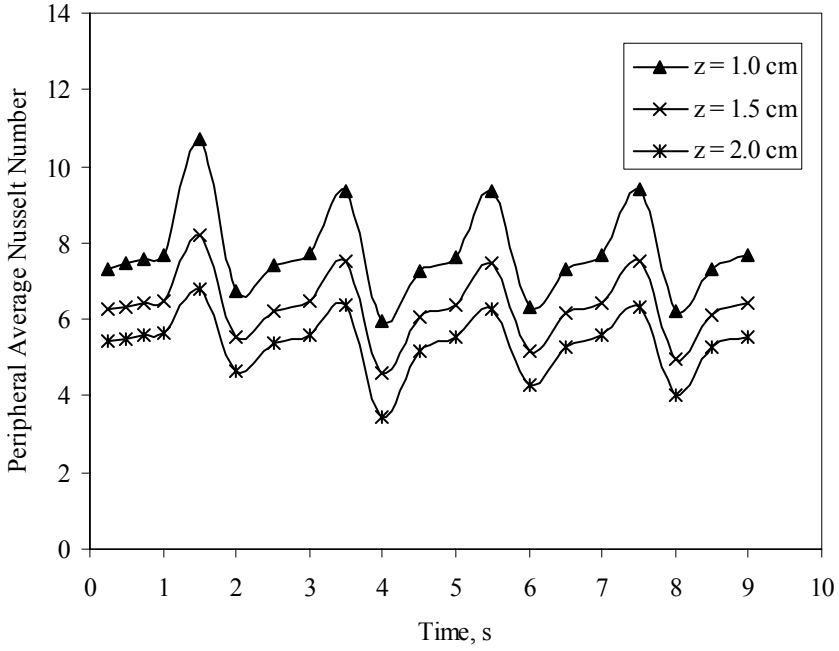

Figure 3.12: Peripheral average Nusselt number at different axial locations with Re = 1000 (G = ±2 T, d = 0.036 cm)

higher fluid bulk temperature. This increases the heat flow rate and, thus, Nusselt number. Lower Reynolds number results in lower heat flow rate and Nusselt number.

Chapter 4 – Transient Heat Transfer in Trapezoidal Microchannels During Activation of Magnetic Heating

4.1 Mathematical Model

The model in hand is a trapezoidal cross-sectional microchannel consisting of two different substrates gadolinium on top and silicon on bottom while the channel was manufactured into the bottom one. The gadolinium substrate on the top is joined to the silicon substrate and the primary working fluid selected was water. Figure 4.1 shows the schematic drawing of the model. Heat is generated in the gadolinium substrate and convected to the water while part of it is conducted to the silicon and then convected to water.

The applicable differential equations for the conservation of mass, momentum, and energy in the Cartesian coordinate system for the fluid can be written as [45],

$$\frac{\partial u}{\partial x}+\frac{\partial v}{\partial y}+\frac{\partial w}{\partial z}=0 \tag{1}$$

$$\frac{\partial u}{\partial t}+u\frac{\partial u}{\partial x}+v\frac{\partial u}{\partial y}+w\frac{\partial u}{\partial z}=-\frac{1}{\rho}\frac{\partial p}{\partial x}+\nu\left(\frac{\partial^2 u}{\partial x^2}+\frac{\partial^2 u}{\partial y^2}+\frac{\partial^2 u}{\partial z^2}\right) \tag{2}$$

$$\frac{\partial v}{\partial t}+u\frac{\partial v}{\partial x}+v\frac{\partial v}{\partial y}+w\frac{\partial v}{\partial z}=-\frac{1}{\rho}\frac{\partial p}{\partial x}+\nu\left(\frac{\partial^2 v}{\partial x^2}+\frac{\partial^2 v}{\partial y^2}+\frac{\partial^2 v}{\partial z^2}\right) \tag{3}$$

$$\frac{\partial w}{\partial t}+u\frac{\partial w}{\partial x}+v\frac{\partial w}{\partial y}+w\frac{\partial w}{\partial z}=-\frac{1}{\rho}\frac{\partial p}{\partial x}+\nu\left(\frac{\partial^2 w}{\partial x^2}+\frac{\partial^2 w}{\partial y^2}+\frac{\partial^2 w}{\partial z^2}\right) \tag{4}$$

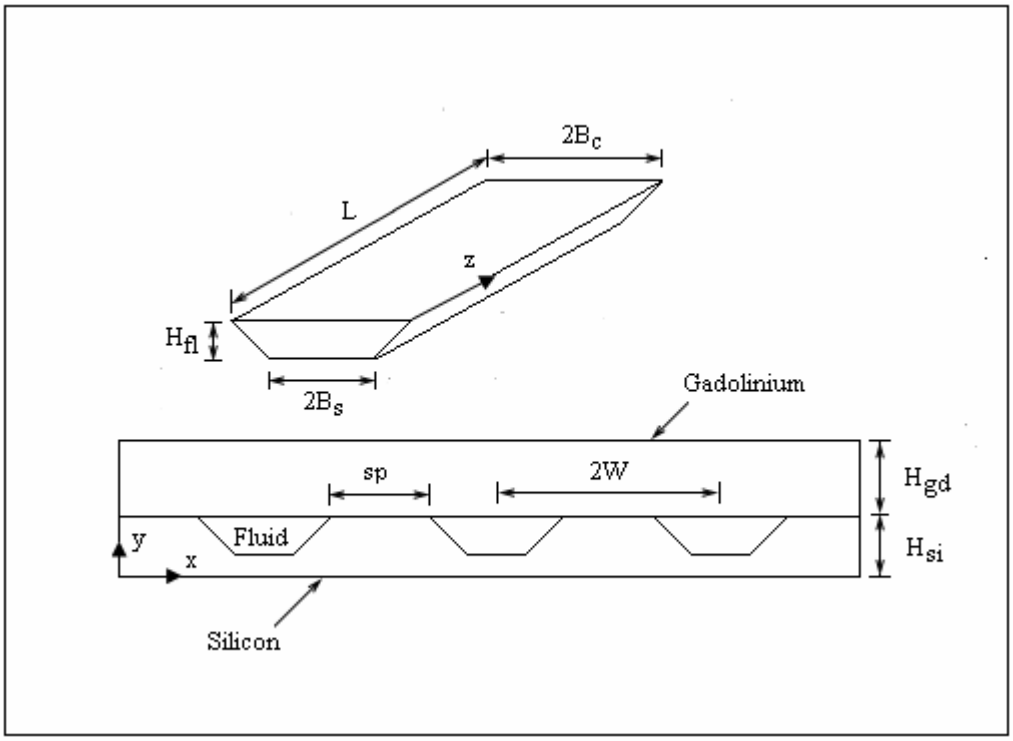

Figure 4.1: Schematic draw for the model of trapezoidal microchannel

$$\frac{\partial T_f}{\partial t} + u\frac{\partial T_f}{\partial x} + v\frac{\partial T_f}{\partial y} + w\frac{\partial T_f}{\partial z} = \alpha\left(\frac{\partial^2 T_f}{\partial x^2} + \frac{\partial^2 T_f}{\partial y^2} + \frac{\partial^2 T_f}{\partial z^2}\right) \tag{5}$$

The energy conservation equation in the solid gadolinium substrate is [46]:

$$\frac{\partial^2 T_{gd}}{\partial x^2} + \frac{\partial^2 T_{gd}}{\partial y^2} + \frac{\partial^2 T_{gd}}{\partial z^2} + \frac{g_0}{k_{gd}} = \frac{1}{\alpha}\frac{\partial T_{gd}}{\partial t} \tag{6}$$

and for the solid silicon substrate is:

$$\frac{\partial^2 T_{si}}{\partial x^2} + \frac{\partial^2 T_{si}}{\partial y^2} + \frac{\partial^2 T_{si}}{\partial z^2} = \frac{1}{\alpha}\frac{\partial T_{si}}{\partial t} \tag{7}$$

Equations (1) – (7) are subject to following initial and boundary conditions:

At t = 0: $T_f = T_{gd} = T_{si} = T_{in}$ (8)

At z = 0, at fluid inlet: $u=0,\ v=0,\ w=w_{in},\ T=T_{in}$ (9)

At z = 0, on solid surface: $\frac{\partial T_{si}}{\partial z} = 0\,,\ \frac{\partial T_{gd}}{\partial z} = 0$ (10)

At z = L, at fluid outlet: $p=0$ (11)

At z = L, on solid surface: $\frac{\partial T_{si}}{\partial z} = 0\,,\ \frac{\partial T_{gd}}{\partial z} = 0$ (12)

At x = 0, $0 < y < (H_{si}-H_{fl})$, $0 < z < L$: $\frac{\partial T_{si}}{\partial z} = 0$ (13)

At x = 0, $(H_{si}-H_{fl}) < y < H_{si}$, $0 < z < L$: $u=0,\ \frac{\partial v}{\partial x} = 0\,,\ \frac{\partial w}{\partial x} = 0\,,\ \frac{\partial T_f}{\partial x} = 0$ (14)

At x = 0, $H_{si} < y < (H_{si}+H_{gd})$, $0 < z < L$: $\frac{\partial T_{gd}}{\partial x} = 0$ (15)

At x = B, $0 < y < H_{si}$, $0 < z < L$: $\frac{\partial T_{si}}{\partial x} = 0$ (16)

At x = B, $H_{ii} < y < (H_{si}+H_{gd})$, $0 < z < L$: $\frac{\partial T_{gd}}{\partial x} = 0$ (16)

At y = 0, $0 < x < B$, $0 < z < L$: $\frac{\partial T_{si}}{\partial y} = 0$ (17)

At y = $(H_{si}-H_{fl})$, $B-B_s < x < B$, $0 < z < L$: $u=0$, $v=0$, $w=0$, $T_f = T_{si}$, and

$$k_f \frac{\partial T_f}{\partial y} = k_{si} \frac{\partial T_{si}}{\partial y} \quad (18)$$

At y = H_{si}, $0 < x < B-B_c$, $0 < z < L$: $u=0$, $v=0$, $w=0$, $T_f = T_{gd}$, and

$$k_f \frac{\partial T_f}{\partial y} = k_{gd} \frac{\partial T_{gd}}{\partial y} \quad (19)$$

At y = H_{si}, $B-B_c < x < B$, $0 < z < L$: $$k_{si} \frac{\partial T_{si}}{\partial y} = k_{gd} \frac{\partial T_{gd}}{\partial y} \quad (20)$$

At y = $(H_{si}+H_{gd})$, $0 < x < B$, $0 < z < L$: $\frac{\partial T_{gd}}{\partial y} = 0$ (21)

The inclined fluid-silicon surface, 0<z<L, u=0, v=0, w=0, $T_f = T_{si}$, and

$$k_f \frac{\partial T_f}{\partial n} = k_{si} \frac{\partial T_{si}}{\partial n} \tag{22}$$

4.2 Numerical Simulation and Parametric Study

The governing equations along with the initial and boundary conditions were solved using the Galerkin finite element method. The Newton-Raphson algorithm was used to solve the nonlinear system of discretized equations. An iterative procedure was used to arrive at the solution for the velocity and temperature fields. The solution was considered converged when the field values did not change from one iteration to the next, and the residuals for each variable became negligible.

For the numerical computations, the Length (L) and the half width (W) of the model were set to a constant value, 2.0 cm and 0.3 cm respectively. The height of the silicon substrate (H_{si}) and the inlet temperature were also set to a constant value, 0.1 cm and 20 ^oC respectively. Time period of 1 second was used. The parameters to be changed were selected to be: Reynolds number, magnetic field, height of fluid microchannel, height of gadolinium substrate, spacing between channels, and working fluid. Initially these parameters were selected as follows: Re = 2000, G = 5 Tesla, H_{fl} = 0.03 cm, H_{gd} = 0.3 cm, Sp = 0.3 cm, and water as the working fluid. One parameter was changed at a time while all other parameters kept constant to study the effect of each parameter separately. Reynolds number was changed to 1500 and 1000, G was changed to 2.5 and 10 Tesla, H_{fl} was changed to 0.02 cm, H_{gd} was changed to 0.4 and 0.5 cm, sp = 0.29 and 0.28 cm, and the working fluid was changed to Ammonia, and R-134a.

4.3 Result and Discussion

Figures 4.2 and 4.3 show a grid independence study carried out in the cross-sectional area of the channel to determine the optimum grid size and to insure accurate results. The number of intervals in the axial direction kept constant because it does not affect the results significantly. The results obtained by using (nx = 24, ny = 16, nz = 10) that had an average error of 0.08% in the silicon side and a maximum error of 0.1% in the interface temperature compared to (nx = 36, ny = 24, nz = 10). The heat flow rate also shows a small error comparing the above two grid systems. The average error for the heat flow rate was 0.78% while the maximum was 1.27%. Figures 4.2 and 4.3 show that the grid size selected was sufficient enough to reach optimum results.

Figure 4.4 shows that gadolinium interface temperature increases by time. This is because of the heat generated in the system. After 4 seconds the system almost reaches steady state. The first 2 seconds has much larger increase in average interface temperature. Heat is generated in the gadolinium substrate and then transferred to the fluid through convection and to the silicon substrate through conduction. The figure shows that there is an increase in the average interface temperature at the gadolinium interface along the axial direction which is caused by the heat generation. The rate of increase in the average interface temperature decreases when reaching the end of the channel. This is because the fluid temperature rises resulting in less heat rejection. Figure 4.5 shows that the heat flow rate at the gadolinium interface increases with time. This is

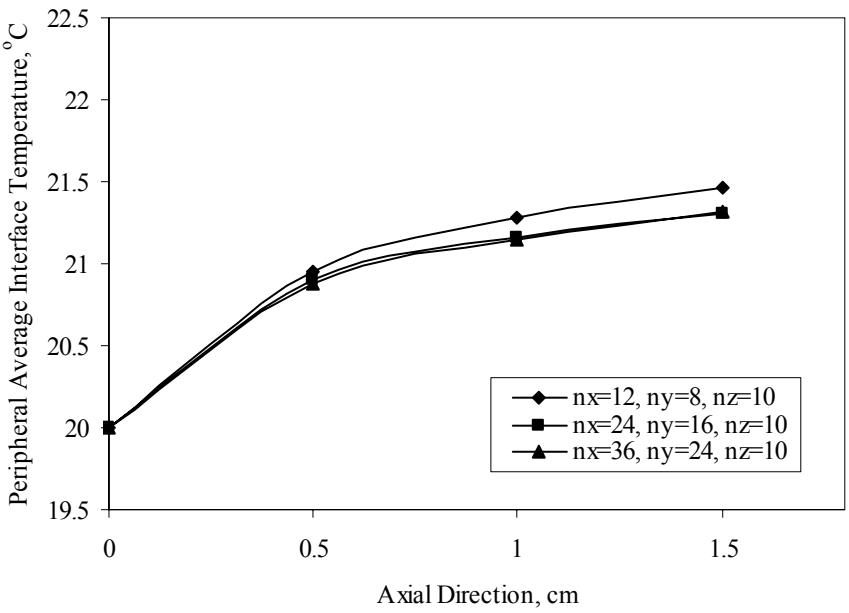

Figure 4.2: Peripheral average interface temperature along the axial direction at the fluid-silicon interface (Re = 2000, G = 5 T, H_{fl} = 0.03 cm)

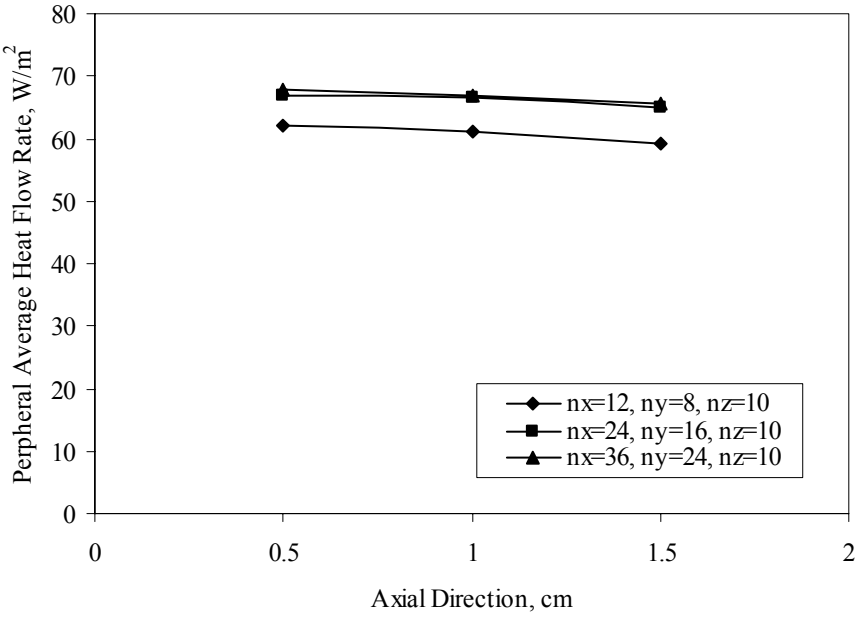

Figure 4.3: Peripheral average heat flow rate along the axial direction at the fluid-silicon interface (Re = 2000, G = 5 T, H_{fl} = 0.03 cm)

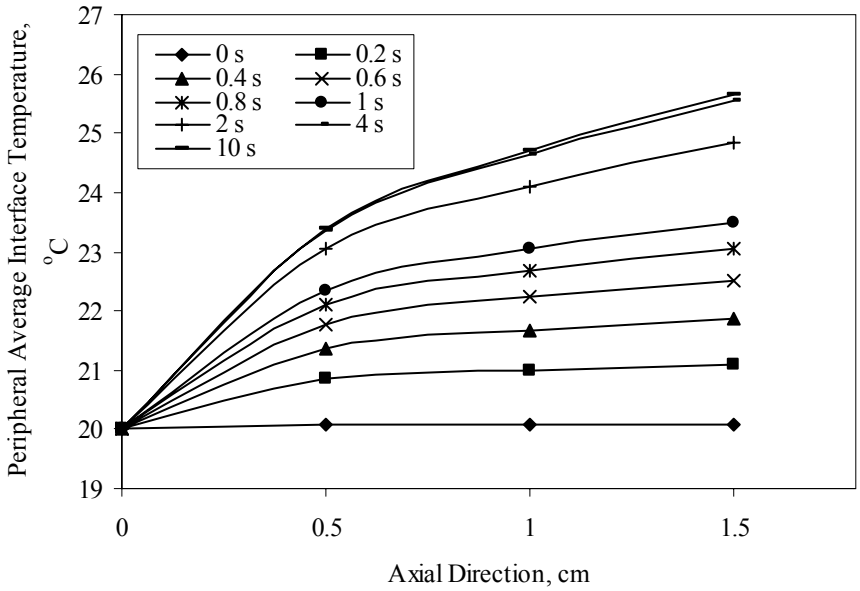

Figure 4.4: Peripheral average interface temperature along the axial direction at different time steps at the fluid-gadolinium interface (Re = 2000, G = 5 T, H_{fl} = 0.03 cm)

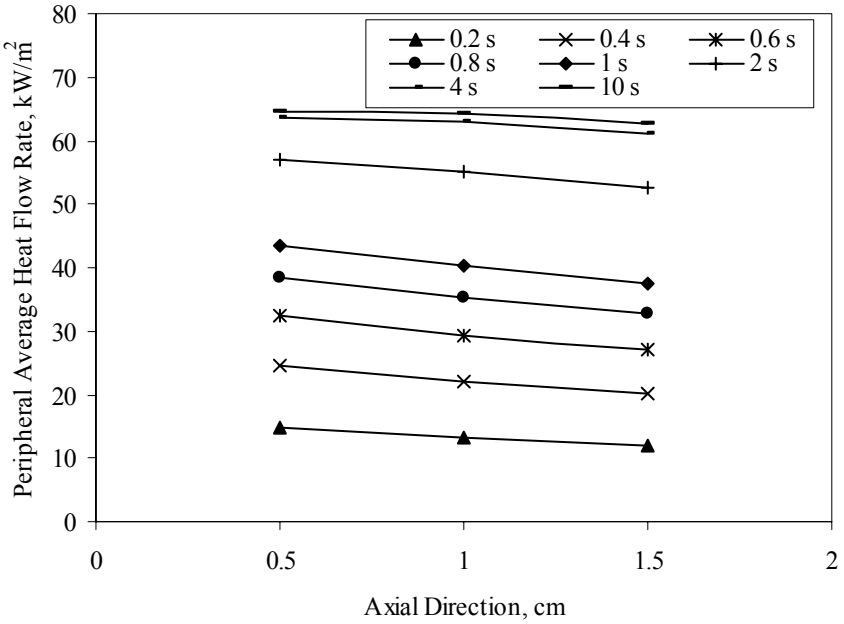

Figure 4.5: Peripheral average heat flow rate along the axial direction at different time steps at the fluid-gadolinium interface (Re = 2000, G = 5 T, H_{fl} = 0.03 cm)

because of the heat generation in the gadolinium substrate. The average interface temperature increases along the axial direction. The fluid bulk temperature increases along the axial direction at a higher rate than the interface temperature. This causes the heat flow rate to decrease along the axial direction. From the figure one can see that heat flow rate across the interface reaches steady state closer to the inlet before locations further away along the axial direction. Figures 4.6 and 4.7 show the average heat transfer coefficient and Nusselt number respectively. Both, heat flow rate and interface-bulk temperature difference, increase by time. The heat transfer coefficient is a ratio of the heat flow rate to the interface-bulk temperature difference. The figure shows that the heat transfer coefficient increases with time closer to the channel entrance while it decreases with time towards the end of the channel. This means that the rate of change in the heat flow rate to the interface-bulk temperature difference ratio decreases along the axial direction. This could be explained by the increase in the fluid bulk temperature which causes more increase the interface-bulk temperature difference further away from the channel entrance. The net result for the combined effects cause the average heat transfer coefficient and thus the Nusselt number to increase by time at closer to the inlet but decrease by time closer to the outlet. The heat flow rate decreases along the axial direction due to the increase in the interface-bulk temperature difference. This insures a decrease in the heat transfer coefficient and thus Nusselt number along the axial direction. Figure 4.8 shows that the silicon interface temperature increases by time. This is because the heat is conducted through the silicon substrate from the heat generated in the gadolinium substrate. Similarly to the gadolinium side, the system almost reaches steady state after 4 seconds. The heat that is conducted from the gadolinium to the

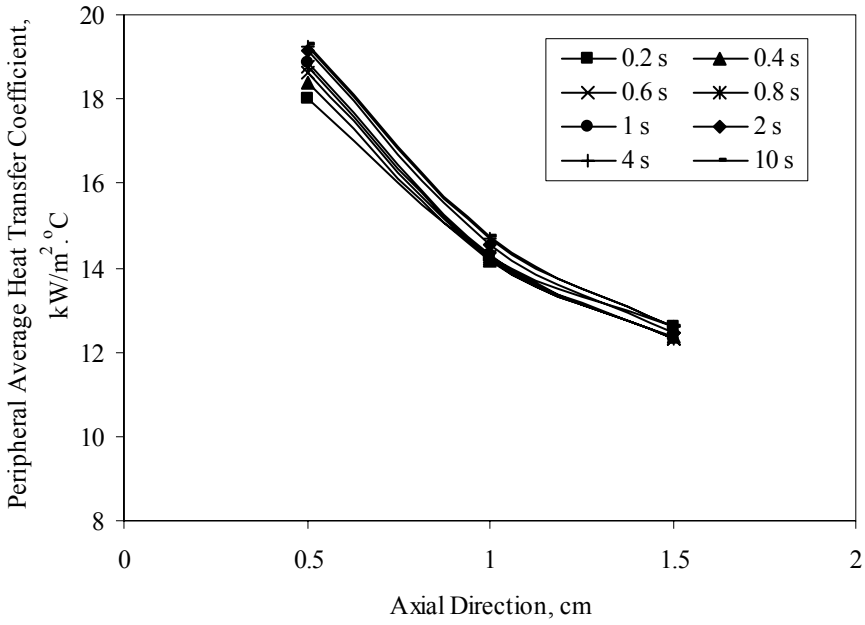

Figure 4.6: Peripheral average heat transfer coefficient along the axial direction at different time steps at the fluid-gadolinium interface (Re = 2000, G = 5 T, H_{fl} = 0.03 cm)

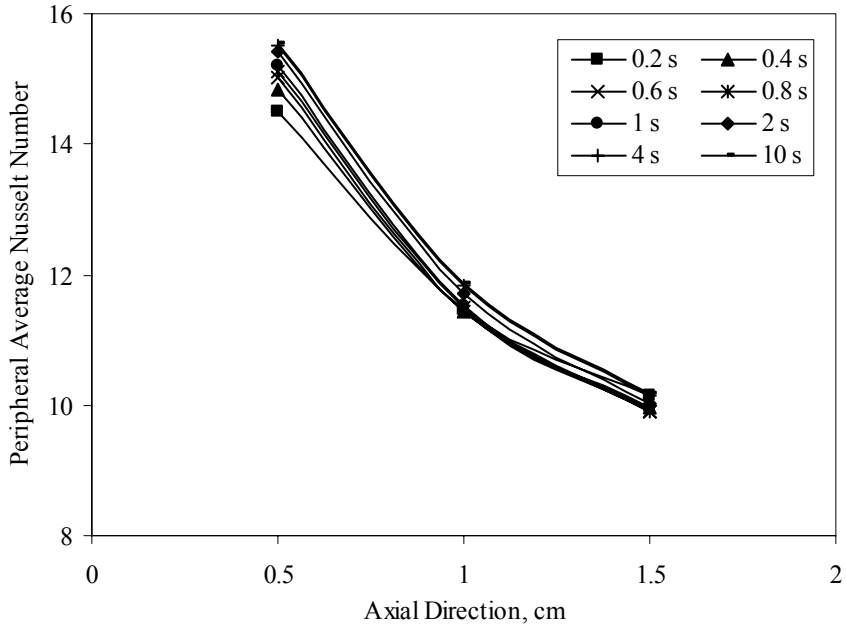

Figure 4.7: Peripheral average Nusselt number along the axial direction at different time steps at the fluid-gadolinium interface (Re = 2000, G = 5 T, H_{fl} = 0.03 cm)

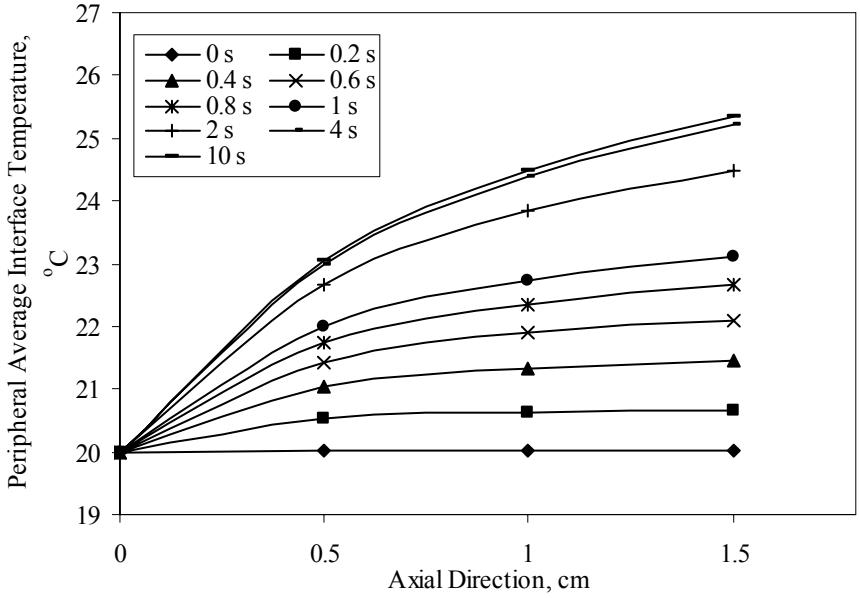

Figure 4.8: Peripheral average interface temperature along the axial direction at different time steps at the fluid-silicon interface (Re = 2000, G = 5 T, H_{fl} = 0.03 cm)

silicon causes the interface temperature increase at the fluid-silicon interface. The figure also shows that there is an increase in the average interface temperature at the silicon interface along the axial direction which is caused by the heat conducted to the silicon from the heat generated in the gadolinium substrate. The rate of increase in the average interface temperature decreases when reaching the end of the channel. This is because the fluid temperature rises resulting in less heat rejection. Figure 4.9 shows that the heat flow rate at the silicon interface increases with time. This is because of the heat conducted to the silicon from the heat generation in the gadolinium substrate. The average interface temperature increases along the axial direction. The heat flow rate is less in the silicon interface compared to the gadolinium interface. This is because the heat flow travels through the silicon substrate by conduction before facing the fluid-silicon interface. This

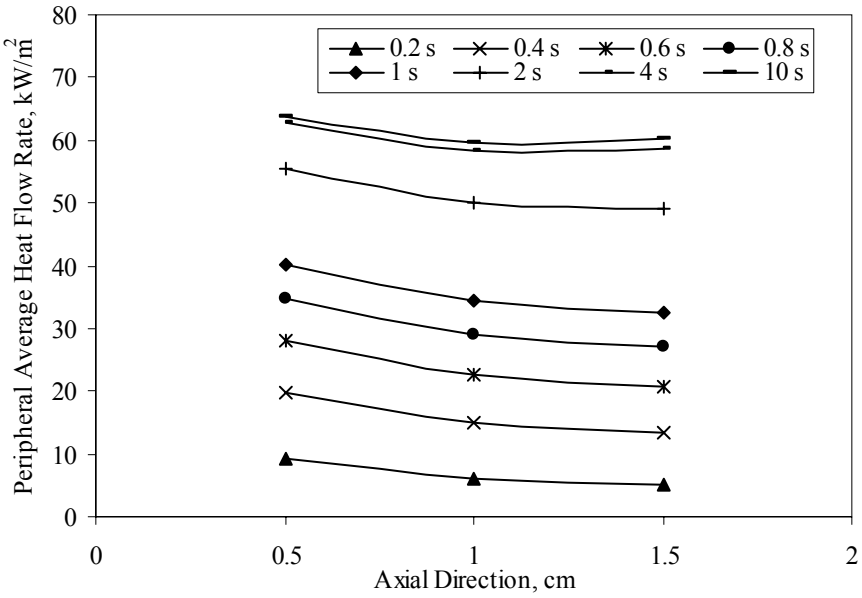

Figure 4.9: Peripheral average heat flow rate along the axial direction at different time steps at the fluid-silicon interface (Re = 2000, G = 5 T, H_{fl} = 0.03 cm)

slows down the heat transfer process in the silicon substrate resulting less temperature gradient than in the gadolinium substrate where the heat is generated. As the fluid travels along the axial direction it gains more heat from the gadolinium substrate and less heat from the silicon side, especially with the rising bulk fluid temperature. This result in lower rate of decrease in the heat flow rate along the axial direction at the silicon interface compared to the gadolinium interface. Figures 4.10 and 4.11 show that after 2 seconds the heat transfer coefficient and Nusselt number changes could be ignored. The heat flow rate and the interface-bulk temperature difference increase with time. The heat flow rate increase is higher which results in an increase in the heat transfer coefficient and Nusselt number with time. The heat flow rate decreases along the axial direction due to the increase in the fluid bulk temperature. Nusselt number follow similar trend to those

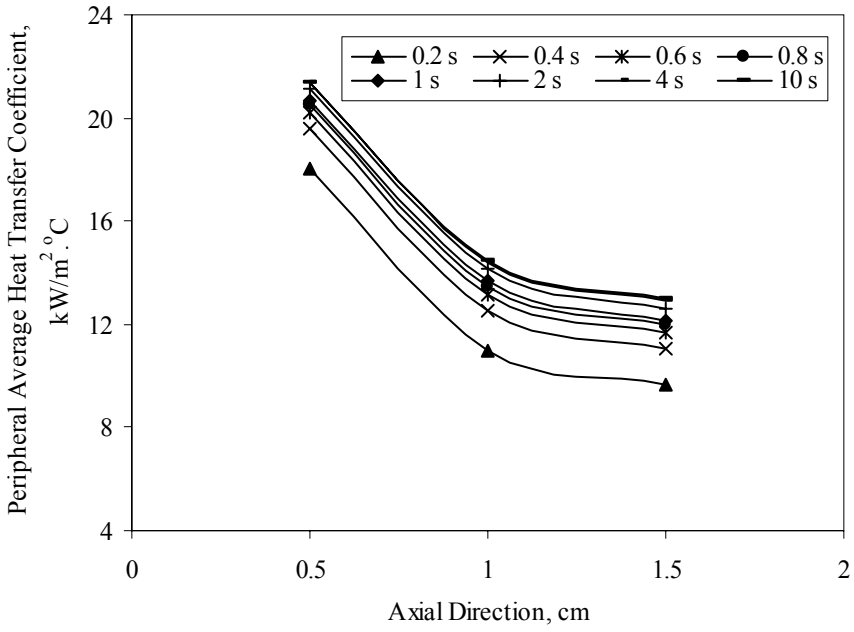

Figure 4.10: Peripheral average heat transfer coefficient along the axial direction at different time steps at the fluid-silicon interface (Re = 2000, G = 5 T, H_{fl} = 0.03 cm)

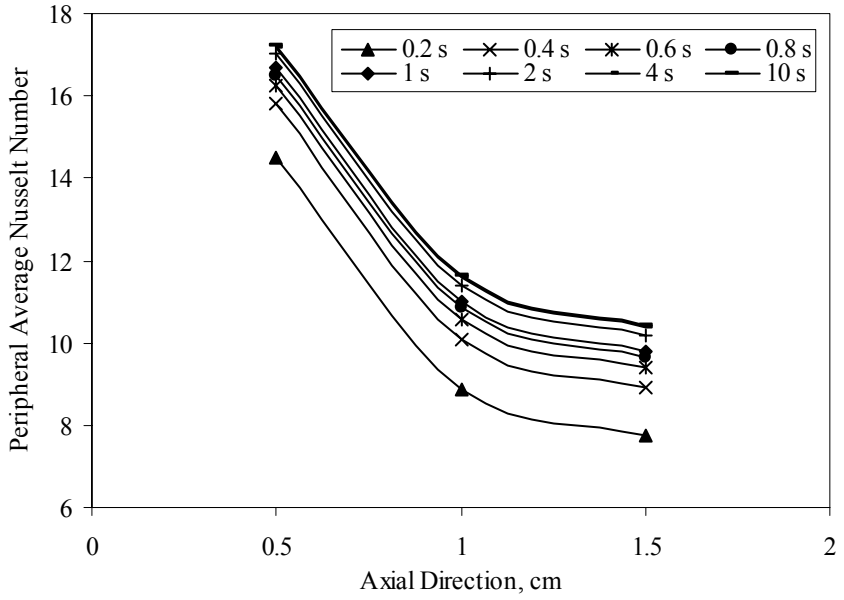

Figure 4.11: Peripheral average Nusselt number along the axial direction at different time steps at the fluid-silicon interface (Re = 2000, G = 5 T, H_{fl} = 0.03 cm)

of heat transfer coefficient. It decreases along the axial direction due to the increase in the fluid bulk temperature.

Figures 4.12, 4.13 and 4.14 show the results of interface temperature, heat flow rate and Nusselt number for different Reynolds number along the axial direction at the gadolinium-fluid interface. Higher fluid velocity increases the heat transfer coefficient at the interface causing lower interface temperature and lower fluid bulk temperature. It will also increase the temperature gradient in the solid substrate increasing the heat flow rate at the interface. Nusselt number increases due to the increase in the heat transfer coefficient.

Figures 4.15, 4.16 and 4.17 show the results of interface temperature, heat flow rate and Nusselt number for different Reynolds number along the axial direction at the silicon-fluid interface. Similar to the gadolinium side, higher fluid velocity increases the heat transfer coefficient at the interface causing lower interface temperature and lower fluid bulk temperature but higher heat flow rate and Nusselt number.

Figures 4.18, 4.19 and 4.20 show the results of interface temperature, heat flow rate and Nusselt number for different magnetic fields along the axial direction at the gadolinium-fluid interface. Higher heat generation increases the temperature profile in the solid substrate causing an increase in the average interface temperature and heat flow rate. The increase in both, interface temperature and heat flow rate, cancel their effects resulting in negligible change in Nusselt number.

Figures 4.21, 4.22 and 4.23 show the results of interface temperature, heat flow rate and Nusselt number for different magnetic fields along the axial direction at the silicon-fluid interface. Similar to the gadolinium side, higher heat generation increases

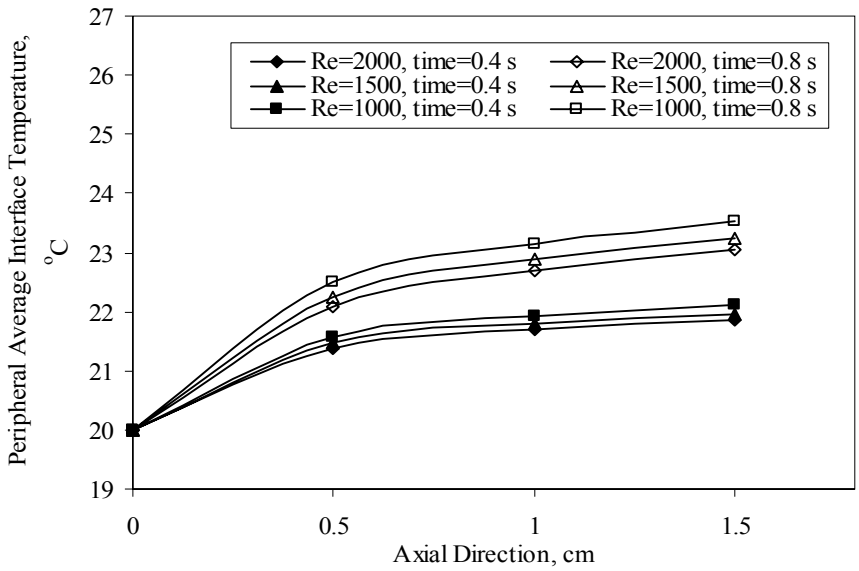

Figure 4.12: The effect of Reynolds number on the peripheral average interface temperature along the axial direction at different time periods at the fluid-gadolinium interface (G = 5 T, H_{fl} = 0.03 cm)

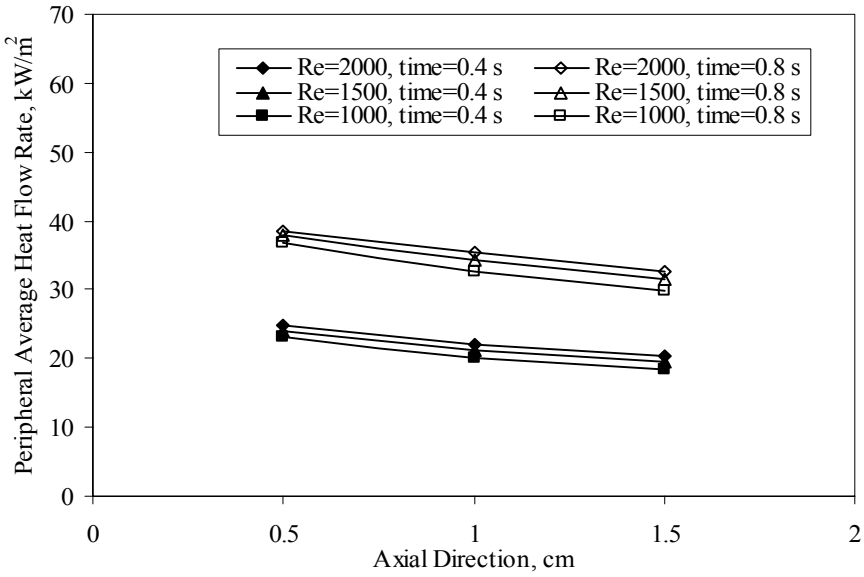

Figure 4.13: The effect of Reynolds number on the peripheral average heat flow rate along the axial direction at different time periods at the fluid-gadolinium interface (G = 5 T, H_{fl} = 0.03 cm)

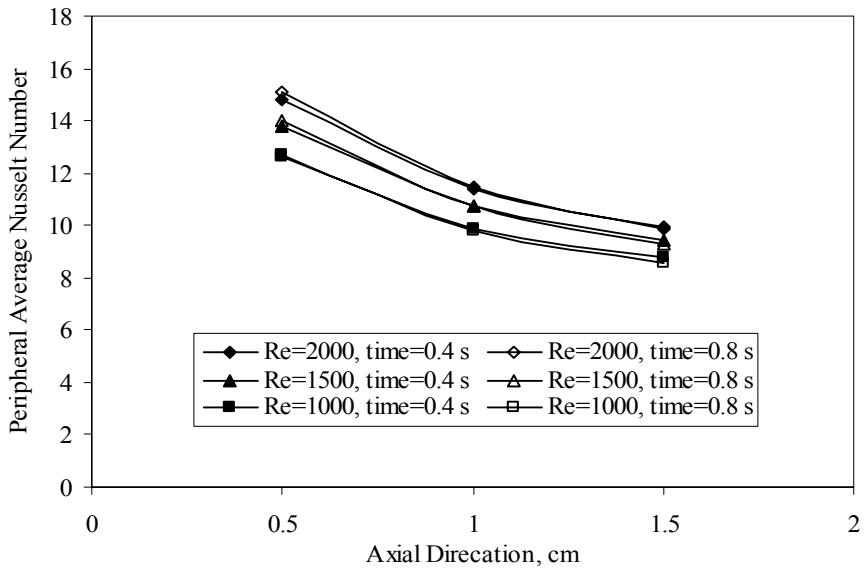

Figure 4.14: The effect of Reynolds number on the peripheral average Nusselt number along the axial direction at different time periods at the fluid-gadolinium interface (G = 5 T, H_{fl} = 0.03 cm)

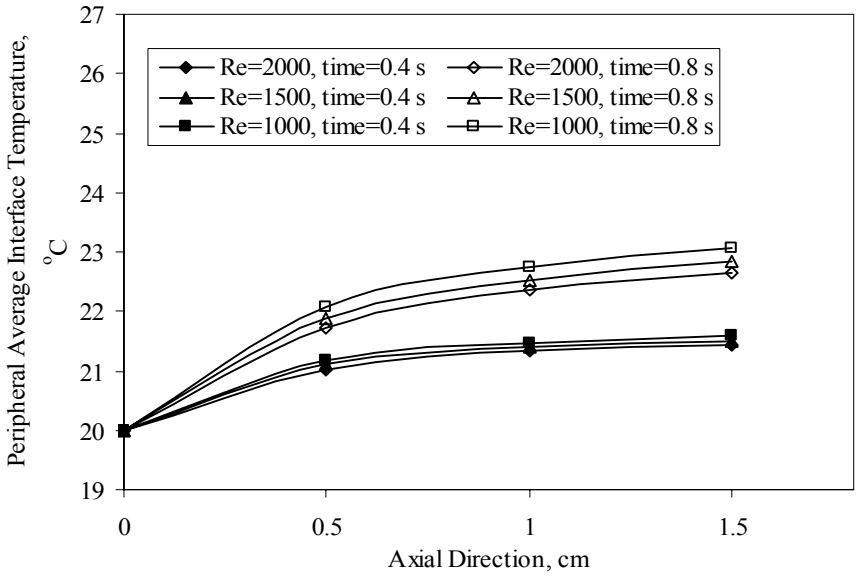

Figure 4.15: The effect of Reynolds number on the peripheral average interface temperature along the axial direction at different time periods at the fluid-silicon interface (G = 5 T, H_{fl} = 0.03 cm)

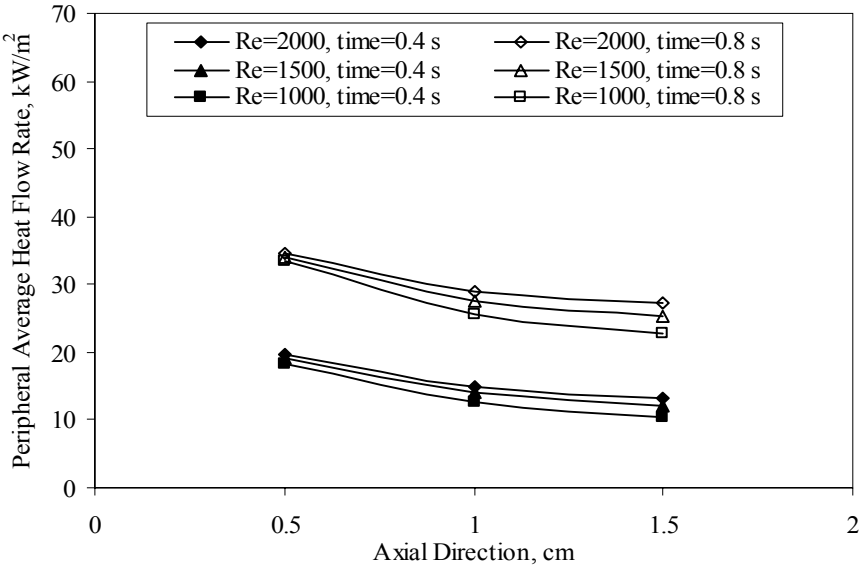

Figure 4.16: The effect of Reynolds number on the Peripheral average heat flow rate along the axial direction at different time periods at the fluid-silicon interface (G = 5 T, H_{fl} = 0.03 cm)

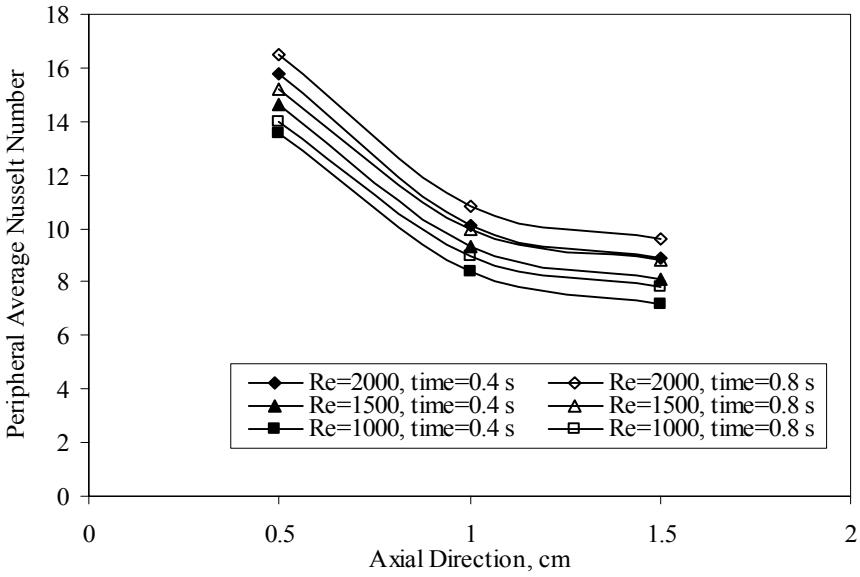

Figure 4.17: The effect of Reynolds number on the peripheral average Nusselt number along the axial direction at different time periods at the fluid-silicon interface (G = 5 T, H_{fl} = 0.03 cm)

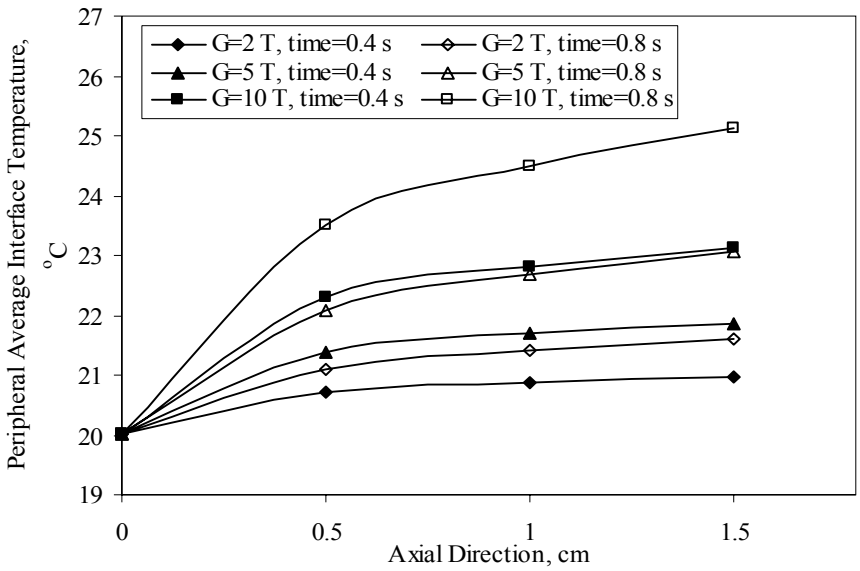

Figure 4.18: The effect of magnetic field on the peripheral average interface temperature along the axial direction at different time periods at the fluid-gadolinium interface (Re = 2000, H_{fl} = 0.03 cm)

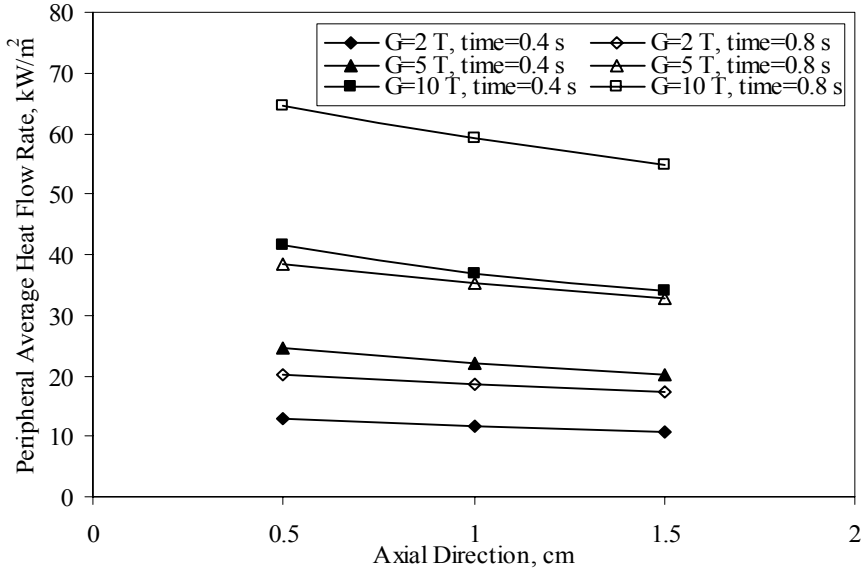

Figure 4.19: The effect of magnetic field on the peripheral average heat flow rate along the axial direction at different time periods at the fluid-gadolinium interface (Re = 2000, H_{fl} = 0.03 cm)

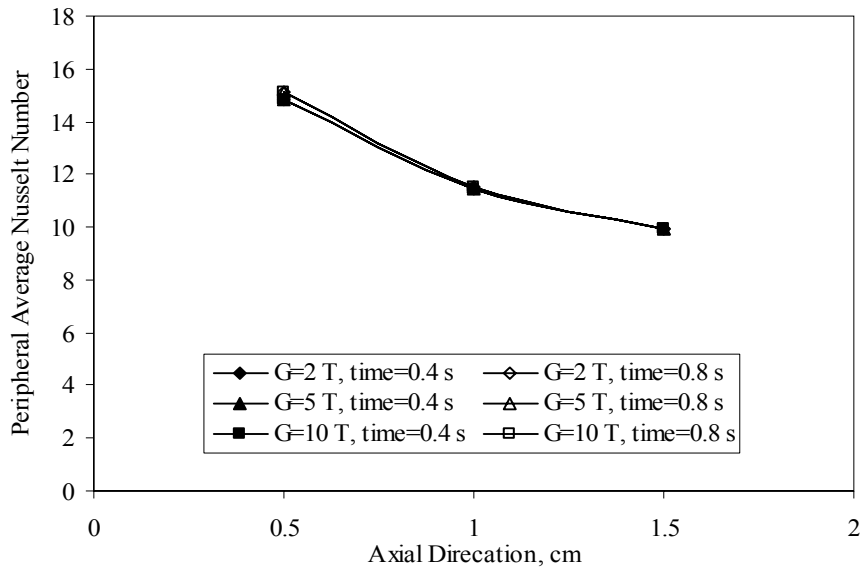

Figure 4.20: The effect of magnetic field on the peripheral average Nusselt number along the axial direction at different time periods at the fluid-gadolinium interface (Re = 2000, H_{fl} = 0.03 cm)

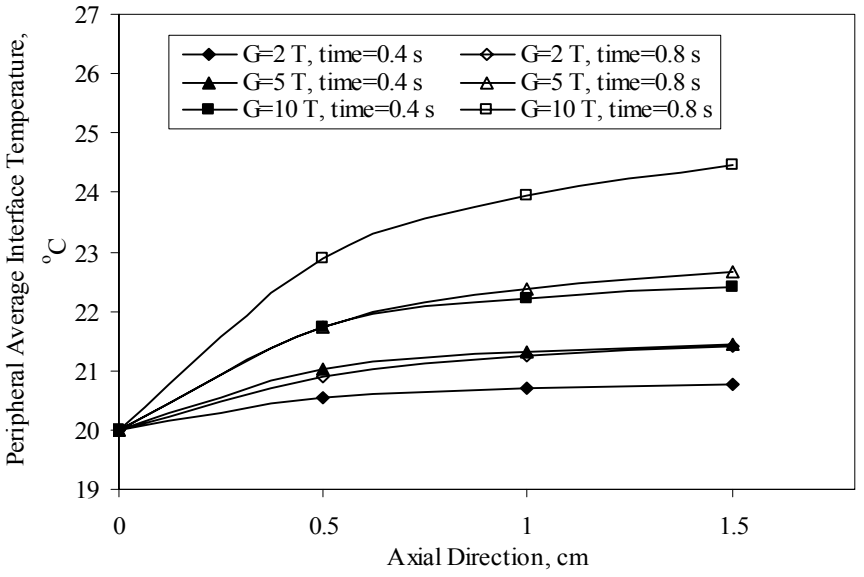

Figure 4.21: The effect of magnetic field on the peripheral average interface temperature along the axial direction at different time periods at the fluid-silicon interface (Re = 2000, H_{fl} = 0.03 cm)

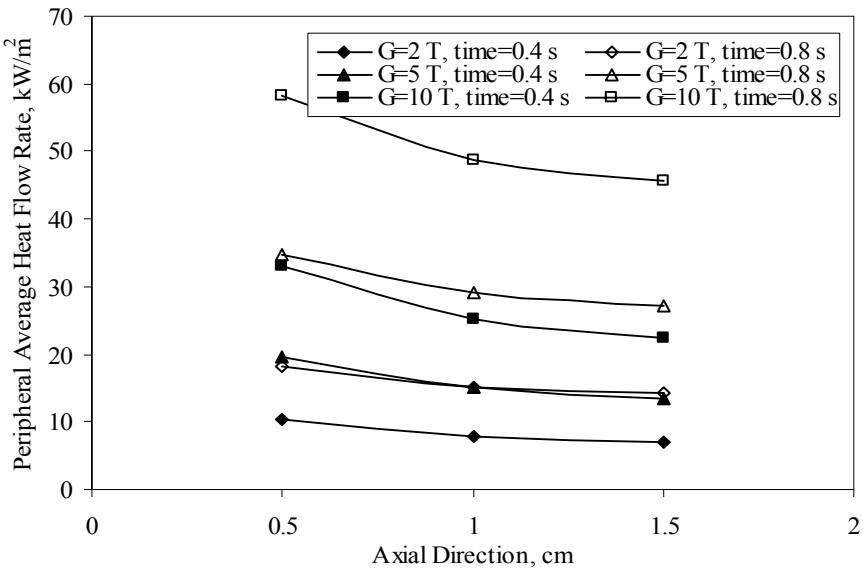

Figure 4.22: The effect of magnetic field on the peripheral average heat flow rate along the axial direction at different time periods at the fluid-silicon interface (Re = 2000, H_{fl} = 0.03 cm)

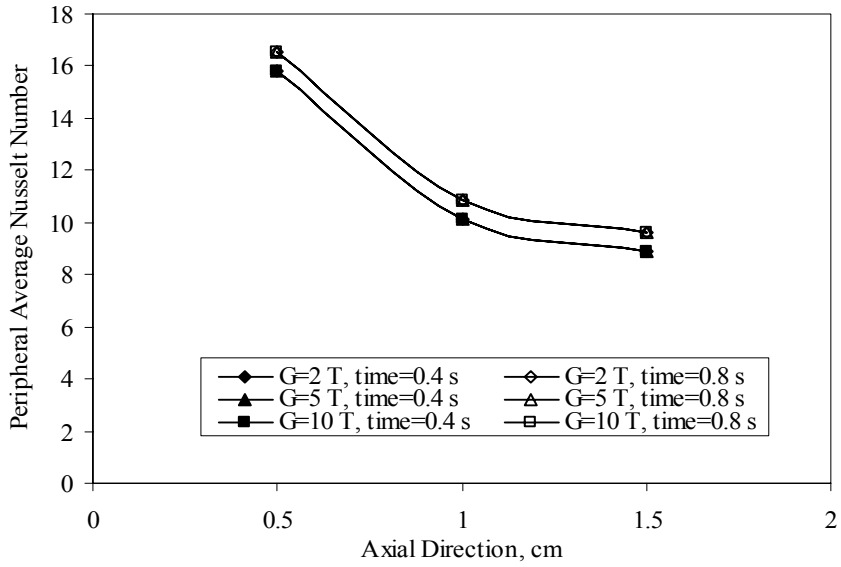

Figure 4.23: The effect of magnetic field on the peripheral average Nusselt number along the axial direction at different time periods at the fluid-silicon interface (Re = 2000, H_{fl} = 0.03 cm)

the temperature profile in the solid substrate causing an increase in the average interface temperature and heat flow rate. The increase in both, interface temperature and heat flow rate, cancel their effects resulting in no change in Nusselt number.

Figures 4.24, 4.25 and 4.26 show the results of interface temperature, heat flow rate and Nusselt number for different channel height along the axial direction at the gadolinium-fluid interface. The reduction in the channel height with maintaining the same Reynolds number results in higher fluid velocity. This enhances the cooling rate and decreases the interface temperature as well as the fluid bulk temperature. On the other hand, the heat flow rate increases due to the higher temperature gradient in the solid substrate. The increase in the heat flow rate increases Nusselt number.

Figures 4.27, 4.28 and 4.29 show the results of interface temperature, heat flow rate and Nusselt number for different channel height along the axial direction at the silicon-fluid interface. Similarly to the gadolinium side, the channel height reduction increases the fluid velocity. This decreases the interface temperature and the fluid bulk temperature. The heat flow rate increases due to the higher temperature gradient in the solid substrate. The increase in the heat flow rate increases Nusselt number.

Figures 4.30, 4.31 and 4.32 show the results of interface temperature, heat flow rate and Nusselt number for different height of gadolinium substrate along the axial direction at the gadolinium-fluid interface. Higher gadolinium height results in higher heat generation but the heat generation per unit volume remains the same. Since the heat generation is calculated per unit volume, it is expected that the increase in gadolinium height does not affect the temperature gradient in the solid. Results showed a small

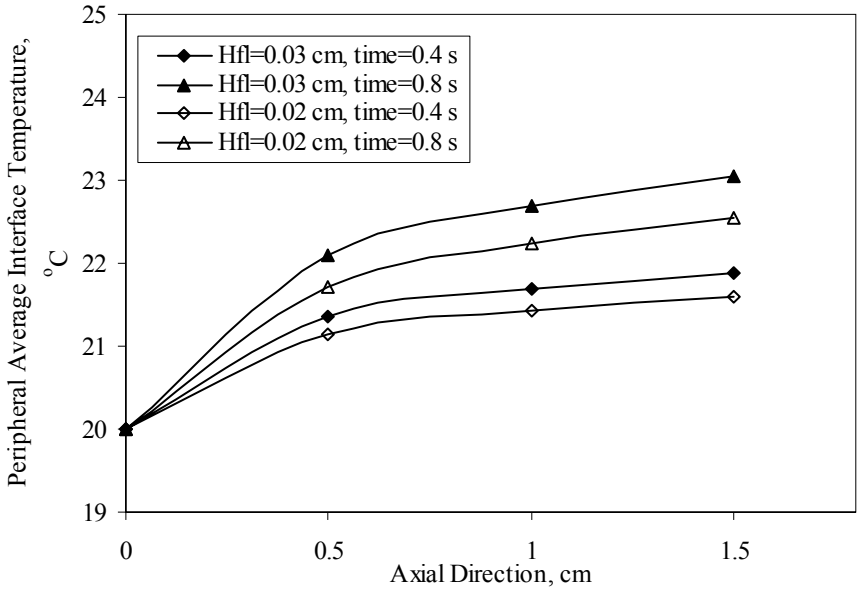

Figure 4.24: The effect of channel depth on the peripheral average interface temperature along the axial direction at different time periods at the fluid-gadolinium interface (Re = 2000, G = 5 T)

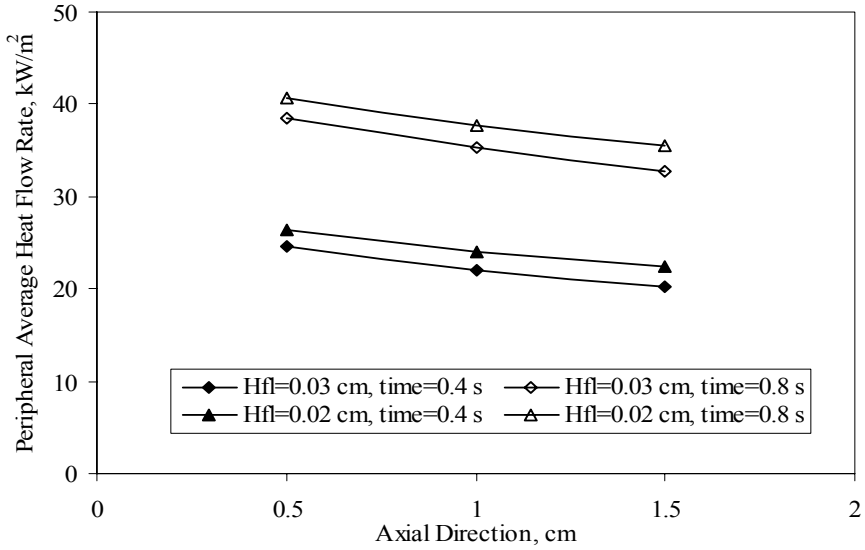

Figure 4.25: The effect of channel depth on the peripheral average heat flow rate along the axial direction at different time periods at the fluid-gadolinium interface (Re = 2000, G = 5 T)

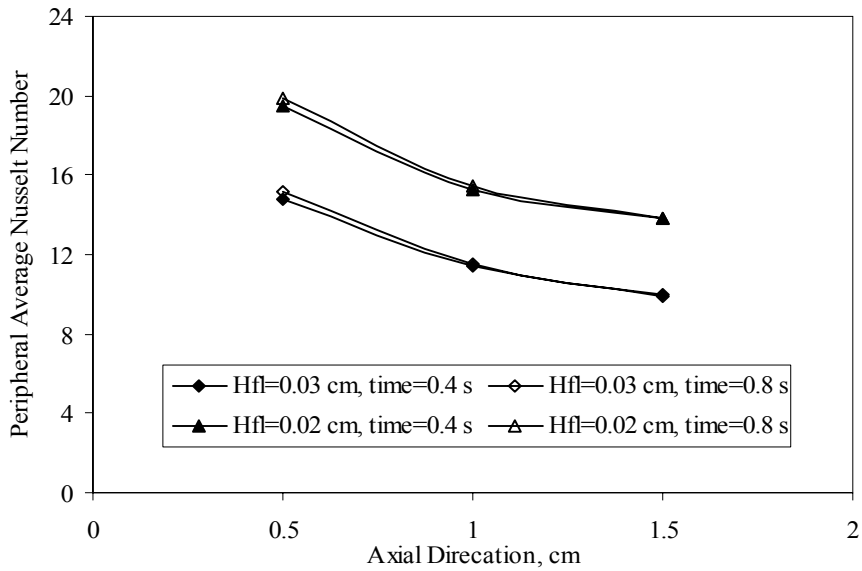

Figure 4.26: The effect of channel depth on the peripheral average Nusselt number along the axial direction at different time periods at the fluid-gadolinium interface (Re = 2000, G = 5 T)

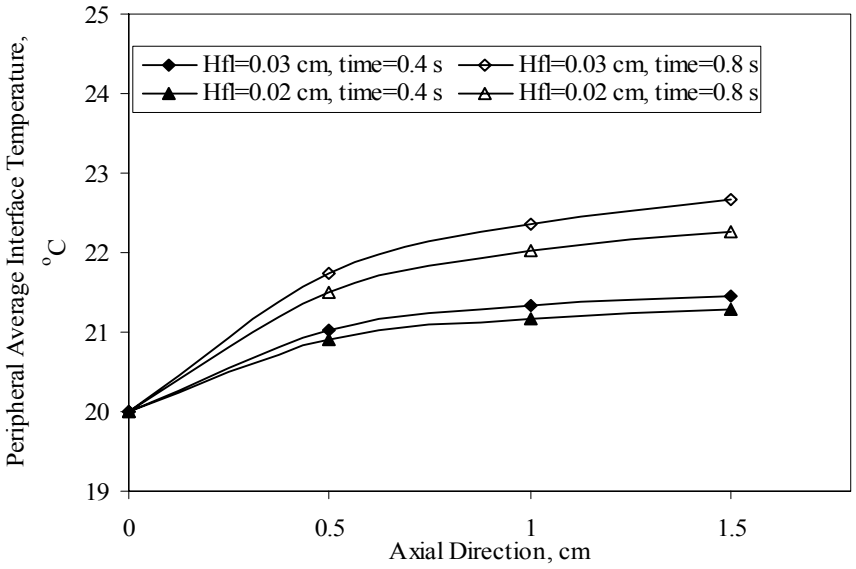

Figure 4.27: The effect of channel depth on the peripheral average interface temperature along the axial direction at different time periods at the fluid-silicon interface (Re = 2000, G = 5 T)

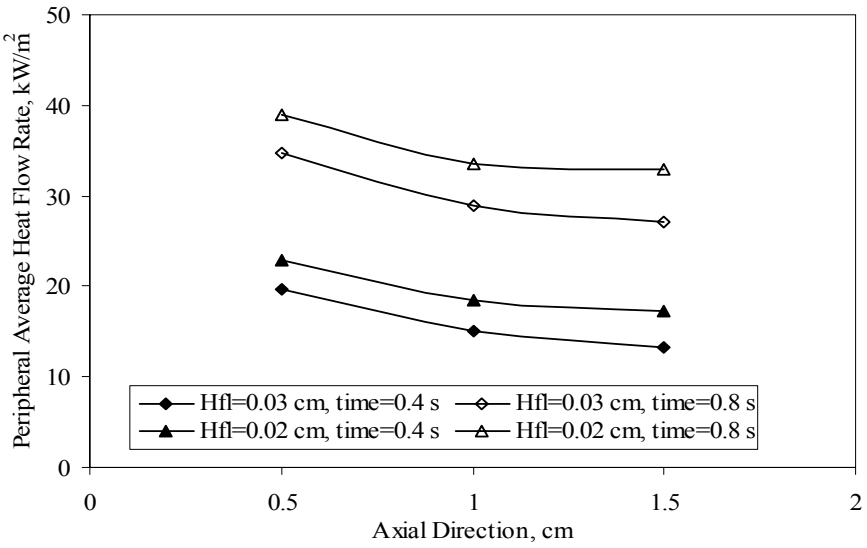

Figure 4.28: The effect of channel depth on the peripheral average heat flow rate along the axial direction at different time periods at the fluid-silicon interface (Re = 2000, G = 5 T)

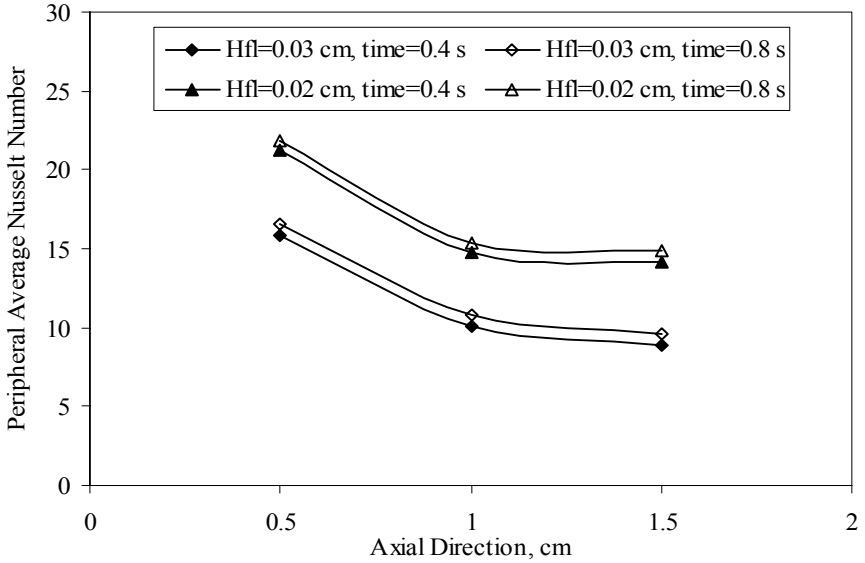

Figure 4.29: The effect of channel depth on the peripheral average Nusselt number along the axial direction at different time periods at the fluid-silicon interface (Re = 2000, G = 5 T)

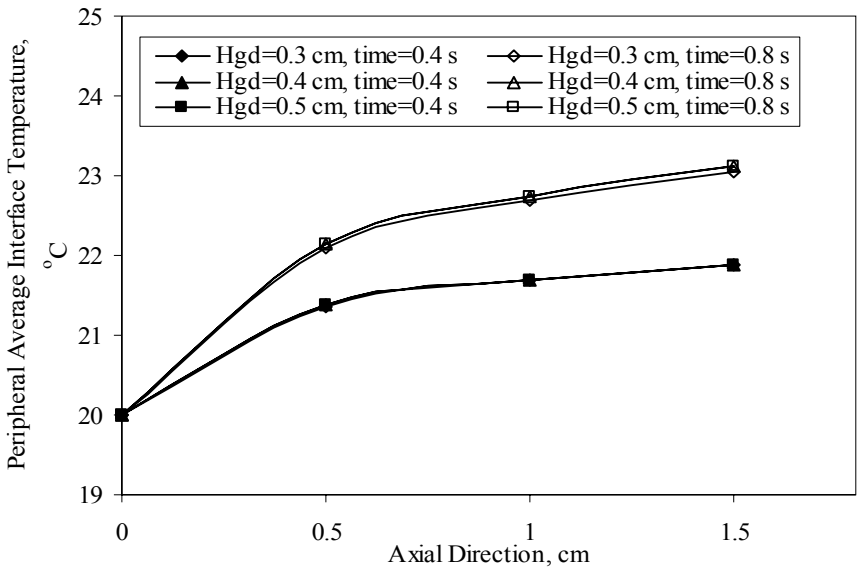

Figure 4.30: The effect of height of gadolinium substrate on the peripheral average interface temperature along the axial direction at different time periods at the fluid-gadolinium interface (Re = 2000, G = 5 T, H_{fl} = 0.03 cm)

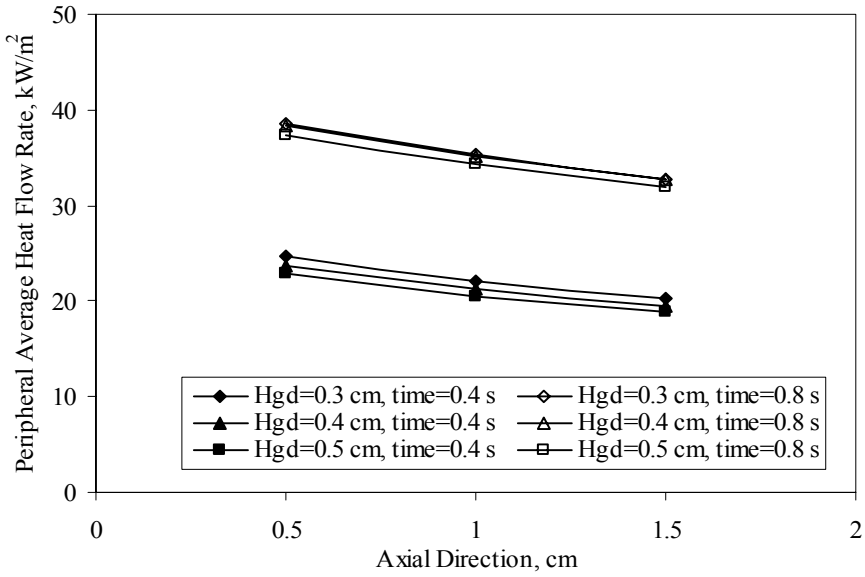

Figure 4.31: The effect of height of gadolinium substrate on the peripheral average heat flow rate along the axial direction at different time periods at the fluid-gadolinium interface (Re = 2000, G = 5 T, H_{fl} = 0.03 cm)

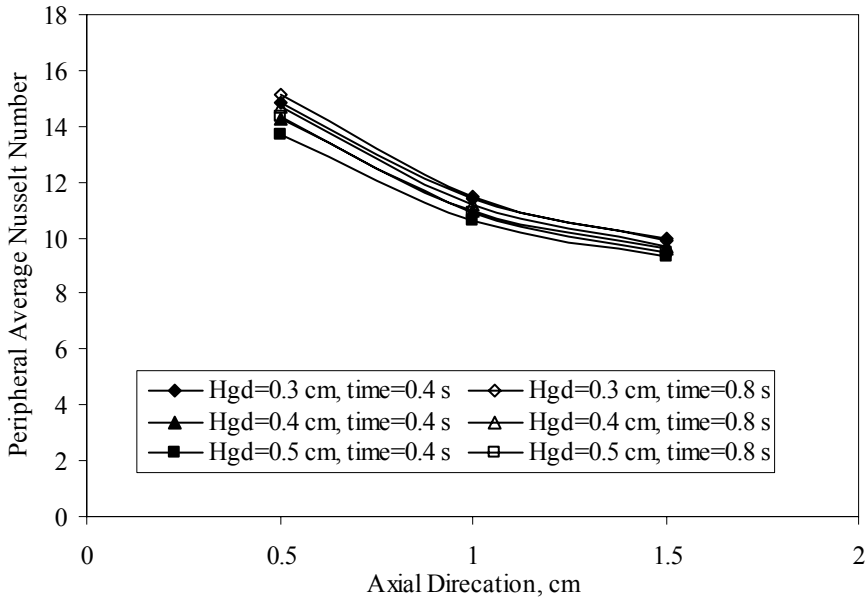

Figure 4.32: The effect of height of gadolinium substrate on the peripheral average Nusselt number along the axial direction at different time periods at the fluid-gadolinium interface (Re = 2000, G = 5 T, H_{fl} = 0.03 cm)

increase in the average interface temperature which indicates a small decrease in the solid temperature gradient. This means that the gadolinium height has a very low effect on the system. The heat flow rate, on the other hand, decreased with higher gadolinium height. This is a direct result for the decrease in the solid temperature gradient. The decrease in the heat flow directly decreases the heat transfer coefficient and thus the Nusselt number.

Figures 4.33, 4.34 and 4.35 show the results of interface temperature, heat flow rate and Nusselt number for different height of gadolinium substrate along the axial direction at the silicon-fluid interface. Higher gadolinium height results in higher heat generation. Similarly to the gadolinium side, this increases the average interface temperature was barely noticeable. The temperature gradient decreased in the gadolinium

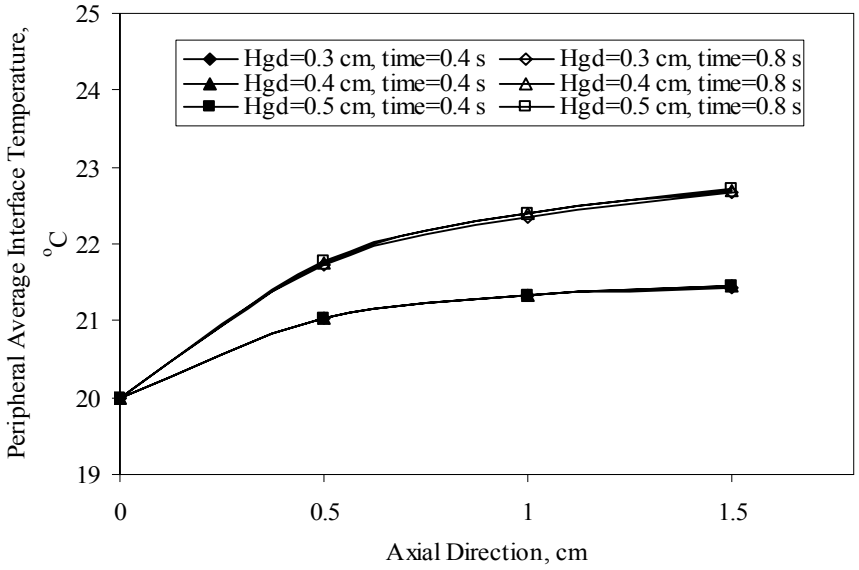

Figure 4.33: The effect of height of gadolinium substrate on the peripheral average interface temperature along the axial direction at different time periods at the fluid-silicon interface (Re = 2000, G = 5 T, H_{fl} = 0.03 cm)

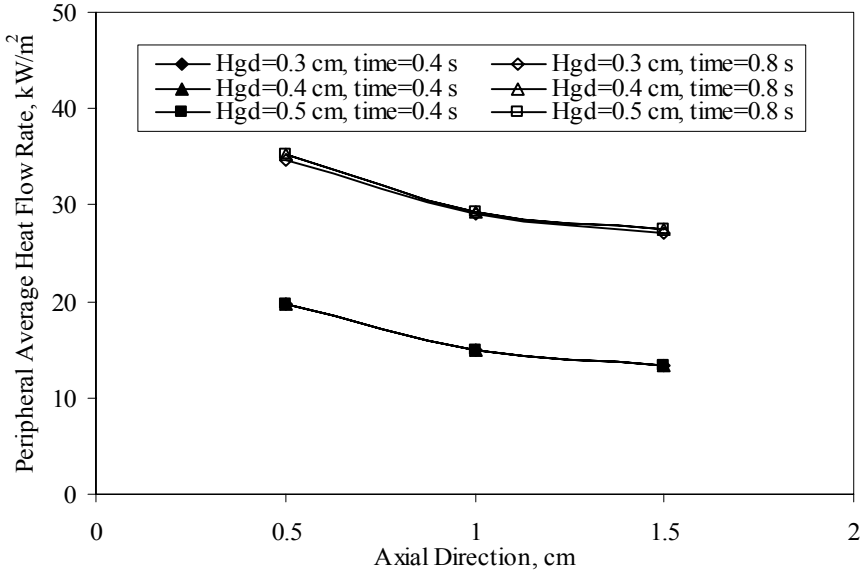

Figure 4.34: The effect of height of gadolinium substrate on the peripheral average heat flow rate along the axial direction at different time periods at the fluid-silicon interface (Re = 2000, G = 5 T, H_{fl} = 0.03 cm)

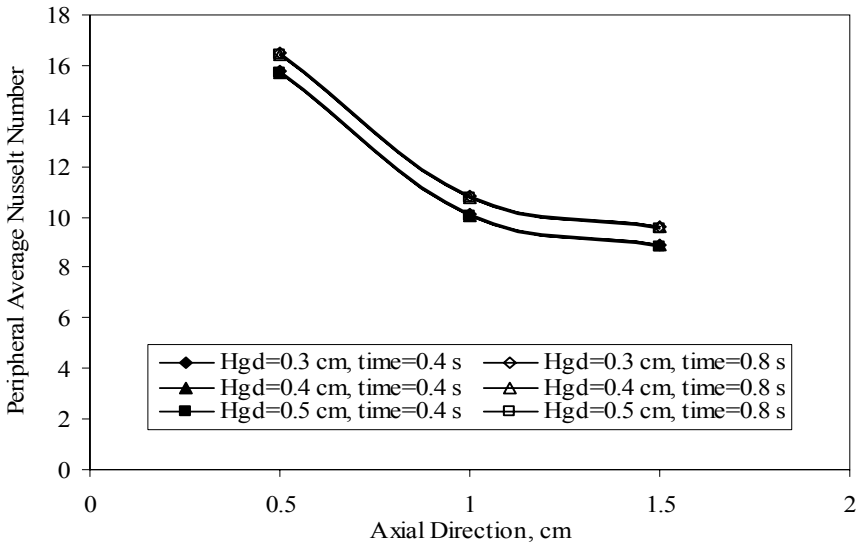

Figure 4.35: The effect of height of gadolinium substrate on the peripheral average Nusselt number along the axial direction at different time periods at the fluid-silicon interface (Re = 2000, G = 5 T, H_{fl} = 0.03 cm)

substrate due to larger solid volume. Unlike the gadolinium side, the temperature gradient in the silicon substrate decreased at earlier times (t = 0.4 s) but increased at later times (t = 0.8 s). This is because of the constant heat conduction from the gadolinium to the silicon substrate which increased the temperature gradient at later times. Both the heat transfer coefficient and Nusselt number are decreasing with larger gadolinium height. This is due to increase in the interface-bulk temperature difference as the interface temperature increases.

Figures 4.36, 4.37 and 4.38 show the results of interface temperature, heat flow rate and Nusselt number for different channel spacing along the axial direction at the gadolinium-fluid interface. Larger spacing for the same model width results in smaller channel. This increases the fluid velocity for the same Reynolds number. Higher fluid

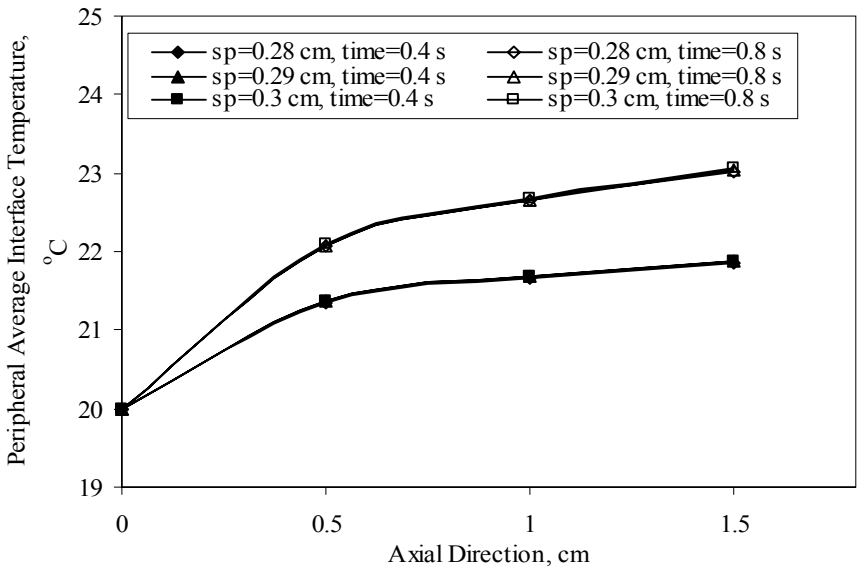

Figure 4.36: The effect of channel spacing on the peripheral average interface temperature along the axial direction at different time periods at the fluid-gadolinium interface (Re = 2000, G = 5 T, H_{fl} = 0.03 cm)

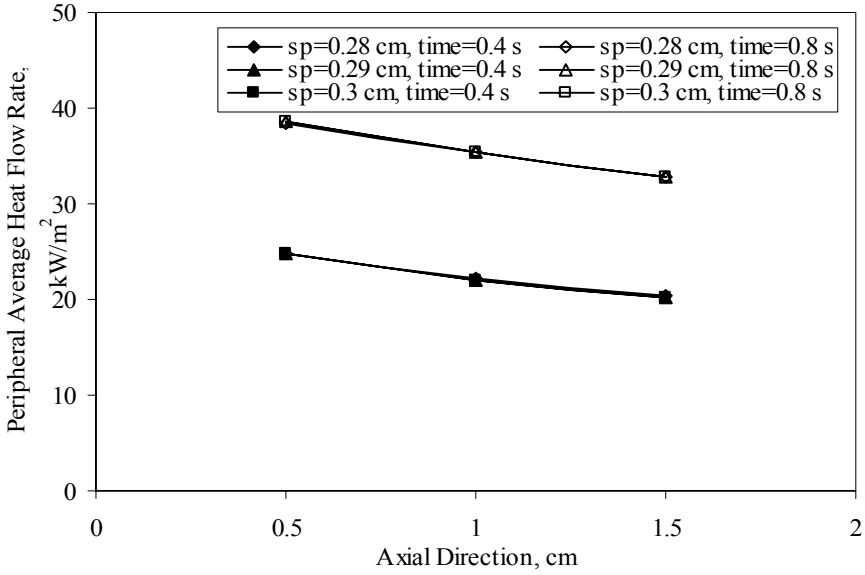

Figure 4.37: The effect of channel spacing on the peripheral average heat flow rate along the axial direction at different time periods at the fluid-gadolinium interface (Re = 2000, G = 5 T, H_{fl} = 0.03 cm)

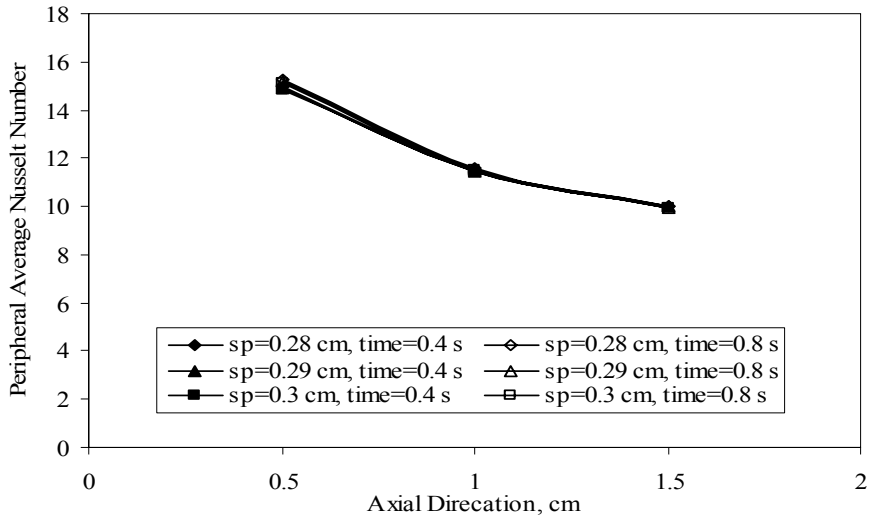

Figure 4.38: The effect of channel spacing on the peripheral average Nusselt number along the axial direction at different time periods at the fluid-gadolinium interface (Re = 2000, G = 5 T, H_{fl} = 0.03 cm)

velocity increases the cooling process and usually results in lower interface temperature and higher heat flow rate. In this case, the solid volume also increases as the channel spacing increase. This provides more heat generation in the solid substrate and increases the interface temperature. Both effects cancel each other and result in negligible change in the interface temperature and heat flow rate. The heat transfer coefficient and Nusselt number depend directly on the heat flow rate. The change in the heat transfer coefficient and the Nusselt number are also negligible.

Figures 4.39, 4.40 and 4.41 show the results of interface temperature, heat flow rate and Nusselt number for different channel spacing along the axial direction at the silicon-fluid interface. Larger spacing for the same model width results in smaller channel. This increases the fluid velocity for the same Reynolds number. Higher fluid

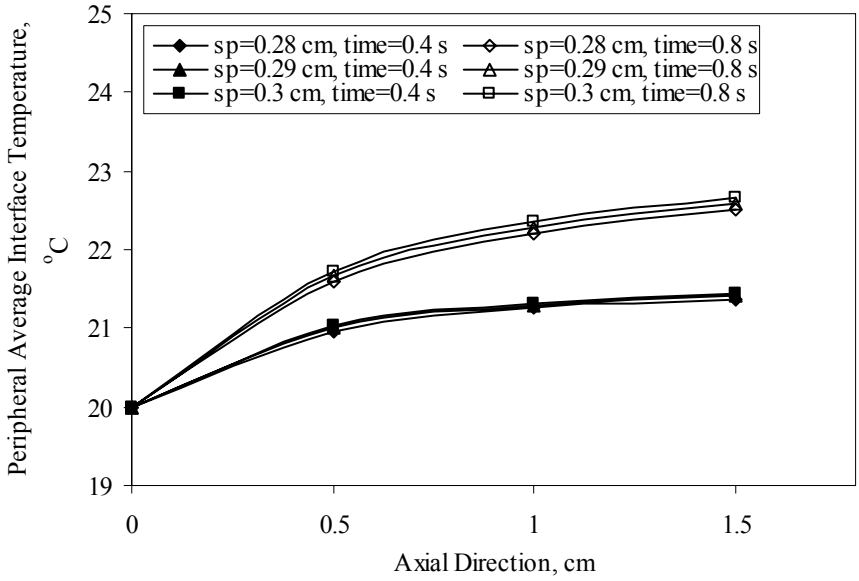

Figure 4.39: The effect of channel spacing on the peripheral average interface temperature along the axial direction at different time periods at the fluid-silicon interface (Re = 2000, G = 5 T, H_{fl} = 0.03 cm)

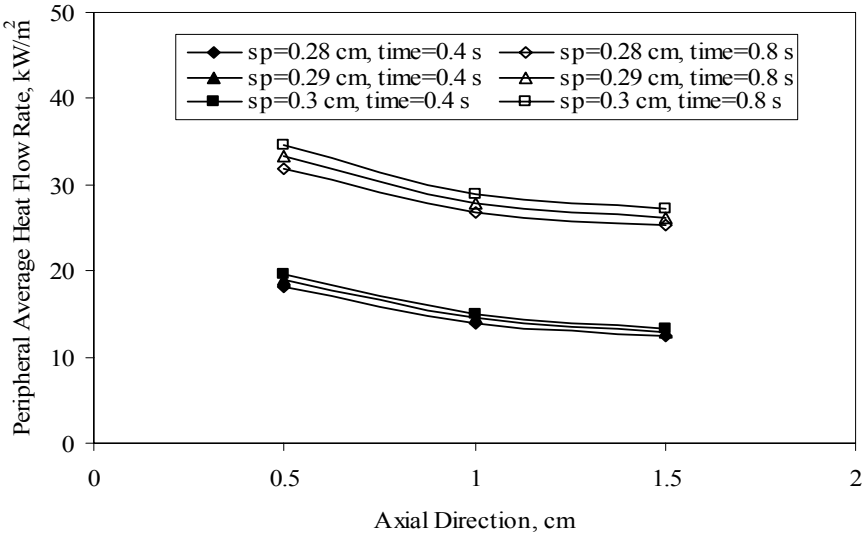

Figure 4.40: The effect of channel spacing on the peripheral average heat flow rate along the axial direction at different time periods at the fluid-silicon interface (Re = 2000, G = 5 T, H_{fl} = 0.03 cm)

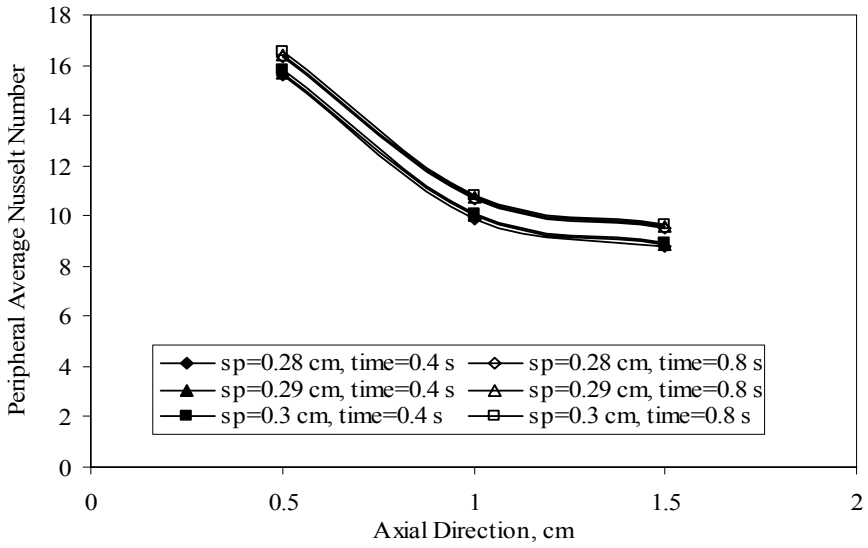

Figure 4.41: The effect of channel spacing on the peripheral average Nusselt number along the axial direction at different time periods at the fluid-silicon interface (Re = 2000, G = 5 T, H_{fl} = 0.03 cm)

velocity increases the cooling process and usually results in lower interface temperature and higher heat flow rate. The solid volume also increases as the channel spacing increase. This provides more heat generation in the solid substrate and increases the interface temperature. The heat generation in the gadolinium substrate increases and is conducted to the silicon substrate. Silicon has high thermal conductivity and this transfers some of the added heat generation in the gadolinium. This additional heat generation conducted to the silicon substrate overcomes the effect of the increase in the fluid velocity and the net result can be observed in higher interface temperature. The additional heat generation conducted to the silicon substrate also enhances the heat flow rate to the fluid at the interface. This increase in the heat flow rate increases the heat transfer coefficient and Nusselt number.

Figures 4.42, 4.43 and 4.44 show the results of interface temperature, heat flow rate and Nusselt number for different working fluids along the axial direction at the gadolinium-fluid interface. Water has the lowest rate of increase in the interface temperature along the axial direction but the highest heat flow rate and Nusselt number. This is because water has the highest conductivity among the fluids tested in this research. The high fluid thermal conductivity reduces the fluid resistance in heat transfer and enhances the heat transfer to the fluid resulting in lower interface temperature. On the other hand, R134a has the lowest fluid thermal conductivity. This cause higher resistance to the heat flow to the fluid resulting in a decrease in the heat flow rate but an increase in the interface temperature. Nusselt number directly depends on the heat flow rate and, therefore, has similar behavior.

Figures 4.45, 4.46 and 4.47 show the results of interface temperature, heat flow rate and Nusselt number for different working fluids along the axial direction at the silicon-fluid interface. Similarly to the gadolinium side, water has lowest interface temperature but the highest heat flow rate and Nusselt number. R134a have highest interface temperature but the lowest heat flow rate and Nusselt number.

4.4 Conclusions

Study of the parameters in transient case of the trapezoidal composite microchannel model with heat generation in gadolinium was done. Mathematical model was developed and computations were done to solve the system. The study showed that the model reaches steady state after approximately 4 seconds. It also showed that gadolinium and silicon sides have similar results and values for interface temperature and

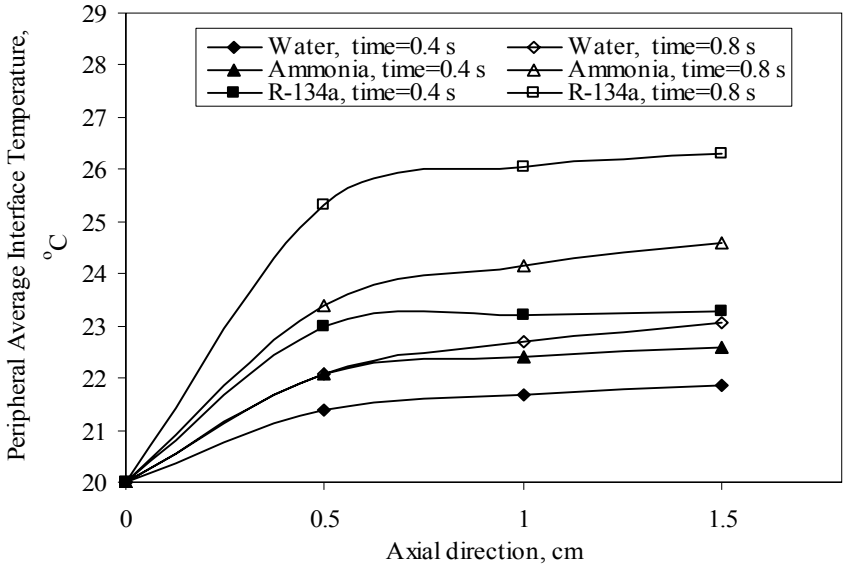

Figure 4.42: The effect of changing the fluid on the peripheral average interface temperature along the axial direction at different time periods at the fluid-gadolinium interface (Re = 2000, G = 5 T, H_{fl} = 0.03 cm)

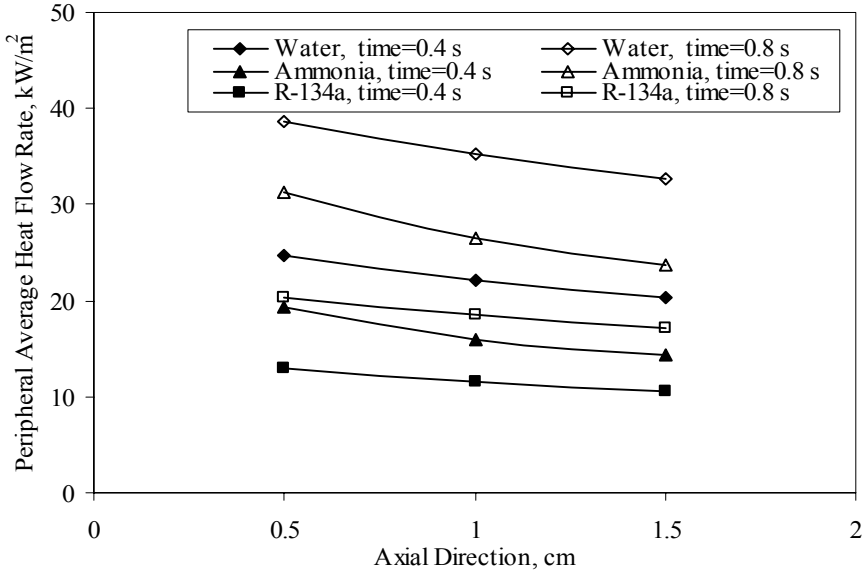

Figure 4.43: The effect of changing the fluid on the peripheral average heat flow rate along the axial direction at different time periods at the fluid-gadolinium interface (Re = 2000, G = 5 T, H_{fl} = 0.03 cm)

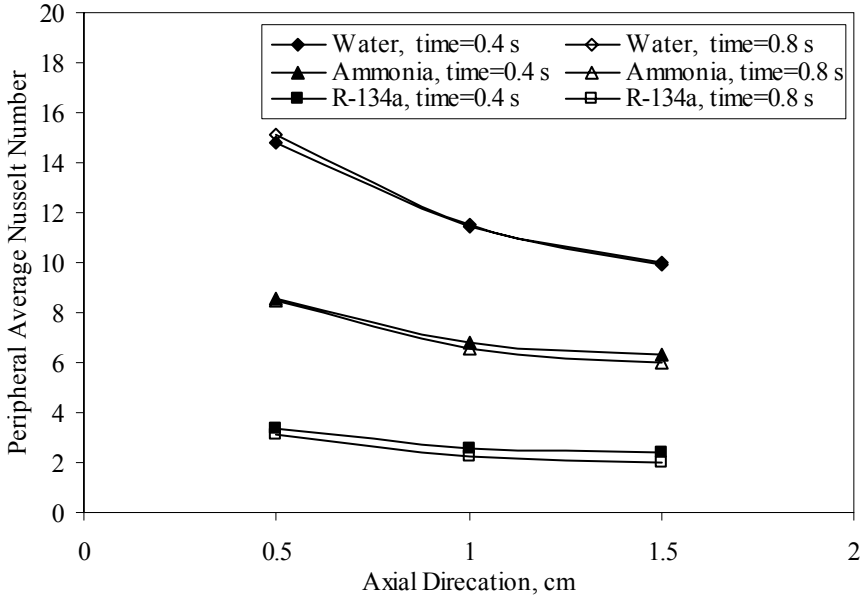

Figure 4.44: The effect of changing the fluid on the peripheral average Nusselt number along the axial direction at different time periods at the fluid-gadolinium interface (Re = 2000, G = 5 T, H_{fl} = 0.03 cm)

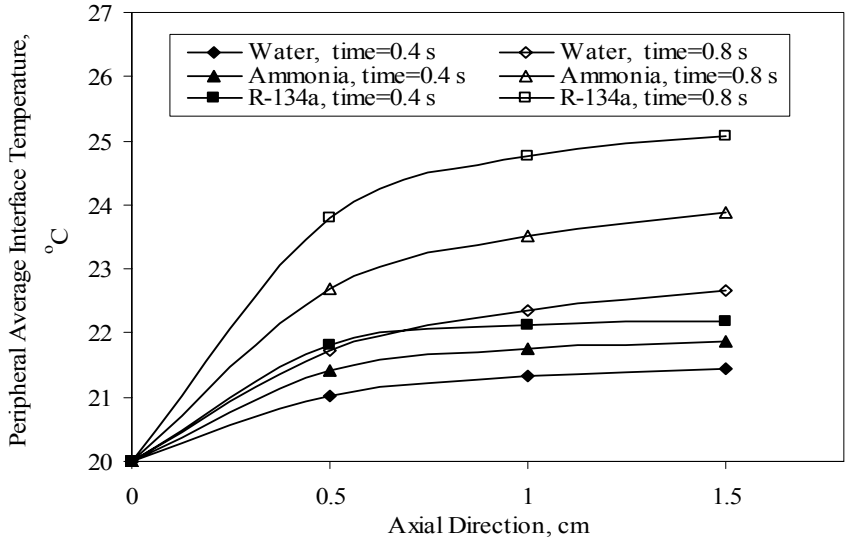

Figure 4.45: The effect of changing the fluid on the peripheral average interface temperature along the axial direction at different time periods at the fluid-silicon interface (Re = 2000, G = 5 T, H_{fl} = 0.03 cm)

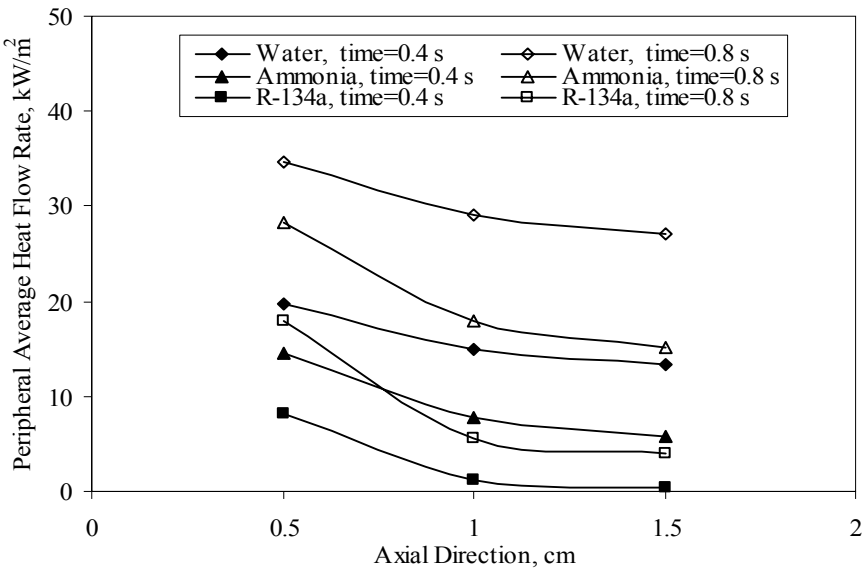

Figure 4.46: The effect of changing the fluid on the peripheral average heat flow rate along the axial direction at different time periods at the fluid-silicon interface (Re = 2000, G = 5 T, H_{fl} = 0.03 cm)

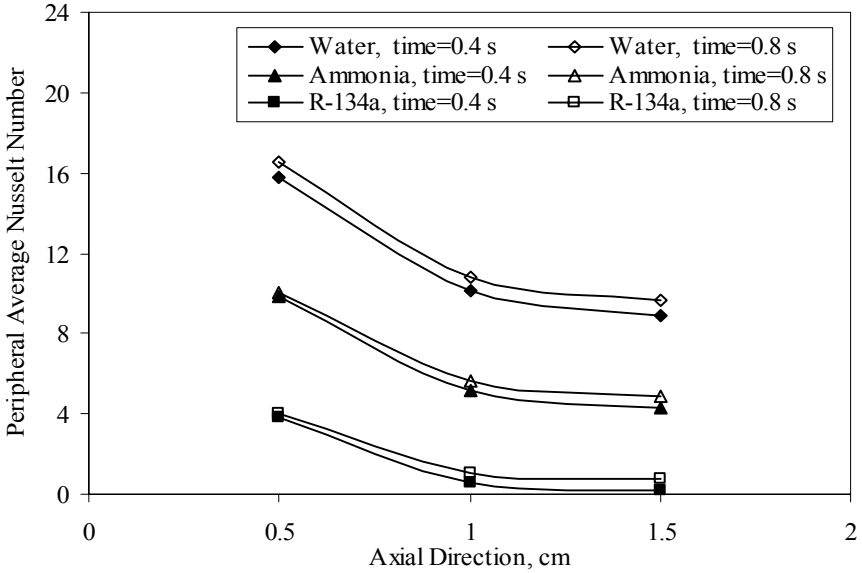

Figure 4.47: The effect of changing the fluid on the peripheral average Nusselt number along the axial direction at different time periods at the fluid-silicon interface (Re = 2000, G = 5 T, H_{fl} = 0.03 cm)

heat flow rate. This is because the silicon has higher conductivity that makes up for the heat generation in the gadolinium side. The increase in Reynolds number increases the heat flow rate and Nusselt number. The increase in the magnetic field increases the heat flow rate and interface temperature. The increase in both cancels each other and results in no change in the Nusselt number. Lowering the channel height for the same Reynolds number increases the heat flow rate and Nusselt number. The change in gadolinium height and channel spacing had the least effect on both the heat flow rate and Nusselt number. Using water results in lower interface temperature but higher heat flow rate while R-134a results in higher interface temperature but lower heat flow rate. The magnetic field and the working fluid had the highest effect on the interface temperature and heat flow rate. Nusselt number was affected the most by the channel height (H_{fl}) and the change in the working fluid.

Chapter 5 – Transient Heat Transfer in Trapezoidal Microchannels Under Time Varying Heat Source

5.1 Mathematical Model

The model in hand is the same as the one described in the previous chapter. It is a trapezoidal cross-sectional microchannel manufactured into a silicon substrate with gadolinium substrate attached on the top. Heat is generated in the Gadolinium substrate and convected to the water while part of it is conducted to the Silicon and then convected to water. In this chapter a time varying heat source is studied rather than a constant one. The magnetic material substrate is subjected to a magnetic field resulting in a heat source and sink periodically. All boundary conditions at all sides are considered adiabatic. Symmetrical condition along only one axis is considered. Figure 5.1 shows the schematic draw of the model. Boundary conditions at the bottom, left and top are adiabatic while it is symmetrical at the right side.

The differential equations for the conservation of mass, momentum and heat in the Cartesian coordinate system for transient case for the fluid are given as [45],

$$\frac{\partial u}{\partial x}+\frac{\partial v}{\partial y}+\frac{\partial w}{\partial z}=0 \tag{1}$$

$$\frac{\partial u}{\partial t}+u\frac{\partial u}{\partial x}+v\frac{\partial u}{\partial y}+w\frac{\partial u}{\partial z}=-\frac{1}{\rho}\frac{\partial p}{\partial x}+\nu\left(\frac{\partial^2 u}{\partial x^2}+\frac{\partial^2 u}{\partial y^2}+\frac{\partial^2 u}{\partial z^2}\right) \tag{2}$$

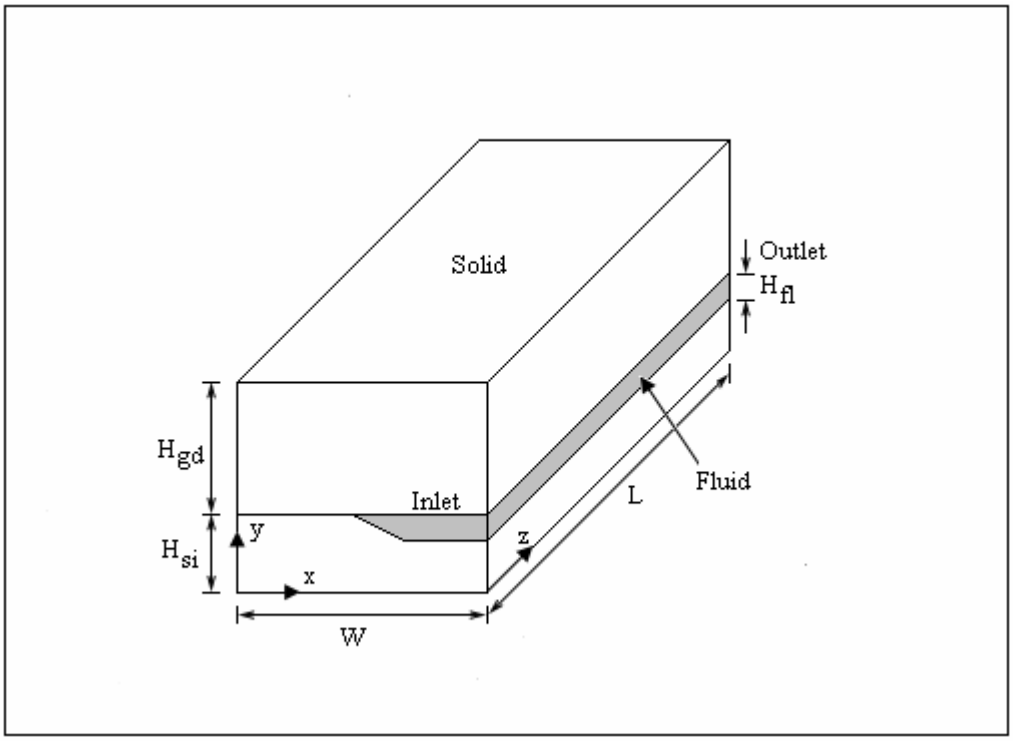

Figure 5.1: Schematic for microchannel heat exchanger model

$$\frac{\partial v}{\partial t}+u\frac{\partial v}{\partial x}+v\frac{\partial v}{\partial y}+w\frac{\partial v}{\partial z}=-\frac{1}{\rho}\frac{\partial p}{\partial x}+\nu\left(\frac{\partial^2 v}{\partial x^2}+\frac{\partial^2 v}{\partial y^2}+\frac{\partial^2 v}{\partial z^2}\right) \tag{3}$$

$$\frac{\partial w}{\partial t}+u\frac{\partial w}{\partial x}+v\frac{\partial w}{\partial y}+w\frac{\partial w}{\partial z}=-\frac{1}{\rho}\frac{\partial p}{\partial x}+\nu\left(\frac{\partial^2 w}{\partial x^2}+\frac{\partial^2 w}{\partial y^2}+\frac{\partial^2 w}{\partial z^2}\right) \tag{4}$$

$$\frac{\partial T_f}{\partial t}+u\frac{\partial T_f}{\partial x}+v\frac{\partial T_f}{\partial y}+w\frac{\partial T_f}{\partial z}=\alpha\left(\frac{\partial^2 T_f}{\partial x^2}+\frac{\partial^2 T_f}{\partial y^2}+\frac{\partial^2 T_f}{\partial z^2}\right) \tag{5}$$

The energy conservation equation in the solid Gadolinium substrate is [46]:

$$\frac{\partial^2 T_{gd}}{\partial x^2}+\frac{\partial^2 T_{gd}}{\partial y^2}+\frac{\partial^2 T_{gd}}{\partial z^2}+\frac{g_0}{k_{gd}}=\frac{1}{\alpha}\frac{\partial T_{gd}}{\partial t} \tag{6}$$

And for the solid Silicon substrate is [46]:

$$\frac{\partial^2 T_{si}}{\partial x^2} + \frac{\partial^2 T_{si}}{\partial y^2} + \frac{\partial^2 T_{si}}{\partial z^2} = \frac{1}{\alpha}\frac{\partial T_{si}}{\partial t} \tag{7}$$

Equations (1) – (7) are subject to following initial and boundary conditions:

At t = 0: $T_f = T_{gd} = T_{si} = T_{in}$ (8)

At z = 0, at fluid inlet: $u=0,\ v=0,\ w=w_{in},\ T=T_{in}$ (9)

At z = 0, on solid surface: $\frac{\partial T_{si}}{\partial z} = 0,\ \frac{\partial T_{gd}}{\partial z} = 0$ (10)

At z = L, at fluid outlet: $p=0$ (11)

At z = L, on solid surface: $\frac{\partial T_{si}}{\partial z} = 0,\ \frac{\partial T_{gd}}{\partial z} = 0$ (12)

At x = 0, $0 < y < (H_{si}-H_{fl})$, $0 < z < L$: $\frac{\partial T_{si}}{\partial z} = 0$ (13)

At x = 0, $(H_{si}-H_{fl}) < y < H_{si}$, $0 < z < L$: $u=0,\ \frac{\partial v}{\partial x} = 0,\ \frac{\partial w}{\partial x} = 0,\ \frac{\partial T_f}{\partial x} = 0$ (14)

At x = 0, $H_{si} < y < (H_{si}+H_{gd})$, $0 < z < L$: $\frac{\partial T_{gd}}{\partial x} = 0$ (15)

At x = B, $0 < y < H_{si}$, $0 < z < L$: $\frac{\partial T_{si}}{\partial x} = 0$ (16)

At x = B, $H_{ii} < y < (H_{si}+H_{gd})$, $0 < z < L$: $\frac{\partial T_{gd}}{\partial x} = 0$ (16)

At y = 0, $0 < x < B$, $0 < z < L$: $\frac{\partial T_{si}}{\partial y} = 0$ (17)

At y = $(H_{si}-H_{fl})$, $B-B_s < x < B$, $0 < z < L$: $u=0,\ v=0,\ w=0,\ T_f = T_{si}$, and

$$k_f \frac{\partial T_f}{\partial y} = k_{si} \frac{\partial T_{si}}{\partial y} \tag{18}$$

At y = H_{si}, $0 < x < B-B_c$, $0 < z < L$: $u=0,\ v=0,\ w=0,\ T_f = T_{gd}$, and

$$k_f \frac{\partial T_f}{\partial y} = k_{gd} \frac{\partial T_{gd}}{\partial y} \quad (19)$$

At $y = H_{si}$, $B-B_c < x < B$, $0 < z < L$: $$k_{si} \frac{\partial T_{si}}{\partial y} = k_{gd} \frac{\partial T_{gd}}{\partial y} \quad (20)$$

At $y = (H_{si}+H_{gd})$, $0 < x < B$, $0 < z < L$: $$\frac{\partial T_{gd}}{\partial y} = 0 \quad (21)$$

At the inclined channel surface between fluid and silicon, $0<z<L$,

$u=0$, $v=0$, $w=0$, $T_f = T_{si}$, and

$$k_f \frac{\partial T_f}{\partial n} = k_{si} \frac{\partial T_{si}}{\partial n} \quad (22)$$

5.2 Numerical Simulation and Parametric Study

The governing equations along with the boundary conditions were solved using the Galerkin finite element method. The Newton-Raphson algorithm was used to solve the nonlinear system of discretized equations. An iterative procedure was used to arrive at the solution for the velocity and temperature fields. The solution was considered converged when the field values did not change from one iteration to the next, and the residuals for each variable became negligible.

For the numerical computations, the Length (L) and the half width (W) of the model were set to a constant value, 2.3 cm and 0.3 cm respectively. The heights of the gadolinium (H_{gd}) and silicon substrate (H_{si}) and the inlet temperature were also set to a constant value, 0.3 cm, 0.1 cm and 20 ^oC respectively. To represent the heat generation and cooling process numerically, the magnetic field value was fluctuated between the values of +5 and -5 T, figure 5.2. Time period of 2 seconds was used. The first period

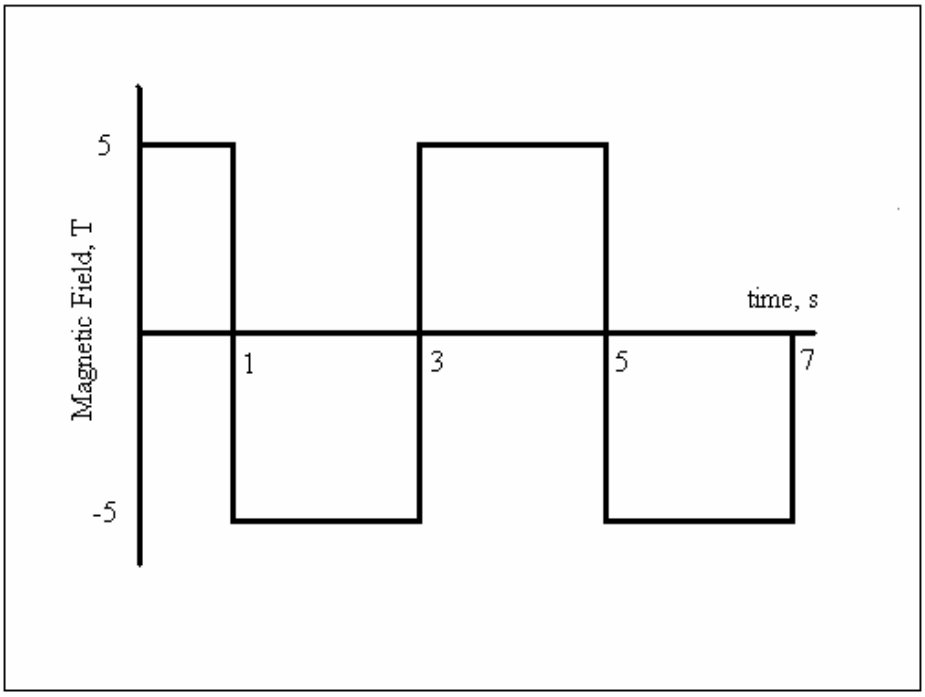

Figure 5.2: Local variation of magnetic field with time

was chosen to be one half of the selected time length since it started from the initial condition. The parameters to be changed were selected to be: magnetic field, height of fluid microchannel, and Reynolds number. Initially these parameters were selected as follows: Re = 2000, G = 5 Tesla, H_{fl} = 0.03 cm, and water as the working fluid. One parameter was changed at a time while all other parameters kept constant to study the effect of each parameter separately. Magnetic field that was changed to the values of +10 and -10 T, H_{fl} was changed to 0.02 cm, and Reynolds number was changed to 1000.

5.3 Results and Discussion

The local interface temperature, heat flow rate, heat transfer coefficient and Nusselt number were calculated from the resulted velocity and temperature distribution.

The heat generation occurred in the 1st, 3rd, and 5th periods while the cooling process occurred in the 2nd and 4th periods.

Figure 5.3 and 5.4 show local Nusselt number along different channel edges. Curves for different axial locations were plotted. Figure 5.3 shows the local Nusselt along the fluid-gadolinium interface at different axial locations at the end of the first time period. It shows that Nusselt number is higher closer to the center of the trapezoidal microchannel. This is because the fluid volume is lesser at the edges of the trapezoidal microchannel which results in lesser resistance in heat transfer. This lesser resistance gives smaller temperature gradient in the solid region resulting in smaller heat flow rate. The heat flow rate increases along the edge towards the center of the channel. This causes the heat transfer coefficient, and thus Nusselt number, to increase. Along the axial direction, the temperature gradient decreases causing the heat flow rate to decrease. The interface-bulk temperature difference increases along the axial direction. Both cause the Nusselt number to decrease along the axial direction.

Figure 5.4 shows the local Nusselt along the fluid-silicon interface at different axial locations at the end of the first time period. The silicon edge is tapered at closer to the side ends of the channel. At the tapered edge, there is small fluid volume where the heat flow rate almost transfers without any resistance. As a result, the temperature gradient is smaller and causes smaller heat flow rate values, and thus, smaller Nusselt number. The heat flows from the gadolinium to the silicon by conduction and then to the fluid by convection. At the very far tip of the tapered edge, the heat flow finds away to travel through the fluid and to the silicon overcoming the small fluid resistance. Further away from the tip of the tapered edge, the heat flow from the silicon takes control giving

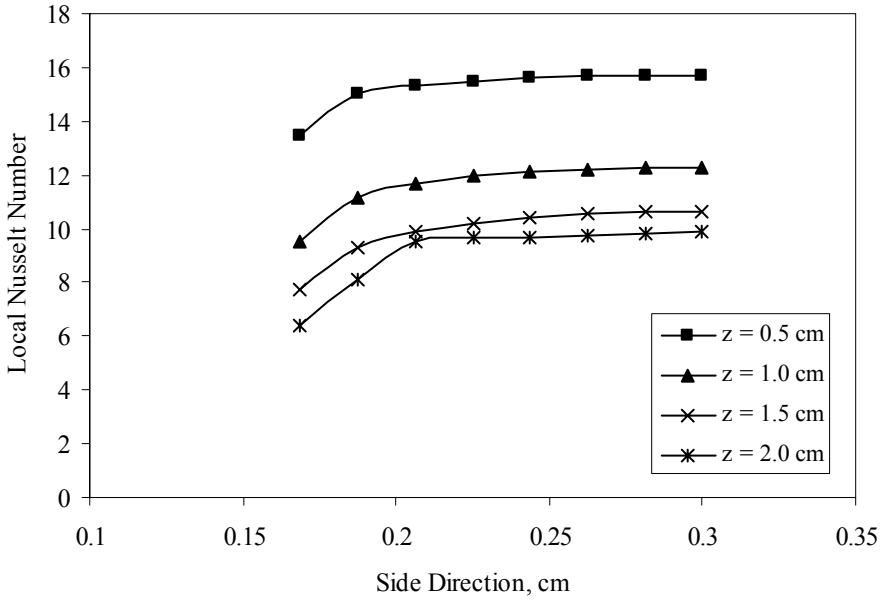

Figure 5.3: Local Nusselt along the fluid-gadolinium interface at different axial locations after 1 second (Re = 2000, G = 5 T, H_{fl} = 0.03 cm)

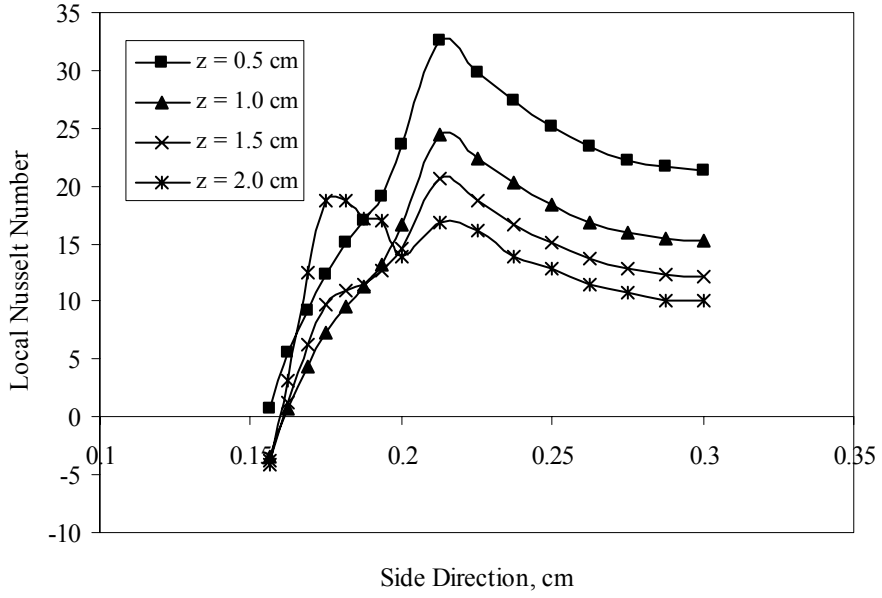

Figure 5.4: Local Nusselt along the fluid-silicon interface at different axial locations after 1 second (Re = 2000, G = 5 T, H_{fl} = 0.03 cm)

positive results. The heat flow rate increases quickly along the tapered edge reaching reasonable values resulting in adequate Nusselt number values. Along the horizontal edge, the temperature gradient and the heat flow rate decrease. This is because part of the heat flow rate that travel through the silicon transfers by convection to the fluid before it reaches the center of the channel. This eventually causes Nusselt number to decrease along the horizontal side of the silicon edge. Similarly to the gadolinium edge, the temperature gradient decreases along the axial direction. This causes the heat flow rate to decrease along the axial direction. The interface-bulk temperature difference increases along the axial direction. Both cause the Nusselt number to decrease along the axial direction.

Figure 5.5 shows the Peripheral average interface temperature over 9 seconds at different axial locations at the fluid-gadolinium interface. Sinusoidal behavior is observed for the interface temperature as the heat generation and cooling process alternates. As heat is generated the interface temperature increases while it decreases when cooling process takes over. The interface temperature rate of change along the axial direction is slow at the beginning of the transient process because of the initial condition effect. The interface temperature rate of change also increases along the axial direction because of the inlet condition effect. Figure 5.6 shows the average heat flow rate over 9 seconds at different axial locations at the fluid-gadolinium interface. It shows that the heat flow rate is supplied to and rejected from the fluid as the heat generation and cooling process alternates in the system. The rate of change in the heat flow rate increases with each new period of heating or cooling process. This is because of the initial condition where the temperature distribution provides the highest interface-solid temperature difference and

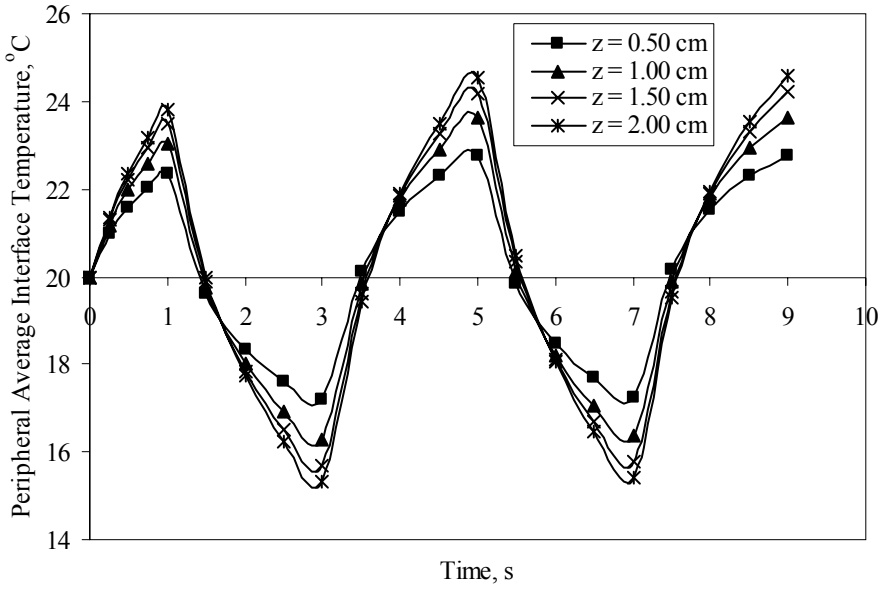

Figure 5.5: Peripheral average interface temperature over 9 seconds at different axial locations at the fluid-gadolinium interface (Re = 2000, G = 5 T, H_{fl} = 0.03 cm)

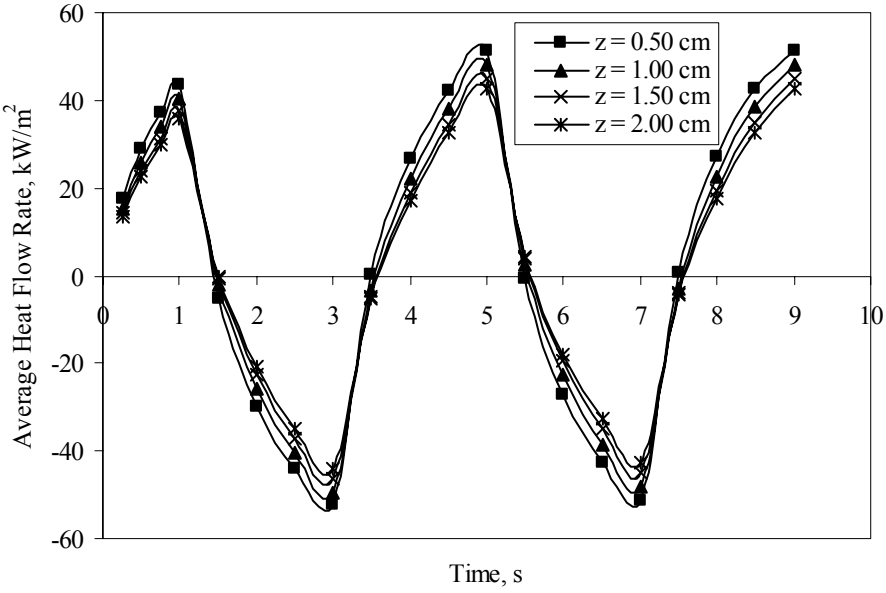

Figure 5.6: Peripheral average heat flow rate over 9 seconds at different axial locations at the fluid-gadolinium interface (Re = 2000, G = 5 T, H_{fl} = 0.03 cm)

thus higher heat flow rate. The initial condition effect diminishes over time. The heat flow rate is higher closer to the inlet because of the constant temperature inlet condition.

Figure 5.7 shows the Peripheral average interface temperature over 9 seconds at different axial locations at the fluid-silicon interface. Sinusoidal behavior is also observed for the interface temperature as the gadolinium interface. Heat is generated in the gadolinium substrate then convected to the fluid directly and conducted to the silicon substrate. Even though this process slows down the heat transfer in the silicon substrate the silicon side has a bit smaller interface temperature than the gadolinium because its high thermal conductivity. Figure 5.8 shows the average heat flow rate over 9 seconds at different axial locations at the fluid-silicon interface. Similar to the gadolinium side, the heat flow rate is supplied to and rejected from the fluid over time. The silicon side shows a less heat flow rate at its interface than the gadolinium. This is because the heat generation occurs in the gadolinium substrate.

Figure 5.9 shows the average Nusselt number over 9 seconds at different axial locations at the total interface including both sides of the channel, gadolinium and silicon. The Nusselt number behavior is shown to be increasing for each time period regardless of the process. At the beginning of each period, the interface and bulk temperature switch because the cooling and heating processes alternate. At certain point of the switching process Nusselt number will be infinite, that is when the interface and bulk temperature are equal. That is why at each time period (3.5 s, 5.5 s and 7.5 s) Nusselt number increase to a high value then decreases to reasonable values where it starts to increase again. Nusselt number is always positive and increasing for both heating and cooling processes because only the absolute value of the heat flow rate is considered. The switch between

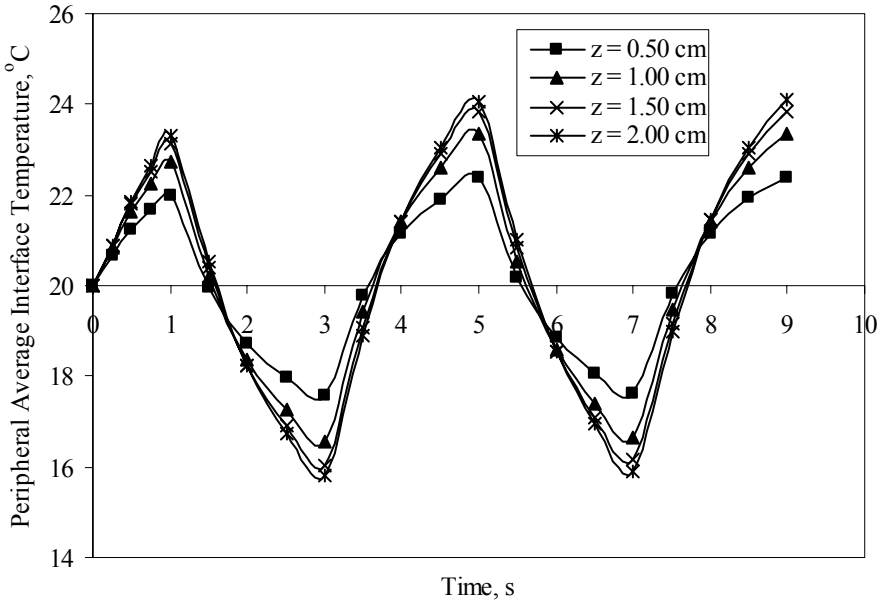

Figure 5.7: Peripheral average interface temperature over 9 seconds at different axial locations at the fluid-silicon interface (Re = 2000, G = 5 T, H_{fl} = 0.03 cm)

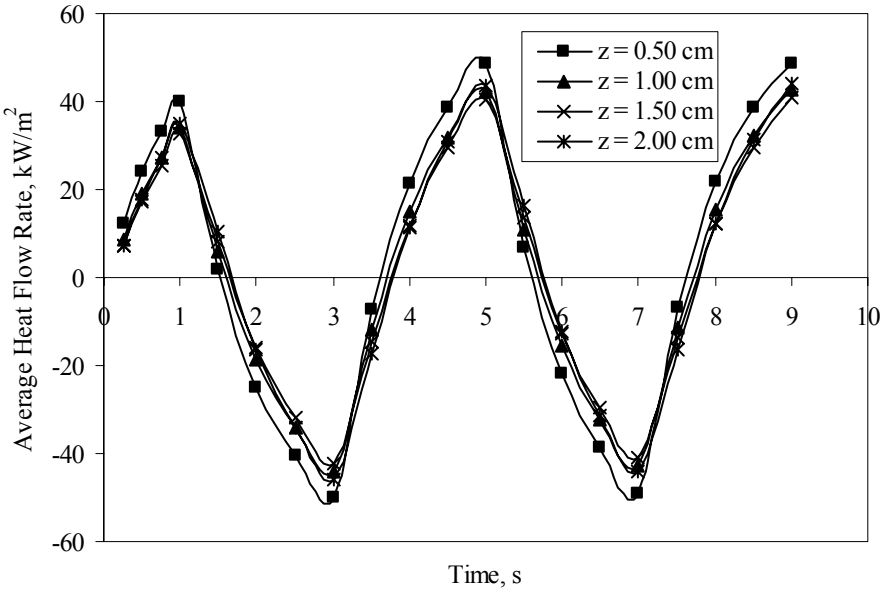

Figure 5.8: Peripheral average heat flow rate over 9 seconds at different axial locations at the fluid-silicon interface (Re = 2000, G = 5 T, H_{fl} = 0.03 cm)

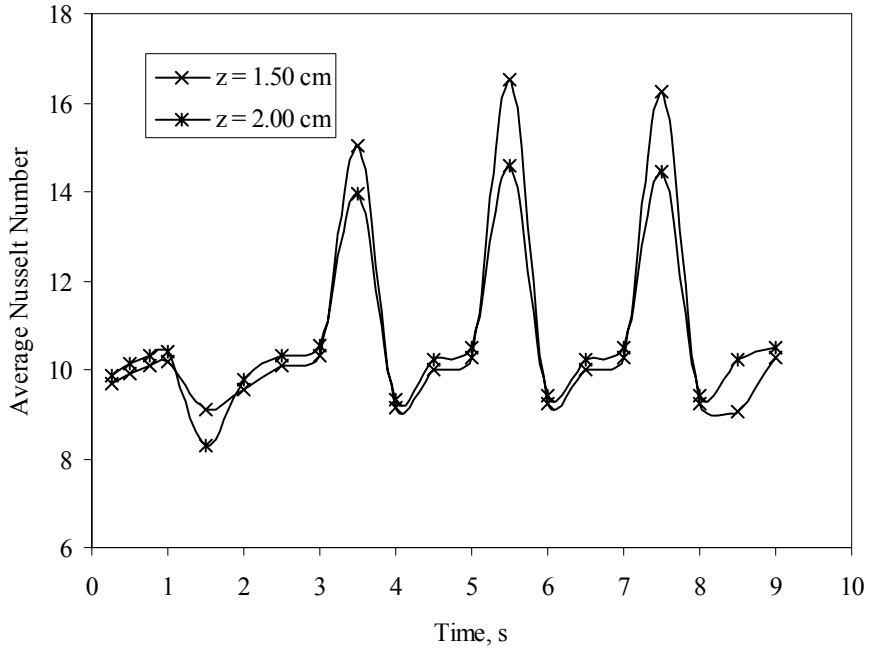

Figure 5.9: Peripheral average Nusselt number over 9 seconds at different axial locations at the fluid-solid interface (Re = 2000, G = 5 T, H_{fl} = 0.03 cm)

interface and bulk temperatures seems to occur early in the second period causing lower Nusselt number at time 1.5 s. Nusselt number seems to be lower further away from the inlet because of the lower heat flow rate that results from lower interface-bulk temperature.

Figure 5.10 shows the peripheral average interface temperature over 9 seconds at different axial locations at the fluid-gadolinium interface with magnetic field alternates between +10 and -10. The interface temperature reaches higher values when heating and lower values when cooling than those of the previous case. This is because of the larger magnetic field applied during heating and cooling. Figure 5.11 shows the average heat flow rate over 9 seconds at different axial locations at the fluid-gadolinium interface with

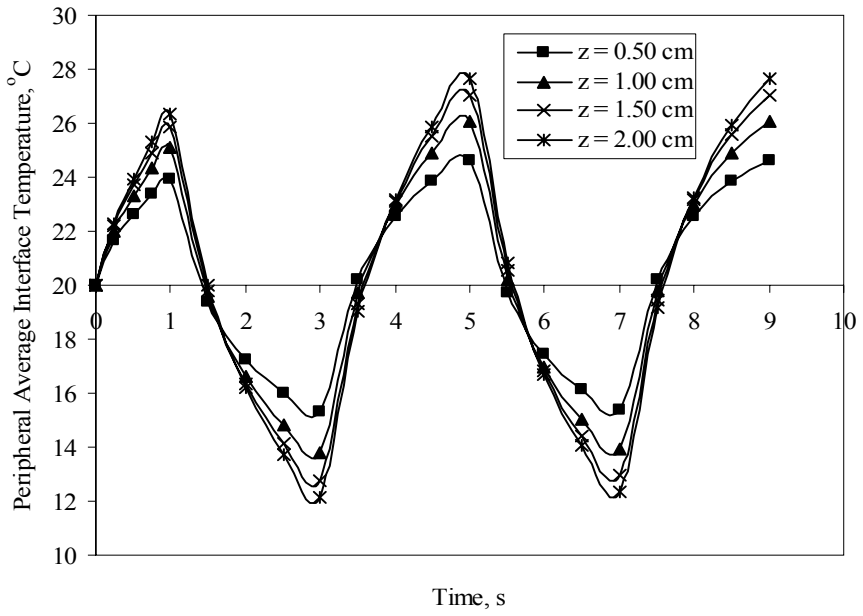

Figure 5.10: Peripheral average interface temperature over 9 seconds at different axial locations at the fluid-gadolinium interface with G = ±10 T (Re = 2000, H_{fl} = 0.03 cm)

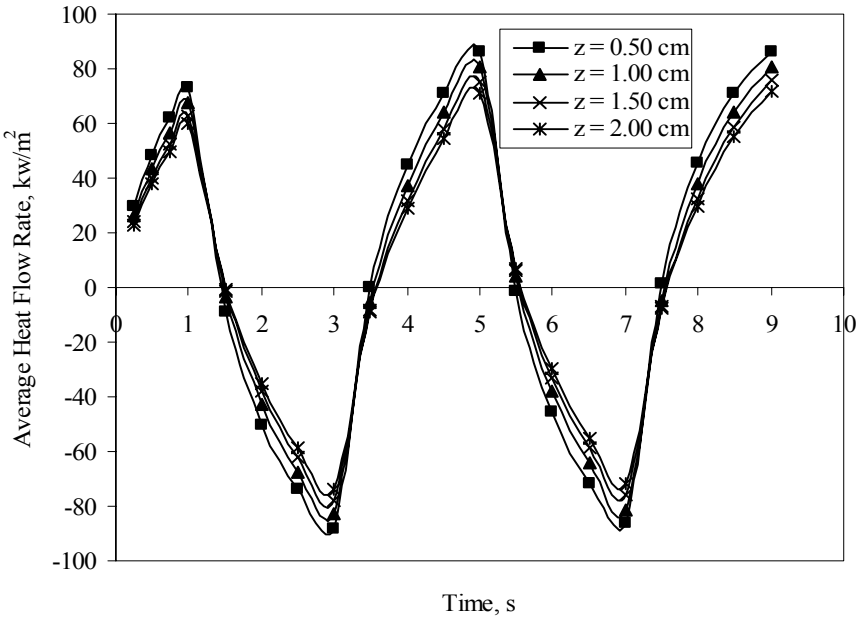

Figure 5.11: Peripheral average heat flow rate over 9 seconds at different axial locations at the fluid-gadolinium interface with G = ±10 T (Re = 2000, H_{fl} = 0.03 cm)

magnetic field alternates between +10 and -10. The heat flow rate is higher when heating and lower when cooling compared to the previous case. This is because of the higher heat source and sink caused by higher magnetic field at both processes. Figures 5.12 and 5.13 show results at the silicon edge similar to those at the gadolinium when compared to the original case. Both sides, gadolinium and silicon, has an increase in the absolute value of the interface temperature and heat flow rates during the heating and cooling processes. Figure 5.14 shows the average Nusselt number over 9 seconds at different axial locations at the fluid-solid interface with magnetic field alternates between +10 and -10. Our experience from previous work tells us that the change in the magnetic field does not affect the Nusselt number. The figure shows very close results to those of the original case.

Figures 5.15 to 5.19 show the effect of using smaller channel height on the heating and cooling performance of the trapezoidal microchannel system. Figure 5.15 shows the peripheral average interface temperature over 9 seconds at different axial locations at the fluid-gadolinium interface with H_{fl} = 0.02 cm. Compared to figure 5.5, the interface temperature is less for smaller channel height. This is because smaller channel with same Reynolds number have higher axial velocity which enhances the convection heat transfer to the fluid. This results in lower interface temperatures during the heating process but higher interface temperature during the cooling process. The absolute value of heat flow rate is higher for smaller channels as shown in figure 5.16. This is because the temperature gradient in the solid is increasing due to higher fluid velocity. Figures 5.17 and 5.18 show similar results of the silicon side to those of the gadolinium side. Figure 5.19 shows the average Nusselt number over 9 seconds at

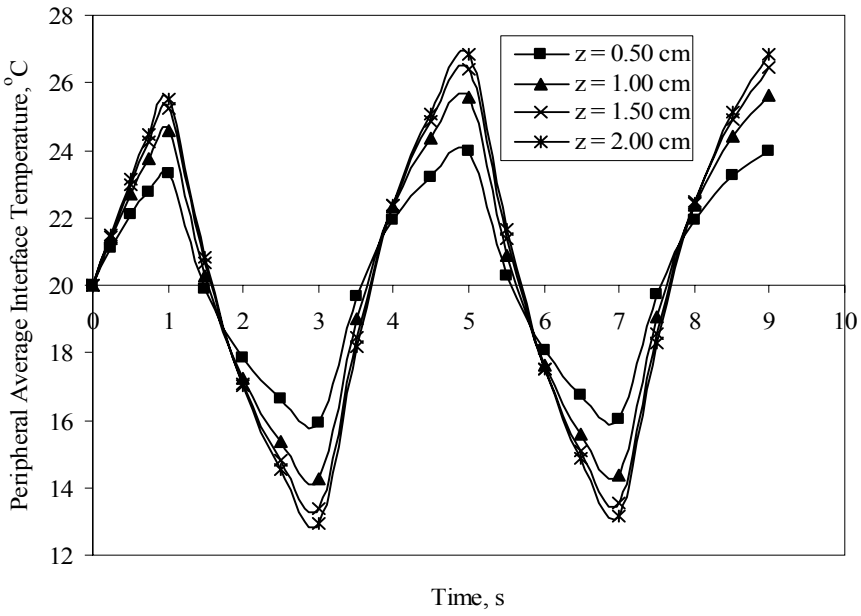

Figure 5.12: Peripheral average interface temperature over 9 seconds at different axial locations at the fluid-silicon interface with G = ±10 T (Re = 2000, H_{fl} = 0.03 cm)

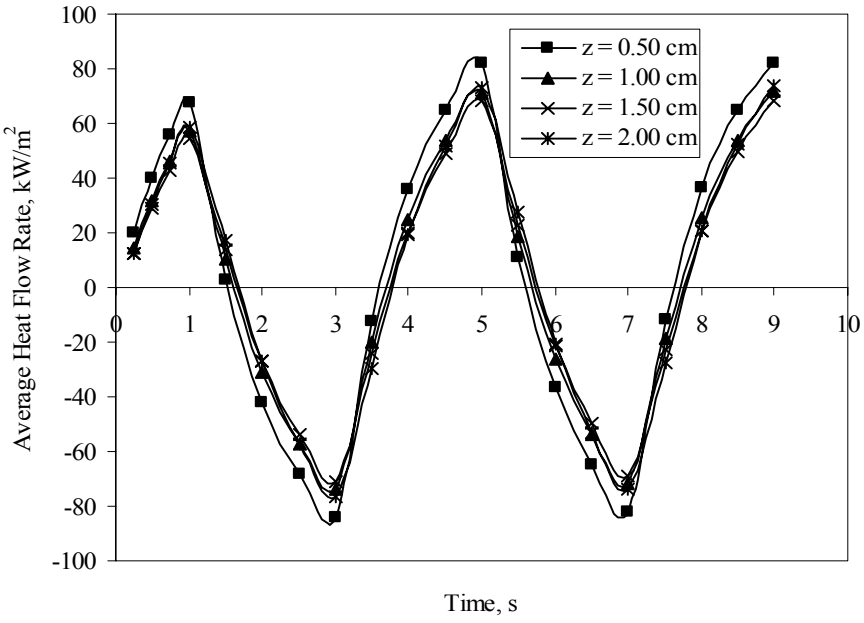

Figure 5.13: Peripheral average heat flow rate over 9 seconds at different axial locations at the fluid-silicon interface with G = ±10 T (Re = 2000, H_{fl} = 0.03 cm)

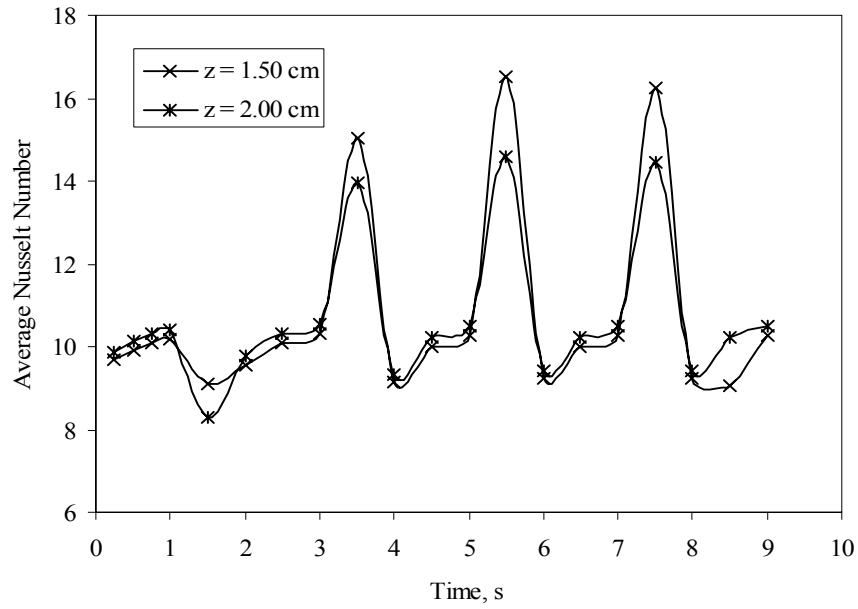

Figure 5.14: Peripheral average Nusselt number over 9 seconds at different axial locations at the fluid-solid interface with G = ±10 T (Re = 2000, H_{fl} = 0.03 cm)

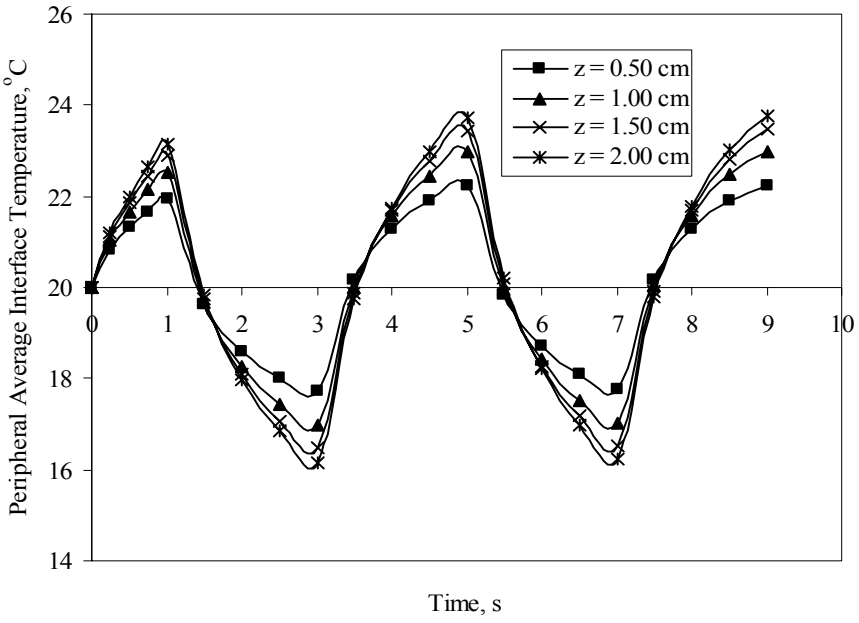

Figure 5.15: Peripheral average interface temperature over 9 seconds at different axial locations at the fluid-gadolinium interface with H_{fl} = 0.02 cm (Re = 2000, G = 5 T)

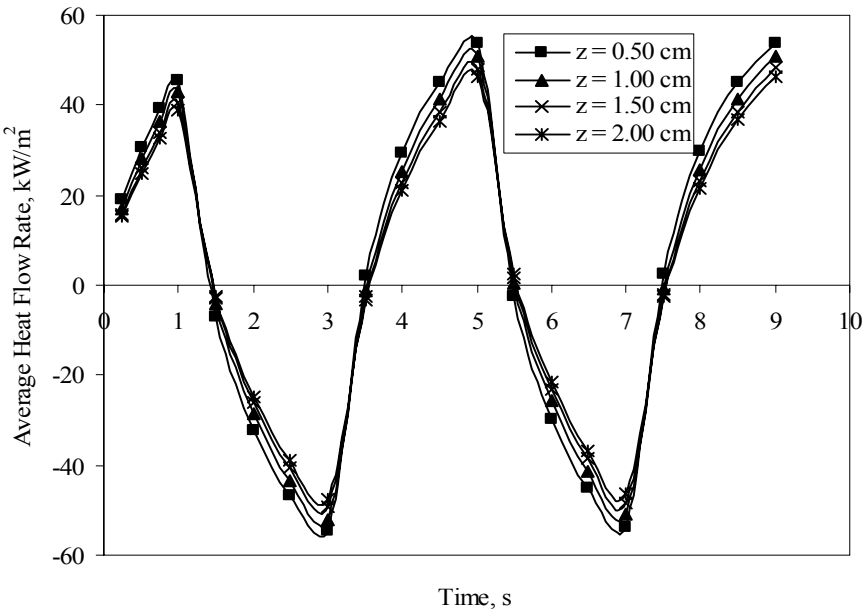

Figure 5.16: Peripheral average heat flow rate over 9 seconds at different axial locations at the fluid-gadolinium interface with H_{fl} = 0.02 cm (Re = 2000, G = 5 T)

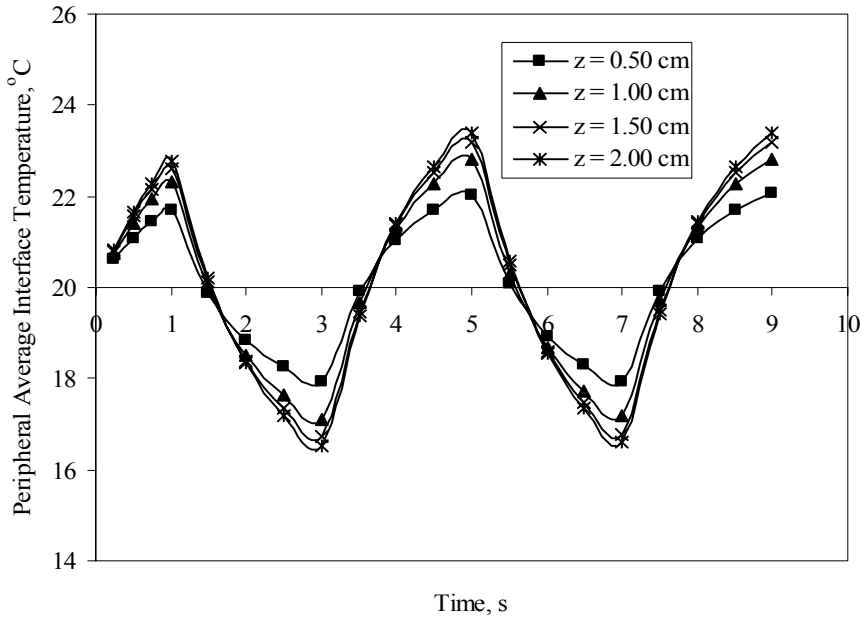

Figure 5.17: Peripheral average interface temperature over 9 seconds at different axial locations at the fluid-silicon interface with H_{fl} = 0.02 cm (Re = 2000, G = 5 T)

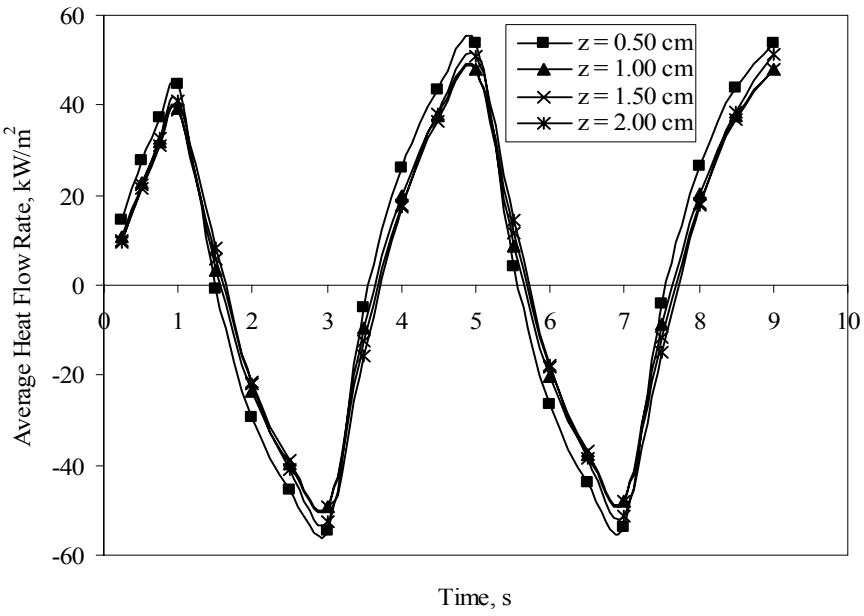

Figure 5.18: Peripheral average heat flow rate over 9 seconds at different axial locations at the fluid-silicon interface with H_{fl} = 0.02 cm (Re = 2000, G = 5 T)

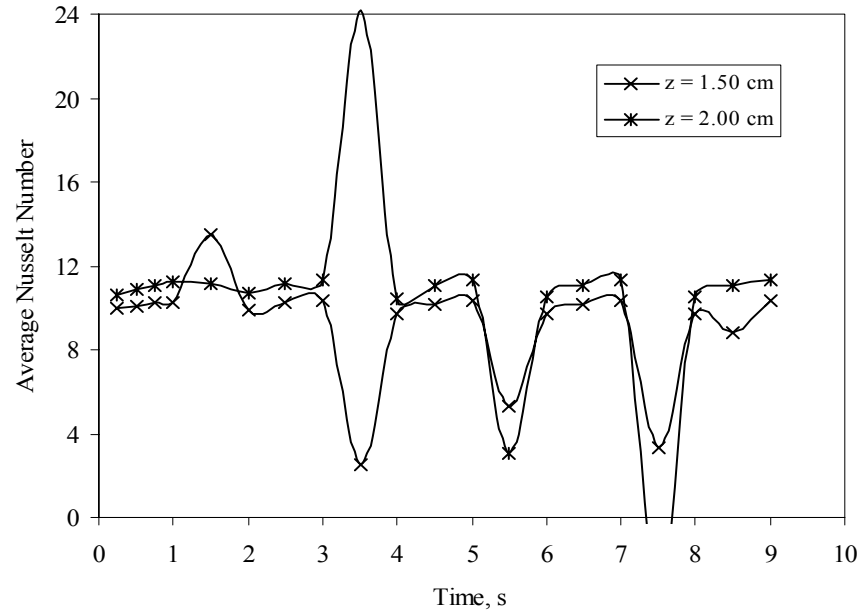

Figure 5.19: Peripheral average Nusselt number over 9 seconds at different axial locations at the fluid-solid interface with H_{fl} = 0.02 cm (Re = 2000, G = 5 T)

different axial locations at the fluid-solid interface with H_{fl} = 0.02 cm. It shows more irregular Nusselt number than the original case. The temperature gradient is the change in temperature in the solid region at the interface. When the heating process takes over, the solid has higher temperature than the interface. When the cooling process takes place the interface temperature becomes higher than the solid. This switch between values takes place at the beginning of every time period. This affects the sign of the heat flow rate indicating a heating or cooling process. The heat flow rate is the nominator for Nusselt number. In addition another switch between the interface and bulk temperatures is taking place. The interface-bulk temperature difference is the denominator of the Nusselt number. The time when the temperature gradient switch has took place while the interface-bulk temperatures are still in the switch process Nusselt number may be negative. After the interface-bulk temperature switch Nusselt number starts its increase to reasonable values. Higher fluid velocity that enhances the heat flow rate and results in earlier temperature gradient switch in the solid might be the reason behind the reason for having low Nusselt numbers. Compared to the original case, Nusselt number is lower with smaller channel height.

Figure 5.20 shows the peripheral average interface temperature over 9 seconds at different axial locations at the fluid-gadolinium interface at Re = 1000. Lower Reynolds number, or lower fluid velocity, slows down the heating or cooling process and thus results in lower interface temperature. It also results in lower absolute value of heat flow rate. This is shown in figure 5.21 in comparison with figure 5.6. Figures 5.22 and 5.23 show the peripheral average interface temperature and heat flow rate over 9 seconds at

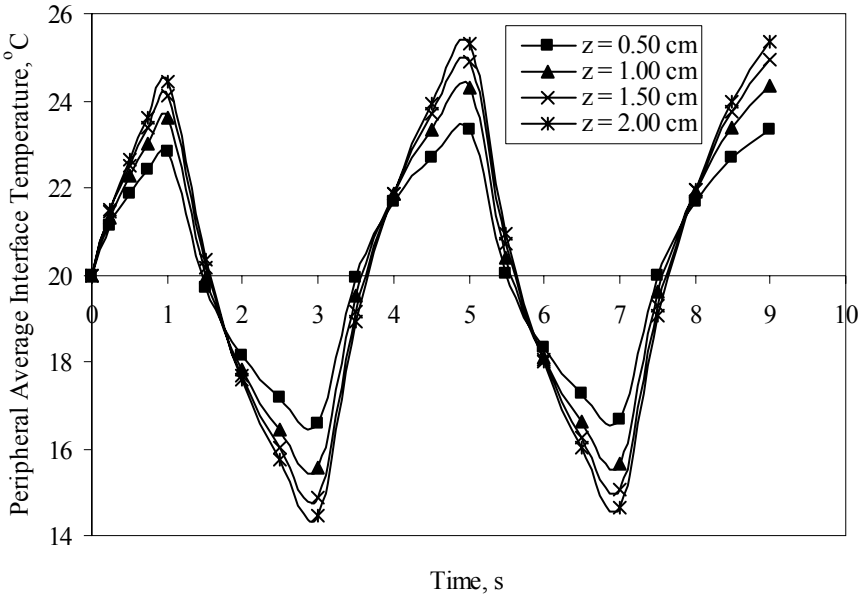

Figure 5.20: Peripheral average interface temperature over 9 seconds at different axial locations at the fluid-gadolinium interface at Re = 1000 (G = 5 T, H_{fl} = 0.03 cm)

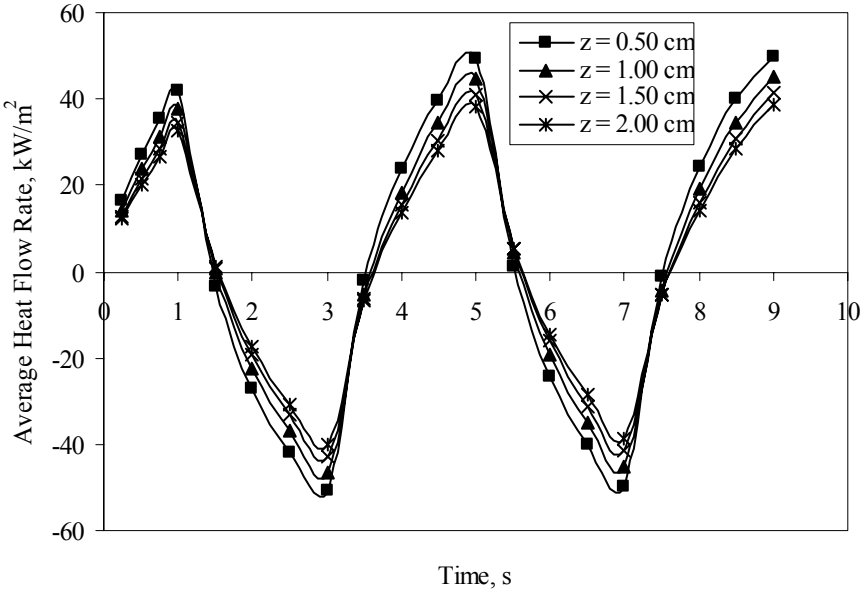

Figure 5.21: Peripheral average heat flow rate over 9 seconds at different axial locations at the fluid-gadolinium interface at Re = 1000 (G = 5 T, H_{fl} = 0.03 cm)

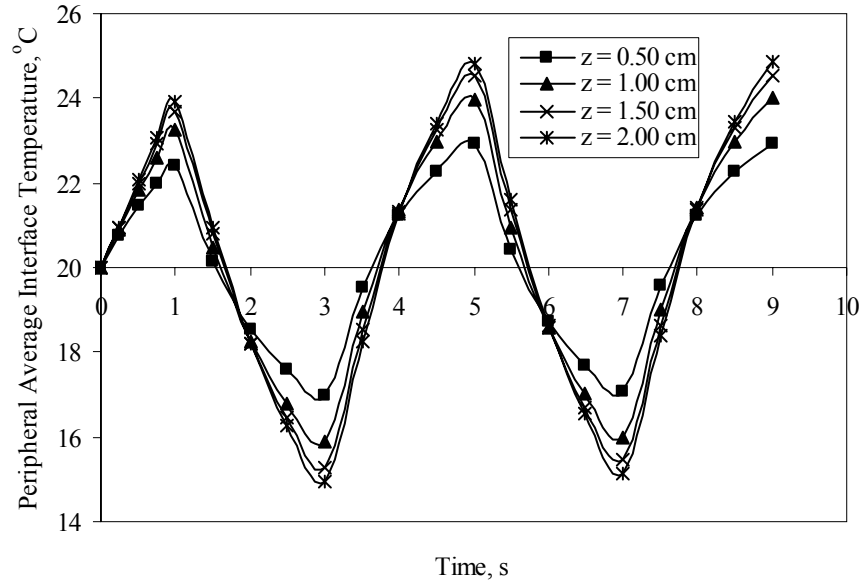

Figure 5.22: Peripheral average interface temperature over 9 seconds at different axial locations at the fluid-silicon interface at Re = 1000 (G = 5 T, H_{fl} = 0.03 cm)

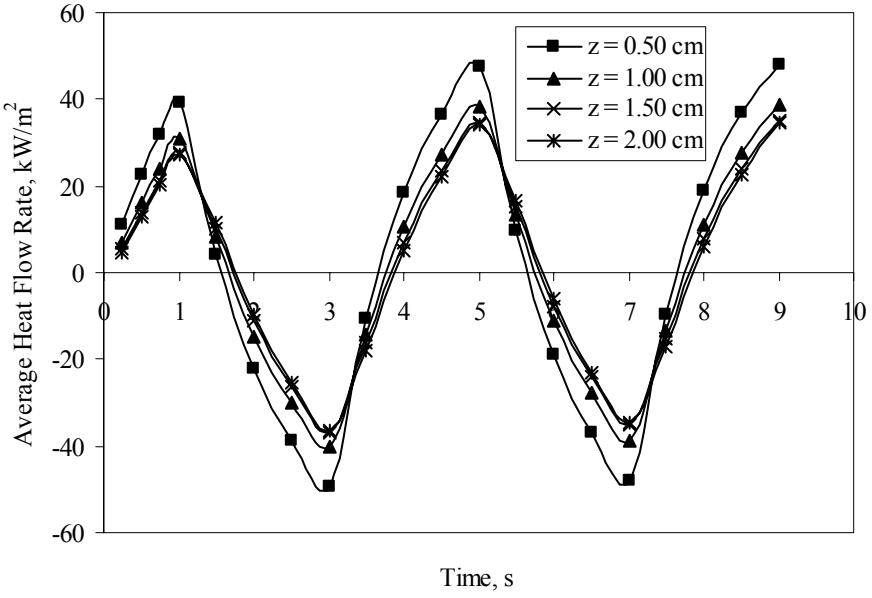

Figure 5.23: Peripheral average heat flow rate over 9 seconds at different axial locations at the fluid-silicon interface with at Re = 1000 (G = 5 T, H_{fl} = 0.03 cm)

different axial locations at the fluid-silicon interface at Re = 1000 respectively. They show similar results of those of gadolinium side when compared to figures 5.7 and 5.8. Nusselt number behavior in figure 5.24 is explained in the same fashion as in the previous case. The value of Nusselt number is less than the original case because of the lower absolute values of the heat flow rate resulted from lower fluid velocity.

5.4 Conclusions

This study of a time varying heat generation in a trapezoidal composite microchannel model with showed the effect of different parameters. The behavior of the interface temperature, heat flow rate, and Nusselt number were mostly sinusoidal. The results showed that the local Nusselt number was higher at the center of the channel. It also showed that Nusselt number decreased along the axial direction. The interface temperature showed sinusoidal behavior as the heating and cooling processes alternates. The heat flow rate increases in absolute value in each time period. Nusselt number found to increase in each time period regardless the process. Higher magnetic field increases the interface temperature and the absolute value of the heat flow rate. It does not have any effect on the behavior of Nusselt number. Smaller channel height decreased the interface temperature but increased the absolute heat flow rate. Nusselt number decreased because of its dependence on the hydraulic diameter of the channel. Lower Reynolds number decreases the interface temperature, heat flow rate, and Nusselt number.

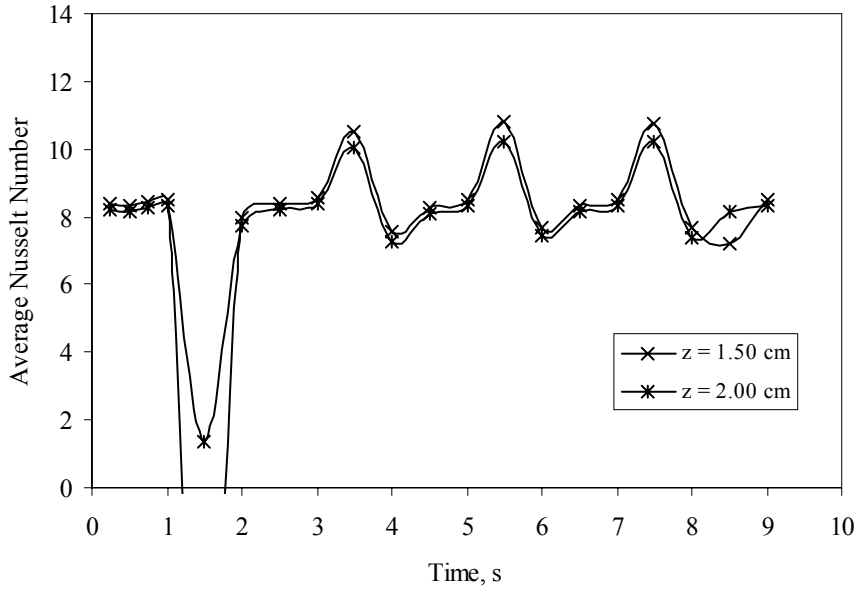

Figure 5.24: Peripheral average Nusselt number over 9 seconds at different axial locations at the fluid-solid interface with at Re = 1000 (G = 5 T, H_{fl} = 0.03 cm)

Chapter 6 – Steady State Heat Transfer Using Nanofluids in Circular Microchannel

6.1 Mathematical Model

The problem in hand is a microchannel assembly with circular channel in a rectangular solid substrate. The channel substrate extends to a length (L). The thickness of the substrate is (H) and distance between tubes in the horizontal direction is 2W. Nanofluid flows through circular channels with diameter (D) and length (L) as single pass from inlet to outlet manifold. Nanofluids are fluids suspended with solid particles. These nanometer-sized particles have high thermal conductivity which enhances the overall fluid's thermal conductivity. The heat is supplied at the bottom of the substrate. Heat is conducted through the solid substrate material and convected to the working fluid. Figure 6.1 shows a schematic drawing for the model simulated.

The governing equations for the conservation of mass, momentum, and energy in the liquid region are [45]:

$$\frac{\partial V_r}{\partial r}+\frac{1}{r}V_r+\frac{1}{r}\frac{\partial V_\phi}{\partial \phi}+\frac{\partial V_z}{\partial z}=0 \tag{1}$$

$$\left(V_r\frac{\partial V_r}{\partial r}+\frac{V_\phi}{r}\frac{\partial V_r}{\partial \phi}+V_z\frac{\partial V_r}{\partial z}-\frac{1}{r}V_\phi^2\right)= -\frac{1}{\rho_f}\frac{\partial p}{\partial r}+\nu\left[\frac{\partial^2 V_r}{\partial r^2}+\frac{1}{r}\frac{\partial V_r}{\partial r}+\frac{1}{r^2}\frac{\partial^2 V_r}{\partial \phi^2}+\frac{\partial^2 V_r}{\partial z^2}-\frac{V_r}{r^2}-\frac{2}{r^2}\frac{\partial V_\phi}{\partial \phi}\right] \tag{2}$$

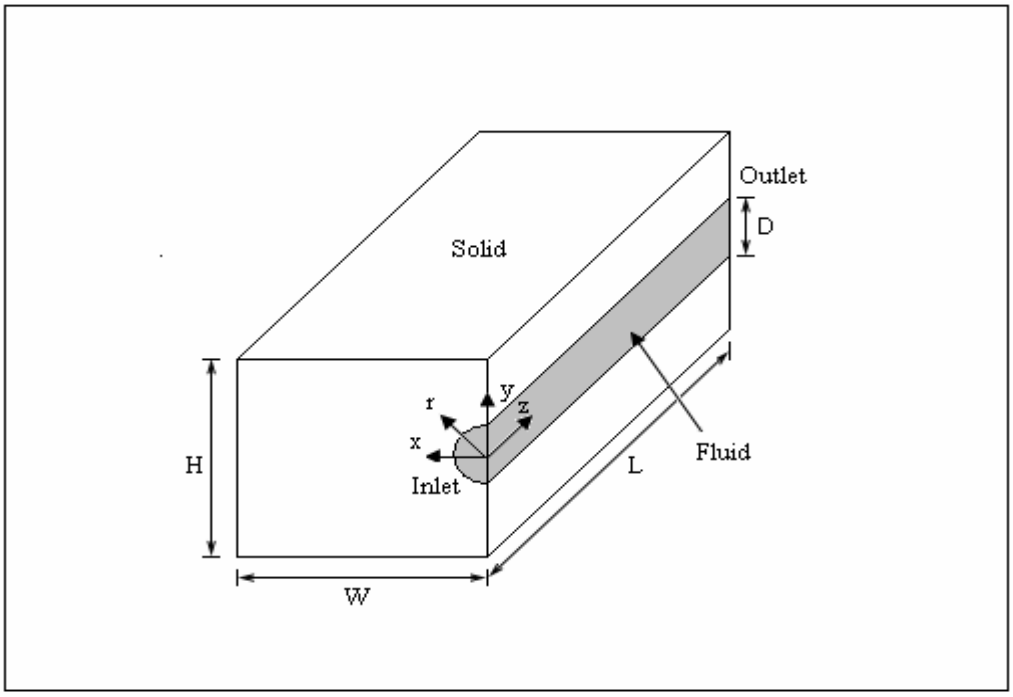

Figure 6.1: Schematic of nanofluid circular microchannel model

$$\left(V_r\frac{\partial V_\phi}{\partial r}+\frac{V_\phi}{r}\frac{\partial V_\phi}{\partial \phi}+V_z\frac{\partial V_\phi}{\partial z}-\frac{V_rV_\phi}{r}\right)= \\ -\frac{1}{\rho_f r}\frac{\partial p}{\partial \phi}+\nu\left[\frac{\partial^2 V_\phi}{\partial r^2}+\frac{1}{r}\frac{\partial V_\phi}{\partial r}+\frac{1}{r^2}\frac{\partial^2 V_\phi}{\partial \phi^2}+\frac{\partial^2 V_\phi}{\partial z^2}-\frac{V_\phi}{r^2}+\frac{2}{r^2}\frac{\partial V_r}{\partial \phi}\right] \tag{3}$$

$$\left(V_r\frac{\partial V_z}{\partial r}+\frac{V_\phi}{r}\frac{\partial V_z}{\partial \phi}+V_z\frac{\partial V_z}{\partial z}\right)=-\frac{1}{\rho_f}\frac{\partial p}{\partial z}+\nu\left[\frac{\partial^2 V_z}{\partial r^2}+\frac{1}{r}\frac{\partial V_z}{\partial r}+\frac{1}{r^2}\frac{\partial^2 V_z}{\partial \phi^2}+\frac{\partial^2 V_r}{\partial z^2}\right] \tag{4}$$

$$\left(V_r\frac{\partial T_f}{\partial r}+\frac{V_\phi}{r}\frac{\partial T_f}{\partial \phi}+V_z\frac{\partial T_f}{\partial z}\right)=\alpha_f\left[\frac{\partial^2 T_f}{\partial r^2}+\frac{1}{r}\frac{\partial T_f}{\partial r}+\frac{1}{r^2}\frac{\partial^2 T_f}{\partial \phi^2}+\frac{\partial^2 T_f}{\partial z^2}\right] \tag{5}$$

Considering constant thermal conductivity, the energy conservation equation in the solid region with heat generation is [46]:

$$\left[\frac{\partial^2 T_s}{\partial x^2}+\frac{\partial^2 T_s}{\partial y^2}+\frac{\partial^2 T_s}{\partial z^2}\right]=0 \tag{6}$$

It may be noted that a cylindrical coordinate system was used to model convection within circular tube while a Cartesian coordinate system was used to model conduction within the solid substrate material. Equations (1) to (6) are subject to the following boundary conditions:

At z = 0, 0 ≤ r < d/2: $$V_r = 0, V_\phi = 0, V_z = V_{z,in}, T_f = T_{f,in} \quad (7)$$

At z = 0, r ≥ d/2, 0 < x < W, 0 < y < H: $$\frac{\partial T_s}{\partial z} = 0 \quad (8)$$

At z = L, r < d/2: $$p = 0 \quad (9)$$

At z = L, r ≥ d/2, 0 < x < W, 0 < y < H: $$\frac{\partial T_s}{\partial z} = 0 \quad (10)$$

At x = 0, -d/2 ≤ y ≤ +d/2, 0 ≤ z ≤ L: $$V_\theta = 0, \frac{\partial V_r}{\partial x} = 0, \frac{\partial V_z}{\partial x} = 0, \frac{\partial T_f}{\partial x} = 0 \quad (11)$$

At x = 0, -H/2 ≤ y ≤ -d/2, 0 ≤ z ≤ L: $$\frac{\partial T_s}{\partial x} = 0 \quad (12)$$

At x = 0, +d/2 ≤ y ≤ +H/2, 0 ≤ z ≤ L: $$\frac{\partial T_s}{\partial x} = 0 \quad (13)$$

At x = W, -H/2 ≤ y ≤ +H/2, 0 ≤ z ≤ L: $$\frac{\partial T_s}{\partial x} = 0 \quad (14)$$

At y = -H/2, 0 ≤ x ≤ W, 0 ≤ z ≤ L: $$\frac{\partial T_s}{\partial y} = 0 \quad (15)$$

At y = +H/2, 0 ≤ x ≤ W, 0 ≤ z ≤ L: $$\frac{\partial T_s}{\partial y} = 0 \quad (16)$$

At 0 ≤ z ≤ L, r = d/2: $$T_f = T_s, k_f \frac{\partial T_f}{dr} = k_s \frac{\partial T_s}{dr} \quad (17)$$

At y = -H/2, 0 ≤ x ≤ W, 0 ≤ z ≤ L: $$\frac{\partial T_s}{dy} = \frac{-q''}{k_s} \quad (18)$$

6.2 Numerical Simulation and Parametric Study

The governing equations along with the boundary conditions were solved using the Galerkin finite element method. Four-node quadrilateral elements were used. In each element, the velocity, pressure, and temperature fields were approximated which led to a set of equations that defined the continuum. An iterative procedure was used to arrive at the solution for the velocity and temperature fields. The solution was considered converged when the field values did not change from one iteration to the next, and the residuals for each variable became negligible.

For the numerical computations, the height (H) and the half width (W) of the model were set to 0.2 cm and 0.1 cm respectively. The channel length (L) was set to 2.3 cm. The diameter was changed from 0.06 cm to 0.14 cm. Reynolds number was varied between 500 and 1500. Silicon was used as the solid substrate material. Another two solid substrate were used: Silicon carbide and stainless steel. Water suspended with 4% volume fraction of Alumina (AL_2O_3) was used as the working fluid. 1% and 2% volume fraction of Alumina suspended into water were used as well. The local solid-fluid interface temperature, heat flow rate, heat transfer coefficient and Nusselt number were calculated from the resulted velocity and temperature distributions.

6.3 Results and Discussions

To establish an independent mesh, several mesh sizing were studied and compared. Interface temperatures and Nusselt numbers were plotted. Figure 6.2 and 6.3 show the interface temperature and Nusselt number for different mesh sizing,

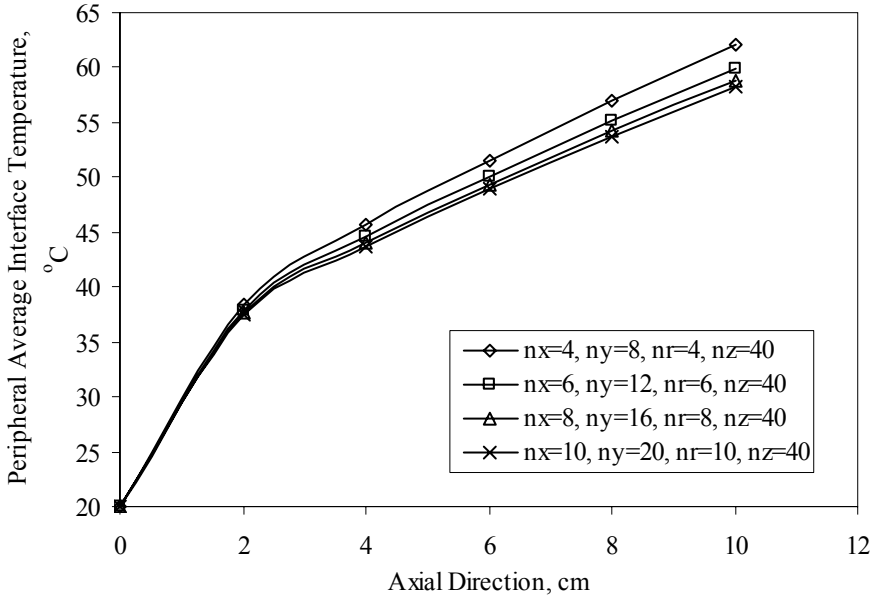

Figure 6.2: Peripheral average interface temperature along the axial direction (Silicon, Water + 4% volume fraction of Alumina, Re = 500, d = 0.06 cm)

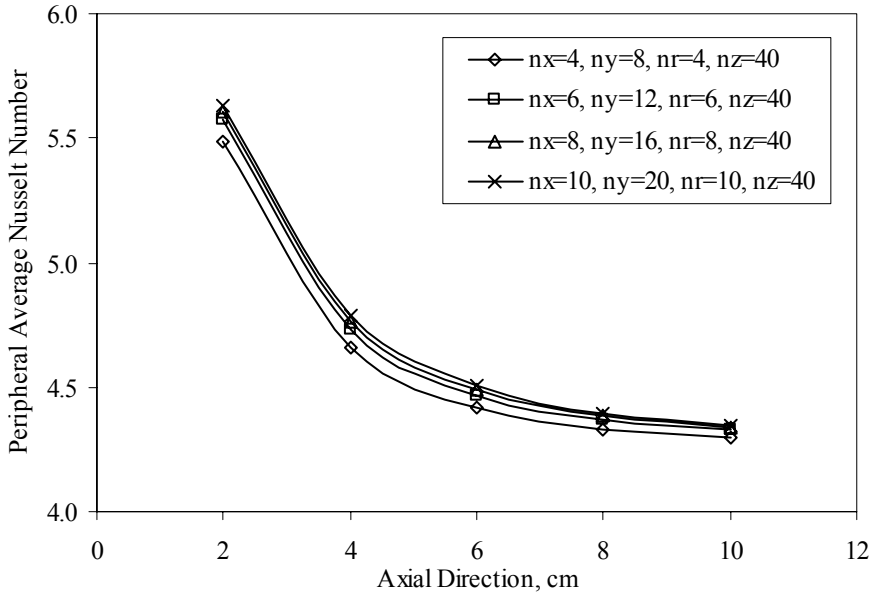

Figure 6.3: Peripheral average Nusselt number along the axial direction (Silicon, Water + 4% volume fraction of Alumina, Re = 500, d = 0.06 cm)

respectively. From both figures the mesh size (nx = 8, ny = 16, nr = 8, nz = 40) was found to be sufficient for mesh independence.

The local interface temperature, heat flow rate, heat transfer coefficient and Nusselt number were calculated from the resulted velocity and temperature distribution. Figure 6.4 shows the interface temperature along the angular direction from bottom to top at different axial locations. This is done because of the one sided heat flux boundary condition from the bottom. The interface temperature is slightly higher at the bottom of the tube, which is closer to the heat source, at all axial locations. Figure 6.5 shows the heat flow rate along the angular direction from bottom to top at different axial locations. The heat flow rate is higher closer to the bottom of the tube, which is closer to the heat source. There is a slight increase in the heat flow rate between the side and bottom of the tube. This is the area where the heat flow stream lines are parallel to the channel tube. The high conductance of the solid material transfers parts the heat towards the sides and top of the tube. This where it slightly re-increase but then continue to decrease afterwards. Notice that the heat flow rate is higher closer to the tube entry. This is expected because of the low inlet fluid temperature that results in higher temperature difference. Figure 6.6 shows the heat transfer coefficient along the angular direction from bottom to top at different axial locations. The heat transfer coefficient is generally decreasing from the bottom of the tube to the top. Similarly to the heat flow rate, the heat transfer coefficient is higher closer to the tube entry. This is because of the fluid low inlet temperature. Figure 6.7 shows the Nusselt number along the angular direction from bottom to top at different axial locations. The Nusselt number follows similar trend of those of heat transfer coefficient because of its direct dependence.

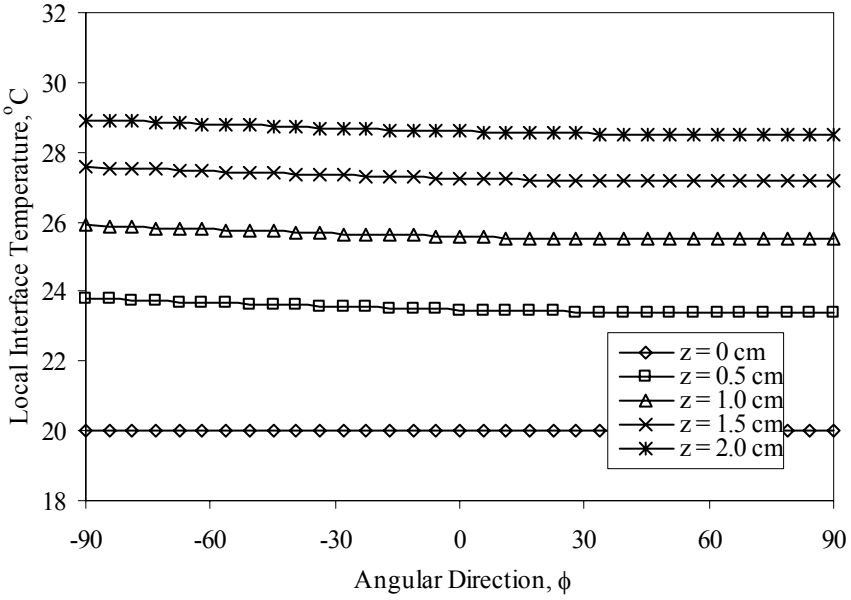

Figure 6.4: Local interface temperature along the angular direction at different axial locations (Silicon, Water + 4% volume fraction of Alumina, Re = 500, d = 0.06 cm)

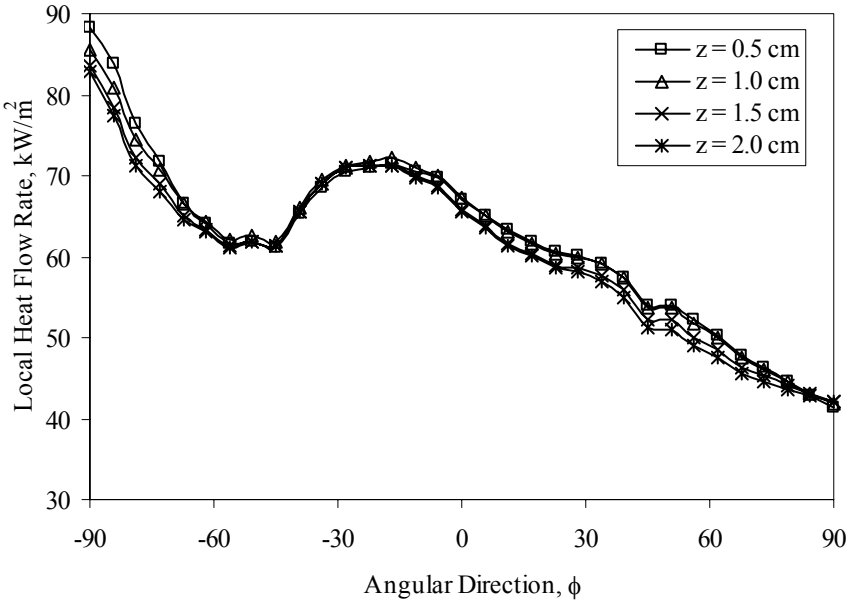

Figure 6.5: Local heat flow rate along the angular direction at different axial locations (Silicon, Water + 4% volume fraction of Alumina, Re = 500, d = 0.06 cm)

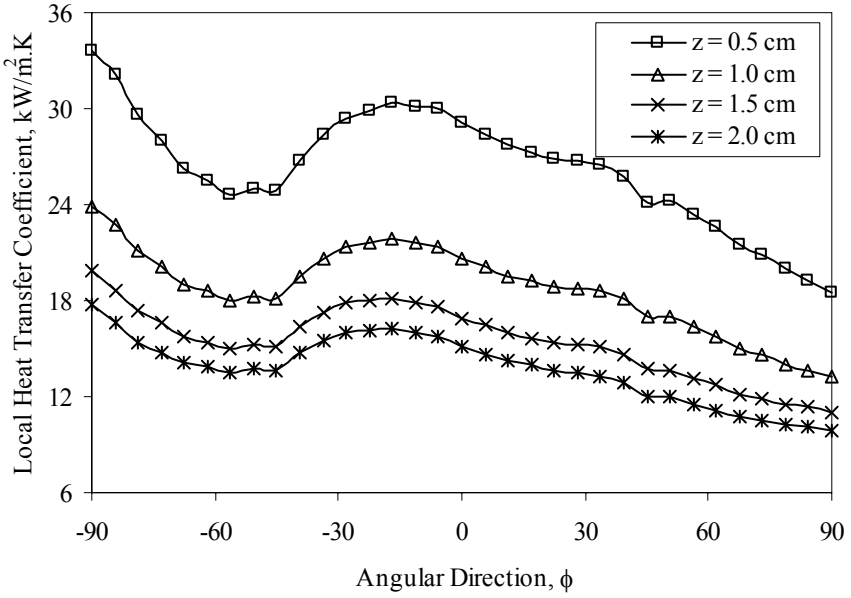

Figure 6.6: Local heat transfer coefficient along the angular direction at different axial locations (Silicon, Water + 4% volume fraction of Alumina, Re = 500, d = 0.06 cm)

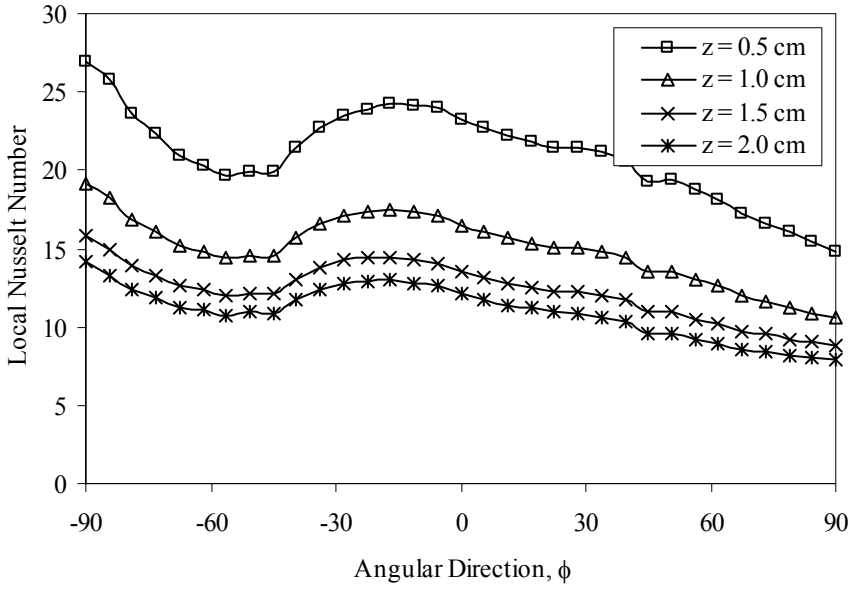

Figure 6.7: Local Nusselt number along the angular direction at different axial locations (Silicon, Water + 4% volume fraction of Alumina, Re = 500, d = 0.06 cm)

Figure 6.8 shows the average peripheral interface temperature and heat flow rate along the axial direction for Silicon substrate and water suspended with 4% volume fraction of Alumina as the working fluid. Reynolds number was 500 and the tube diameter was 0.06 cm. The interface temperature increases along the axial direction because of the heat flux. The heat flow rate is decreasing along the axial direction because the fluid temperature rises along the axial direction. Figure 6.9 shows the peripheral average heat transfer coefficient and Nusselt number along the axial direction. The Nusselt number follows similar trend of those of heat transfer coefficient because of its direct dependence. The average peripheral heat transfer coefficient and Nusselt number decrease along the axial direction because of the interface-bulk temperature difference that is increasing along the axial direction.

Detailed analysis is represented to study the angular effect on the interface temperature, heat flow rate, and Nusselt number. Because of the one sided heat flux boundary condition the top, side and bottom lines of the tube were analyzed separately. It is expected that the bottom side will have the highest interface temperature and heat flow rate. Figure 6.10 shows the interface temperature along the axial direction at different angular locations. The bottom of the tube has higher interface temperature while the top of the tube has the lowest. This is because of the heat flux boundary condition at the bottom of the substrate. Figure 6.11 shows the heat flow rate along the axial direction at different angular locations. The heat flow rate is decreasing along the axial because of the fluid bulk temperature rises. At the bottom of the tube the heat flow rate decreasing rate along the axial direction decreases because of the heat source. Figure 6.12 shows Nusselt number along the axial direction at different angular locations. Nusselt number decreases

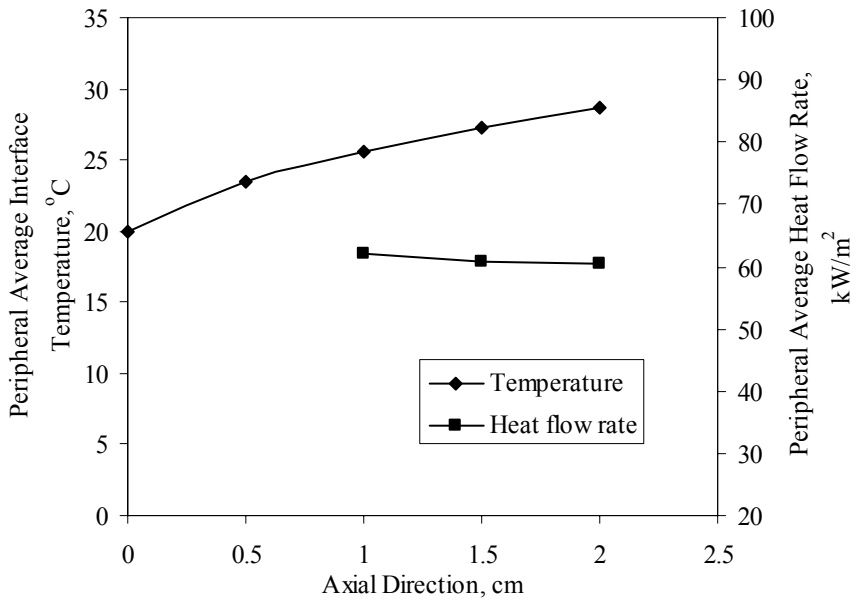

Figure 6.8: Peripheral average interface temperature and heat flow rate along the axial direction (Silicon, Water + 4% volume fraction of Alumina, Re = 500, d = 0.06 cm)

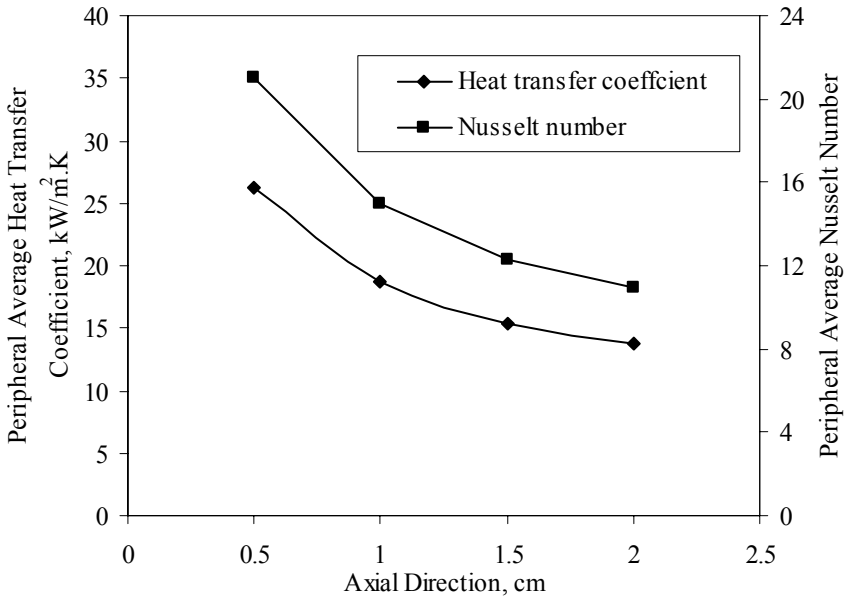

Figure 6.9: Peripheral average heat transfer coefficient and Nusselt number along the axial direction (Silicon, Water + 4% volume fraction of Alumina, Re = 500, d = 0.06 cm)

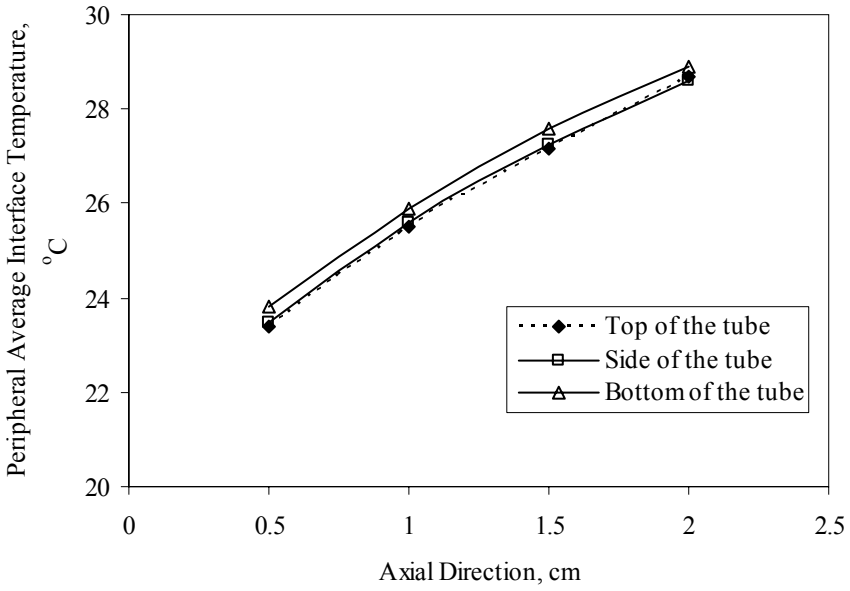

Figure 6.10: Interface temperature along the axial direction at different angular location (Silicon, Water + 4% volume fraction of Alumina, Re = 500, d = 0.06 cm)

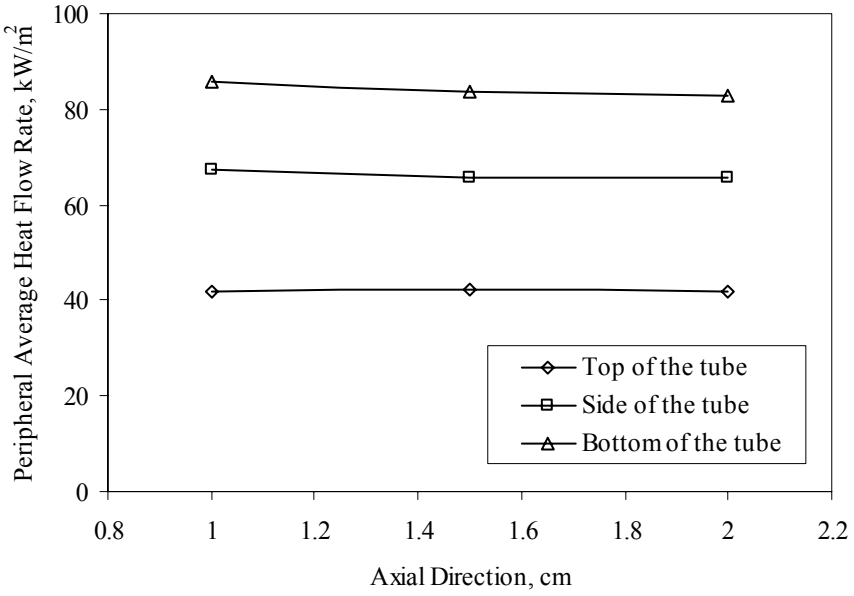

Figure 6.11: Heat flow rate along the axial direction at different angular location (Silicon, Water + 4% volume fraction of Alumina, Re = 500, d = 0.06 cm)

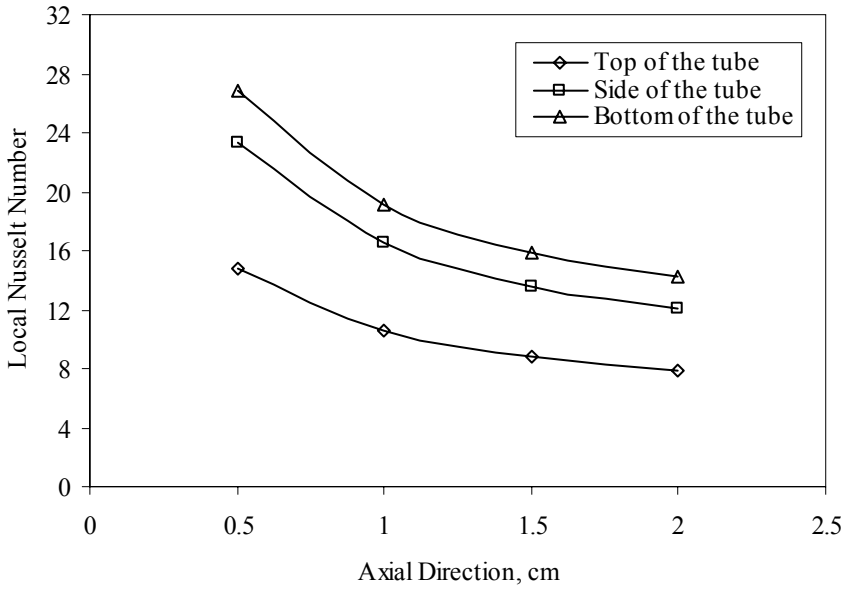

Figure 6.12: Nusselt number along the axial direction at different angular location (Silicon, Water + 4% volume fraction of Alumina, Re = 500, d = 0.06 cm)

along the axial direction because the interface-bulk temperature difference decreases along the axial direction.

Figure 6.13 shows the interface temperature along the axial direction using different working fluids. Four fluids used are: pure water and water suspended with Alumina (Al_2O_3) at different volume fractions of 4%, 2% and 1%. To maintain the same Reynolds number the fluid velocity must be adjusted for each fluid. The water suspended with higher volume fraction of Alumina has higher thermal conductivity. This thermal conductivity enhancement is caused by the high thermal conductivity of the solid particles. This causes more heat rejection to the working fluid and thus lower interface temperatures. On the other hand, the fluid velocity decreases with higher volume fraction, because of the change in properties and maintaining the same Reynolds number, which

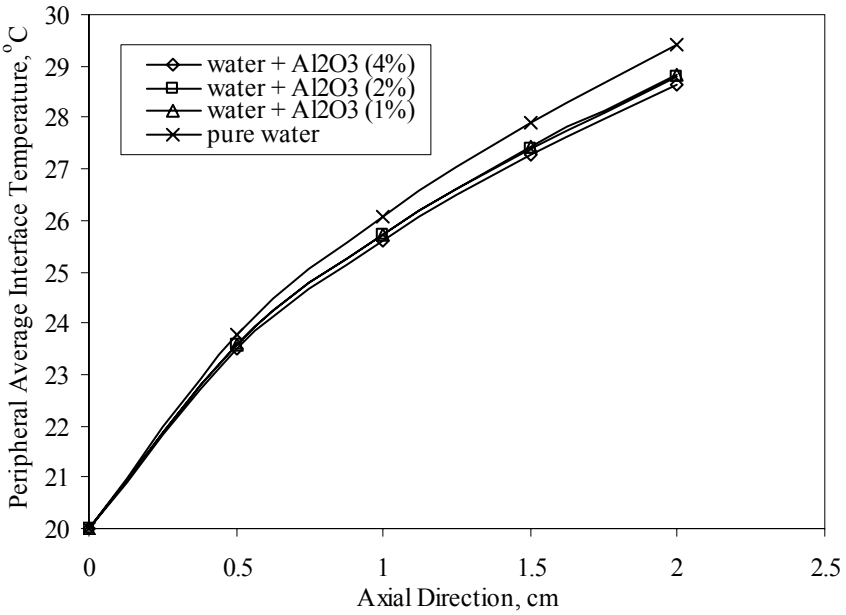

Figure 6.13: Peripheral average interface temperature along the axial direction at different working fluids (Silicon, Re = 500, d = 0.06 cm)

cause an increase to the interface temperature. The net result is a decrease in the interface temperature. Figure 6.14 shows the heat flow rate along the axial direction using different working fluids. The heat flow rate decreases along the axial direction because of the increase in the fluid bulk temperature. It is expected that higher volume fraction of the nanoparticles in the fluid will enhance the heat flow rate at the interface of the tube. On the other hand, the heat flow rate decreases because of the lower fluid velocity due to the change in properties and maintaining the same Reynolds number. The net result is an increase in the heat flow rate with lower volume fraction. Nusselt number directly depends on the heat flow rate and the fluid conductivity. Figure 6.15 shows the Nusselt number along the axial direction at different angular locations. Nusselt number depends on the heat transfer coefficient and the fluid thermal conductivity. Both are changing but

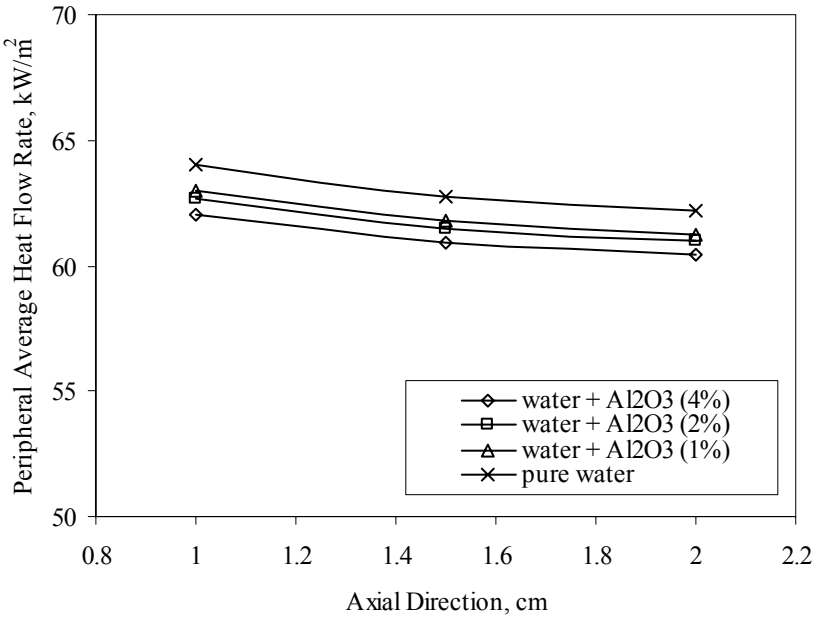

Figure 6.14: Peripheral average heat flow rate along the axial direction at different working fluids (Silicon, Re = 500, d = 0.06 cm)

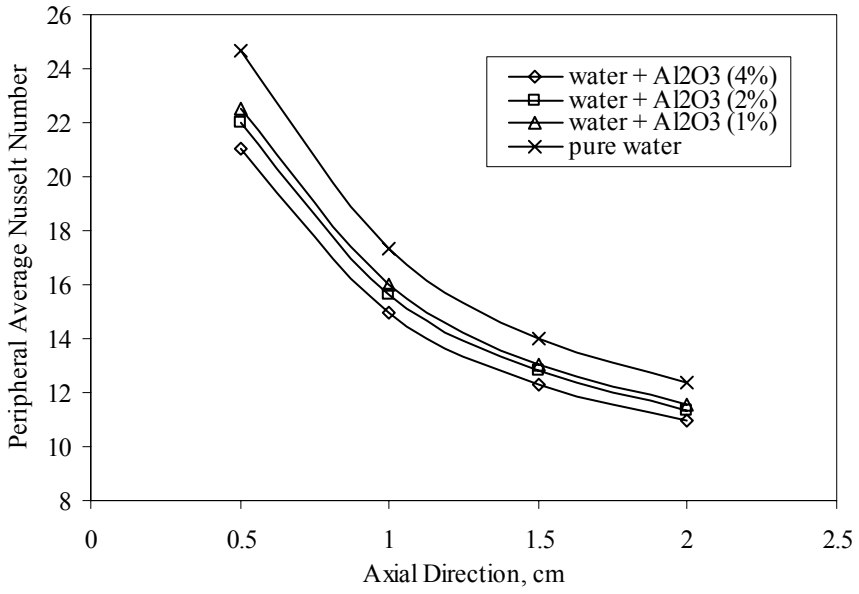

Figure 6.15: Peripheral average Nusselt number along the axial direction at different working fluids (Silicon, Re = 500, d = 0.06 cm)

the heat flow rate has higher effect on Nusselt number. This results in a decreasing Nusselt number with higher nanoparticles volume fraction.

Figure 6.16 shows the interface temperature along the axial direction using different solid materials. The three solids used are: Silicon, silicon carbide, and stainless steel. Silicon and silicon carbide has close property values and hence the effect of this change was negligible. Stainless steel, on the other hand, has much lower thermal conductivity. The lower thermal conductivity works as a thermal resistance and reduces the heat flow rate increases the interface temperature at the interface. Figure 6.17 shows the heat flow rate along the axial direction using different solid materials. The stainless steel has lower thermal conductivity which leads to lower heat flow rate at the interface. This results in lower Nusselt number for stainless steel as shown in figure 6.18.

Figure 6.19 shows the interface temperature along the axial direction using different Reynolds numbers. Higher Reynolds number enhances the cooling rate and thus decreases the interface temperature. This is because it increases the heat rejection in the system causing the heat flow rate at the interface to increase as shown in figure 6.20. Nusselt number is directly dependent on the heat flow rate and thus it also increases with Reynolds number. The relatively higher Nusselt numbers shown in figure 6.21 resulted from higher Reynolds number is because the thermal development of the fluid depends on the value of Reynolds number. Higher Reynolds numbers require longer tube which causes the Nusselt number to be higher at the same axial location.

Figure 6.22 shows the interface temperature along the axial direction using different diameters. Larger diameter reduces the fluid velocity to maintain its Reynolds number and hence slows down the cooling process. It is expected that this causes the

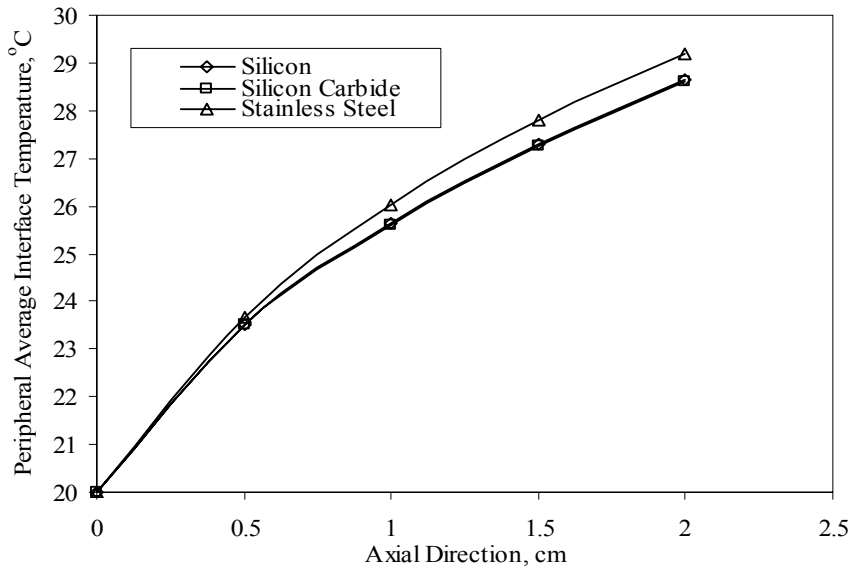

Figure 6.16: Peripheral average interface temperature along the axial direction at different solid substrates (Water + 4% volume fraction of Alumina, Re = 500, d = 0.06 cm)

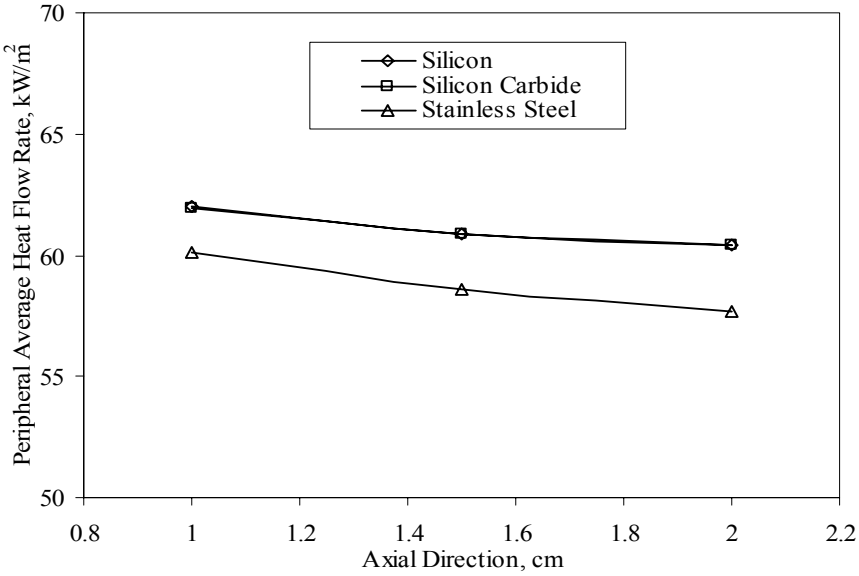

Figure 6.17: Peripheral average heat flow rate along the axial direction at different solid substrates (Water + 4% volume fraction of Alumina, Re = 500, d = 0.06 cm)

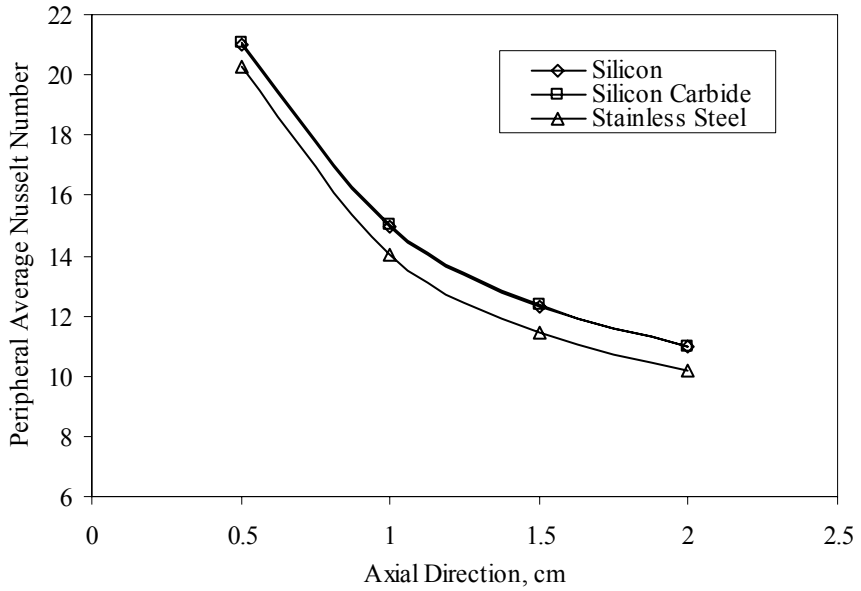

Figure 6.18: Peripheral average Nusselt number along the axial direction at different solid substrates (Water + 4% volume fraction of Alumina, Re = 500, d = 0.06 cm)

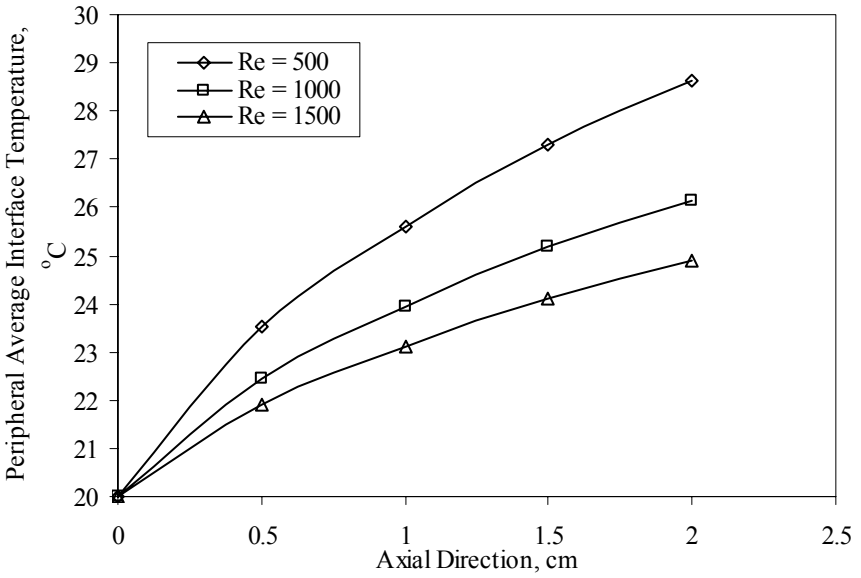

Figure 6.19: Peripheral average interface temperature along the axial direction at different Reynolds numbers (Silicon, Water + 4% volume fraction of Alumina, d = 0.06 cm)

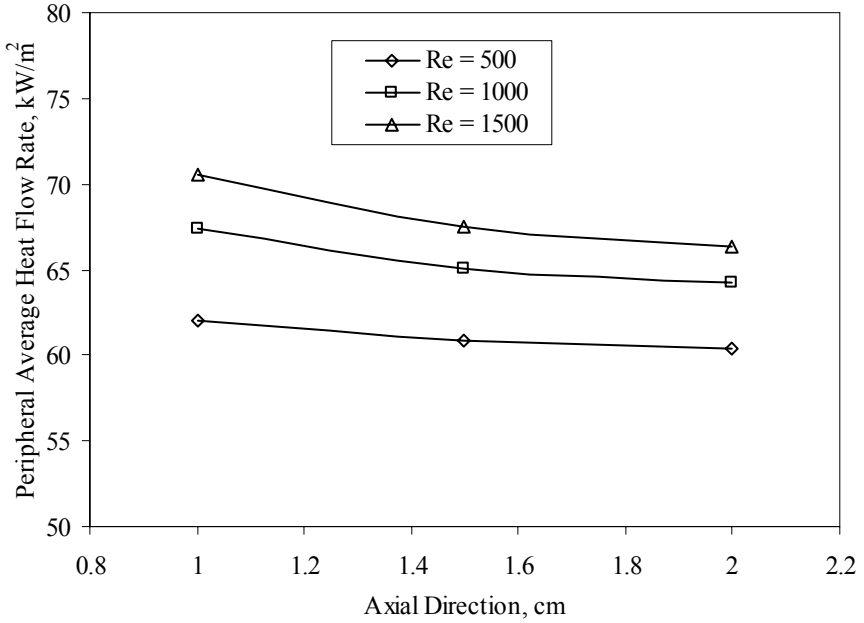

Figure 6.20: Peripheral average heat flow rate along the axial direction at different Reynolds numbers (Silicon, Water + 4% volume fraction of Alumina, d = 0.06 cm)

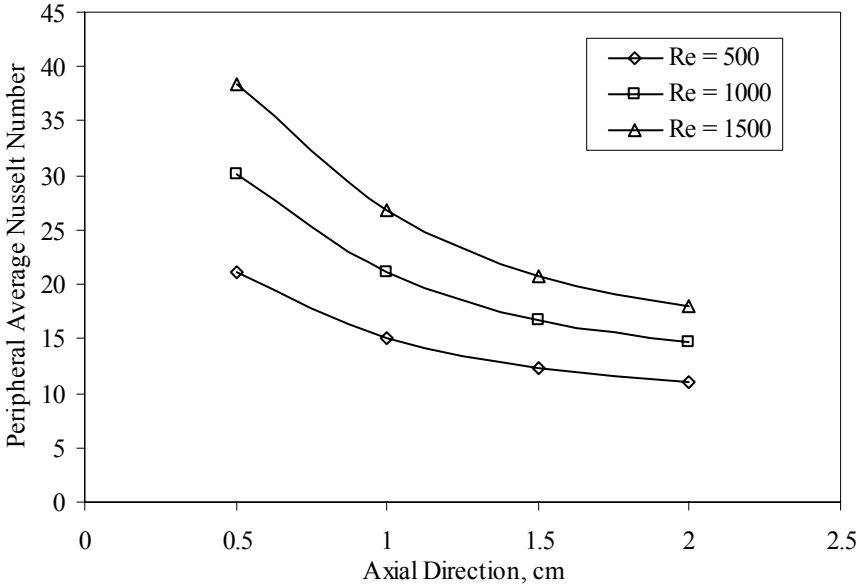

Figure 6.21: Peripheral average Nusselt number along the axial direction at different Reynolds numbers (Silicon, Water + 4% volume fraction of Alumina, d = 0.06 cm)

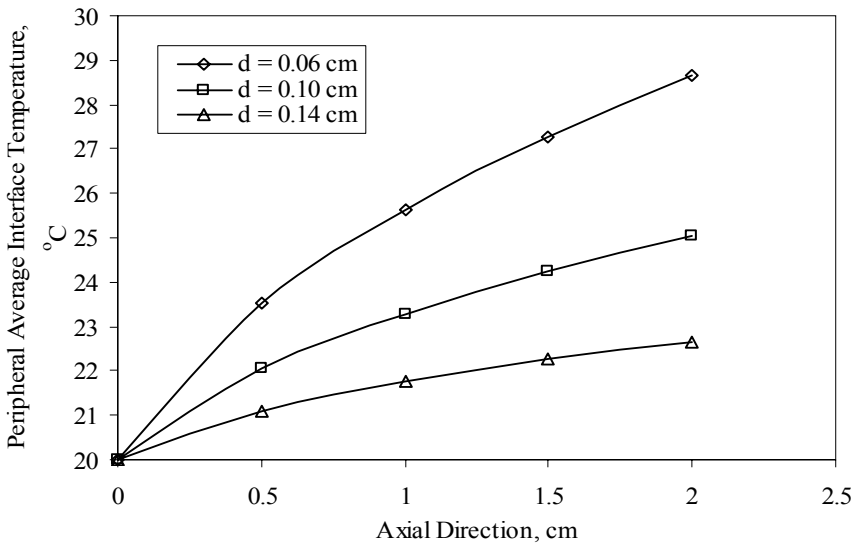

Figure 6.22: Peripheral average interface temperature along the axial direction at different tube diameters (Silicon, Water + 4% volume fraction of Alumina, Re = 500)

interface temperature to increase. It also reduces the volume of the solid substrate. Less solid volume results in less temperature rise in the model. In this case, the interface temperature decreased with higher diameter. Figure 6.23 shows the heat flow rate along the axial direction using different diameters. Higher diameters results in lower fluid velocity which slows down the cooling process. Thus, the heat flow rate reduces with larger diameter. The heat transfer coefficient has similar trend to those of the heat flow rate as shown in figure 6.24 because of its direct dependence. Nusselt number, on the other hand, depends on the heat transfer coefficient and diameter. As the diameter increases, the heat transfer coefficient decreases. This decrease is not enough to overcome the diameter increase. Thus Nusselt number increases with the diameter increase as shown in figure 6.25. This is also the reason why the change of Nusselt number is smaller in ratio than those of heat transfer coefficient.

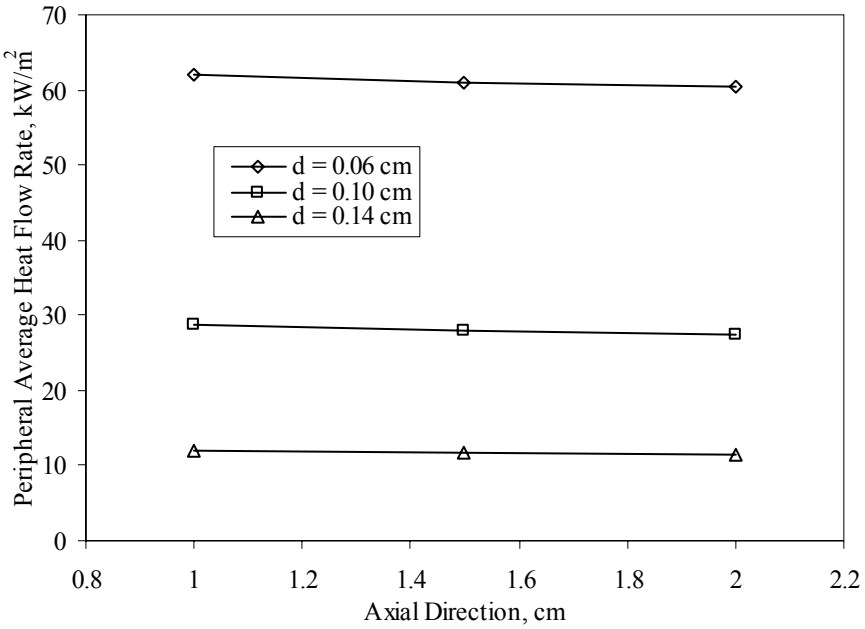

Figure 6.23: Peripheral average heat flow rate along the axial direction at different tube diameters (Silicon, Water + 4% volume fraction of Alumina, Re = 500)

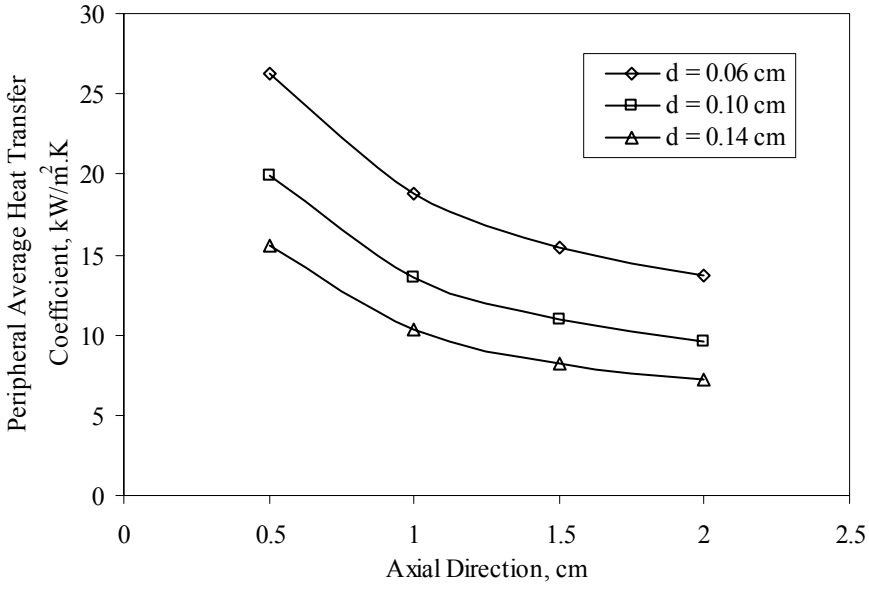

Figure 6.24: Peripheral average heat transfer coefficient along the axial direction at different tube diameters (Silicon, Water + 4% volume fraction of Alumina, Re = 500)

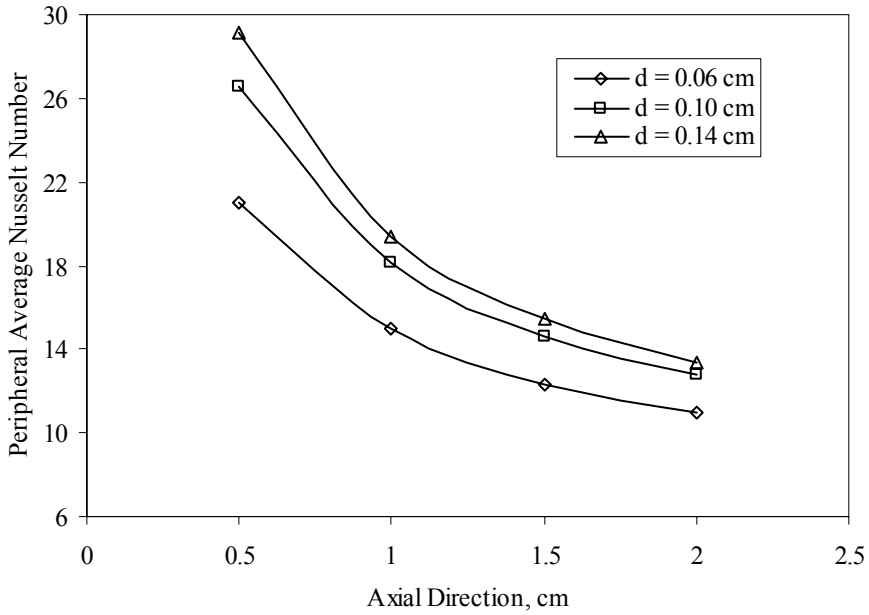

Figure 6.25: Peripheral average Nusselt number along the axial direction at different tube diameters (Silicon, Water + 4% volume fraction of Alumina, Re = 500)

6.4 Conclusions

Grid test was performed for the nanofluid system to select an appropriate meshing. The model was simulated and solved for the velocity and temperature distribution. The results were presented in terms of the interface temperature, heat flow rate, and Nusselt number along the axial direction and at different parameters. The interface temperature increased along the axial direction while the heat flow rate decreased. Nusselt number, on the other hand, decreased along the axial direction. Angular analysis was carried out to understand the effect of one-sided heating boundary condition. It showed that the heat flow rate and the Nusselt number are higher on the side of the tube where it is closer to the heated edge. Increasing the volumetric fraction of the nanoparticles decreased the interface temperature and the heat flow rate as well as

Nusselt number. Stainless steel has a higher interface temperature but lower heat flow rate and Nusselt number than the Silicon. The increase in the Reynolds number decreases the interface temperature but increases the heat flow rate and Nusselt number. Larger diameters decreased the interface temperature and the heat flow rate. Nusselt number depends on the heat flow rate and diameter. The increase in diameter overcomes the decrease in the heat transfer coefficient and increases Nusselt number.

Chapter 7 – Steady State Analysis of Hydronic Snow Melting System

7.1 Mathematical Model

The problem in hand is a hydronic snow melting system. It consists of stainless steel pipe embedded in a concrete slab exposed to snow weather condition. Hot fluid is passing through the pipe to heat the slab and melt the snow accumulated. The slab is mounted over a soil ground. Because of the symmetry in the system, only half of one pipe is modeled. To consider the heat loss to the ground it was assumed to be of height ten times the height of the concrete slab. The assumption of isothermal boundary condition at the bottom of the ground is now valid. The symmetry lines also have isothermal boundary condition. Figure 7.1 shows the model to be studied. The model has a slab width of 15 cm and height of 12 cm. The depth of the ground was considered to be ten times of the slab height (120 cm) to insure taking into account the heat loss to the ground. The governing equations for the conservation of mass, momentum, and energy in the liquid region are [45]:

$$\frac{\partial V_r}{\partial r}+\frac{1}{r}V_r+\frac{1}{r}\frac{\partial V_\phi}{\partial \phi}+\frac{\partial V_z}{\partial z}=0 \tag{1}$$

$$\left(V_r\frac{\partial V_r}{\partial r}+\frac{V_\phi}{r}\frac{\partial V_r}{\partial \phi}+V_z\frac{\partial V_r}{\partial z}-\frac{1}{r}V_\phi^2\right)=-\frac{1}{\rho_f}\frac{\partial p}{\partial r}+ \\ \left(\nu+\nu_t\right)\left[\frac{1}{r}\frac{\partial}{\partial r}\left(r\frac{\partial V_r}{\partial r}\right)+\frac{1}{r^2}\frac{\partial}{\partial \phi}\left(\frac{\partial V_r}{\partial \phi}\right)+\frac{\partial}{\partial z}\left(\frac{\partial V_r}{\partial z}\right)-\frac{V_r}{r^2}-\frac{2}{r^2}\frac{\partial V_\phi}{\partial \phi}\right] \tag{2}$$

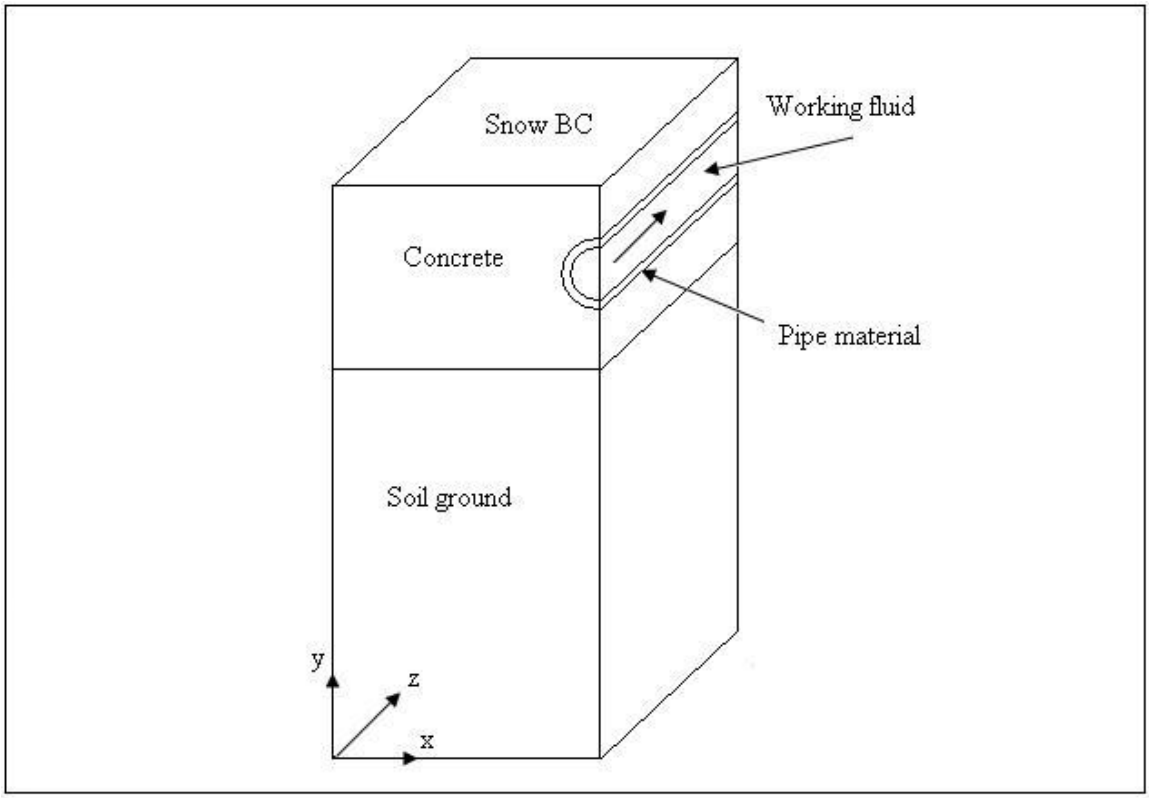

Figure 7.1: The three dimensional snow melting system model for steady state analysis

$$\left(V_r\frac{\partial V_\phi}{\partial r}+\frac{V_\phi}{r}\frac{\partial V_\phi}{\partial \phi}+V_z\frac{\partial V_\phi}{\partial z}-\frac{V_rV_\phi}{r}\right)=-\frac{1}{\rho_f r}\frac{\partial p}{\partial \phi}+$$
$$(\nu+\nu_t)\left[\frac{1}{r}\frac{\partial}{\partial r}\left(r\frac{\partial V_\phi}{\partial r}\right)+\frac{1}{r^2}\frac{\partial}{\partial \phi}\left(\frac{\partial V_\phi}{\partial \phi}\right)+\frac{\partial}{\partial z}\left(\frac{\partial V_\phi}{\partial z}\right)-\frac{V_\phi}{r^2}+\frac{2}{r^2}\frac{\partial V_r}{\partial \phi}\right] \quad (3)$$

$$\left(V_r\frac{\partial V_z}{\partial r}+\frac{V_\phi}{r}\frac{\partial V_z}{\partial \phi}+V_z\frac{\partial V_z}{\partial z}\right)=-\frac{1}{\rho_f}\frac{\partial p}{\partial z}+$$
$$(\nu+\nu_t)\left[\frac{1}{r}\frac{\partial}{\partial r}\left(r\frac{\partial V_z}{\partial r}\right)+\frac{1}{r^2}\frac{\partial}{\partial \phi}\left(\frac{\partial V_z}{\partial \phi}\right)+\frac{\partial}{\partial z}\left(\frac{\partial V_z}{\partial z}\right)\right] \quad (4)$$

The k-ε model was used for simulation of turbulence. In this model, equations governing the conservation of turbulence kinetic energy and its rate of dissipation were solved. These equations can be expressed as:

$$\left(V_r\frac{\partial k}{\partial r}+\frac{V_\phi}{r}\frac{\partial k}{\partial \phi}+V_z\frac{\partial k}{\partial z}\right)=$$
$$\left[\frac{1}{r}\frac{\partial}{\partial r}\left(\left(\nu+\frac{\nu_t}{\sigma_k}\right)r\frac{\partial k}{\partial r}\right)+\frac{1}{r^2}\frac{\partial}{\partial \phi}\left(\left(\nu+\frac{\nu_t}{\sigma_k}\right)\frac{\partial k}{\partial \phi}\right)+\frac{\partial}{\partial z}\left(\left(\nu+\frac{\nu_t}{\sigma_k}\right)\frac{\partial k}{\partial z}\right)\right] \quad (5)$$
$$+\nu_t\left[\left(\frac{1}{r}\frac{\partial V_r}{\partial \phi}\right)^2+\left(\frac{\partial V_r}{\partial z}\right)^2+\left(\frac{\partial V_\phi}{\partial r}-\frac{V_\phi}{r}\right)^2+\left(\frac{\partial V_\phi}{\partial z}\right)^2+\left(\frac{\partial V_z}{\partial r}\right)^2+\left(\frac{1}{r}\frac{\partial V_z}{\partial \phi}\right)^2\right]-\varepsilon$$

$$\left(V_r\frac{\partial \varepsilon}{\partial r}+\frac{V_\phi}{r}\frac{\partial \varepsilon}{\partial \phi}+V_z\frac{\partial \varepsilon}{\partial z}\right)=-C_2\frac{\varepsilon^2}{k}+$$
$$\left[\frac{1}{r}\frac{\partial}{\partial r}\left(\left(\nu+\frac{\nu_t}{\sigma_\varepsilon}\right)r\frac{\partial \varepsilon}{\partial r}\right)+\frac{1}{r^2}\frac{\partial}{\partial \phi}\left(\left(\nu+\frac{\nu_t}{\sigma_\varepsilon}\right)\frac{\partial \varepsilon}{\partial \phi}\right)+\frac{\partial}{\partial z}\left(\left(\nu+\frac{\nu_t}{\sigma_\varepsilon}\right)\frac{\partial \varepsilon}{\partial z}\right)\right] \quad (6)$$
$$+C_1\frac{\varepsilon}{k}\nu_t\left[\left(\frac{1}{r}\frac{\partial V_r}{\partial \phi}\right)^2+\left(\frac{\partial V_r}{\partial z}\right)^2+\left(\frac{\partial V_\phi}{\partial r}-\frac{V_\phi}{r}\right)^2+\left(\frac{\partial V_\phi}{\partial z}\right)^2+\left(\frac{\partial V_z}{\partial r}\right)^2+\left(\frac{1}{r}\frac{\partial V_z}{\partial \phi}\right)^2\right]$$

where $\nu_t=C_\mu k^2/\varepsilon$ (7)

The empirical constants appearing in equations (5) to (7) are given by the following values, $C_\mu = 0.09$, $C_1 = 1.44$, $C_2 = 1.92$, $\sigma_k = 1.0$, $\sigma_\varepsilon = 1.3$. The energy equation in the fluid region is:

$$\left(V_r\frac{\partial T_f}{\partial r}+\frac{V_\phi}{r}\frac{\partial T_f}{\partial \phi}+V_z\frac{\partial T_f}{\partial z}\right)=\left(\alpha_f+\frac{\nu_t}{\mathrm{Pr}_t}\right)\left[\frac{\partial^2 T_f}{\partial r^2}+\frac{1}{r}\frac{\partial T_f}{\partial r}+\frac{1}{r^2}\frac{\partial^2 T_f}{\partial \phi^2}+\frac{\partial^2 T_f}{\partial z^2}\right] \quad (8)$$

Considering constant thermal conductivity, the energy conservation equation in the solid region is [46]:

$$\left[\frac{\partial^2 T_s}{\partial x^2}+\frac{\partial^2 T_s}{\partial y^2}+\frac{\partial^2 T_s}{\partial z^2}\right]=0 \quad (9)$$

Note that a cylindrical coordinate system was used to model convection within the circular tube while a cartesian coordinate system was used to model conduction within the solid substrate material.

Equations (1) to (6) are subject to the following boundary conditions:

At z = 0, $0 \le r < d/2$: $$V_r = 0, V_\phi = 0, V_z = V_{z,in}, T_f = T_{f,in} \quad (10)$$

At z = 0, $r \ge d/2$, $0 < x < W$, $0 < y < H$: $$\frac{\partial T_s}{\partial z} = 0 \quad (11)$$

At z = L, r < d/2: $$p = 0 \quad (12)$$

At z = L, $r \ge d/2$, $0 < x < W$, $0 < y < H$: $$\frac{\partial T_s}{\partial z} = 0 \quad (13)$$

At x = W, $(H-d)/2 \le y \le (H+d)/2$, $0 \le z \le L$: $$V_\phi = 0, \frac{\partial V_r}{\partial x} = 0, \frac{\partial V_z}{\partial x} = 0, \frac{\partial T_f}{\partial x} = 0 \quad (14)$$

At x = W, $-E \le y \le (H-d)/2$, $0 \le z \le L$: $$\frac{\partial T_s}{\partial x} = 0 \quad (15)$$

At x = W, $(H+d)/2 \le y \le H$, $0 \le z \le L$: $$\frac{\partial T_s}{\partial x} = 0 \quad (16)$$

At x = 0, $-E \le y \le H$, $0 \le z \le L$: $$\frac{\partial T_s}{\partial x} = 0 \quad (17)$$

At y = -E, $0 \le x \le W$, $0 \le z \le L$: $$\frac{\partial T_s}{\partial y} = 0 \quad (18)$$

At y = H, $0 \le x \le W$, $0 \le z \le L$: $$\frac{\partial T_s}{\partial y} = 0 \quad (19)$$

At $0 \le z \le L$, r = d/2: $$V_r = 0, V_\phi = 0, V_z = 0, T_f = T_s, k_f \frac{\partial T_f}{dr} = k_s \frac{\partial T_s}{dr} \quad (20)$$

7.2 Numerical Simulation and Parametric Study

The governing equations along with the boundary conditions were solved using the Galerkin finite element method. An iterative procedure was used to arrive at the solution for the velocity and temperature fields. The solution was considered converged

when the field values did not change from one iteration to the next, and the residuals for each variable became negligible.

This study is a parametric study that has an original case and several other cases to study the effect of each parameter. In each case only one parameter is changed. The parameters to be changed are the working fluid, Reynolds number, inlet fluid temperature, pipe diameter and pipe spacing. The working fluid for the original case is water and the fluid was considered turbulent at Reynolds number = 3000. Fluid entered at 80 ^{o}C to a ¾ in. stainless steel pipe. The spacing was taken as 15 cm. The working fluid was changed to Ethylene Glycol in one case. Variable properties were used for the Ethylene Glycol while water properties were considered constant. Reynolds number was increased to 5000 and the inlet fluid temperature was changed to 60 ^{o}C. The pipe diameter was changed to 1.0 in. keeping the Reynolds number constant. Finally, the spacing was increased to 20 cm.

7.3 Results and Discussion

Studying the results for the temperature distribution in the model one can calculate the heat flow rate at various locations in the model. The following figures show the results of all cases with the effect of each parameter. Figures 7.2 to 7.5 represent the original case. Figure 7.2 shows the heat flow rate along the angular direction. It is clear that the heat flow rate is higher at the top of the pipe and lower at the bottom. This is because the top of the pipe is facing the snow boundary condition which causes higher temperature difference resulting in higher heat flow rate. Notice that the heat flow rate drops along the axial direction. This is a direct result for the drop of the fluid temperature

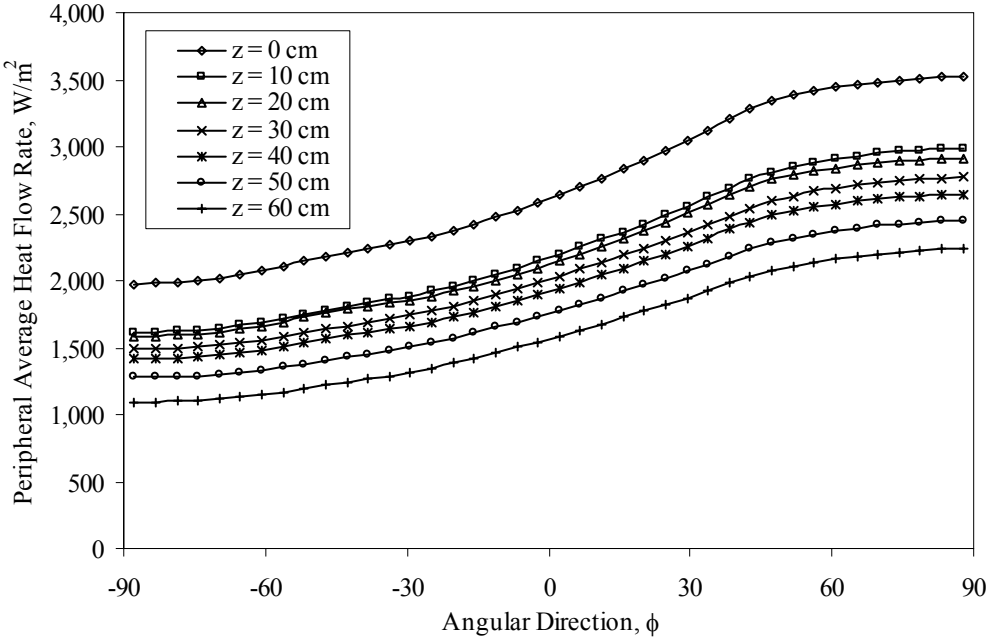

Figure 7.2: Heat flow rate at the outer pipe surface along the angular direction

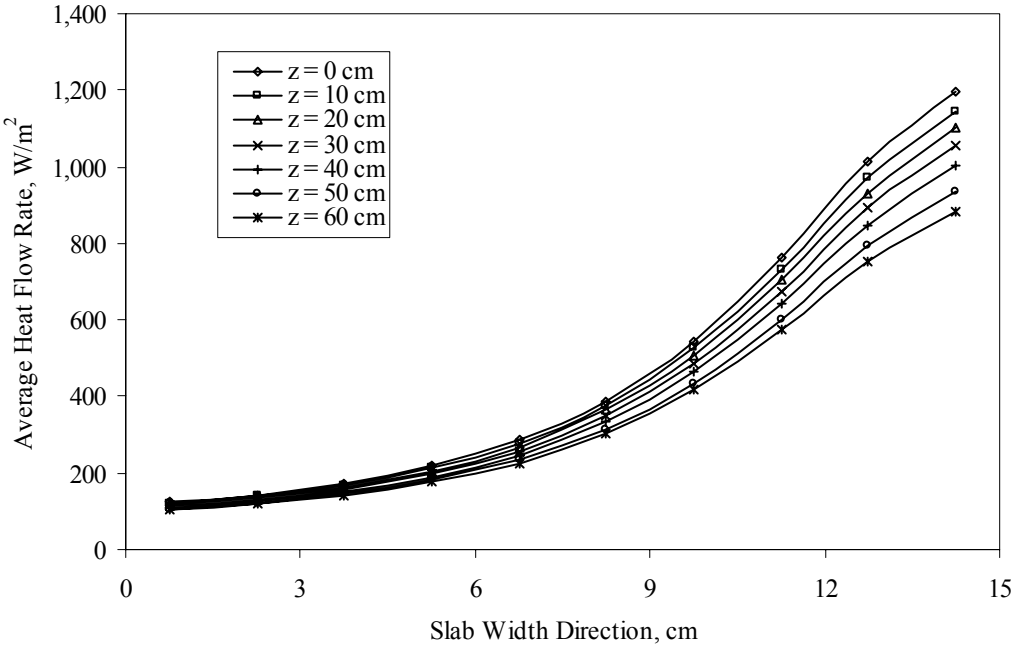

Figure 7.3: Heat flow rate at the snow boundary surface along the width of the slab

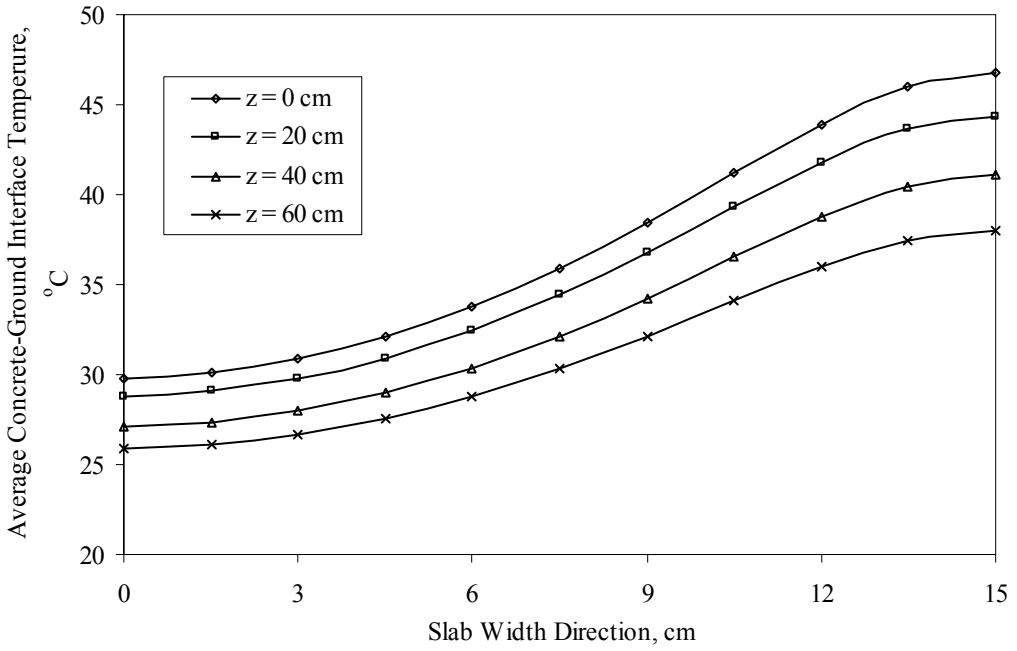

Figure 7.4: Average temperature at the concrete-ground interface along the width of the slab

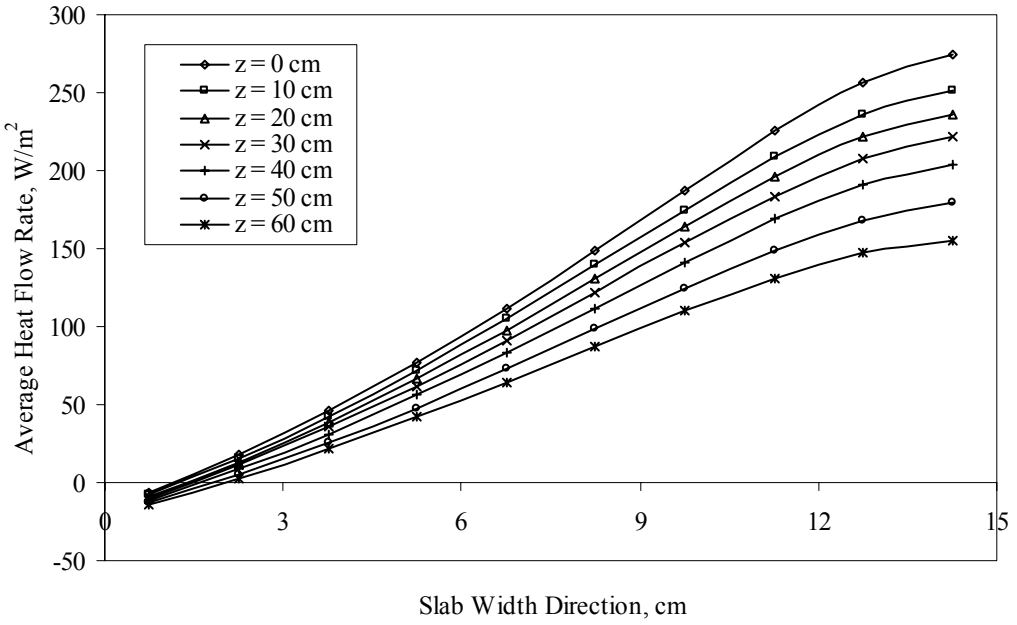

Figure 7.5: Heat flow rate at the concrete-ground interface along the width of the slab

along the axial direction of the pipe due to heat rejection. Figure 7.3 shows the heat flow rate at the snow boundary condition along the width of the slab. It is obvious that the heat flow rate is higher at the snow surface where it is closer to the pipe (x = 15 cm). This is because that location is closer to the heat source, hot fluid. It is also shown that the heat flow rate drops in the axial direction. This is a direct result for the drop of the fluid temperature axially. Figure 7.4 shows the interface temperature at the concrete-ground interface along the width of slab. The temperature is higher at locations closer to the pipe and it is decreasing along the axial direction. Figure 7.5 is the heat flow rate at the concrete-ground interface along the width of slab. The heat flow rate is higher at locations closer to the pipe because it is closer to the heat source. Notice that it becomes a negative value at the midway between two pipes. This is because the heat flow is escaping through the space between two pipes to support the snow melting process. Using less spacing or inlet temperature may not allow it.

The above figures were for the original case explained above. To study the effect of each parameter alone, several cases were studied where only one parameter was changed for each case while the rest are kept constant. Figures present the results for all cases compared to the original one. Figures 7.6 to 7.7 represent the interface temperature at the inner pipe surface and the fluid bulk temperature along the axial direction at different parameters.

Figure 7.6 shows the average interface temperature along the axial direction. Ethylene Glycol has a slightly higher density and very high viscosity compared to water. The ratio of density to viscosity for water is 7 times that of Ethylene Glycol. This means for the same Reynolds number Ethylene Glycol gives much higher fluid velocity. This

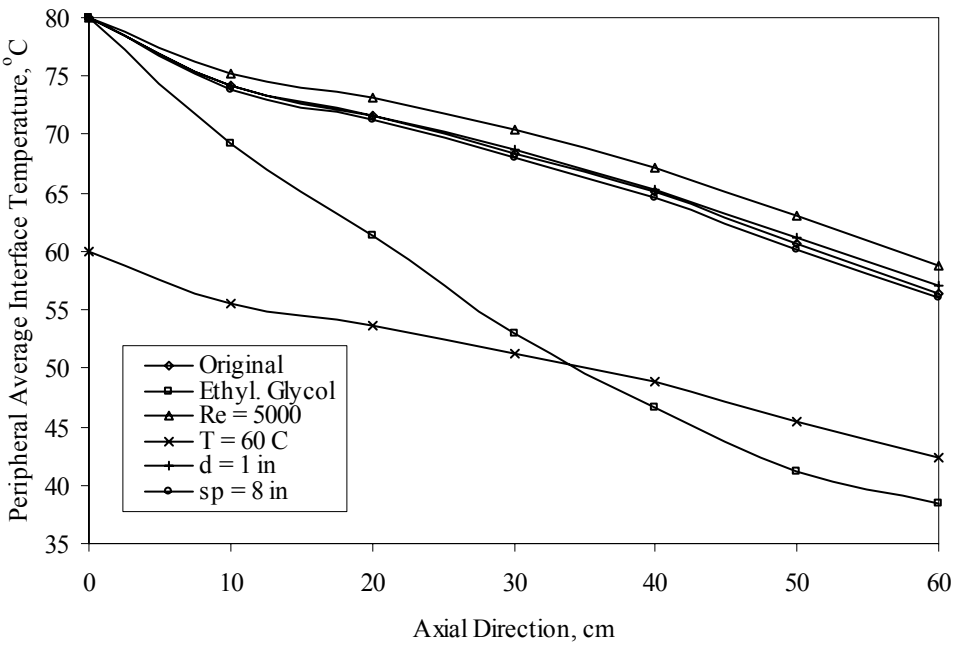

Figure 7.6: Average interface temperature at the inner pipe surface along the axial direction

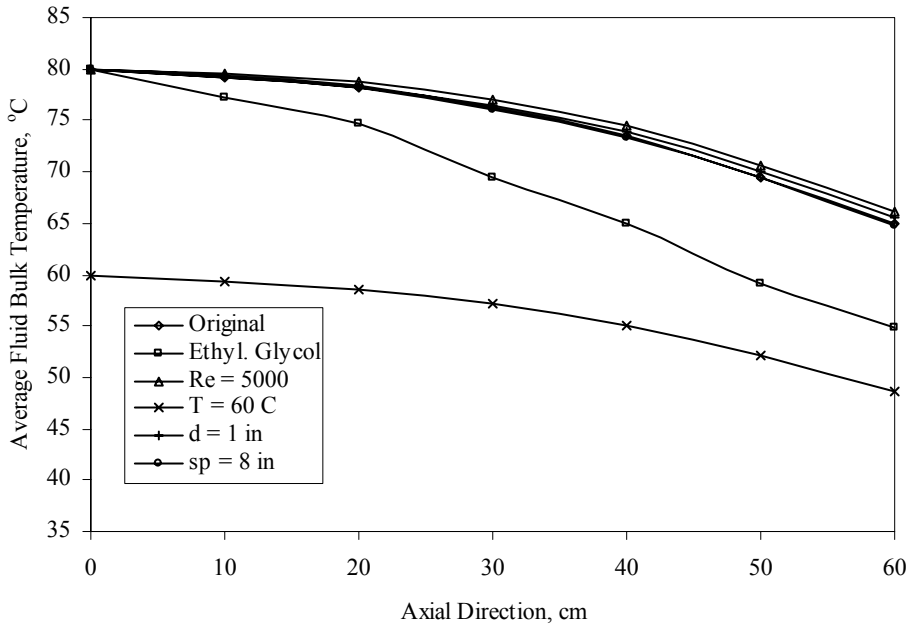

Figure 7.7: Average bulk temperature of the fluid along the axial direction

enhances the convection heat transfer and cause the wall temperature at the inner pipe surface to drop drastically. Higher Reynolds number means higher fluid velocity. The higher velocity enhances the heat flow rate from the fluid to the solid. This results in higher temperature at the inner pipe surface. Lower inlet temperature have same trend as the original case with higher temperature. On the contrary, its rate of decrease is less than the original case along the axial direction. This is because the temperature difference between the lower inlet temperature and the boundary condition is less which results in lower heat flow rate through the system. Enlarging the pipe diameter reduces the solid material which acts as a resistance to the heat flow rate. Larger pipe also increases the pipe surface area enhancing the heat flow rate. This increases the interface temperature at the fluid-pipe interface. Larger spacing, on the other hand, enlarges the solid material and adds more resistance to the heat flow rate. There was a slight decrease in the interface temperature with larger spacing.

Figure 7.7 shows the average bulk temperature along the axial direction. The results of figure 7.7 are similar to those of figure 7.6. Both the bulk and inner interface temperature has similar trend along the axial direction. This is because the interface temperature is a direct result for the change in the fluid bulk temperature. Using Ethylene Glycol is the only case when the bulk temperature has a different slope than the interface temperature because it has different thermal conductivity.

Figure 7.8 shows the average interface temperature along the axial direction at the pipe-concrete surface. It has very similar trend as the average interface temperature at the inner pipe surface in figure 7.6. This is because the pipe is very thin and has high conductivity. Figure 7.9 shows the heat flow rate at the outer pipe surface, pipe-concrete

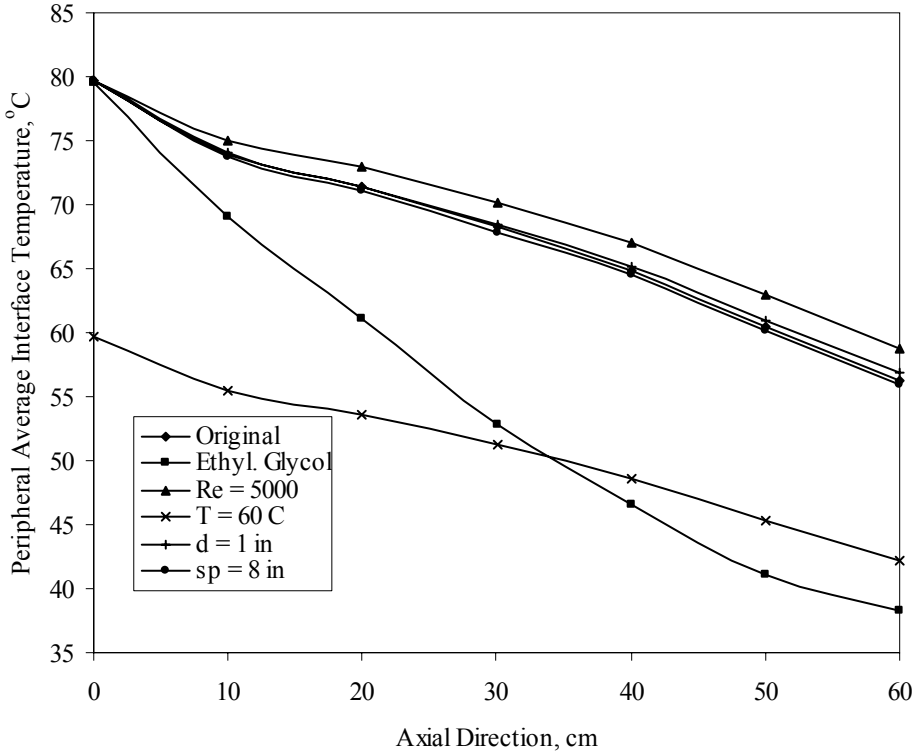

Figure 7.8: Average interface temperature at the outer pipe surface along the axial direction

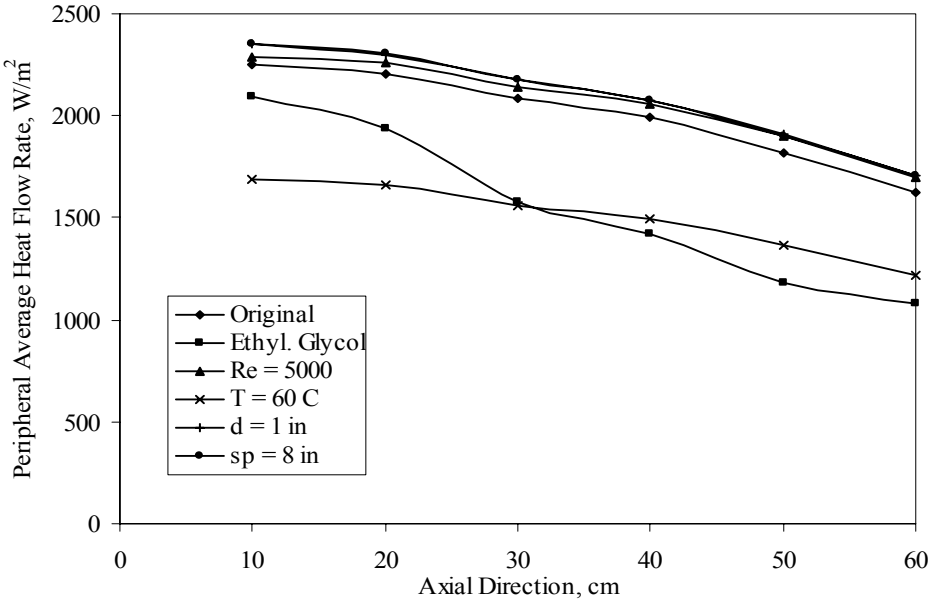

Figure 7.9: Average heat flow rate at the outer pipe surface along the axial direction

interface, along the axial direction. Ethylene Glycol causes smaller temperature gradient in the solid substrate as explained before. Therefore, it decreases the heat flow rate at the interface. For higher Reynolds number the fluid velocity is higher. This increases the heat flow rate from the fluid to the solid. Hence it increases the heat flow rate at the outer pipe surface. Lower inlet temperature gives less temperature gradient in the solid causing the heat flow rate to decrease. It is obvious that the heat flow rate decreases in a lower rate in the axial direction. This is because lower inlet temperature causes less interface-bulk temperature difference and thus reduces the heat flow rate from the working fluid to the system. Larger diameter results in a reduction in the solid volume and an increase the pipe surface area. Both increase in the heat flow rate to the model. Larger spacing between the pipes means more heating load per pipe. This cool down the pipe walls and decreases the pipe wall temperature. This results in a high interface-bulk temperature difference and increases the heat flow rate to the system.

Figure 7.10 shows the average heat flow rate at the snow surface along the axial direction. As explained above Ethylene Glycol decreases the temperature gradient in the substrate. This results in a decrease in the heat flow rate on the snow surface. Higher Reynolds number with higher fluid velocity increases the heat flow rate from the fluid to the solid. The increase in the heat flow rate at the snow surface is a direct result. Lower inlet temperature results in a decrease in the heat flow in the system. This also reflects on the snow surface heat flow. Using larger diameter results in an increase the pipe surface area. This increases the heat flow rate to the snow surface. With larger spacing between the pipes the amount of heat flow is distributed over a larger area reducing the average heat rate per unit area.

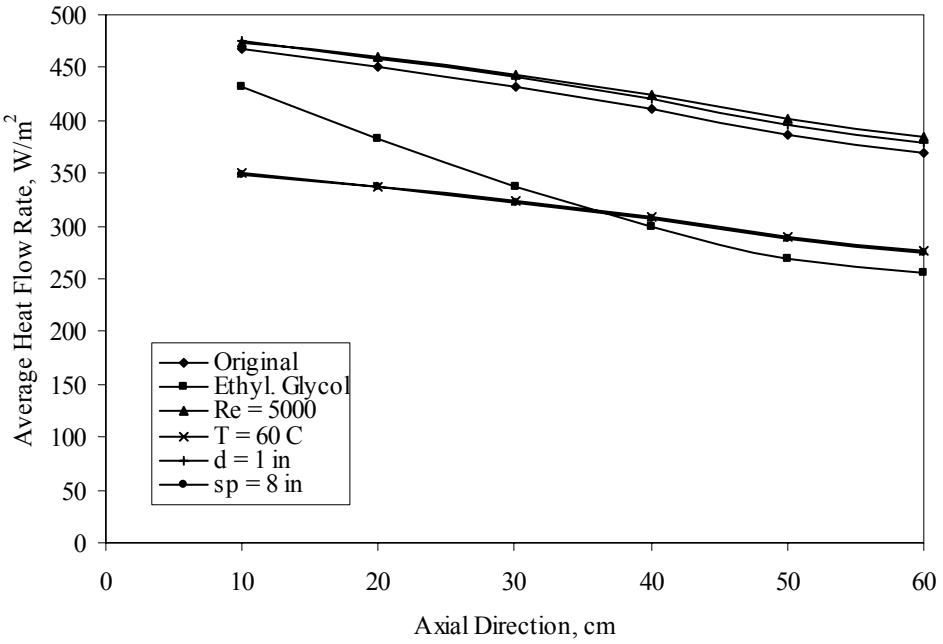

Figure 7.10: Average heat flow rate at the snow surface along the axial direction

. Figure 7.11 shows the average heat flow rate at the ground-concrete interface along the axial direction. This represents the heat loss to the ground. Ethylene Glycol causes smaller temperature gradient in the solid. This results in a decrease in the heat flow rate to the ground. Higher Reynolds number with higher fluid velocity increases the heat flow rate from the fluid to the solid and hence the heat flow rate to the system. The increase in the heat flow rate to the ground is a direct result. Lower inlet temperature results in a decrease in the heat flow in the system. This also reflects on the heat loss to the ground. As explained above the increase in diameter increases the heat flow rate. This increases the heat loss to the ground as well. Larger spacing increases the heat flow rate from as explained above. It also gives space to the heat flow to pass through the pipes to the top. The increase in the heat flow rate overcomes the heat amount passes to the top between the pipes and increases the heat loss to the ground.

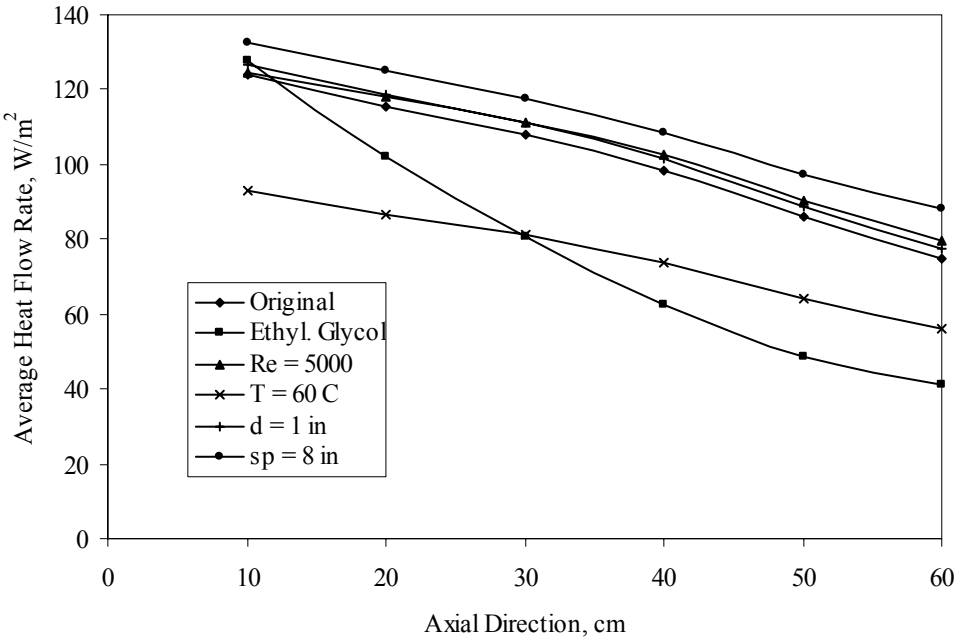

Figure 7.11: Average heat flow rate lost to the ground along the axial direction

7.4 Conclusions

Three dimensional steady state snow melting model was developed. A numerical scheme was applied to come up with the heat flow rate calculations within the system. Parametric study was carried out to understanding the effect of different parameters. The heat flow rate was higher at the top of the pipe where it faces the snow boundary condition. Using Ethylene Glycol, as the working fluid, results in lower heat flow rate at the fluid interface and the snow boundary condition. The increase in Reynolds number increases the heat flow rate at the fluid interface and the snow boundary condition. Lower inlet temperature results in less heat flow rate at the fluid interface and the snow boundary condition. Larger diameter for the same Reynolds number results in larger heat flow rate at the fluid interface and snow boundary condition. Larger spacing between

pipes increases the heat flow rate at the fluid interface but reduces it at the snow surface. The heat loss to the ground was analyzed and plotted. Ethylene Glycol and lower inlet temperature decrease the heat loss to the ground. On the other hand, higher Reynolds number, larger diameter and spacing increase the heat loss to the ground.

Chapter 8 – Transient Analysis of Hydronic Snow Melting System

8.1 Mathematical Model

The problem in hand is a hydronic snow melting system. It consists of stainless steel pipe embedded in a concrete slab exposed to snow weather condition. Hot fluid is passing through the pipe to heat the slab and melt the snow accumulated. The slab is mounted over a soil ground. Because of the symmetry in the system, only half of one pipe is modeled. To consider the heat loss to the ground it was assumed to be of height ten times the height of the concrete slab. The assumption of isothermal boundary condition at the bottom of the ground is now valid. The symmetry lines also have isothermal boundary condition. Figure 8.1 shows the model to be studied.

The model in figure 8.1 has a width, or pipe spacing, of 15 cm and height of 12 cm. The pipe depth was at the center of the model at 6 cm. The depth of the ground was considered to be ten times of the slab height (120 cm) to insure taking into account the heat loss to the ground.

The governing equations for the conservation of mass, momentum, and energy in the liquid region are [45]:

$$\frac{\partial V_r}{\partial r} + \frac{1}{r} V_r + \frac{1}{r} \frac{\partial V_\phi}{\partial \phi} + \frac{\partial V_z}{\partial z} = 0 \qquad (1)$$

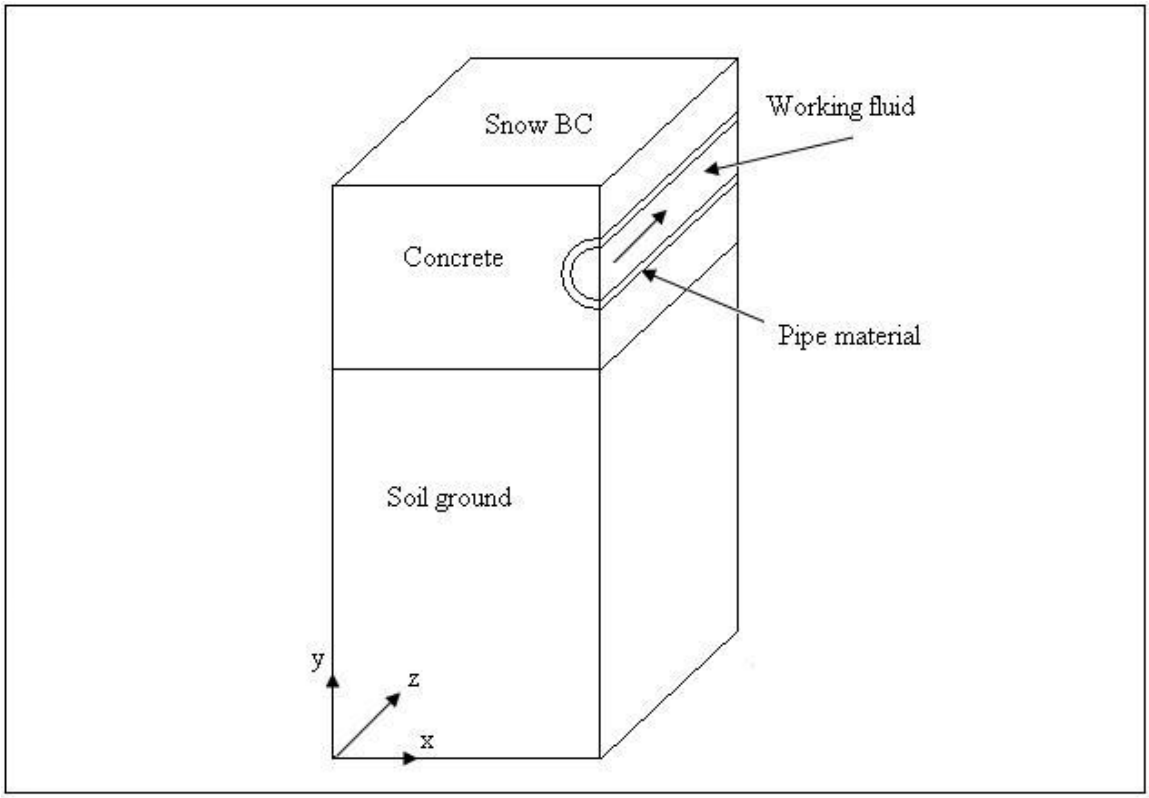

Figure 8.1: The three dimensional snow melting system model for transient analysis

$$\frac{\partial V_r}{\partial t}+\left(V_r\frac{\partial V_r}{\partial r}+\frac{V_\phi}{r}\frac{\partial V_r}{\partial \phi}+V_z\frac{\partial V_r}{\partial z}-\frac{1}{r}V_\phi^2\right)=-\frac{1}{\rho_f}\frac{\partial p}{\partial r}+$$
$$(\nu+\nu_t)\left[\frac{1}{r}\frac{\partial}{\partial r}\left(r\frac{\partial V_r}{\partial r}\right)+\frac{1}{r^2}\frac{\partial}{\partial \phi}\left(\frac{\partial V_r}{\partial \phi}\right)+\frac{\partial}{\partial z}\left(\frac{\partial V_r}{\partial z}\right)-\frac{V_r}{r^2}-\frac{2}{r^2}\frac{\partial V_\phi}{\partial \phi}\right] \quad (2)$$

$$\frac{\partial V_\phi}{\partial t}+\left(V_r\frac{\partial V_\phi}{\partial r}+\frac{V_\phi}{r}\frac{\partial V_\phi}{\partial \phi}+V_z\frac{\partial V_\phi}{\partial z}-\frac{V_rV_\phi}{r}\right)=-\frac{1}{\rho_f r}\frac{\partial p}{\partial \phi}+$$
$$(\nu+\nu_t)\left[\frac{1}{r}\frac{\partial}{\partial r}\left(r\frac{\partial V_\phi}{\partial r}\right)+\frac{1}{r^2}\frac{\partial}{\partial \phi}\left(\frac{\partial V_\phi}{\partial \phi}\right)+\frac{\partial}{\partial z}\left(\frac{\partial V_\phi}{\partial z}\right)-\frac{V_\phi}{r^2}+\frac{2}{r^2}\frac{\partial V_r}{\partial \phi}\right] \quad (3)$$

$$\frac{\partial V_z}{\partial t}+\left(V_r\frac{\partial V_z}{\partial r}+\frac{V_\phi}{r}\frac{\partial V_z}{\partial \phi}+V_z\frac{\partial V_z}{\partial z}\right)=-\frac{1}{\rho_f}\frac{\partial p}{\partial z}+$$
$$(\nu+\nu_t)\left[\frac{1}{r}\frac{\partial}{\partial r}\left(r\frac{\partial V_z}{\partial r}\right)+\frac{1}{r^2}\frac{\partial}{\partial \phi}\left(\frac{\partial V_z}{\partial \phi}\right)+\frac{\partial}{\partial z}\left(\frac{\partial V_z}{\partial z}\right)\right] \quad (4)$$

The k-ε model was used for simulation of turbulence. In this model, equations governing the conservation of turbulence kinetic energy and its rate of dissipation were solved. These equations can be expressed as:

$$\frac{\partial k}{\partial t}+\left(V_r\frac{\partial k}{\partial r}+\frac{V_\phi}{r}\frac{\partial k}{\partial \phi}+V_z\frac{\partial k}{\partial z}\right)=$$
$$\left[\frac{1}{r}\frac{\partial}{\partial r}\left(\left(\nu+\frac{\nu_t}{\sigma_k}\right)r\frac{\partial k}{\partial r}\right)+\frac{1}{r^2}\frac{\partial}{\partial \phi}\left(\left(\nu+\frac{\nu_t}{\sigma_k}\right)\frac{\partial k}{\partial \phi}\right)+\frac{\partial}{\partial z}\left(\left(\nu+\frac{\nu_t}{\sigma_k}\right)\frac{\partial k}{\partial z}\right)\right] \quad (5)$$
$$+\nu_t\left[\left(\frac{1}{r}\frac{\partial V_r}{\partial \phi}\right)^2+\left(\frac{\partial V_r}{\partial z}\right)^2+\left(\frac{\partial V_\phi}{\partial r}-\frac{V_\phi}{r}\right)^2+\left(\frac{\partial V_\phi}{\partial z}\right)^2+\left(\frac{\partial V_z}{\partial r}\right)^2+\left(\frac{1}{r}\frac{\partial V_z}{\partial \phi}\right)^2\right]-\varepsilon$$

$$\frac{\partial \varepsilon}{\partial t}+\left(V_r\frac{\partial \varepsilon}{\partial r}+\frac{V_\phi}{r}\frac{\partial \varepsilon}{\partial \phi}+V_z\frac{\partial \varepsilon}{\partial z}\right)=-C_2\frac{\varepsilon^2}{k}+$$
$$\left[\frac{1}{r}\frac{\partial}{\partial r}\left(\left(\nu+\frac{\nu_t}{\sigma_\varepsilon}\right)r\frac{\partial \varepsilon}{\partial r}\right)+\frac{1}{r^2}\frac{\partial}{\partial \phi}\left(\left(\nu+\frac{\nu_t}{\sigma_\varepsilon}\right)\frac{\partial \varepsilon}{\partial \phi}\right)+\frac{\partial}{\partial z}\left(\left(\nu+\frac{\nu_t}{\sigma_\varepsilon}\right)\frac{\partial \varepsilon}{\partial z}\right)\right] \quad (6)$$
$$+C_1\frac{\varepsilon}{k}\nu_t\left[\left(\frac{1}{r}\frac{\partial V_r}{\partial \phi}\right)^2+\left(\frac{\partial V_r}{\partial z}\right)^2+\left(\frac{\partial V_\phi}{\partial r}-\frac{V_\phi}{r}\right)^2+\left(\frac{\partial V_\phi}{\partial z}\right)^2+\left(\frac{\partial V_z}{\partial r}\right)^2+\left(\frac{1}{r}\frac{\partial V_z}{\partial \phi}\right)^2\right]$$

where $\nu_t=C_\mu k^2/\varepsilon$ (7)

The empirical constants appearing in equations (5) to (7) are given by the following values, $C_\mu = 0.09$, $C_1 = 1.44$, $C_2 = 1.92$, $\sigma_k = 1.0$, $\sigma_\varepsilon = 1.3$. The energy equation in the fluid region, considering $Pr_t = 1$, is:

$$\frac{\partial T_f}{\partial t}+\left(V_r\frac{\partial T_f}{\partial r}+\frac{V_\phi}{r}\frac{\partial T_f}{\partial \phi}+V_z\frac{\partial T_f}{\partial z}\right)=$$
$$\left(\alpha_f+\frac{\nu_t}{\mathrm{Pr}_t}\right)\left[\frac{\partial^2 T_f}{\partial r^2}+\frac{1}{r}\frac{\partial T_f}{\partial r}+\frac{1}{r^2}\frac{\partial^2 T_f}{\partial \phi^2}+\frac{\partial^2 T_f}{\partial z^2}\right] \quad (8)$$

Considering constant thermal conductivity, the energy conservation equation in the solid region is [46]:

$$\left[\frac{\partial^2 T_s}{\partial x^2}+\frac{\partial^2 T_s}{\partial y^2}+\frac{\partial^2 T_s}{\partial z^2}\right]=\frac{1}{\alpha}\frac{\partial T_s}{\partial t} \tag{9}$$

Note that a cylindrical coordinate system was used to model convection within the circular tube while a cartesian coordinate system was used to model conduction within the solid substrate material.

Equations (1) to (9) are subject to the following boundary conditions:

At t = 0: $T_s = T_f = T_{in}$ (10)

At z = 0, 0 ≤ r < d/2: $V_r = 0, V_\phi = 0, V_z = V_{z,in}, T_f = T_{f,in}$ (11)

At z = 0, r ≥ d/2, 0 < x < W, 0 < y < H: $\frac{\partial T_s}{\partial z} = 0$ (12)

At z = L, r < d/2: $p = 0$ (13)

At z = L, r ≥ d/2, 0 < x < W, 0 < y < H: $\frac{\partial T_s}{\partial z} = 0$ (14)

At x = W, (H-d)/2 ≤ y ≤ (H+d)/2, 0 ≤ z ≤ L: $V_{\theta\phi} = 0, \frac{\partial V_r}{\partial x} = 0, \frac{\partial V_z}{\partial x} = 0, \frac{\partial T_f}{\partial x} = 0$ (15)

At x = W, -E ≤ y ≤ (H-d)/2, 0 ≤ z ≤ L: $\frac{\partial T_s}{\partial x} = 0$ (16)

At x = W, (H+d)/2 ≤ y ≤ H, 0 ≤ z ≤ L: $\frac{\partial T_s}{\partial x} = 0$ (17)

At x = 0, -E ≤ y ≤ H, 0 ≤ z ≤ L: $\frac{\partial T_s}{\partial x} = 0$ (18)

At y = -E, 0 ≤ x ≤ W, 0 ≤ z ≤ L: $\frac{\partial T_s}{\partial y} = 0$ (19)

At y = H, 0 ≤ x ≤ W, 0 ≤ z ≤ L: $\frac{\partial T_s}{\partial y} = 0$ (20)

At $0 \leq z \leq L$, $r = d/2$: $$V_r = 0, V_\phi = 0, V_z = 0, T_f = T_s, k_f \frac{\partial T_f}{dr} = k_s \frac{\partial T_s}{dr} \qquad (21)$$

8.2 Numerical Simulation and Parametric Simulation

The governing equations along with the boundary conditions were solved using the Galerkin finite element method. An iterative procedure was used to arrive at the solution for the velocity and temperature fields. The solution was considered converged when the field values did not change from one iteration to the next, and the residuals for each variable became negligible.

This work is a parametric study that has an original case and several other cases to study the effect of each parameter. In each case only one parameter is changed. The parameters to be changed are the Reynolds number, pipe diameter, pipe depth and pipe spacing. The original case used water as the working fluid and the fluid was considered turbulent at Reynolds number = 3000. Fluid entered at 80 oC to a ¾ in stainless steel pipe. The spacing was taken as 15 cm. Reynolds number was increased to 45000 and 6000 while the pipe diameter was changed to ½ and 1 in keeping the Reynolds number constant. The pipe depth was changed to 3 and 9 cm while pipe spacing was changed to 12 and 9 cm.

8.3 Results and Discussion

To study the transient effect a storm scenario was selected and applied to the model. This provides us with understanding about how the model will perform during a real storm. Another storm was selected with 6 times of the snow fall of the first one to

make sure the model will handle severe storm. Figures 8.2 to 8.6 represent results for the first storm scenario while figures 8.7 to 8.11 represent results for the second storm scenario. The second storm had 6 times the snow fall than the first and lasted for 9 hours longer.

Figure 8.2 shows the average peripheral interface temperature along the axial direction over the storm time length of 5 hours. Two more hours added for both storm scenarios to understand how the model performs after the storm is over. The fluid enters at 80 ^{o}C and cools down along the axial direction because of the storm. The fluid heats up the model over time and thus the interface temperature. Notice that the temperature curve along the axial direction comes into a steady state over the 5 hours storm length. The last tow hours represent the time when the storm is over and the weather condition is removed. The temperature curve increases as the model warms up with the end of the storm. Figure 8.3 shows the heat flow rate at the interface along the axial direction over time. The heat flow rate seems to be constant along the axial direction. This is because both the interface and bulk temperature drop together along the axial direction maintaining constant temperature difference. The transient behavior is a little different where the bulk temperature seems to be increasing more rapidly than the interface temperature causing the heat flow rate at the interface to slow down over time. This could be understood because the interface temperature increasing rate drops with more accumulated snow where the fluid could maintain decent bulk temperature.

Figure 8.4 shows average temperature at the surface along the axial direction over time. The surface temperature is decreasing along the axial direction because the fluid is at higher temperature at the inlet. On the other hand, the surface temperature is increasing

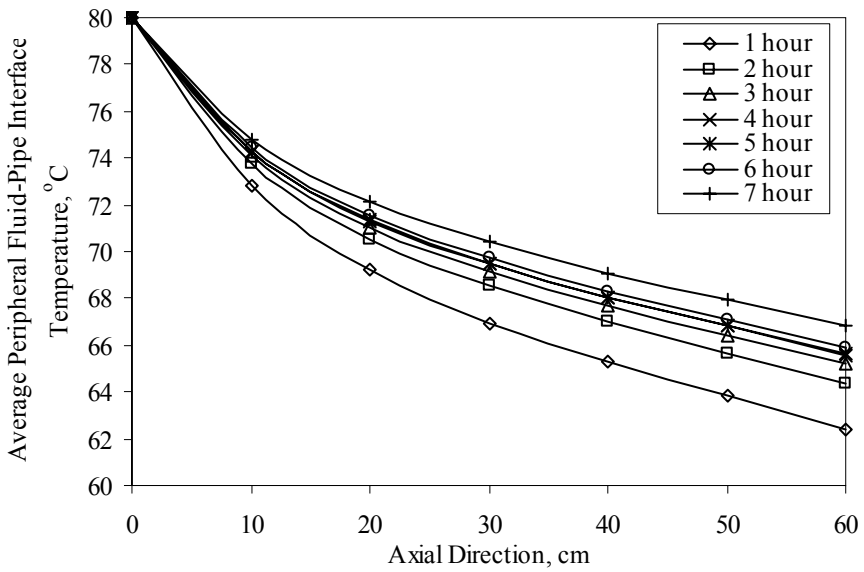

Figure 8.2: Average peripheral interface temperature along axial direction at different times

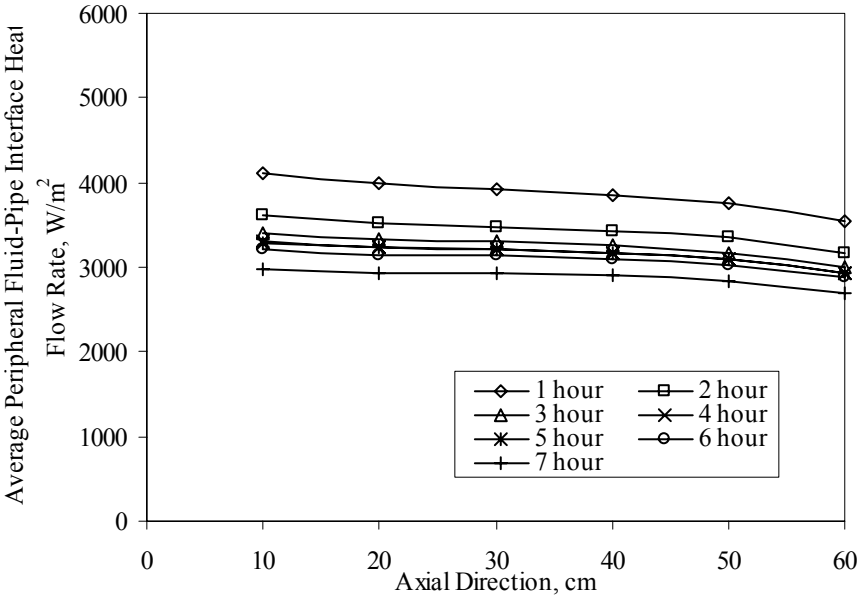

Figure 8.3: Average peripheral interface heat flow rate along axial direction at different times

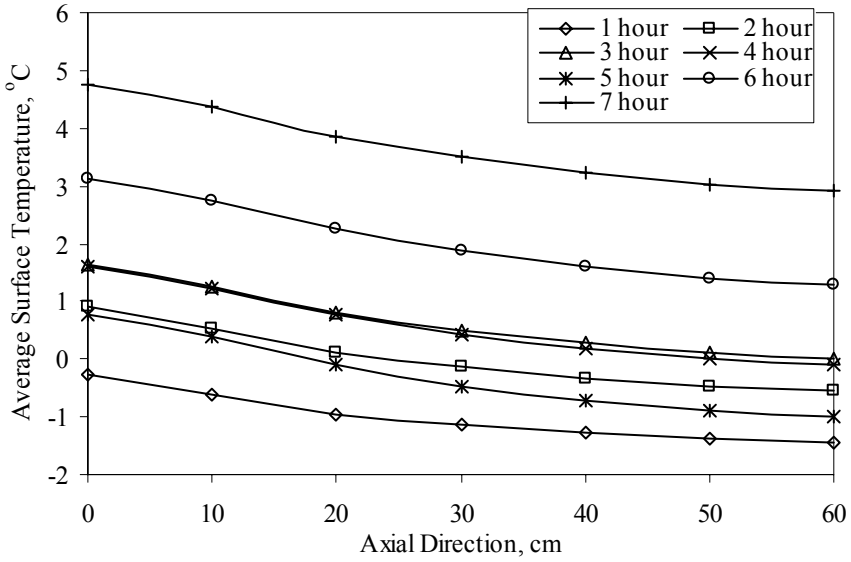

Figure 8.4: Average surface temperature along axial direction at different times

with respect to time. This is because the fluid enters at a temperature high enough to overcome the storm condition and heat up the system and the surface temperature. This could be different if a lower inlet temperature is used or more snow fall occurred. This shows the importance of trying a different storm scenario with more snow fall. Similarly to previous cases, the last tow hours of the time length studied has higher surface temperature as it increases with the end of storm condition. Figure 8.5 shows the average ground interface temperature at the bottom of the concrete slab along the axial direction over time. The ground temperature decreases along the axial direction as the fluid temperature drops. This is because as the fluid temperature drop the heat transfer to the ground decrease reducing temperature at the ground interface. Notice that the rate of ground temperature drop is less than the rate of surface temperature drop along the axial direction. This is because the surface temperature is exposed to the cold weather while

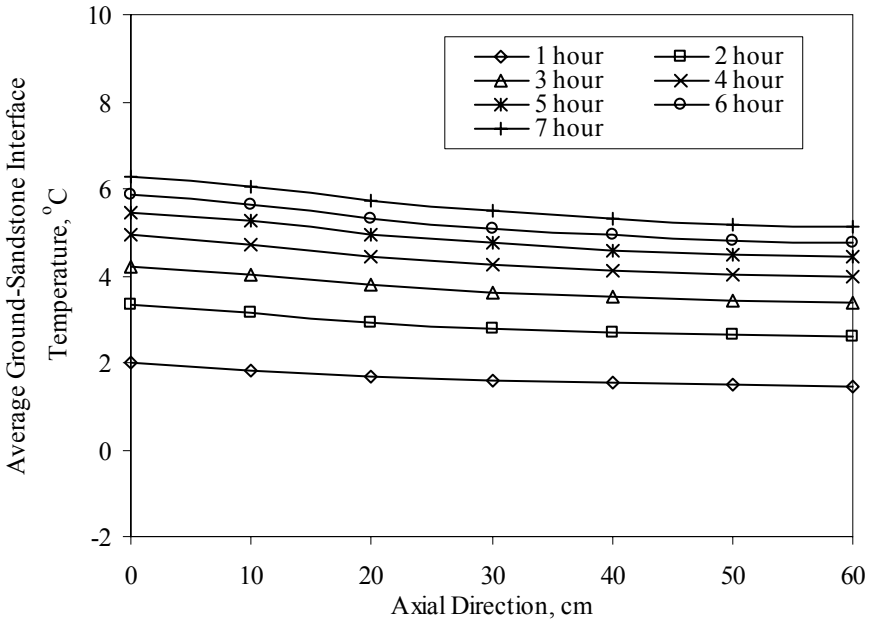

Figure 8.5: Average ground interface temperature along axial direction at different times

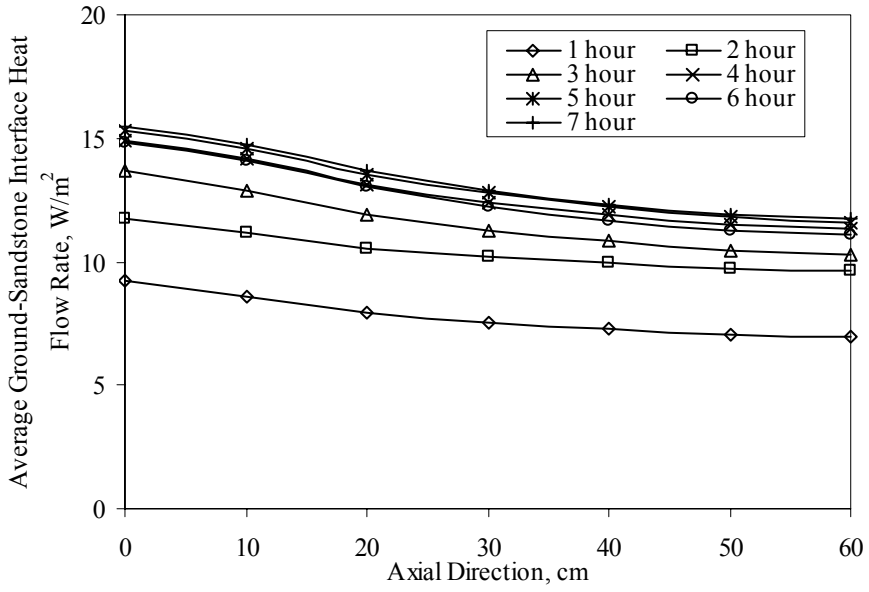

Figure 8.6: Average ground interface heat flow rate along axial direction at different times

the ground is kept warmer under the heated slab. The ground temperature increases with time because of the high inlet temperature that heat up the model. Figure 8.6 shows the average heat flow rate at the ground interface along the axial direction over time. This is the heat loss to the ground. Because the fluid temperature drops along the axial direction the heat flow rate also drops. As the model heat up with time the heat flow rate to the ground increases.

The second storm studied has 6 times the snow fall of the previous storm. It lasted 14 hours and the time length considered 2 more hours to observe the model performance after the storm is over. Figure 8.7 shows the average peripheral interface temperature along the axial direction over time. The fluid inlet temperature used was higher at 95 ^{o}C. This is to study the highest possible inlet temperature use and check if it will give good results. The temperature curve along the axial direction comes into a steady state within the first 2 hours. This could be caused by the severity of storm that cools the model fast enough to reach the steady state in a short time. Steady state occurred fast in both axial direction and over time. It is also noticed that the temperature drop along the channel is lesser than the previous storm which means using 95 ^{o}C overcome six times the snow fall of the previous storm. The temperature curve increases as the model warms up with the end of the storm. Figure 8.8 shows the heat flow rate at the interface along the axial direction over time. The heat flow rate is constant along the axial direction because both the interface and bulk temperature drop together along the axial direction maintaining constant temperature difference. Because of the storm condition the heat flow rate from the fluid to the model slows down. Figure 8.9 shows average temperature at the surface along the axial direction over time. The surface temperature is decreasing along the axial

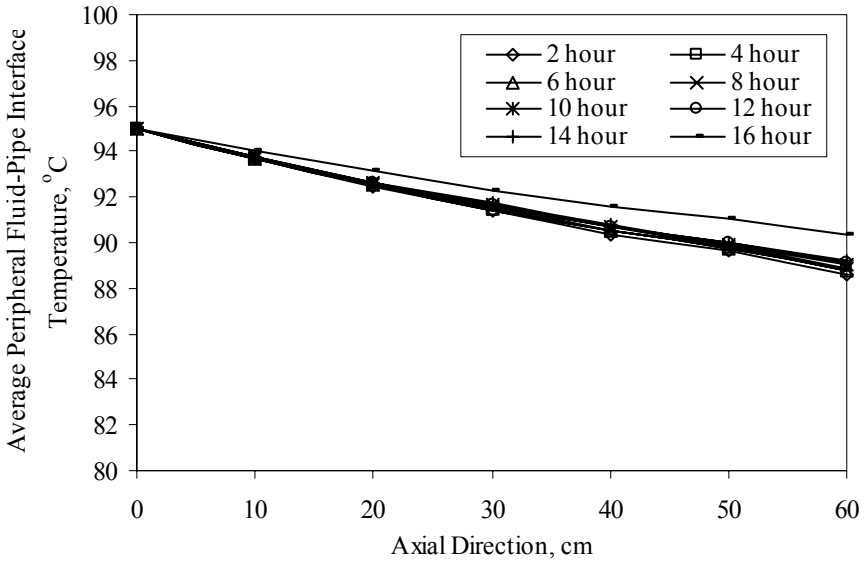

Figure 8.7: Average peripheral interface temperature along axial direction at different times

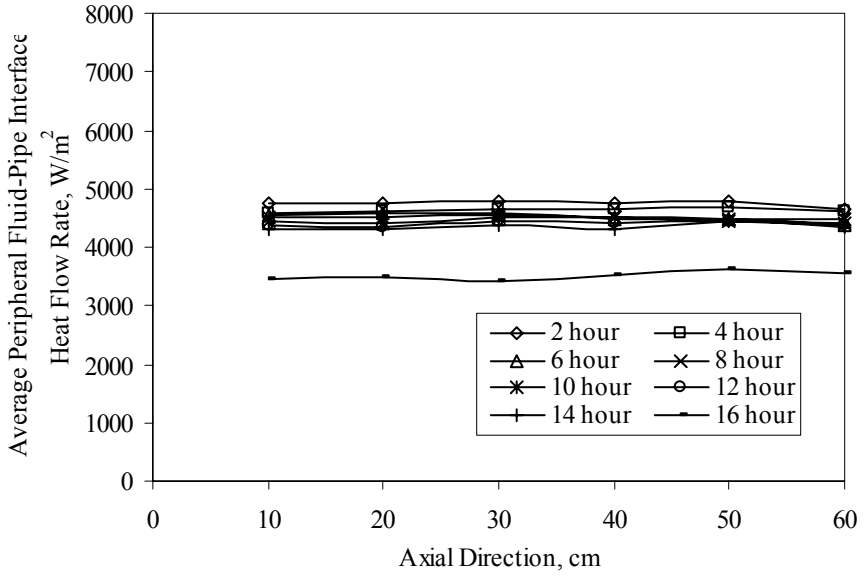

Figure 8.8: Average peripheral interface heat flow rate along axial direction at different times

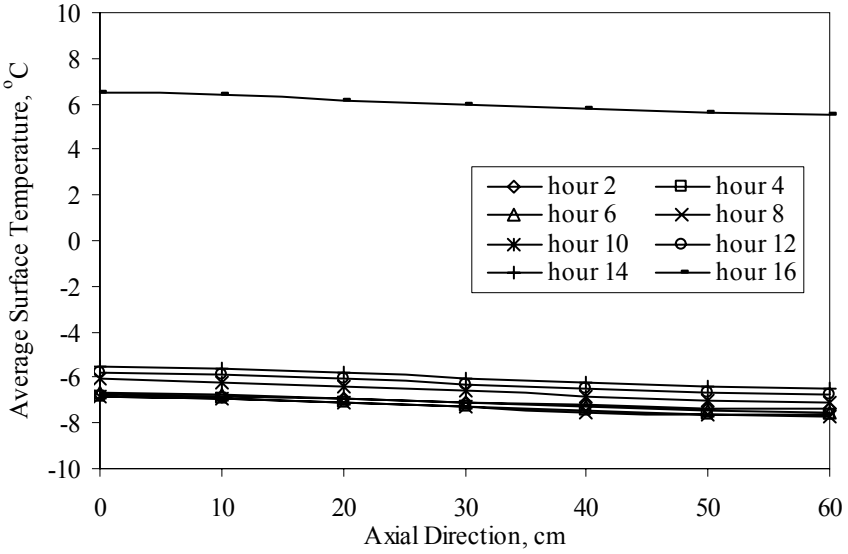

Figure 8.9: Average surface temperature along axial direction at different times

direction because the fluid is at higher temperature at the inlet. Comparing the rate of decrease in the surface temperature along the axial direction for both storm scenarios shows that the rate of decrease is less for the second storm. This also shows that using inlet temperature of 95 ^{o}C was sufficient to warm up the concrete slab. The surface temperature maintains almost constant value with respect to time. This also supports our conclusion of sufficient inlet temperature. One can see how fast the surface temperature rises at the last tow hours when the storm ends. Figure 8.10 shows the average ground interface temperature at the bottom of the concrete slab along the axial direction over time. The ground temperature is almost constant along the axial direction with a slight decrease as the fluid temperature drops. This could be explained by the small drop in the channel temperature along the axial direction caused by the fact that the inlet temperature at 95 ^{o}C overcomes the accumulated snow for the second storm, which is six times the first storm scenario. The ground temperature increases with time because of the high inlet

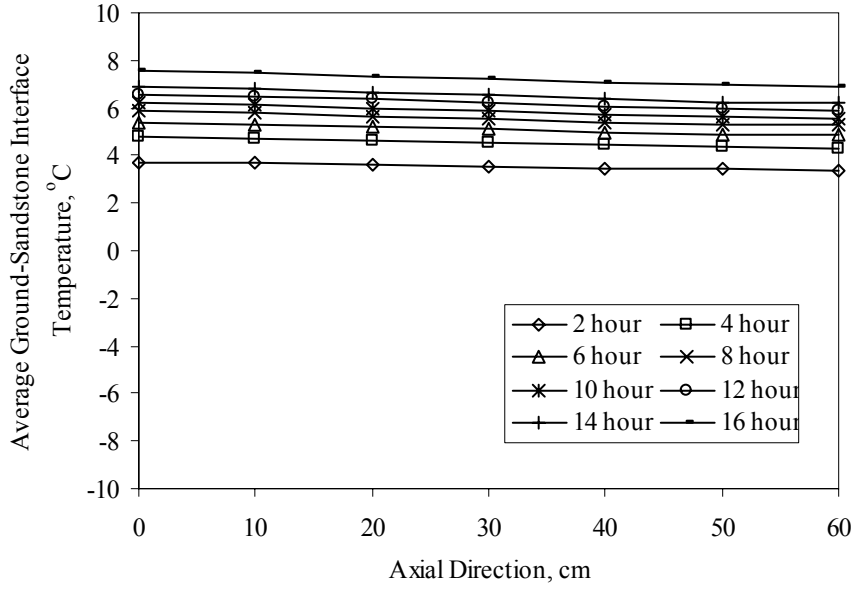

Figure 8.10: Average ground interface temperature along axial direction at different times

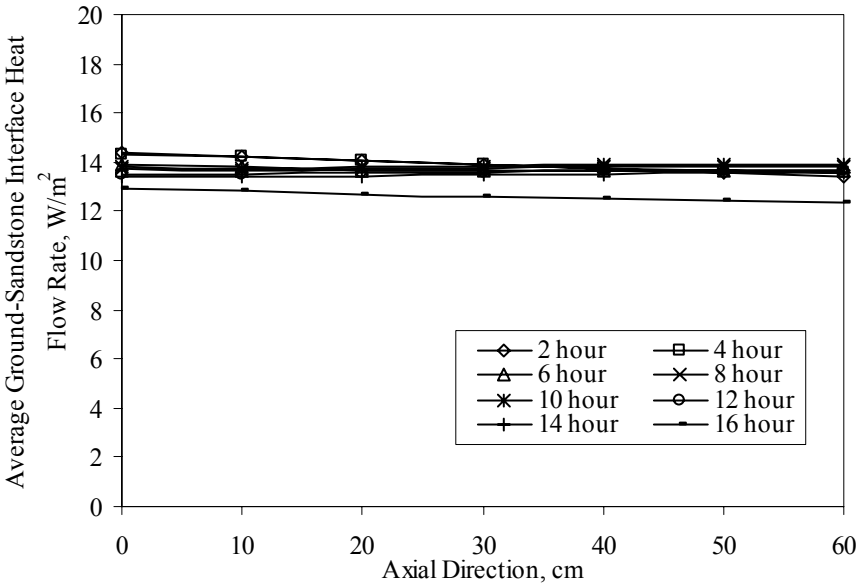

Figure 8.11: Average ground interface heat flow rate along axial direction at different times

temperature that heat up the model. Figure 8.11 shows the average heat flow rate at the ground interface along the axial direction over time. Because the ground temperature gradient was negligible at the ground interface along the axial direction, the heat flow rate also remains negligible. The heat flow rate to the ground remains constant with time because of its negligible value.

8.4 Conclusions

Three dimensional transient snow melting system model was developed. A numerical scheme was applied to come up with the heat flow rate calculations within the system. Calculated heat flow rates were plotted and presented. Two different storm scenarios were studied. The heat flow rate at the fluid interface showed a constant behavior along the axial direction for heavier storms. The temperature at the surface was decreasing along the axial direction. The heat loss to the ground decrease in the axial direction too. The rate of change in the surface temperature was less for the heavier storm. Results presented showed that considering a higher inlet temperature can overcome as much as six times the snow fall. The third dimension provided much understanding of the model behavior in the axial direction.

Chapter 9 – Conclusions

9.1 Conclusion

Different types and designs of microchannels were studied in this project. Transient as well as steady state cases with different boundary conditions were implemented in this study to understand the microchannel cooling performance under different conditions and designs. Numerical simulation models were developed for this project with the desired designs and boundary conditions. Computer software was used to solve the conservation equations for the velocity and temperature distribution. A parametric study was conducted for each of the designs and results were presented in terms of interface temperature, heat flow rate and Nusselt number at the fluid-solid interface. The parameters that were varied are Reynolds number, Magnetic field strength, channel diameter or height, and working fluid.

The results showed that an increase in Reynolds number decreases the interface temperature but increases the heat flow rate and Nusselt number. The change in magnetic field value had the greatest impact on the interface temperature and the heat flow rate. On the other hand, it did not have any significant effect on the Nusselt number at the fluid-solid interface. When the heat source varied with time, by applying and removing the magnetic field, the interface temperature, heat flow rate, and Nusselt number attained a periodic variation with time. The absolute heat flow rate and the Nusselt number were

increasing with time at each period. The decrease in the diameter at constant Reynolds number decreases the interface temperature and increases the heat flow rate at the fluid-solid interface. Nusselt number depends on the diameter and the heat flow rate. Therefore, it will either increase or decrease with the change in diameter according to the change in the heat flow rate. Using different fluids revealed that water results in the lower interface temperature and highest heat flow rate. In nanofluids, the increase in the solid volumetric ratio decreases the heat flow rate and Nusselt number. Using stainless steel substrate results in lower heat flow rate and Nusselt number compared to Silicon. The increase in Reynolds number increases both the heat flow rate and the Nusselt number. Larger diameter decreases the heat flow rate and the heat flow rate coefficient. The Nusselt number could decrease due to lower heat transfer coefficient or increase due to larger diameter. This is determined separately for each case. Nusselt number increased with diameter in this study.

Hydronic snow melting system was also simulated to carry out a parametric study in order to arrive to an understanding how different parameters affect the melting process. Ethylene Glycol showed less heat flow rate in the model compared to water. The increase in Reynolds number increased the heat flow rate in the model. Higher heat flow rate could be achieved by increasing the inlet temperature or using smaller pipe diameter. The heat loss to the ground increased with higher Reynolds number or larger diameter. The most important addition to the literature is the three-dimensional model that showed a great drop in the bulk fluid temperature along the axial direction. This temperature drop reduces the quality the performance of the energy transfer to melt the snow along the axial direction. This temperature reduction must be taken into consideration when

designing the system. Transient cases were studied by analyzing two different snow storm scenarios. They were simulated to understand their effect on the melting system with time. The heat flow rate at the fluid interface showed constant behavior along the axial direction for the heavier storm. The rate of change in the surface temperature was less for the heavier storm. It was also found that the system could also work in heavy storms with a slight increase in the inlet temperature.

9.2 Recommendations for Future Research

Researchers could continue studying different designs for microchannels. Other channel geometries or parameters that are not included in this work could be good material for future studies. Only one composite material was studied in this work. There are many other combinations of other composite material and design that could be used in an effort to find the optimum design. Steady state parametric study was done on nanofluids in this work. Transient problem was not considered for this research as well as other nanoparticles which might have better thermal conductivity. Concrete was the only solid used for the hydronic snow melting system and only circular pipes were considered. Other material such as asphalt and other channel geometries can be included in future research.

References

[1] Rahman, M. M. and Rosario, L., "Thermodynamic Analysis Magnetic Refrigeration," *ASME Int. Mechanical Engineering Congress and Exposition*, Anaheim, CA, November 13-19, 2004.

[2] Rahman, M. M., "Measurements of Heat Transfer in Microchannel Heat Sinks," *Int. Comm. Heat Mass Transfer*, Vol. 27, 2000, pp. 495-506.

[3] ASHRAE Inc., ASHRAE Handbook HVAC Application. ASHRAE Inc., 1995.

[4] Peng, X. F., and Peterson, G. P., "Convective Heat Transfer and Flow Friction for Water Flow in Microchannel Structures," *Int. J. Heat Mass Transfer*, Vol. 39, 1996, pp. 2599-2608..

[5] Papautsky I., Gale B., Mohanty S., Ameel T., and Frazier B., "Effects of Rectangular Microchannel Aspect Ratio on Laminar Friction Constant," *Proceedings of SPIE, The Int. Society of Optical Engineering*, Vol. 3877, 1999, pp. 147-158.

[6] Qu W., Mala G. M., and Lee D., "Heat Transfer for Water Flow in Trapezoidal Silicon Microchannels," *Int. J. Heat and Mass Transfer*, Vol. 43, No. 21, 2000, pp. 3925-3936.

[7] Yang, R. J., Fu. L. M., and Hwang, C. C., "Electroosmotic Entry Flow in a Microchannel," *J. of Colloid and Interface Science*, Vol. 244, No. 1, 2001, pp. 173-179.

[8] Quadir G. A., Mydin A., and Seetharamu K. N., "Analysis of Microchannel Heat Exchangers Using FEM," *Int. J. of Numerical Methods for Heat and Fluid Flow*, Vol. 11, 2001, pp. 59-75.

[9] Rahman, M. M. and Shevade, S. S., "Microchannel Thermal Management during Volumetric Heating or Cooling," *Proc. First International Energy Conversion Engineering Conference,* 2003.

[10] Rahman M. M. and Shevade S. S., "Flow in Microchannel with Time Varying Heat Source," *Proceedings of IMECE, ASME International Mechanical Engineering Congress and Exposition*, Washington, D. C., November 16-21, 2003.

[11] Tunc, G. and Bayazitoglu, Y., "Heat Transfer in Rectangular Microchannels," *Int. J. of Heat and Mass Transfer*, Vol. 45, 2002, pp. 765-773.

[12] Pfund, D., Rector, D., Shekarriz, A., Popescu, A., Welty, J. "Pressure Drop Measurements in a Microchannel," *American Institute of Chemical Engineers Journal*, Vol. 46, No. 8, 2000, pp. 1496-1507.

[13] Kohl, M. J., Abdel-Khalik, S. I., Jeter, S. M., and Sadowski, D. L. "An Experimental Investigation of Microchannel Flow with Internal Pressure Measurements," *Int. J. of Heat and Mass Transfer*, Vol. 48, 2005, pp. 1518-1533.

[14] Koo, J., Kleinstreuer, C., "Viscous Dissipation Effects in Microtubes and Microchannels," *International Journal of Heat and Mass Transfer*, Vol. 47, No. 14/16, 2004. pp. 3159-3169.

[15] Lelea, D., Nishio, S., and Takano, K., "The Experimental Research on Microtube Heat Transfer and Fluid Flow of Distilled water," *Int. J. of Heat and Mass Transfer*, Vol. 47, 2004, pp. 2817-2830.

[16] Yu, D., Warrington, R., Barron, R., and Ameel, T., "An Experimental and Theoretical Investigation of Fluid Flow and Heat Transfer in Microtubes," *ASME/JSME Thermal Engineering Conference*, Vol. 1, 1995, pp. 523-530.

[17] Adams, T. M., Abdel-Khalik, S. I., Jeter, S. M., and Qureshi, Z. H., "An Experimental Investigation of Single-Phase Forced Convection in Microchannels," *Int.Chemical Engineering*, Vol. 41, 1998, pp. 851-857.

[18] Owhaib, W., and Palm, B., "Experimental of Single-Phase Forced Convection Heat Transfer in Circular Microchannels," *Experimental Thermal and fluid Science*, Vol. 28, 2004, pp. 105-110.

[19] Celata, G. P., Cumo, M., and Zummo, G., "Thermal-hydraulic Characteristics of Single-Phase Flow in Capillary Pipes," *Experimental Thermal and fluid Science*, Vol. 28, 2004, pp. 87-95.

[20] Rao, P. S. C. and Rahman, M. M., "Analysis of Steady State Conjugate Heat Transfer in a Circular Microtube Inside a Substrate," *Proc. 2004 ASME International Mechanical Engineering Congress and Exposition*, Anaheim, CA, November 13-19, 2004.

[21] Nield, D. A., and Kuznetsov, A. V., "Investigation of Forced Convection in an Almost Circular Microtube with Rough Walls," *International Journal of Fluid Mechanics Research*, Vol. 30, No. 1, 2003, pp. 1-10.

[22] Giulio, C., and D'Agaro, P., "Numerical Simulation of Roughness Effect on Microchannel Heat Transfer and Pressure Drop in Laminar Flow," *Journal of Physics. D: Applied Physics*, Vol. 38, 2005, pp. 1518-1530.

[23] Grohmann, S., "Measurements and Modeling of Single-Phase and Flow-Boiling Heat Transfer in Microtubes," *International Journal of Heat and Mass Transfer*, Vol. 48, No. 19/20, 2005, pp. 4073-4089.

[24] Broderick, S. L., Webb, B. W., and Maynes, D., "Thermally Developing Electro-Osmotic Convection in Microchannels with Finite Debye-Layer Thickness," *Numerical Heat Transfer; Part A: Applications*, Vol. 48, No. 10, 2005, pp. 941-964.

[25] Chakraborty, S., "Analytical Solutions of Nusselt Number for Thermally Fully Developed Flow in Microtubes under a Combined Action of Electroosmotic Forces and Imposed Pressure Gradients," *International Journal of Heat and Mass Transfer*, Vol. 49, No. 3/4, 2006, pp. 810-813.

[26] Hwang, Y. W., and Kim, M. S., "The Pressure Drop in Microtubes and Correlation Development," *International Journal of Heat and Mass Transfer*, Vol. 49, No. 11/12, 2006, pp. 1804-1812.

[27] Yang C., Beng C., and Chan V., "Transient Analysis of Electroosmotic Flow in a Slit Microchannel," *J. of Colloid and Interface Science*, Vol. 248, No. 2, 2002, pp. 524-527.

[28] Eastman J. A., Choi S. U. S., Li S., Yu W., and Thompson L. J., "Anomalously Increased Effective Thermal Conductivities of Ethylene Glycol-Based Nanofluids Containing Copper Nanoparticles," *App. Phys. Lett.*, Vol. 78, No. 6, 2001, pp. 718-720.

[29] keblinski P., Phillpot S. R., Choi S. U. S., and Eastman J. A., "Mechanism of Heat Flow in Suspensions of Nano-sized Particles (Nanofluids)," *Int. J. Heat and Mass Transfer*, Vol. 45, No. 21, 2002, pp. 855-863.

[30] Cheng N. S. C., and Law A. W. K., "Exponential Formula for Computing Effective Viscosity," *Powder Tech.,* Vol. 129, 2003, pp. 156-160.

[31] Putra N., Roetzel W., and Das S. K., "Natural Convection of Nano-fluids," *Int. J. Heat and Mass Transfer*, Vol. 39, 2003, pp. 775-784.

[32] Bang I., C. and Chang S. H., "Boiling Heat Ttransfer Performance and Phenomena of Al_2O_3-water Nano-fluids from a Plain Surface in a Pool," *Int. J. Heat and Mass Transfer*, Vol. 48, 2005, pp. 2407-2419.

[33] Vadasz J. J., Saneshan G., and Vadasz P., "Heat Transfer Enhancement in Nano-Fluids Suspensions: Possible Mechanism and Explanations," *Int. J. Heat and Mass Transfer*, Vol. 48, 2005, pp. 2673-2683.

[34] Wen D. and Ding Y., "Effect of Particle Migration on Heat Transfer in Suspensions of Nanoparticles Flowing through Minichannels," *Microfluids Nanofluids*, Vol. 1, 2005, pp. 183-189.

[35] Maiga S. E. B., Nguyen C. T., Galanis N., and Roy G., "Heat Transfer Behaviors of Nanofluids in a Uniformly Heated Tube," *Superlattices and Microstructures*, Vol. 35, 2004, pp. 543-557.

[36] Wang X., Xu X., and Choi S. U. S., "Thermal Conductivity of Nanoparticles-Fluid Mixture," *Journal of Thermophysics and Heat Transfer*, Vol. 13, No. 4, 1999, pp. 474-480.

[37] Chapman, W. P., "Design of Snow Melting Systems," *Heating and Ventilating*, Vol. 49, No. 11, 1952, pp. 88-91.

[38] Chapman, W. P., "Design of Snow Melting Systems," *Heating and Ventilating*, Vol. 49, No. 4, 1952 , pp. 96-102.

[39] Chapman, W. P., "A Review of Snow Melting Systems Design," *ASHRAE Transactions*, 1999.

[40] Ramsey, J. W., Hewett, M. J., Kuehn, T. H., and Peterson, S. D., "Updated Design Guidelines for Snow Melting Systems." *ASHRAE Transactions*, 1999.

[41] Kilkis, B. I., "An Analytical Algorithm for Hydronic Circuit Analysis and Assessment of Equipment Performance." *ASHRAE Transaction*, Vol. 105, Part 1, 1999, pp 368-374.

[42] Kilkis, I. B., "Design of Embedded Snow Melting Systems part 1." *ASHRAE Transaction*, Vol. 100, Part 1, 1994, pp 423-433.

[43] Kilkis, I. B., "Design of Embedded Snow Melting Systems part 2." *ASHRAE Transaction*, Vol. 100, Part 2, 1994, pp 434-441.

[44] Rees, S. J., Spitler, J. D., and Xiao, X., "Transient Analysis of Snow Melting System Performance." *ASHRAE Transaction*, Vol. 108, Part 2, 2002, pp 406-423.

[45] White F. M., 1991, Viscous Fluid Flow. 2nd Ed., McGraw-Hill, New York.

[46] Ozisik, M. N., 1993, Heat Conduction. 2nd Ed., John Wiley and Sons, New York.

[47] Pechasky, V. K., and Gschneider, K. A., "Magnetocaloric Effect and Magnetic Refrigeration." *Journal of Magnetism and Magnetic Materials*, Vol. 200, 1999, pp. 44-56.

Appendices

Appendix A: FIDAP Program for Steady State Heat Transfer in Circular Microchannels During Magnetic Heating or Cooling Simulation

```
FIPREP(  )
CONDUCTIVITY( ADD, SET = "Fluid", CONS = 0.0014435, ISOT )
CONDUCTIVITY( ADD, SET = "Solid", CONS = 0.0250956, ISOT )
DENSITY( ADD, SET = "Fluid", CONS = 0.9974 )
DENSITY( ADD, SET = "Solid", CONS = 7.895 )
SPECIFICHEAT( ADD, SET = "Fluid", CONS = 0.9988 )
SPECIFICHEAT( ADD, SET = "Solid", CONS = 0.054971 )
VISCOSITY( ADD, SET = "Fluid", CONS = 0.0098 )
ENTITY( ADD, NAME = "Fluid-b", FLUI, PROP = "Fluid" )
ENTITY( ADD, NAME = "Fluid-t", FLUI, PROP = "Fluid" )
ENTITY( ADD, NAME = "Gadolinium", SOLI, PROP = "Solid" )
ENTITY( ADD, NAME = "f-bin", PLOT )
ENTITY( ADD, NAME = "f-tin", PLOT )
ENTITY( ADD, NAME = "f-bsym", PLOT )
ENTITY( ADD, NAME = "f-tsym", PLOT )
ENTITY( ADD, NAME = "f-bout", PLOT )
ENTITY( ADD, NAME = "f-tout", PLOT )
ENTITY( ADD, NAME = "Gd-in", PLOT )
ENTITY( ADD, NAME = "Gd-top", PLOT )
ENTITY( ADD, NAME = "Gd-lwall", PLOT )
ENTITY( ADD, NAME = "Gd-bottom", PLOT )
ENTITY( ADD, NAME = "Gd-bsym", PLOT )
ENTITY( ADD, NAME = "Gd-tsym", PLOT )
ENTITY( ADD, NAME = "Gd-out", PLOT )
ENTITY( ADD, NAME = "f-bwall1", PLOT, ATTA = "Gadolinium", NATT = "Fluid-b" )
ENTITY( ADD, NAME = "f-bwall2", PLOT, ATTA = "Gadolinium", NATT = "Fluid-b" )
ENTITY( ADD, NAME = "f-twall1", PLOT, ATTA = "Gadolinium", NATT = "Fluid-t" )
ENTITY( ADD, NAME = "f-twall2", PLOT, ATTA = "Gadolinium", NATT = "Fluid-t" )
BCNODE( ADD, UX, ENTI = "f-bin", ZERO )
BCNODE( ADD, UX, ENTI = "f-tin", ZERO )
BCNODE( ADD, UY, ENTI = "f-bin", ZERO )
BCNODE( ADD, UY, ENTI = "f-tin", ZERO )
BCNODE( ADD, UZ, ENTI = "f-bin", CONS = 436.690952 )
BCNODE( ADD, UZ, ENTI = "f-tin", CONS = 436.690952 )
BCNODE( ADD, TEMP, ENTI = "f-bin", CONS = 20 )
BCNODE( ADD, TEMP, ENTI = "f-tin", CONS = 20 )
BCNODE( ADD, VELO, ENTI = "f-bwall1", ZERO )
BCNODE( ADD, VELO, ENTI = "f-bwall2", ZERO )
BCNODE( ADD, VELO, ENTI = "f-twall1", ZERO )
BCNODE( ADD, VELO, ENTI = "f-twall2", ZERO )
BCNODE( ADD, UX, ENTI = "f-bsym", ZERO )
BCNODE( ADD, UY, ENTI = "f-bsym", ZERO )
BCNODE( ADD, UX, ENTI = "f-tsym", ZERO )
BCNODE( ADD, UY, ENTI = "f-tsym", ZERO )
SOURCE( ADD, HEAT, CONS = 5.13, ENTI = "Gadolinium" )
BCFLUX( ADD, HEAT, ENTI = "Gd-top", CONS = 0 )
BCFLUX( ADD, HEAT, ENTI = "Gd-lwall", CONS = 0 )
BCFLUX( ADD, HEAT, ENTI = "Gd-bsym", CONS = 0 )
BCFLUX( ADD, HEAT, ENTI = "Gd-tsym", CONS = 0 )
DATAPRINT( ADD, CONT )
EXECUTION( ADD, NEWJ )
```

Appendix A: (Continued)

```
PRINTOUT( ADD, NONE )
OPTIONS( ADD, UPWI )
PROBLEM( ADD, 3-D, INCO, STEA, LAMI, NONL, NEWT, MOME, ENER, FIXE, SING )
SOLUTION( ADD, N.R. = 7500, VELC = 0.02, RESC = 0.02, ACCF = 0.05 )
WIND = 0.75, NOFI = 3 )
CLIPPING( ADD, MINI )
   0,    0,    0,    0,   20,    0
END(  )
```

Appendix B: FIDAP Program for Transient Heat Transfer in Circular Microchannels Under Time Varying Heat Source Simulation

```
FIPREP(  )

/=========================================
/                                   MATERIAL PROPERTIES
/=========================================

CONDUCTIVITY( ADD, SET = "Fluid", CONS = 0.0014435, ISOT )
CONDUCTIVITY( ADD, SET = "Solid", CONS = 0.0250956, ISOT )
DENSITY( ADD, SET = "Fluid", CONS = 0.9974 )
DENSITY( ADD, SET = "Solid", CONS = 7.895 )
SPECIFICHEAT( ADD, SET = "Fluid", CONS = 0.9988 )
SPECIFICHEAT( ADD, SET = "Solid", CONS = 0.054971 )
VISCOSITY( ADD, SET = "Fluid", CONS = 0.0098 )

/=========================================
/                                   ENTITY NAMES
/=========================================

ENTITY( ADD, NAME = "Fluid-b", FLUI, PROP = "Fluid" )
ENTITY( ADD, NAME = "Fluid-t", FLUI, PROP = "Fluid" )
ENTITY( ADD, NAME = "Gadolinium", SOLI, PROP = "Solid" )

ENTITY( ADD, NAME = "f-bin", PLOT )
ENTITY( ADD, NAME = "f-bsym", PLOT )
ENTITY( ADD, NAME = "f-bout", PLOT )

ENTITY( ADD, NAME = "f-tin", PLOT )
ENTITY( ADD, NAME = "f-tsym", PLOT )
ENTITY( ADD, NAME = "f-tout", PLOT )

ENTITY( ADD, NAME = "Gd-in", PLOT )
ENTITY( ADD, NAME = "Gd-top", PLOT )
ENTITY( ADD, NAME = "Gd-lwall", PLOT )
ENTITY( ADD, NAME = "Gd-bottom", PLOT )
ENTITY( ADD, NAME = "Gd-bsym", PLOT )
ENTITY( ADD, NAME = "Gd-tsym", PLOT )
ENTITY( ADD, NAME = "Gd-out", PLOT )

ENTITY( ADD, NAME = "f-bwall1", PLOT, ATTA = "Gadolinium", NATT = "Fluid-b" )
ENTITY( ADD, NAME = "f-bwall2", PLOT, ATTA = "Gadolinium", NATT = "Fluid-b" )
ENTITY( ADD, NAME = "f-twall1", PLOT, ATTA = "Gadolinium", NATT = "Fluid-t" )
ENTITY( ADD, NAME = "f-twall2", PLOT, ATTA = "Gadolinium", NATT = "Fluid-t" )

/=========================================
/                                   BOUNDARY CONDITION COMMANDS
/=========================================

BCNODE( ADD, UX, ENTI = "f-bin", ZERO )
BCNODE( ADD, UY, ENTI = "f-bin", ZERO )
BCNODE( ADD, UZ, ENTI = "f-bin", CONS = 436.69 )
BCNODE( ADD, TEMP, ENTI = "f-bin", CONS = 20 )
```

Appendix B: (Continued)

```
BCNODE( ADD, UX, ENTI = "f-tin", ZERO )
BCNODE( ADD, UY, ENTI = "f-tin", ZERO )
BCNODE( ADD, UZ, ENTI = "f-tin", CONS = 436.69 )
BCNODE( ADD, TEMP, ENTI = "f-tin", CONS = 20 )

BCNODE( ADD, VELO, ENTI = "f-bwall1", ZERO )
BCNODE( ADD, VELO, ENTI = "f-bwall2", ZERO )
BCNODE( ADD, VELO, ENTI = "f-twall1", ZERO )
BCNODE( ADD, VELO, ENTI = "f-twall2", ZERO )

BCNODE( ADD, UX, ENTI = "f-bsym", ZERO )
BCNODE( ADD, UY, ENTI = "f-bsym", ZERO )
BCNODE( ADD, UX, ENTI = "f-tsym", ZERO )
BCNODE( ADD, UY, ENTI = "f-tsym", ZERO )

SOURCE( ADD, HEAT, CONS = 2.56, ENTI = "Gadolinium" )
SOURCE( ADD, HEAT, CONS = -2.56, ENTI = "Gadolinium" )

ICNODE( ADD, TEMP, CONS = 20, ENTI = "Fluid-b" )
ICNODE( ADD, TEMP, CONS = 20, ENTI = "Fluid-t" )
ICNODE( ADD, TEMP, CONS = 20, ENTI = "Gadolinium" )
ICNODE( ADD, VELO, READ)
ICNODE( ADD, TEMP, READ )

/=========================================
/                                  EXECUTION COMMANDS
/=========================================

DATAPRINT( ADD, CONT )
EXECUTION( ADD, NEWJ )
PRINTOUT( ADD, NONE )
OPTIONS( ADD, UPWI )
PROBLEM( ADD, 3-D, INCO, TRAN, LAMI, NONL, NEWT, MOME, ENER, FIXE, SING )
PROBLEM( ADD, 3-D, INCO, TRAN, LAMI, NONL, NEWT, NOMO, ENER, FIXE, SING )
SOLUTION( ADD, N.R. = 100, VELC = 0.001)

TIMEINTEGRATION( ADD, BACK, NSTE = 200, TSTA = 0.0, DT = 0.005, FIXE)
TIMEINTEGRATION( ADD, BACK, NSTE = 400, TSTA = 1.0, DT = 0.005, FIXE)

POSTPROCESS( ADD, NBLO = 2, NOPT, NOPA )
2, 10, 2
20, 200, 20
POSTPROCESS( ADD, NBLO = 1, NOPT, NOPA )
20, 400, 20

END(  )
```

Appendix C: FIDAP Program for Transient Heat Transfer in Trapezoidal Microchannels During Activation of Magnetic Heating Simulation

```
FIPREP(  )

/=======================================
/                                  MATERIAL PROPERTIES
/=======================================

CONDUCTIVITY( ADD, SET = "si", CONS = 0.29637, ISOT )
DENSITY( ADD, SET = "si", CONS = 2.329 )
SPECIFICHEAT( ADD, SET = "si", CONS = 0.16778 )

CONDUCTIVITY( ADD, SET = "fl", CONS = 0.0014435, ISOT )
DENSITY( ADD, SET = "fl", CONS = 0.9974 )
SPECIFICHEAT( ADD, SET = "fl", CONS = 0.9988 )
VISCOSITY( ADD, SET = "fl", CONS = 0.0098 )

CONDUCTIVITY( ADD, SET = "gd", CONS = 0.0250956, ISOT )
DENSITY( ADD, SET = "gd", CONS = 7.895 )
SPECIFICHEAT( ADD, SET = "gd", CONS = 0.054971 )

/=======================================
/                                  ENTITY NAMES
/=======================================

ENTITY( ADD, NAME = "si1", SOLI, PROP = "si" )
ENTITY( ADD, NAME = "si2", SOLI, PROP = "si" )
ENTITY( ADD, NAME = "si3", SOLI, PROP = "si" )
ENTITY( ADD, NAME = "fl", FLUI, PROP = "fl" )
ENTITY( ADD, NAME = "gd", SOLI, PROP = "gd" )

ENTITY( ADD, NAME = "si1-in", PLOT )
ENTITY( ADD, NAME = "si1-out", PLOT )
ENTITY( ADD, NAME = "si1-bot", PLOT )
ENTITY( ADD, NAME = "si1-right", PLOT )
ENTITY( ADD, NAME = "si1-top", PLOT )
ENTITY( ADD, NAME = "si1-left", PLOT )

ENTITY( ADD, NAME = "si2-in", PLOT )
ENTITY( ADD, NAME = "si2-out", PLOT )
ENTITY( ADD, NAME = "si2-bot", PLOT )
ENTITY( ADD, NAME = "si2-right", PLOT )
ENTITY( ADD, NAME = "si2-int", PLOT, ATTA = "fl", NATTA = "si2" )

ENTITY( ADD, NAME = "si3-in", PLOT )
ENTITY( ADD, NAME = "si3-out", PLOT )
ENTITY( ADD, NAME = "si3-bot", PLOT )
ENTITY( ADD, NAME = "si3-axi", PLOT )
ENTITY( ADD, NAME = "si3-int", PLOT, ATTA = "fl", NATTA = "si3" )

ENTITY( ADD, NAME = "fl-in", PLOT )
ENTITY( ADD, NAME = "fl-out", PLOT )
ENTITY( ADD, NAME = "fl-axi", PLOT )
```

Appendix C: (Continued)

```
ENTITY( ADD, NAME = "fl-int", PLOT, ATTA = "fl", NATTA = "gd"  )
ENTITY( ADD, NAME = "gd-in", PLOT )
ENTITY( ADD, NAME = "gd-out", PLOT )
ENTITY( ADD, NAME = "gd-axi", PLOT )
ENTITY( ADD, NAME = "gd-top", PLOT )
ENTITY( ADD, NAME = "gd-left", PLOT )

/=========================================
/                                  BOUNDARY CONDITION COMMANDS
/=========================================

BCNODE( ADD, UX, ENTI = "fl-in", ZERO )
BCNODE( ADD, UY, ENTI = "fl-in", ZERO )
BCNODE( ADD, UZ, ENTI = "fl-in", CONS = 403.91)
BCNODE( ADD, TEMP, ENTI = "fl-in", CONS = 20 )

BCNODE( ADD, VELO, ENTI = "si2-int", ZERO )
BCNODE( ADD, VELO, ENTI = "si3-int", ZERO )
BCNODE( ADD, VELO, ENTI = "fl-int", ZERO )
BCNODE( ADD, UX, ENTI = "fl-axi", ZERO )

SOURCE( ADD, HEAT, CONS = 5.12, ENTI = "gd" )

ICNODE( ADD, TEMP, CONS = 20, ENTI = "si1" )
ICNODE( ADD, TEMP, CONS = 20, ENTI = "si2" )
ICNODE( ADD, TEMP, CONS = 20, ENTI = "si3" )
ICNODE( ADD, TEMP, CONS = 20, ENTI = "fl" )
ICNODE( ADD, TEMP, CONS = 20, ENTI = "gd" )

/=========================================
/                                  EXECUTION COMMANDS
/=========================================

DATAPRINT( ADD, CONT )
EXECUTION( ADD, NEWJ )
PRINTOUT( ADD, NONE )
OPTIONS( ADD, UPWI )
PROBLEM( ADD, 3-D, INCO, TRAN, LAMI, NONL, NEWT, MOME, ENER, FIXE, SING )
SOLUTION( ADD, N.R. = 100, VELC = 0.001)

/TIME LENGTH = 1s
TIMEINTEGRATION( ADD, BACK, NSTE = 200, TSTA = 0.0, DT = 0.005, FIXE)
POSTPROCESS( ADD, NBLO = 2, NOPT, NOPA )
2, 10, 2
20, 200, 20

END(  )
```

Appendix D: FIDAP Program for Transient Heat Transfer in Trapezoidal Microchannels Under Time Varying Heat Source Simulation

```
FIPREP(  )

/=========================================
/                                  MATERIAL PROPERTIES
/=========================================

CONDUCTIVITY( ADD, SET = "si", CONS = 0.29637, ISOT )
DENSITY( ADD, SET = "si", CONS = 2.329 )
SPECIFICHEAT( ADD, SET = "si", CONS = 0.16778 )

CONDUCTIVITY( ADD, SET = "fl", CONS = 0.0014435, ISOT )
DENSITY( ADD, SET = "fl", CONS = 0.9974 )
SPECIFICHEAT( ADD, SET = "fl", CONS = 0.9988 )
VISCOSITY( ADD, SET = "fl", CONS = 0.0098 )

CONDUCTIVITY( ADD, SET = "gd", CONS = 0.0250956, ISOT )
DENSITY( ADD, SET = "gd", CONS = 7.895 )
SPECIFICHEAT( ADD, SET = "gd", CONS = 0.054971 )

/=========================================
/                                  ENTITY NAMES
/=========================================

ENTITY( ADD, NAME = "si1", SOLI, PROP = "si" )
ENTITY( ADD, NAME = "si2", SOLI, PROP = "si" )
ENTITY( ADD, NAME = "si3", SOLI, PROP = "si" )
ENTITY( ADD, NAME = "fl", FLUI, PROP = "fl" )
ENTITY( ADD, NAME = "gd", SOLI, PROP = "gd" )

ENTITY( ADD, NAME = "si1-in", PLOT )
ENTITY( ADD, NAME = "si1-out", PLOT )
ENTITY( ADD, NAME = "si1-bot", PLOT )
ENTITY( ADD, NAME = "si1-right", PLOT )
ENTITY( ADD, NAME = "si1-top", PLOT )
ENTITY( ADD, NAME = "si1-left", PLOT )

ENTITY( ADD, NAME = "si2-in", PLOT )
ENTITY( ADD, NAME = "si2-out", PLOT )
ENTITY( ADD, NAME = "si2-bot", PLOT )
ENTITY( ADD, NAME = "si2-right", PLOT )
ENTITY( ADD, NAME = "si2-int", PLOT, ATTA = "fl", NATTA = "si2" )

ENTITY( ADD, NAME = "si3-in", PLOT )
ENTITY( ADD, NAME = "si3-out", PLOT )
ENTITY( ADD, NAME = "si3-bot", PLOT )
ENTITY( ADD, NAME = "si3-axi", PLOT )
ENTITY( ADD, NAME = "si3-int", PLOT, ATTA = "fl", NATTA = "si3" )

ENTITY( ADD, NAME = "fl-in", PLOT )
ENTITY( ADD, NAME = "fl-out", PLOT )
ENTITY( ADD, NAME = "fl-axi", PLOT )
```

Appendix D: (Continued)

```
ENTITY( ADD, NAME = "fl-int", PLOT, ATTA = "fl", NATTA = "gd"  )
ENTITY( ADD, NAME = "gd-in", PLOT )
ENTITY( ADD, NAME = "gd-out", PLOT )
ENTITY( ADD, NAME = "gd-axi", PLOT )
ENTITY( ADD, NAME = "gd-top", PLOT )
ENTITY( ADD, NAME = "gd-left", PLOT )

/=========================================
/                                  BOUNDARY CONDITION COMMANDS
/=========================================

BCNODE( ADD, UX, ENTI = "fl-in", ZERO )
BCNODE( ADD, UY, ENTI = "fl-in", ZERO )
BCNODE( ADD, UZ, ENTI = "fl-in", CONS = 403.91)
BCNODE( ADD, TEMP, ENTI = "fl-in", CONS = 20 )

BCNODE( ADD, VELO, ENTI = "si2-int", ZERO )
BCNODE( ADD, VELO, ENTI = "si3-int", ZERO )
BCNODE( ADD, VELO, ENTI = "fl-int", ZERO )
BCNODE( ADD, UX, ENTI = "fl-axi", ZERO )

SOURCE( ADD, HEAT, CONS = 5.12, ENTI = "gd" )
SOURCE( ADD, HEAT, CONS = -5.12, ENTI = "gd" )

ICNODE( ADD, TEMP, CONS = 20, ENTI = "si1" )
ICNODE( ADD, TEMP, CONS = 20, ENTI = "si2" )
ICNODE( ADD, TEMP, CONS = 20, ENTI = "si3" )
ICNODE( ADD, TEMP, CONS = 20, ENTI = "fl" )
ICNODE( ADD, TEMP, CONS = 20, ENTI = "gd" )
ICNODE( ADD, VELO, READ )
ICNODE( ADD, TEMP, READ )
/=========================================
/                                  EXECUTION COMMANDS
/=========================================

DATAPRINT( ADD, CONT )
EXECUTION( ADD, NEWJ )
PRINTOUT( ADD, NONE )
OPTIONS( ADD, UPWI )
PROBLEM( ADD, 3-D, INCO, TRAN, LAMI, NONL, NEWT, MOME, ENER, FIXE, SING )
PROBLEM( ADD, 3-D, INCO, TRAN, LAMI, NONL, NEWT, NOMO, ENER, FIXE, SING )SOLUTION(
ADD, N.R. = 100, VELC = 0.001)

TIMEINTEGRATION( ADD, BACK, NSTE = 200, TSTA = 0.0, DT = 0.005, FIXE)
TIMEINTEGRATION( ADD, BACK, NSTE = 400, TSTA = 1.0, DT = 0.005, FIXE)

POSTPROCESS( ADD, NBLO = 2, NOPT, NOPA )
2, 10, 2
20, 200, 20
POSTPROCESS( ADD, NBLO = 1, NOPT, NOPA )
20, 400, 20

END(  )
```

Appendix E: FIDAP Program for Steady State Heat Transfer Using Nanofluids in Circular Microchannels Simulation

```
FIPREP(  )

/=========================================
/                                  MATERIAL PROPERTIES
/=========================================

CONDUCTIVITY( ADD, SET = "wtr", CONS = 0.001434, ISOT )
DENSITY( ADD, SET = "wtr", CONS = 0.9982 )
SPECIFICHEAT( ADD, SET = "wtr", CONS = 0.9995 )
VISCOSITY( ADD, SET = "wtr", CONS = 0.01003 )

/composite of Alumina suspended in water with 1%
CONDUCTIVITY( ADD, SET = "wa1", CONS = 0.0016491, ISOT )
DENSITY( ADD, SET = "wa1", CONS = 1.0281 )
SPECIFICHEAT( ADD, SET = "wa1", CONS = 0.96954 )
VISCOSITY( ADD, SET = "wa1", CONS = 0.010331 )

/composite of Alumina suspended in water with 4%
CONDUCTIVITY( ADD, SET = "wa4", CONS = 0.0017925, ISOT )
DENSITY( ADD, SET = "wa4", CONS = 1.1180 )
SPECIFICHEAT( ADD, SET = "wa4", CONS = 0.87958 )
VISCOSITY( ADD, SET = "wa4", CONS = 0.011033 )

CONDUCTIVITY( ADD, SET = "si", CONS = 0.29637, ISOT )
DENSITY( ADD, SET = "si", CONS = 2.329 )
SPECIFICHEAT( ADD, SET = "si", CONS = 0.16778 )

CONDUCTIVITY( ADD, SET = "gd", CONS = 0.0250956, ISOT )
DENSITY( ADD, SET = "gd", CONS = 7.895 )
SPECIFICHEAT( ADD, SET = "gd", CONS = 0.054971 )

/=========================================
/                                  ENTITY NAMES
/=========================================

ENTITY( ADD, NAME = "fb", FLUI, PROP = "wa4" )
ENTITY( ADD, NAME = "ft", FLUI, PROP = "wa4" )
ENTITY( ADD, NAME = "s", SOLI, PROP = "si" )

ENTITY( ADD, NAME = "sin", PLOT )
ENTITY( ADD, NAME = "sout", PLOT )
ENTITY( ADD, NAME = "sbot", PLOT )
ENTITY( ADD, NAME = "sbaxi", PLOT )
ENTITY( ADD, NAME = "int1", PLOT, ATTA = "s", NATT = "fb" )
ENTITY( ADD, NAME = "int2", PLOT, ATTA = "s", NATT = "fb" )
ENTITY( ADD, NAME = "int3", PLOT, ATTA = "s", NATT = "ft" )
ENTITY( ADD, NAME = "int4", PLOT, ATTA = "s", NATT = "ft" )
ENTITY( ADD, NAME = "staxi", PLOT )
ENTITY( ADD, NAME = "stop", PLOT )
ENTITY( ADD, NAME = "sleft", PLOT )
```

Appendix E: (Continued)

```
ENTITY( ADD, NAME = "fbin", PLOT )
ENTITY( ADD, NAME = "fbout", PLOT )
ENTITY( ADD, NAME = "fbaxi", PLOT )
ENTITY( ADD, NAME = "fint", PLOT )

ENTITY( ADD, NAME = "ftin", PLOT )
ENTITY( ADD, NAME = "ftout", PLOT )
ENTITY( ADD, NAME = "ftaxi", PLOT )

/=========================================
/                                   BOUNDARY CONDITION COMMANDS
/=========================================

/for 4% composite Vin=164.48 ===> Re=1000
/                 vin=32.896 ---> Re=200
/for 1% composite Vin=167.48 ===> Re=1000
/                 vin=33.496 ---> Re=200
/for pure water   Vin=167.47 ===> Re=1000
/                 vin=33.494 ---> Re=200
BCNODE( ADD, UX, ENTI = "fbin", ZERO )
BCNODE( ADD, UY, ENTI = "fbin", ZERO )
BCNODE( ADD, UZ, ENTI = "fbin", CONS = 32.896 )
BCNODE( ADD, TEMP, ENTI = "fbin", CONS = 20 )

BCNODE( ADD, UX, ENTI = "ftin", ZERO )
BCNODE( ADD, UY, ENTI = "ftin", ZERO )
BCNODE( ADD, UZ, ENTI = "ftin", CONS = 32.896 )
BCNODE( ADD, TEMP, ENTI = "ftin", CONS = 20 )

BCNODE( ADD, VELO, ENTI = "int1", ZERO )
BCNODE( ADD, VELO, ENTI = "int2", ZERO )
BCNODE( ADD, VELO, ENTI = "int3", ZERO )
BCNODE( ADD, VELO, ENTI = "int4", ZERO )

BCNODE( ADD, UX, ENTI = "fbaxi", ZERO )
BCNODE( ADD, UY, ENTI = "fbaxi", ZERO )
BCNODE( ADD, UX, ENTI = "ftaxi", ZERO )
BCNODE( ADD, UY, ENTI = "ftaxi", ZERO )

/These 7 lines are default but include them any way just in case
BCFLUX( ADD, HEAT, ENTI = "sbot", CONS = 7.1702 )
BCFLUX( ADD, HEAT, ENTI = "sbaxi", CONS = 0 )
BCFLUX( ADD, HEAT, ENTI = "fbaxi", CONS = 0 )
BCFLUX( ADD, HEAT, ENTI = "ftaxi", CONS = 0 )
BCFLUX( ADD, HEAT, ENTI = "staxi", CONS = 0 )
BCFLUX( ADD, HEAT, ENTI = "stop", CONS = 0 )
BCFLUX( ADD, HEAT, ENTI = "sleft", CONS = 0 )

/=========================================
/                                   EXECUTION COMMANDS
/=========================================

DATAPRINT( ADD, CONT )
```

Appendix E: (Continued)

```
EXECUTION( ADD, NEWJ )
PRINTOUT( ADD, NONE )
OPTIONS( ADD, UPWI )
PROBLEM( ADD, 3-D, INCO, STEA, LAMI, NONL, NEWT, MOME, ENER, FIXE, SING )
SOLUTION( ADD, S.S. = 100, VELC = 0.001)
/SOLUTION( ADD, N.R. = 100, VELC = 0.001)

END(  )
```

Appendix F: FIDAP Program for Steady State Analysis in Hydronic Snow Melting System Simulation

```
FIPREP

/=========================================
/                                   EXECUTION COMMANDS
/=========================================
EXECUTION (NEWJOB)
PROBLEM (ADD, 3-D, TURB, NONLINE, ENERGY)
SOLUTION (ADD, SEGR=10)
DATAPRINT (ADD,CONT)
PRINTOUT (ALL)

/=========================================
/                                   ENTITY NAMES
/=========================================
/continium
ENTITY (ADD, NAME = "fluid-t", FLUID, PROP = "fl")
ENTITY (ADD, NAME = "fluid-b", FLUID, PROP = "fl")
ENTITY (ADD, NAME = "pipe-t", SOLID, PROP = "pi")
ENTITY (ADD, NAME = "pipe-b", SOLID, PROP = "pi")
ENTITY (ADD, NAME = "solid-t", SOLID, PROP = "so")
ENTITY (ADD, NAME = "solid-b", SOLID, PROP = "so")
ENTITY (ADD, NAME = "solid-1", SOLID, PROP = "so")
ENTITY (ADD, NAME = "solid-2", SOLID, PROP = "so")
ENTITY (ADD, NAME = "solid-3", SOLID, PROP = "so")
ENTITY (ADD, NAME = "ground", SOLID, PROP = "gr")
/inlet
ENTITY( ADD, NAME = "ft-in", PLOT)
ENTITY( ADD, NAME = "fb-in", PLOT)
ENTITY( ADD, NAME = "pt-in", PLOT)
ENTITY( ADD, NAME = "pb-in", PLOT)
ENTITY( ADD, NAME = "st-in", PLOT)
ENTITY( ADD, NAME = "sb-in", PLOT)
ENTITY( ADD, NAME = "s1-in", PLOT)
ENTITY( ADD, NAME = "s2-in", PLOT)
ENTITY( ADD, NAME = "s3-in", PLOT)
ENTITY( ADD, NAME = "g-in", PLOT)
/MS1
ENTITY( ADD, NAME = "ft-out", PLOT)
ENTITY( ADD, NAME = "ft-axi", PLOT)
ENTITY( ADD, NAME = "ft-intt", WALL, ATTA = "fluid-t", NATT = "pipe-t")
ENTITY( ADD, NAME = "ft-intb", WALL, ATTA = "fluid-t", NATT = "pipe-t")
ENTITY( ADD, NAME = "ft-bot", PLOT)
/MS2
ENTITY( ADD, NAME = "fb-out", PLOT)
ENTITY( ADD, NAME = "fb-axi", PLOT)
ENTITY( ADD, NAME = "fb-intt", WALL, ATTA = "fluid-b", NATT = "pipe-b")
ENTITY( ADD, NAME = "fb-intb", WALL, ATTA = "fluid-b", NATT = "pipe-b")
/MS3
ENTITY( ADD, NAME = "pt-out", PLOT)
ENTITY( ADD, NAME = "pt-axi", PLOT)
ENTITY( ADD, NAME = "pt-intt", PLOT)
```

Appendix F: (Continued)

```
ENTITY( ADD, NAME = "pt-intb", PLOT)
ENTITY( ADD, NAME = "pt-bot", PLOT)
/MS4
ENTITY( ADD, NAME = "pb-out", PLOT)
ENTITY( ADD, NAME = "pb-axi", PLOT)
ENTITY( ADD, NAME = "pb-intt", PLOT)
ENTITY( ADD, NAME = "pb-intb", PLOT)
/MS5
ENTITY( ADD, NAME = "st-out", PLOT)
ENTITY( ADD, NAME = "st-axi", PLOT)
ENTITY( ADD, NAME = "st-intt", PLOT)
ENTITY( ADD, NAME = "st-intb", PLOT)
ENTITY( ADD, NAME = "st-bot", PLOT)
/MS6
ENTITY( ADD, NAME = "sb-out", PLOT)
ENTITY( ADD, NAME = "sb-axi", PLOT)
ENTITY( ADD, NAME = "sb-intt", PLOT)
ENTITY( ADD, NAME = "sb-intb", PLOT)
/MS7
ENTITY( ADD, NAME = "s1-out", PLOT)
ENTITY( ADD, NAME = "s1-axi", PLOT)
ENTITY( ADD, NAME = "s1-top", PLOT)
ENTITY( ADD, NAME = "s1-bot", PLOT)
/MS8
ENTITY( ADD, NAME = "s2-out", PLOT)
ENTITY( ADD, NAME = "s2-left", PLOT)
ENTITY( ADD, NAME = "s2-bot", PLOT)
/MS9
ENTITY( ADD, NAME = "s3-out", PLOT)
ENTITY( ADD, NAME = "s3-axi", PLOT)
ENTITY( ADD, NAME = "s3-bot", PLOT)
/MS10
ENTITY( ADD, NAME = "g-out", PLOT)
ENTITY( ADD, NAME = "g-axi", PLOT)
ENTITY( ADD, NAME = "g-left", PLOT)
ENTITY( ADD, NAME = "g-bot", PLOT)

/=========================================
/                                  BOUNDARY CONDITION COMMANDS
/=========================================
/inlet
BCNODE (ADD, UX, CONS=0, ENTITY = "ft-in")
BCNODE (ADD, UY, CONS=0, ENTITY = "ft-in")
BCNODE (ADD, UZ, CONS=6.1869, ENTITY = "ft-in")
BCNODE (ADD, UX, CONS=0, ENTITY = "fb-in")
BCNODE (ADD, UY, CONS=0, ENTITY = "fb-in")
BCNODE (ADD, UZ, CONS=6.1869, ENTITY = "fb-in")
/interface
BCNODE (VELOCITY, ZERO, ENTITY = "ft-intt")
BCNODE (VELOCITY, ZERO, ENTITY = "ft-intb")
BCNODE (VELOCITY, ZERO, ENTITY = "fb-intt")
BCNODE (VELOCITY, ZERO, ENTITY = "fb-intb")
/axi
```

Appendix F: (Continued)

```
BCNODE( ADD, UX, ENTI = "ft-axi", ZERO )
BCNODE( ADD, UX, ENTI = "fb-axi", ZERO )

/temperature
BCNODE (ADD, TEMPERATURE, CONS = 80, ENTITY = "ft-in")
BCNODE (ADD, TEMPERATURE, CONS = 80, ENTITY = "fb-in")
BCNODE (ADD, TEMPERATURE, CONS = 0, ENTITY = "s1-top")
/insulation/symmetry
BCFLUX (HEAT, CONS = 0.0, ENTITY = "ft-axi")
BCFLUX (HEAT, CONS = 0.0, ENTITY = "fb-axi")
BCFLUX (HEAT, CONS = 0.0, ENTITY = "pt-axi")
BCFLUX (HEAT, CONS = 0.0, ENTITY = "pb-axi")
BCFLUX (HEAT, CONS = 0.0, ENTITY = "st-axi")
BCFLUX (HEAT, CONS = 0.0, ENTITY = "sb-axi")
BCFLUX (HEAT, CONS = 0.0, ENTITY = "s1-axi")
BCFLUX (HEAT, CONS = 0.0, ENTITY = "s3-axi")
BCFLUX (HEAT, CONS = 0.0, ENTITY = "s2-left")
BCFLUX (HEAT, CONS = 0.0, ENTITY = "g-left")
BCFLUX (HEAT, CONS = 0.0, ENTITY = "g-bot")
BCFLUX (HEAT, CONS = 0.0, ENTITY = "g-axi")
/in face and out face
BCFLUX (HEAT, CONS = 0.0, ENTITY = "st-in")
BCFLUX (HEAT, CONS = 0.0, ENTITY = "sb-in")
BCFLUX (HEAT, CONS = 0.0, ENTITY = "s1-in")
BCFLUX (HEAT, CONS = 0.0, ENTITY = "s2-in")
BCFLUX (HEAT, CONS = 0.0, ENTITY = "s3-in")
BCFLUX (HEAT, CONS = 0.0, ENTITY = "g-in")
BCFLUX (HEAT, CONS = 0.0, ENTITY = "st-out")
BCFLUX (HEAT, CONS = 0.0, ENTITY = "sb-out")
BCFLUX (HEAT, CONS = 0.0, ENTITY = "s1-out")
BCFLUX (HEAT, CONS = 0.0, ENTITY = "s2-out")
BCFLUX (HEAT, CONS = 0.0, ENTITY = "s3-out")
BCFLUX (HEAT, CONS = 0.0, ENTITY = "g-out")
/special
BCNODE( KINE, CONS = 0.00, ENTI = "ft-in" )
BCNODE( KINE, CONS = 0.00, ENTI = "fb-in" )
BCNODE( DISS, CONS = 0.00, ENTI = "ft-in" )
BCNODE( DISS, CONS = 0.00, ENTI = "fb-in" )
/BCNODE( KINE, CONS = 0.001, ENTI = "ft-in" )
/BCNODE( KINE, CONS = 0.001, ENTI = "fb-in" )
/BCNODE( DISS, CONS = 0.00045, ENTI = "ft-in" )
/BCNODE( DISS, CONS = 0.00045, ENTI = "fb-in" )
/IC
/ICNODE( KINE, CONS = 0.003, ALL )
/ICNODE( DISS, CONS = 0.00045, ALL )

/=========================================
/                                  MATERIAL PROPERTIES
/=========================================

/fluid=fl (water)
DENSITY (ADD, SET = "fl", CONS = 0.98)
CONDUCTIVITY (ADD, SET = "fl", CONS = 0.0015750478)
```

Appendix F: (Continued)

```
SPECIFICHEAT (ADD, SET = "fl", CONS = 1.000717)
VISCOSITY( ADD, SET = "fl", TWO-, CONS = 0.00423 )
/EDDY(BOUS)
/pipe=pi (Carbon Steel 1%)
DENSITY (ADD, SET = "pi", CONS = 7.801)
CONDUCTIVITY (ADD, SET = "pi", CONS = 0.102772467)
SPECIFICHEAT (ADD, SET = "pi", CONS = 0.113049713)
/solid=so (concrete)
DENSITY (ADD, SET = "so", CONS = 2.3)
CONDUCTIVITY (ADD, SET = "so", CONS = 0.00239005736)
SPECIFICHEAT (ADD, SET = "so", CONS = 0.210325048)
/ground=gr (sandstone)
DENSITY (ADD, SET = "gr", CONS = 1.5)
CONDUCTIVITY (ADD, SET = "gr", CONS = 0.00239005736)
SPECIFICHEAT (ADD, SET = "gr", CONS = 0.454110899)

END
```

Appendix G: FIDAP Program for Transient Analysis in Hydronic Snow Melting System Simulation

```
FIPREP

/=========================================
/                                   EXECUTION COMMANDS
/=========================================
EXECUTION (NEWJOB)
PROBLEM (ADD, 3-D, TRAN, TURB, NONLINE, ENERGY)
SOLUTION (ADD, SEGR=1000, CR, CGS, VELC=0.01, RESC=0.01, SCHANGE=0)
DATAPRINT (ADD,CONT)
PRINTOUT (NONE)

TIMEINTEGRATION( ADD, BACK, NSTE = 5040, TSTA = 0.0, DT = 5, FIXE)
POSTPROCESS( NBLO = 2 )
120, 600, 120
720, 5040, 720

/=========================================
/                                   ENTITY NAMES
/=========================================
/continium
ENTITY (ADD, NAME = "fluid-t", FLUID, PROP = "fl")
ENTITY (ADD, NAME = "fluid-b", FLUID, PROP = "fl")
ENTITY (ADD, NAME = "pipe-t", SOLID, PROP = "pi")
ENTITY (ADD, NAME = "pipe-b", SOLID, PROP = "pi")
ENTITY (ADD, NAME = "solid-t", SOLID, PROP = "so")
ENTITY (ADD, NAME = "solid-b", SOLID, PROP = "so")
ENTITY (ADD, NAME = "solid-1", SOLID, PROP = "so")
ENTITY (ADD, NAME = "solid-2", SOLID, PROP = "so")
ENTITY (ADD, NAME = "solid-3", SOLID, PROP = "so")
ENTITY (ADD, NAME = "ground", SOLID, PROP = "gr")
/inlet
ENTITY( ADD, NAME = "ft-in", PLOT)
ENTITY( ADD, NAME = "fb-in", PLOT)
ENTITY( ADD, NAME = "pt-in", PLOT)
ENTITY( ADD, NAME = "pb-in", PLOT)
ENTITY( ADD, NAME = "st-in", PLOT)
ENTITY( ADD, NAME = "sb-in", PLOT)
ENTITY( ADD, NAME = "s1-in", PLOT)
ENTITY( ADD, NAME = "s2-in", PLOT)
ENTITY( ADD, NAME = "s3-in", PLOT)
ENTITY( ADD, NAME = "g-in", PLOT)
/MS1
ENTITY( ADD, NAME = "ft-out", PLOT)
ENTITY( ADD, NAME = "ft-axi", PLOT)
ENTITY( ADD, NAME = "ft-intt", WALL, NATTA = "fluid-t", ATTA = "pipe-t")
ENTITY( ADD, NAME = "ft-intb", WALL, NATTA = "fluid-t", ATTA = "pipe-t")
ENTITY( ADD, NAME = "ft-bot", PLOT)
/MS2
ENTITY( ADD, NAME = "fb-out", PLOT)
ENTITY( ADD, NAME = "fb-axi", PLOT)
ENTITY( ADD, NAME = "fb-intt", WALL, NATTA = "fluid-b", ATTA = "pipe-b")
```

Appendix G: (Continued)

```
ENTITY( ADD, NAME = "fb-intb", WALL, NATTA = "fluid-b", ATTA = "pipe-b")

/MS3
ENTITY( ADD, NAME = "pt-out", PLOT)
ENTITY( ADD, NAME = "pt-axi", PLOT)
ENTITY( ADD, NAME = "pt-intt", PLOT)
ENTITY( ADD, NAME = "pt-intb", PLOT)
ENTITY( ADD, NAME = "pt-bot", PLOT)
/MS4
ENTITY( ADD, NAME = "pb-out", PLOT)
ENTITY( ADD, NAME = "pb-axi", PLOT)
ENTITY( ADD, NAME = "pb-intt", PLOT)
ENTITY( ADD, NAME = "pb-intb", PLOT)
/MS5
ENTITY( ADD, NAME = "st-out", PLOT)
ENTITY( ADD, NAME = "st-axi", PLOT)
ENTITY( ADD, NAME = "st-intt", PLOT)
ENTITY( ADD, NAME = "st-intb", PLOT)
ENTITY( ADD, NAME = "st-bot", PLOT)
/MS6
ENTITY( ADD, NAME = "sb-out", PLOT)
ENTITY( ADD, NAME = "sb-axi", PLOT)
ENTITY( ADD, NAME = "sb-intt", PLOT)
ENTITY( ADD, NAME = "sb-intb", PLOT)
/MS7
ENTITY( ADD, NAME = "s1-out", PLOT)
ENTITY( ADD, NAME = "s1-axi", PLOT)
ENTITY( ADD, NAME = "s1-top", PLOT)
ENTITY( ADD, NAME = "s1-bot", PLOT)
/MS8
ENTITY( ADD, NAME = "s2-out", PLOT)
ENTITY( ADD, NAME = "s2-left", PLOT)
ENTITY( ADD, NAME = "s2-bot", PLOT)
/MS9
ENTITY( ADD, NAME = "s3-out", PLOT)
ENTITY( ADD, NAME = "s3-axi", PLOT)
ENTITY( ADD, NAME = "s3-bot", PLOT)
/MS10
ENTITY( ADD, NAME = "g-out", PLOT)
ENTITY( ADD, NAME = "g-axi", PLOT)
ENTITY( ADD, NAME = "g-left", PLOT)
ENTITY( ADD, NAME = "g-bot", PLOT)

/=========================================
/                                  BOUNDARY CONDITION COMMANDS
/=========================================
/inlet
BCNODE (ADD, UX, CONS=0, ENTITY = "ft-in")
BCNODE (ADD, UY, CONS=0, ENTITY = "ft-in")
BCNODE (ADD, UZ, CONS=6.1869, ENTITY = "ft-in")
BCNODE (ADD, UX, CONS=0, ENTITY = "fb-in")
BCNODE (ADD, UY, CONS=0, ENTITY = "fb-in")
BCNODE (ADD, UZ, CONS=6.1869, ENTITY = "fb-in")
```

Appendix G: (Continued)

```
/interface
BCNODE (VELOCITY, ZERO, ENTITY = "ft-intt")
BCNODE (VELOCITY, ZERO, ENTITY = "ft-intb")
BCNODE (VELOCITY, ZERO, ENTITY = "fb-intt")
BCNODE (VELOCITY, ZERO, ENTITY = "fb-intb")
/axi
BCNODE( ADD, UX, ENTI = "ft-axi", ZERO )
BCNODE( ADD, UX, ENTI = "fb-axi", ZERO )
/temperature
BCNODE (ADD, TEMPERATURE, CONS = 80, ENTITY = "ft-in")
BCNODE (ADD, TEMPERATURE, CONS = 80, ENTITY = "fb-in")
/variable heat transfer/storm data
BCFLUX (HEAT, CONS = 1, CURV = 1, FACT = 1, ENTITY = "s1-top")
TMFUNCTION(SET=1, NPOI = 8)
/CURVE=16)
0000 -0.008537614
3600 -0.008686007
7200 -0.008811232
10800 -0.009111684
14400 -0.010630406
18000 -0.012986843
21600 -0.005518975
25200 -0.00667844

/insulation/symmetry
BCFLUX (HEAT, CONS = 0.0, ENTITY = "ft-axi")
BCFLUX (HEAT, CONS = 0.0, ENTITY = "fb-axi")
BCFLUX (HEAT, CONS = 0.0, ENTITY = "pt-axi")
BCFLUX (HEAT, CONS = 0.0, ENTITY = "pb-axi")
BCFLUX (HEAT, CONS = 0.0, ENTITY = "st-axi")
BCFLUX (HEAT, CONS = 0.0, ENTITY = "sb-axi")
BCFLUX (HEAT, CONS = 0.0, ENTITY = "s1-axi")
BCFLUX (HEAT, CONS = 0.0, ENTITY = "s3-axi")
BCFLUX (HEAT, CONS = 0.0, ENTITY = "s2-left")
BCFLUX (HEAT, CONS = 0.0, ENTITY = "g-left")
BCFLUX (HEAT, CONS = 0.0, ENTITY = "g-bot")
BCFLUX (HEAT, CONS = 0.0, ENTITY = "g-axi")
/in face and out face
BCFLUX (HEAT, CONS = 0.0, ENTITY = "pt-in")
BCFLUX (HEAT, CONS = 0.0, ENTITY = "pb-in")
BCFLUX (HEAT, CONS = 0.0, ENTITY = "st-in")
BCFLUX (HEAT, CONS = 0.0, ENTITY = "sb-in")
BCFLUX (HEAT, CONS = 0.0, ENTITY = "s1-in")
BCFLUX (HEAT, CONS = 0.0, ENTITY = "s2-in")
BCFLUX (HEAT, CONS = 0.0, ENTITY = "s3-in")
BCFLUX (HEAT, CONS = 0.0, ENTITY = "g-in")
BCFLUX (HEAT, CONS = 0.0, ENTITY = "pt-out")
BCFLUX (HEAT, CONS = 0.0, ENTITY = "pb-out")
BCFLUX (HEAT, CONS = 0.0, ENTITY = "st-out")
BCFLUX (HEAT, CONS = 0.0, ENTITY = "sb-out")
BCFLUX (HEAT, CONS = 0.0, ENTITY = "s1-out")
BCFLUX (HEAT, CONS = 0.0, ENTITY = "s2-out")
BCFLUX (HEAT, CONS = 0.0, ENTITY = "s3-out")
```

Appendix G: (Continued)

```
BCFLUX (HEAT, CONS = 0.0, ENTITY = "g-out")
/special
BCNODE( KINE, CONS = 0.00, ENTI = "ft-in" )
BCNODE( KINE, CONS = 0.00, ENTI = "fb-in" )
BCNODE( DISS, CONS = 0.00, ENTI = "ft-in" )
BCNODE( DISS, CONS = 0.00, ENTI = "fb-in" )
/IC
ICNODE( ADD, TEMP, CONS = 0, ENTI = "fluid-t" )
ICNODE( ADD, TEMP, CONS = 0, ENTI = "fluid-b" )
ICNODE( ADD, TEMP, CONS = 0, ENTI = "pipe-t" )
ICNODE( ADD, TEMP, CONS = 0, ENTI = "pipe-b" )
ICNODE( ADD, TEMP, CONS = 0, ENTI = "solid-t" )
ICNODE( ADD, TEMP, CONS = 0, ENTI = "solid-b" )
ICNODE( ADD, TEMP, CONS = 0, ENTI = "solid-1" )
ICNODE( ADD, TEMP, CONS = 0, ENTI = "solid-2" )
ICNODE( ADD, TEMP, CONS = 0, ENTI = "solid-3" )
ICNODE( ADD, TEMP, CONS = 0, ENTI = "ground" )

/=========================================
/                                  MATERIAL PROPERTIES
/=========================================

/fluid=fl (water)
DENSITY (ADD, SET = "fl", CONS = 0.98)
CONDUCTIVITY (ADD, SET = "fl", CONS = 0.0015750478)
SPECIFICHEAT (ADD, SET = "fl", CONS = 1.000717)
VISCOSITY( ADD, SET = "fl", TWO-, CONS = 0.00423 )
/pipe=pi (Carbon Steel 1%)
DENSITY (ADD, SET = "pi", CONS = 7.801)
CONDUCTIVITY (ADD, SET = "pi", CONS = 0.102772467)
SPECIFICHEAT (ADD, SET = "pi", CONS = 0.113049713)
/solid=so (concrete)
DENSITY (ADD, SET = "so", CONS = 2.3)
CONDUCTIVITY (ADD, SET = "so", CONS = 0.00239005736)
SPECIFICHEAT (ADD, SET = "so", CONS = 0.210325048)
/ground=gr (sandstone)
DENSITY (ADD, SET = "gr", CONS = 1.5)
CONDUCTIVITY (ADD, SET = "gr", CONS = 0.00239005736)
SPECIFICHEAT (ADD, SET = "gr", CONS = 0.454110899)

END
```

Appendix H: Design of Experiment on Parameters and Quantitative Error Analysis of the Grid Test

Design of experiment

Design of experiment is a technique to study the effect of different parameters on a specific data output by applying a combination of parameter changes. Using combinations of three parameters will end up with 8 runs and 8 data outputs. This study was performed at two different locations: Z = 0.4 and Z = 0.8. The parameters used in this study are: Reynolds number, magnetic field intensity, and tube diameter. The parameter combinations used are listed together with the resulting data as follows:

		Z = 0.4	Z = 0.8
Re = 1000, G = 5, d = 0.036	Nu =	7.55	6.64
Re = 1600, G = 5, d = 0.036	Nu =	8.92	7.71
Re = 1000, G = 10, d = 0.036	Nu =	7.55	6.64
Re = 1600, G = 10, d = 0.036	Nu =	8.92	7.71
Re = 1000, G = 5, d = 0.048	Nu =	9.23	8.01
Re = 1600, G = 5, d = 0.048	Nu =	10.94	9.34
Re = 1000, G = 10, d = 0.048	Nu =	9.23	8.01
Re = 1600, G = 10, d = 0.048	Nu =	10.94	9.34

The contrast constants for each parameter and parameter combinations are obtained by performing a series of mathematical operations, adding, and subtracting the data according to the run they were generated from. The contrast for the parameters and parameter combinations are shown as follows:

		Z = 0.4	Z = 0.8
Contrast Re	=	6.16	4.80
Contrast G	=	0	0
Contrast Re, G	=	0	0
Contrast d	=	7.40	6.00
Contrast Re, d	=	0.68	0.52
Contrast G, d	=	0	0
Contrast Re, G, d	=	0	0

Sum of the squares for the effects are calculated using the following formula:

$$SS_{eff} = \frac{(Contrast)^2}{2^3 n}$$

where,

n = number of runs

Appendix H: (Continued)

Then, Total sum of squares is calculate by adding all the sum of squares as follows:

$$SS_T = SS_{\text{Re}} + SS_G + SS_{\text{Re},G} + \ldots\ldots\ldots\ldots + SS_{\text{Re},G,d}$$

This is done for each effect ending up with the following results:

		Z = 0.4	Z = 0.8
SS_{Re}	=	0.5929	0.3600
SS_G	=	0	0
$SS_{Re, G}$	=	0	0
SS_d	=	0.8556	0.5625
$SS_{Re, d}$	=	0.007225	0.004225
$SS_{G, d}$	=	0	0
$SS_{Re, G, d}$	=	0	0

The percentage contribution of each of the effects is obtained by taking the ratio of the sum of squares of the effect to the total sum of squares and then multiplying the results with 100. For example, the percentage contribution of effect Re is given as:

$$\textit{Percentage contribution of } \text{Re} = \frac{SS_{\text{Re}}}{SS_T} \times 100$$

The factor having the highest percentage contribution is said to have the most effect on the experiment. The results were as follows:

		Z = 0.4	Z = 0.8
% contribution of Re	=	40.73 %	38.85 %
% contribution of G	=	0 %	0 %
% contribution of Re, G	=	0 %	0 %
% contribution of d	=	58.78 %	60.70 %
% contribution of Re, d	=	0.496 %	0.456 %
% contribution of G, d	=	0 %	0 %
% contribution of Re, G, d	=	0 %	0 %

The results clearly show that the change in Reynolds number and diameter have the most effect on Nusselt number but the change in the magnetic field is the least.

Appendix H: (Continued)

Quantitative error analysis

To insure accurate results, the number of elements that were used to mesh the geometry had to be deemed adequate. This was done by performing computations for several combinations of elements in the axial and cross-sectional directions. These combinations were: 4 x 8 x 20, 6 x 12 x 30, and 8 x 16 x 40. The quantitative difference in grid independence can be calculated using the equation:

$$T = C + \frac{D}{N^e}$$

N is the number of elements along an axis, and C, D, and e are constants to be evaluated. Three different grid tests provides three equations with known T and N. This results in a set of non-linear equations with three variables. An initial value of e was assumed, and after performing a number of iterations, a correct value for e is determined. Afterwards, the percentage error could be obtained by:

$$\left|\frac{T - C}{C}\right| \times 100$$

This test is performed at two different axial locations: Z = 0.4 and Z = 0.8. The results are shown below.

	Z = 0.4	Z = 0.8
e =	0.561867	1.204276
C =	27.49269	30.61695
D =	8.22457	41.05001
% error for 4 x 8 x 20 =	5.56 %	3.63 %
% error for 6 x 12 x 30 =	4.42 %	2.23 %
% error for 8 x 16 x 40 =	3.76 %	1.58 %

About the Author

Abdullatif Gari was born in Saudi Arabia and lived there until he achieved his Bachelor's degree in April of 1994 in Mechanical Engineering Department at King Abdul Aziz University in Jeddah. He received a scholarship from his country to continue his higher education career abroad. He finished his Master's degree in Mechanical Engineering at Oklahoma State University in December of 1999. He also finished his Ph.D. degree in Mechanical Engineering at the University of South Florida. He is going to work as an Assistant Professor in the thermal Engineering Department at King Abdul Aziz University in Jeddah, Saudi Arabia.